UNIVERSITÀ DEGLI STUDI DI TRIESTE

XX CICLO
DEL DOTTORATO DI RICERCA IN
FISICA

Measurement of transverse spin effects in COMPASS

Settore scientifico-disciplinare
FISICA NUCLEARE E SUBNUCLEARE (FIS/04)

Dottoranda
Federica Sozzi

Coordinatore del collegio dei docenti
chiar.mo prof. Gaetano Senatore

Tutore
chiar.mo prof. Paolo Schiavon

Relatore
chiar.mo prof. Paolo Schiavon

Correlatrice
chiar.ma prof.ssa Anna Martin

Contents

Introduction

The study of the spin structure of the nucleon has been a central issue along the last decades. The importance of understanding the contributions to the proton spin for longitudinal polarization has been widely recognized: after the surprising result of the European Muon Collaboration (EMC, 1987) that the spin of the quarks only contributes to a small fraction $\Delta\Sigma$ of the proton spin [1], an intense theoretical and experimental activity has been devoted to the investigation of the origin of the nucleon spin structure. Several deep-inelastic scattering experiments on proton, deuteron and ^{3}He (SMC at CERN, E143, E155 at SLAC and HERMES at DESY) have confirmed the original EMC result, establishing $\Delta\Sigma$ between 20% and 30%. The spin equation for the nucleon can be written as:

$$\frac{1}{2} = \frac{1}{2}\Delta\Sigma + \Delta G + \langle L_z \rangle \tag{1}$$

where $\Delta\Sigma$ is the contribution of the quark spins, ΔG is the contribution of the gluons, and $\langle L_z \rangle$ is a possible contribution from the gluons and quarks orbital angular momentum. The smallness of $\Delta\Sigma$ implies the investigation of the other two terms of the equation. While measurements of $\langle L_z \rangle$ are for the moment out of reach, direct measurements of ΔG have become a priority issue for both polarized semi-inclusive deep inelastic scattering (SIDIS) experiments as COMPASS, HERMES, and for high energy polarized $p\,p$ scattering experiments, as those at RHIC.

The knowledge of the helicity distributions does not exhaust the spin structure of the nucleon. To fully specify the quark structure of the nucleon at the twist - two level, the transverse spin distribution $\Delta_T q(x)$ must be added to the momentum distribution $q(x)$ and to the helicity distribution $\Delta q(x)$. The transversity distribution function $\Delta_T q(x)$ describes the probability of finding transversely polarized quarks in a transversely polarized proton. It was first introduced in 1979 [2] and was then reappraised [3, 4] in 1990, when the interest on transverse spin physics was renewed thanks to many different experimental results.

The importance of transverse spin effects at high energy in hadronic physics was first suggested by the discovery in 1976 that Λ hyperons were produced polarized in unpolarized collisions of a 300 GeV proton beam on various targets (Be and p) at Fermilab, experiment E8 [5]. This result (fig. 1.a) was largely unexpected and

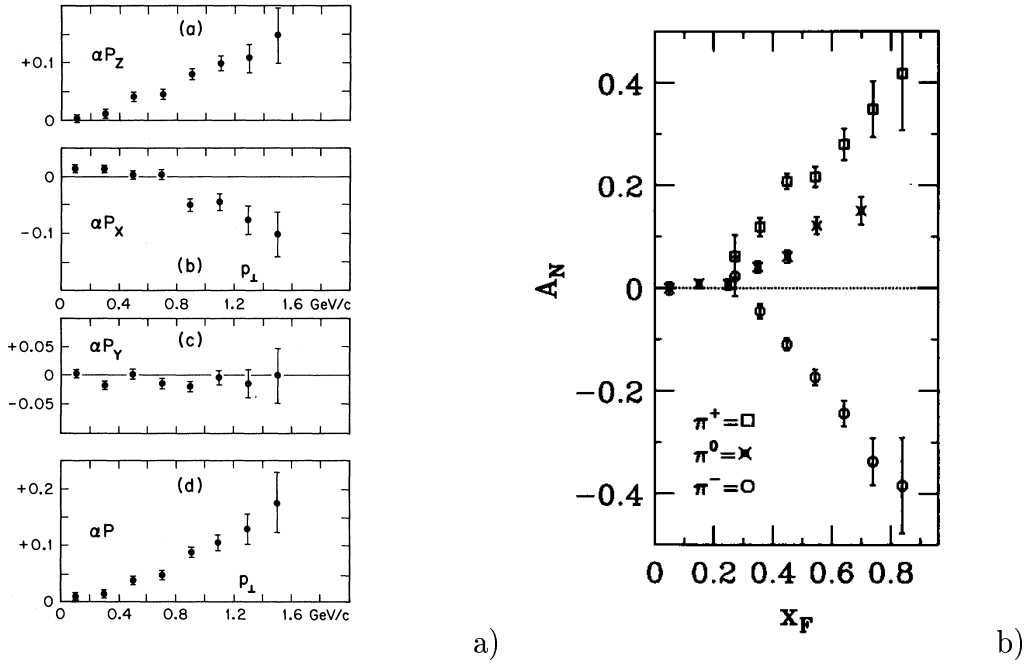

Figure 1: **a)** Λ polarization measured for inclusive production from proton-Beryllium scattering at Fermilab [5]; **b)** asymmetries in the inclusive production of pions using a polarized proton beam at Fermilab [8].

could not be easily explained: in particular it was not clear if it could be interpreted within a hard scattering framework, or was due to unknown soft physics processes.

Large single transverse spin asymmetries were successively observed at CERN [6] and in IHEP [7], in inclusive π^0 production in polarized pp scattering. The common belief was that these asymmetries were due to low energy phenomena, that would disappear at higher energy.

During the 90s, the E704 [8] Collaboration at Fermilab set the stage at a different level, thanks to the large center of mass energy available ($\sqrt{s} \sim 20$ GeV) and the extension in the covered range of hadron transverse momentum, P_T^h. The E704 Collaboration collected single spin asymmetries data for pp and $p\bar{p}$ collisions using secondary polarized proton antiproton beams for different produced hadrons (p and Λ). The main results gathered by the E704 Collaboration were the very large single spin asymmetries, up to 30-40% measured in inclusive pion production in the large x_f region, both for polarized proton and antiprotons beams colliding on hydrogen target (fig. 1.b). For both charged and neutral pions the asymmetries are compatible with zero at low x_f, and increase for higher x_f values. The asymmetries have different signs for opposite charge of the pions. Similar results were achieved also in inclusive Λ and η production. In order to study and to understand the origin

of such effects, the RHIC-Spin collaboration at BNL put forward a proposal for polarized $p\,p$ experiments [9]; in Europe, the HELP Collaboration [10], and later on the HERMES and the COMPASS Collaborations proposed SIDIS experiments with transversely polarized targets.

Starting from the end of the 90s, very interesting results on transverse single spin asymmetries in polarized hadronic collisions came up and are currently collected at RHIC by different collaboration (STAR, PHENIX, BRAHMS). For the first time, polarized proton proton collision, with one or both beams longitudinally or transversely polarized, have been studied at center of mass energies as large as 200 GeV, with the possibility to reach $\sqrt{s} \sim 500$ GeV in near future. The results from STAR [11] for single transverse spin asymmetries for forward neutral pion production at high pseudo-rapidity of $\langle \eta \rangle = 3.8$ with a proton beam transversely polarized are in agreement with the E704 results (fig. 2.b). At mid-rapidity, the single spin asymmetries for both neutral and charged pions were found to be consistent with zero, as the results from E704 at lower energies and in similar kinematical conditions.

Even if perturbative QCD can describe with high accuracy the cross sections at a similar energy and kinematical region, these large effects cannot be explained in the standard collinear pQCD framework, in which the intrinsic transverse momentum k_T effect is integrated and all partons/hadrons are assumed to be collinear with parent hadrons/partons. The failure of standard collinear pQCD led to a special attention on the role played by parton distributions and fragmentation functions in pQCD approaches, and in particular on the intrinsic transverse momentum of partons inside hadrons involved in high-energy processes. It was originally suggested by Sivers [12] that pQCD with the inclusion of transverse momentum effects in parton distribution functions could be able to explain such large transverse physics effects. The Sivers function is related to an asymmetry in the intrinsic transverse momentum of the quarks or gluons in a transversely polarized proton, resulting in an azimuthal asymmetry in the hadrons produced in the quark fragmentation process. Another possible explanation is that the large asymmetries can be created in the fragmentation process of a transversely polarized quark in the final hadron, as suggested by Collins [13]. The so called Collins asymmetry comes from the coupling of the Collins fragmentation function with the transversity distribution $\Delta_T q(x)$.

The non trivial effects underlying the large asymmetries observed at E704 led to different interpretations along the time. In a first moment, the asymmetries were interpreted as the manifestation of the Collins effect, and later on as a combination of the Collins and Sivers effects. Indeed, it has been shown that in the complete asymmetry formula both terms appear, together with contributions due to other transverse momentum dependent parton distribution functions, like the Boer-Mulders function [14, 15] convoluted with the transversity distribution. Predictions [16] using a parametrization for the Sivers function explain very well the

data (fig. 2.a). In a similar way, also the STAR results have been interpreted as resulting from the Sivers effect (fig. 2.b).

a) b)

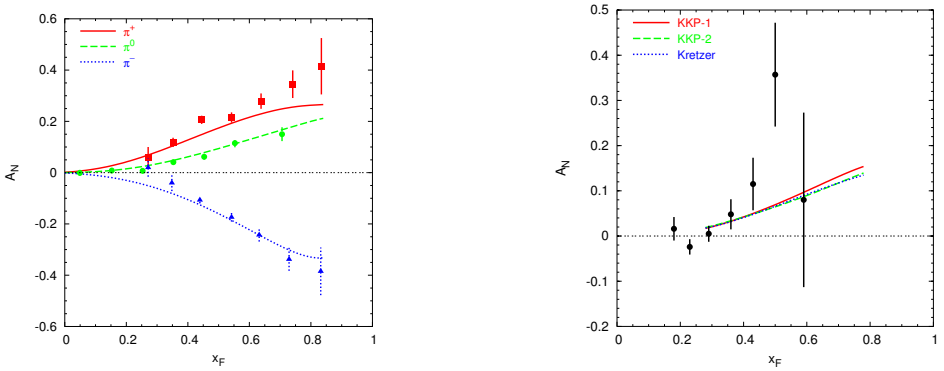

Figure 2: **a)** A_N asymmetries measured for inclusive pions production in pp collisions at E704 [8]; the curves are a fit on π^0 data and predictions for charged pions due to the Sivers effect from [16] **b)** A_N for inclusive π^0 production in pp collisions at STAR [11]; the curves are predictions for STAR kinematics due to the Sivers effect [16].

At variance with the pp experiments, in the semi-inclusive hadron production in deep inelastic scattering of leptons off a transversely polarized target, the Collins and the Sivers effects can be disentangled, since they give rise to different azimuthal asymmetries. The Collins and Sivers effects do not exhaust the possible mechanisms giving rise to the asymmetries: the complete description of a quark in the nucleon and in the fragmentation process involves several parton distribution functions and fragmentation functions depending on the intrinsic transverse momentum, that can be studied in SIDIS experiments. The measurements of the Collins and Sivers asymmetries from the COMPASS and HERMES experiments are presented in section 1.4.

Transverse spin effects can be probed also measuring azimuthal asymmetries in unpolarized cross sections for e^+e^- processes. The Belle Collaboration at the KEKB asymmetric-energy e^+e^- storage rings has published very interesting results on the inclusive production of hadrons pairs (namely pion pairs) in e^+e^- annihilation [17]. They have found evidence of statistically significant azimuthal asymmetries. As we will see in details in section 5.4, these results are related and give access to the product of two Collins fragmentation functions, allowing the extraction of the transversity distribution function from the Collins asymmetries measured in SIDIS.

Today the importance of transverse spin effects has been recognized by the entire spin physics community and is a main part of the scientific program of different experiments using different channels: pp and $p\bar{p}$ collisions, polarized SIDIS and

e^+e^- annihilation.

The study of transverse spin asymmetries in polarized SIDIS reaction is one of the goals of the COMPASS experiment at CERN. COMPASS has taken data from 2002 to 2004, using a deuterium target and a muon beam of 160 GeV/c; for 20% of the time the target was polarized transversely with respect to the beam direction. The transversity distribution function is studied at COMPASS via different probes: Λ production, two-hadrons asymmetries and single hadron asymmetries. The measurements of the Collins and Sivers asymmetries for unidentified hadrons have been published for the first data taking period (2002) [18] and for the total collected statistics [19].

The work done for this thesis has been devoted to the measurement of the Collins and Sivers asymmetries on identified hadrons (pions and kaons). The thesis is structured as follows: in Chapter 1 the inclusive polarized DIS approach to access helicity distributions is briefly reviewed, and the relevance of the semi-inclusive DIS to assess transverse spin effects is presented. The Collins and Sivers asymmetries are introduced, and an overview of the existing measurements is given. Chapter 2 contains a description of the COMPASS apparatus. The COMPASS RICH-1 detector is the argument of Chapter 3: after a brief description of the detector, the work done to understand its response during data taking, which is of big importance in order to properly use the detector capabilities to identify the hadrons, is presented. In Chapter 4 the data analysis, from the stability studies, the selection of the SIDIS events in the data, the method used to extract the asymmetries and the systematic studies, is presented. In the last part the final measurements of the Collins and Sivers asymmetries for pions and kaons are shown. The interpretation of the results is the subject of the Chapter 5. With a flavor separation analysis on the measured asymmetries, together with the asymmetries of the HERMES and Belle experiments, we extracted the Sivers and the transversity distribution functions for the u and d-quark, and the Collins fragmentation functions. The analysis has been done on the SIDIS asymmetries as a function of x, while the SIDIS asymmetries as a function of z have been used to check the predictions corresponding to our results. Other similar works exist in literature, but this global analysis uses different parameterizations for the extracted functions and are based on the pion asymmetries presented in this thesis and on recent data from HERMES and Belle. The conclusions and the outlook are presented in the last chapter.

Chapter 1

The spin structure of the nucleon

The transverse structure of the nucleon is investigated by COMPASS by means of semi-inclusive Deep Inelastic Scattering reactions of muons on a polarized nucleon target. The Deep Inelastic Scattering (DIS) technique has been of the utmost importance along the last 40 years to achieve the actual knowledge about the nucleon structure. In particular, most of the experimental knowledge about the quark unpolarized distribution and quark helicity distribution derives from (polarized) DIS experiment. In the first part of the chapter the DIS formalism is recalled, together with the experimental measurements to access the unpolarized and polarized structure functions; an interpretation of the functions via the naïve and the QCD improved parton model is given. The transversity distribution function is then introduced, with a short historical introduction and a review of its characteristics. One way to access transversity is the semi-inclusive DIS: after having shown the complete cross section expression for this process, the structure functions containing the Collins and Sivers distribution functions are object of further attention. In particular it is shown how the Collins and Sivers asymmetries are measured in COMPASS. The final part of the chapter contains a brief description of the experimental techniques to access the transversity function used in outgoing experiments.

1.1 Polarized inclusive DIS

Consider the inelastic scattering of polarized leptons on polarized nucleons indicated in fig. 1.1. In the Deep Inelastic Scattering, the nucleon structure breaks up and forms a final hadronic state X:

$$\ell(\mathbf{k}) + \mathbf{N}(\mathbf{P}) \rightarrow \ell'(\mathbf{k}') + \mathbf{X} \ . \tag{1.1}$$

In inclusive DIS, only the final lepton is detected, while the hadrons produced are detected in semi-inclusive DIS; if the final hadronic state X is totally reconstructed,

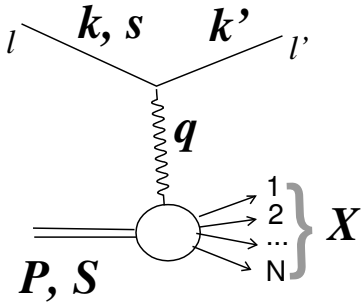

Figure 1.1: Deep Inelastic Scattering

the process is called exclusive. For a fixed target experiment as COMPASS, the 4-momentum of the initial nucleon in the laboratory frame is $\mathbf{P}$= (M, $\vec{0}$), with M the mass of the nucleon; the 4-momentum of the incoming (outgoing) lepton is $\mathbf{k}$ = (E,$\vec{p}$) ($\mathbf{k'}$ = (E', $\vec{p'}$)). The relevant kinematic variables used to describe a DIS reaction are summarized in table 1.1.

The squared momentum transfer Q^2 is a measure of the spatial resolution of the reaction: in DIS processes, Q^2 is large enough to resolve the constituents of the nucleons. The kinematics of the DIS reaction in COMPASS is characterized by Q^2 values between 1 and 100 (GeV/c)^2 and a center of mass energy $\sqrt{s} \sim 300$ GeV, the momentum of the initial lepton being 160 GeV/c.

The Bjorken scaling variable x can vary in the range between 0 and 1, and gives an indication of the inelasticity of the reaction: in the elastic case, the hadronic mass of the final state is equal to the nucleon initial mass, $W = M$, implying $x = 1$; on the contrary, in the case $W > M$, x is below 1; the DIS regime is defined when $Q^2 \to \infty$ and $\nu \to \infty$, while x takes a finite value (Bjorken limit).

The differential cross section for detecting the final lepton in the solid angle $d\Omega$ and in the final energy range (E', $E' + dE'$) in the laboratory frame, can be written as [20, 21]:

$$\frac{d^2\sigma}{d\Omega\ dE'} = \frac{\alpha^2}{2Mq^4}\frac{E'}{E}\ L_{\mu\nu}\ W^{\mu\nu}\,; \tag{1.2}$$

where α is the fine structure constant, and $L_{\mu\nu}$ and $W_{\mu\nu}$ the leptonic and hadronic tensor respectively. In the following, we will assume the one photon exchange approximation and we will sum over all the spin configuration of the final lepton (since the scattered lepton polarization is not measured in the experiment). Considering the behavior under μ, ν interchange, both tensors can be split in a symmetric (S)

θ	lepton scattering angle in the lab system
$s = (\mathbf{P} + \mathbf{k})^2 \overset{lab}{\sim} M^2 + 2ME$	squared center of mass energy
$\mathbf{q} = \mathbf{k} - \mathbf{k}'$	4-momentum transfer to the target
$Q^2 = -\mathbf{q}^2 \overset{lab}{\sim} 4EE' sin^2(\frac{\theta}{2})$	squared momentum transfer
$\nu = \frac{\mathbf{P}\cdot\mathbf{q}}{M} \overset{lab}{=} E - E'$	in lab the energy transfer from the lepton to the nucleon
$W^2 = (\mathbf{P} + \mathbf{q})^2 \overset{lab}{=} M^2 + 2M\nu - Q^2$	squared mass of the hadronic final state
$x = \frac{Q^2}{2\mathbf{P}\cdot\mathbf{q}} \overset{lab}{=} \frac{Q^2}{2M\nu}$	Bjorken scaling variable
$y = \frac{\mathbf{P}\cdot\mathbf{q}}{\mathbf{P}\cdot\mathbf{k}} \overset{lab}{=} \frac{\nu}{E}$	fractional energy transfer to the nucleon

Table 1.1: The kinematical variables used to describe a DIS process. The relationships with the label "lab" hold in the laboratory frame in case of a fixed target experiment, neglecting the lepton mass.

part, not depending on the spin, and in a antisymmetric (A) part, depending on the spin:

$$\begin{aligned} L_{\mu\nu}(\mathbf{k}, \mathbf{s}; \mathbf{k}') &= L^{(S)}_{\mu\nu}(\mathbf{k}; \mathbf{k}') + iL^{(A)}_{\mu\nu}(\mathbf{k}, \mathbf{s}; \mathbf{k}'); \\ W_{\mu\nu}(\mathbf{q}; \mathbf{P}, \mathbf{S}) &= W^{(S)}_{\mu\nu}(\mathbf{q}; \mathbf{P}) + i\, W^{(A)}_{\mu\nu}(\mathbf{q}; \mathbf{P}, \mathbf{S}); \end{aligned} \tag{1.3}$$

therefore the cross section reads:

$$\frac{d^2\sigma}{d\Omega\, dE'} = \frac{\alpha^2}{2Mq^4}\frac{E'}{E}\left[L^{(S)}_{\mu\nu}\, W^{\mu\nu(S)} - L^{(A)}_{\mu\nu}\, W^{\mu\nu(A)}\right]. \tag{1.4}$$

At variance with the leptonic tensor, that can be calculated in QED, it is not possible to evaluate exactly the hadronic tensor, due to the complex inner structure of the nucleon. Therefore a parametrization involving structure functions is used.

If we consider cross sections or difference between cross sections with particular initial and final polarization, it is possible to single out the two terms $L^{(S)}_{\mu\nu}\, W^{\mu\nu(S)}$ and $L^{(A)}_{\mu\nu}\, W^{\mu\nu(A)}$. For example, the unpolarized cross section, obtained summing over all the spin configuration of the initial lepton and of the nucleon, reads:

$$\frac{d^2\sigma^{unp}}{d\Omega\, dE'}\left(\mathbf{k}, \mathbf{P}; \mathbf{k}'\right) = \frac{1}{4}\sum_{s,S}\frac{d^2\sigma}{d\Omega\, dE'}\left(\mathbf{k}, \mathbf{s}, \mathbf{P}, \mathbf{S}; \mathbf{k}'\right) = \frac{\alpha^2}{2Mq^4}\,\frac{E'}{E}\, 2L^{(S)}_{\mu\nu}\, W^{\mu\nu(S)}. \tag{1.5}$$

Neglecting the lepton mass, in the laboratory frame the cross section can be written explicitly as:

$$\frac{d^2\sigma^{unp}}{d\Omega\ dE'} = \frac{4\alpha^2 E'^2}{q^4}\left[2W_1 \sin^2\frac{\theta}{2} + W_2 \cos^2\frac{\theta}{2}\right]; \tag{1.6}$$

where W_1 and W_2 are the unpolarized structure functions. In the Bjorken limit, they are known to approximately scale:

$$MW_1(\mathbf{P}\cdot\mathbf{q}, Q^2) \to F_1(x); \quad \nu W_2(\mathbf{P}\cdot\mathbf{q}, Q^2) \to F_2(x); \tag{1.7}$$

meaning that $F_{1,2}$ vary very slowly with Q^2 at fixed x. The $F_{1,2}$ structure functions describe the deviation from the cross section for the scattering of a spin-1/2 particle off a point like constituent; they correspond to the electrical and magnetic form factor in lepton-nucleon elastic scattering. The actual knowledge about the F_2 form factor is shown in fig. 1.2; the F_1 form factor is connected to F_2 through the following relationship:

$$F_1 = \frac{F_2(1+\gamma^2)}{2x(1+R)}, \tag{1.8}$$

where $\gamma = \frac{2Mx}{Q}$ and R is the ratio of cross sections for longitudinally and transversally polarized virtual photons on an unpolarized target. In naive quark parton model, eq. 1.8 simplifies in the so called Callan-Gross relationship, $2xF_1(x) = F_2(x)$.

Differences of cross sections with opposite target spins single out the $L^{(A)}_{\mu\nu}\ W^{\mu\nu(A)}$ term of the cross section:

$$\frac{d^2\sigma^{s,S}}{d\Omega\ dE'} - \frac{d^2\sigma^{s,-S}}{d\Omega\ dE'} = -\frac{\alpha^2}{2Mq^4}\ \frac{E'}{E}\ 4L^{(A)}_{\mu\nu}\ W^{\mu\nu(A)} = \tag{1.9}$$

$$= \frac{8m\alpha^2 E'}{q^4 E}\left\{\left[(\mathbf{q}\cdot\mathbf{S})(\mathbf{q}\cdot\mathbf{s}) + Q^2(\mathbf{s}\cdot\mathbf{S})\right] MG_1 + Q^2\Big[(\mathbf{s}\cdot\mathbf{S})(\mathbf{P}\cdot\mathbf{q}) - (\mathbf{q}\cdot\mathbf{S})(\mathbf{P}\cdot\mathbf{s})\Big]\frac{G_2}{M}\right\};$$

here $G_1(\mathbf{P}\cdot\mathbf{q}, Q^2)$ and $G_2(\mathbf{P}\cdot\mathbf{q}, Q^2)$ are the polarized structure functions. They also, in the Bjorken limit, are approximately expected to scale:

$$\frac{(\mathbf{P}\cdot\mathbf{q})^2}{\nu}\ G_1(\mathbf{P}\cdot\mathbf{q}, Q^2) \to g_1(x); \quad \nu\ (\mathbf{P}\cdot\mathbf{q})\ G_2(\mathbf{P}\cdot\mathbf{q}, Q^2) \to g_2(x)\,. \tag{1.10}$$

1.1.1 Measurement of g_1 and g_2

To assess the polarized structure functions g_1 and g_2 we consider particular spin configurations of the incoming leptons and target nucleons. In the case of longitudinally polarized leptons, that is initial leptons with spin along ($\rightarrow$) or opposite ($\leftarrow$) the direction of motion, and of nucleons at rest polarized along ($\Rightarrow$) or opposite ($\Leftarrow$) the initial lepton direction of motion, eq. 1.9 becomes [20, 21]:

$$\frac{d^2\sigma^{\overrightarrow{\Rightarrow}}}{d\Omega\ dE'} - \frac{d^2\sigma^{\overrightarrow{\Leftarrow}}}{d\Omega\ dE'} = -\frac{4\alpha^2}{Q^2}\ \frac{E'}{E}\left[(E + E'\cos\theta)M\frac{\nu}{(\mathbf{P}\cdot\mathbf{q})^2}g_1 - Q^2\frac{g_2}{\nu(\mathbf{P}\cdot\mathbf{q})}\right]. \tag{1.11}$$

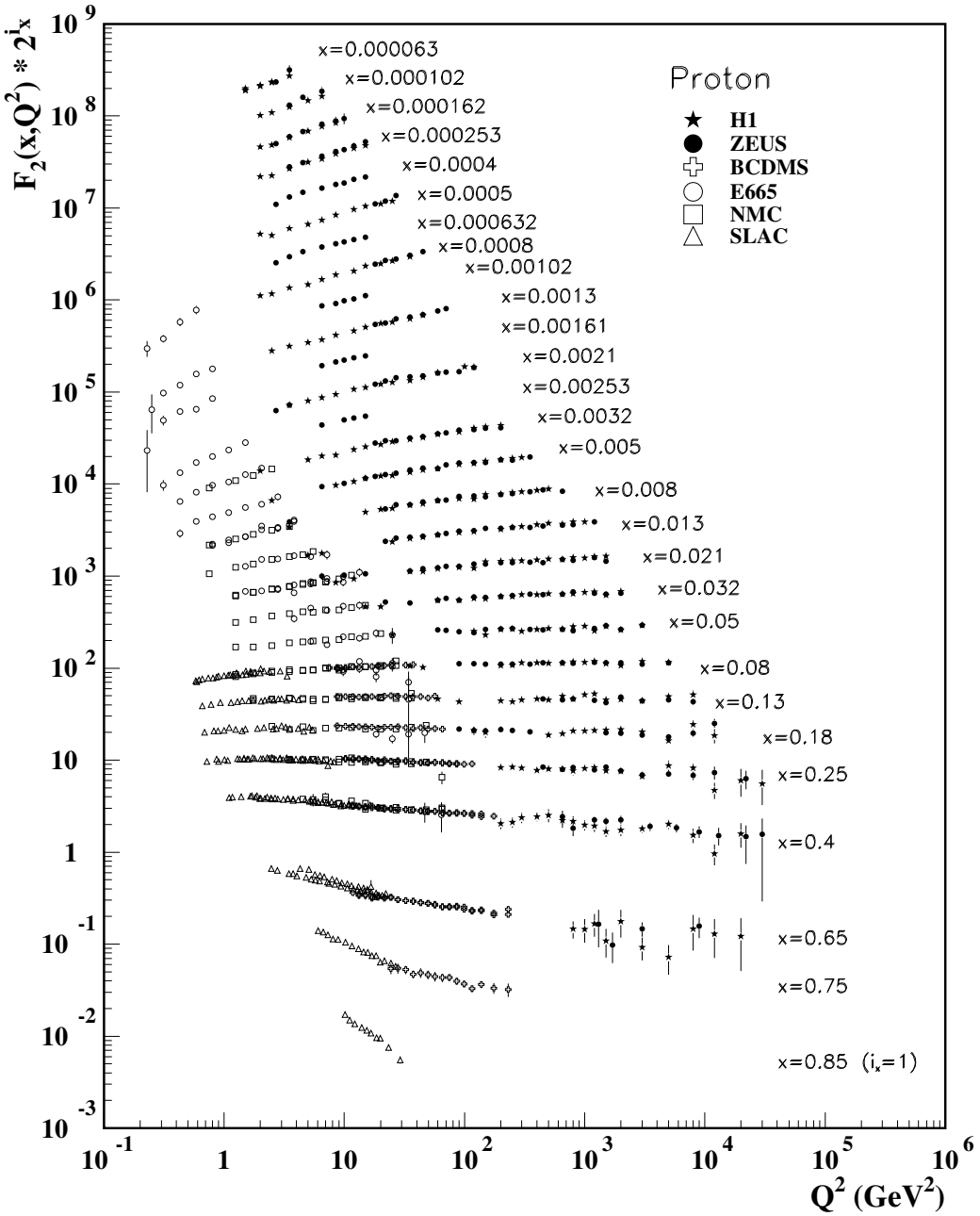

Figure 1.2: The proton structure function F_2^p measured in electromagnetic scattering of positrons on protons (experiments ZEUS[22] and H1[23]) at HERA, for $x > 0.00006$, and for electrons (SLAC[24]) and muons (BCDMS[25], E665[26], NMC[27]) on a fixed target. Statistical and systematic errors added in quadrature are shown. The data are plotted as a function of Q^2 in bins of x. For clarity, F_2^p has been multiplied by 2^{i_x}, where i_x is the number of the x bin, ranging from $i_x = 1$ ($x = 0.85$) to $i_x = 28$ ($x = 0.000063$). The figure has been taken from [28].

If the nucleons are transversely polarized with respect to the direction of the incoming lepton, the cross section is given by:

$$\frac{d^2\sigma^{\rightarrow\Uparrow}}{d\Omega\, dE'} - \frac{d^2\sigma^{\rightarrow\Downarrow}}{d\Omega\, dE'} = -\frac{4\alpha^2}{Q^2}\,\frac{E'^2}{E}\,\sin\theta\cos\phi\left(M\frac{\nu}{(\mathbf{P}\cdot\mathbf{q})^2}g_1 + 2E\frac{g_2}{\nu(\mathbf{P}\cdot\mathbf{q})}\right), \quad (1.12)$$

where ϕ is the azimuthal angle between the scattering plane and the $(\hat{p}, \hat{S})$ polarization plane.

In the performed experiments using a longitudinally polarized target the quantity actually measured is the longitudinal spin-spin asymmetry:

$$A_{\parallel} \equiv \frac{d\sigma^{\rightleftarrows} - d\sigma^{\rightrightarrows}}{d\sigma^{\rightrightarrows} + d\sigma^{\rightleftarrows}}\,, \quad (1.13)$$

where $d\sigma$ is short for $d^2\sigma/(d\Omega\, dE')$, and the denominator is simply twice the unpolarized cross sections.

The measurement of $A_{\parallel}$ gives us information on the combination of g_1 and g_2, rather than on g_1 or g_2 alone. However, the g_2 term is usually neglected due to its smallness, and $A_{\parallel}$ provides essentially a direct measurement of the polarized structure function g_1. The measurements of g_1 from DIS experiments on proton, deuteron, and neutron are shown in figure 1.3.

To measure the structure function g_2, one should consider other spin-spin asymmetries. By scattering longitudinally polarized leptons on transversely polarized nucleons, one can measure the asymmetry:

$$A_{\perp} \equiv \frac{d\sigma^{\rightarrow\Downarrow} - d\sigma^{\rightarrow\Uparrow}}{d\sigma^{\rightarrow\Uparrow} + d\sigma^{\rightarrow\Downarrow}}\,; \quad (1.14)$$

where, again, $d\sigma$ is short for $d^2\sigma/(d\Omega\, dE')$ and the denominator is twice the unpolarized cross section. From eq. 1.12, it is clear as a measurement of $A_{\perp}$ provides direct information on a combination of g_2 and g_1. In this case the usual approach is to extract g_2 relying on the knowledge of g_1 obtained from the $A_{\parallel}$ measurement. The first measurements of g_2 date back to less than a decade ago; in the last few years accurate results have been reported by the E155 collaboration [37, 38] and the E143 collaboration [30].

1.1.2 The parton model

A simple interpretation of the form factors can be derived in the framework of the quark parton model, in which the hadron is composed by granular constituents, the partons. The parton model interpretation has been suggested by the scaling

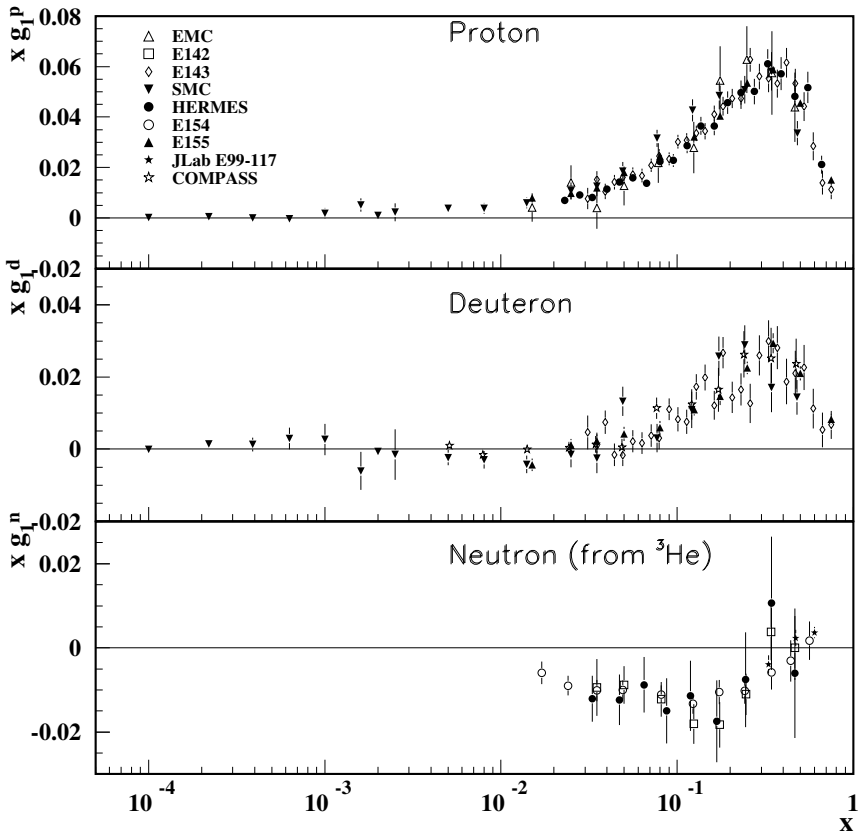

Figure 1.3: The spin-dependent structure function $xg_1(x)$ of the proton (top), deuteron (middle), and neutron (bottom) measured in deep inelastic scattering of polarized electrons/positrons: E142[29] ($Q^2\sim$ 0.3–10 GeV^2), E143[30] ($Q^2\sim$ 0.3 – 10 GeV^2), E154[31] ($Q^2\sim$ 1 – 17 GeV^2), E155[32] ($Q^2\sim$ 1 – 40 GeV^2), JLab E99-117[33]($Q^2\sim$ 2.71 – 4.83 GeV^2), HERMES[34] ($Q^2\sim$ 0.8 – 20 GeV^2) and muons: EMC[1] ($Q^2\sim$ 1.5 – 100 GeV^2), SMC[35] ($Q^2\sim$ 0.01 – 100 GeV^2), COMPASS[36] ($Q^2\sim$ 1 – 100 GeV^2), shown at the measured Q^2 (except for EMC data given at $Q^2 = 10.7$ GeV^2 and E155 data given at $Q^2 = 5$ GeV^2). Statistical and systematic errors are added in quadrature. The figure has been taken from [28].

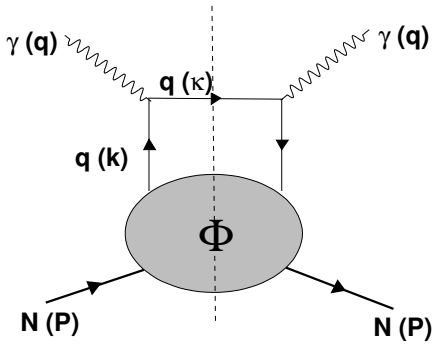

Figure 1.4: The so-called handbag diagram.

behavior of the F_1 and F_2 form factors, which implies the nucleon to be composed of point-like constituents. It is usual to consider the DIS kinematics in the infinite momentum frame, where the nucleon moves with very large momentum along a direction, allowing to consider the quark as massless constituents moving parallel to the nucleon (this means neglecting the transverse component of the quark momentum). In this frame the Bjorken x variable is the fraction of the momentum of the nucleon carried by the struck quark. The quarks are considered as free, and therefore all the interactions between themselves and with the target remnants are neglected. The hadronic tensor is usually represented by the handbag diagram shown in fig. 1.4. To describe the density of partons of a certain type q with momentum xP, the parton distributions functions $q(x)$ (PDFs) are introduced. The structure functions for DIS reactions are built up from the incoherent sum of elastic scatterings of the virtual photon on the constituents:

$$F_2(x) = \sum_q e_q^2 x q(x); \tag{1.15}$$

for F_1, the Callan Gross relationship holds, and indeed it is a prediction of the model. In this picture, the form factors are interpreted in terms of probability to find a parton with a fraction x of the nucleon momentum.

The quantity $\sum_q \int_0^1 xq(x)dx$ is the contribution of the quarks and antiquarks to the nucleons momentum, and it is expected to be 1 if the identification partons = quarks + antiquark is correct. Considering the experimental world data on $F_2(x)$ for proton and neutron, it comes that the contribution of the u and d-quark is only $\sim$0.5, implying that an important nucleon constituent is missing (see section 1.1.3).

Introducing the probability density function of a parton with spin parallel to the longitudinal nucleon spin ($q(x,S;S)$) or antiparallel ($q(x,-S;S)$), we can decompose g_1 in terms of parton contribution:

$$g_1(x) = \frac{1}{2}\sum_q e_q^2(q(x,S;S) - q(x,-S;S)) = \frac{1}{2}\sum_q e_q^2 \Delta q(x,S)\ . \tag{1.16}$$

The eq. 1.16 shows that g_1 has a probabilistic interpretation in the framework of the parton model. The structure function g_2 has not a simple interpretation in this framework and is expected to be zero[1].

The first moment of g_1 for the proton and for the neutron, $\Gamma_1^{p,n} = \int_0^1 dx\ g_1^{p,n}(x)$ admits the following decomposition [20]:

$$\Gamma_1^{p,n} = \pm\frac{1}{12}\underbrace{(\Delta u - \Delta d)}_{a_3} + \frac{1}{36}\underbrace{(\Delta u + \Delta d - 2\Delta s)}_{\sqrt{3}a_8} + \frac{1}{9}\underbrace{(\Delta u + \Delta d + \Delta s)}_{a_0}; \tag{1.17}$$

the a_3 and a_8 components can be obtained from data on hyperon β-decay. Note that in eq. 1.17 we have adopted the imprecise but common writing convention: $\Delta q \equiv \int_0^1 dx\ (\Delta q(x) + \Delta\bar{q}(x))$.

From eq. 1.17, we obtain the so called Bjorken sum rule:

$$\Gamma_1^p - \Gamma_1^n = \frac{1}{6}a_3, \tag{1.18}$$

which is considered a fundamental rule in QCD, since it can be derived independently from the parton model framework. The EMC collaboration measured for the first time Γ_1^p [39], while Γ_1^n was measured from the SMC collaboration [40], allowing a first check of the Bjorken sum rule. The Bjorken sum rule was found to be consistent with its expectation value, predicted using the known value of a_3.

With the assumption $\Delta s = \Delta\bar{s} = 0$, we have $a_0 = \sqrt{3}a_8$, and eq. 1.17 reads:

$$\Gamma_1^{p,n} = \frac{1}{12}a_3\left\{\pm 1 + \frac{5}{\sqrt{3}}\cdot\frac{a_8}{a_3}\right\}. \tag{1.19}$$

which it is known as the Ellis-Jaffe sum rule. The Γ_1^p measured from EMC indicated a large violation of the Ellis-Jaffe sum rule. This implied that the assumption $\Delta s = \Delta\bar{s} = 0$ had to be released. The measured Γ_1^p was used to extract the a_0 term, and also the Δu, Δd and Δs components.

In the parton model the sum of the spin contribution of all the quark and antiquark flavors, usually indicated with $\Delta\Sigma$, should account for the total nucleon spin:

$$S_z = \frac{1}{2}\sum_q \Delta q = \frac{\Delta\Sigma}{2}. \tag{1.20}$$

[1]Non zero values of g_2 can be obtained allowing the quark to have an intrinsic Fermi motion inside the nucleon [20, 21].

As it is clear from eq. 1.17, in parton model the a_0 term coincides with $\Delta\Sigma$, so that the spin 1/2 of the nucleon implies a value of a_0 near to 1. The EMC measurement for a_0 was unexpectedly small and compatible with zero [20]:

$$a_0 = 0.06 \pm 0.12 \pm 0.17; \tag{1.21}$$

that came as a big surprise and was the cause of the so-called "spin crisis".

1.1.3 QCD improved parton model

The failure of the momentum sum rule indicates that some nucleon constituents are missing, that can be easily identified with the gluons. Although the gluons do not interact directly with the virtual photon, they are supposed to mediate the strong interaction and to give rise to the QCD corrections to the quark-parton model. The QCD corrections to the model are taken into account by allowing the parton number densities to depend upon Q^2 in a way calculable in QCD. In this way the formalism used in the parton model remains unchanged, except that each of the density $q(x)$ is replaced by $q(x, Q^2)$, implying a dynamical breaking of the Bjorken scaling.

The dependence of the quark densities from Q^2 can be interpreted as arising from the fact that the photon resolution increases with Q^2. Since quarks and gluons interact, at large Q^2 the photon starts to see the cloud of gluons and virtual $q\bar{q}$ pairs (the so called sea quarks), so that the number of resolved partons increases.

The Q^2 evolution of the quark structure functions is described by the DGLAP equations[41]. The equation expresses the fact that a quark with momentum fraction x could come from a parent quark with a larger momentum which has radiated a gluon, or from a parent gluon creating a $q\bar{q}$ pair. If the PDFs are known at a certain Q^2 scale, they can be computed at any other scale using the DGLAP equations.

In QCD, the conservation of the SU(3) singlet axial current, valid for massless quarks, is broken; in particular the singlet axial current has a non zero anomalous contribution [42], that induces a gluon contribution via the diagrams represented in fig. 1.5. Taking into account the anomaly, the connection between a_0 and $\Delta\Sigma$ is quite different from what it is in the Naïve Parton Model, namely:

$$a_0(Q^2) = \Delta\Sigma - 3\,\frac{\alpha_s(Q^2)}{2\pi}\,\Delta G(Q^2); \tag{1.22}$$

therefore the a_0 measurement from the EMC collaboration does no longer mean a small contribution of the quark and antiquark to the nucleon spin but a possible cancellation with the anomalous gluonic part. It has to be noted that the term ΔG behaves like $1/\alpha_s$ when $Q^2 \to \infty$, so that the term appearing in eq. 1.22 is not a correction vanishing at high Q^2.

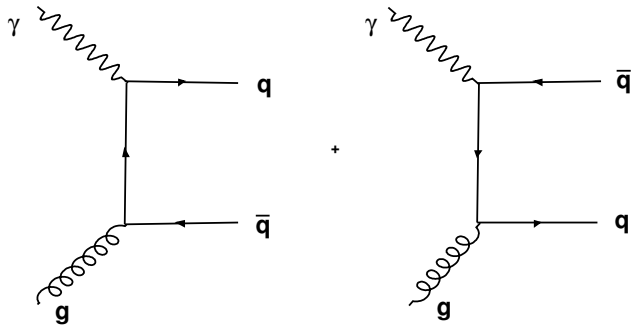

Figure 1.5: Diagrams contributing to the mixing between g_1^p and the polarized gluon parton density.

A measurement of ΔG appears to be needed, both for itself and as an element of the spin puzzle; taking into account this new contribution, eq. 1.20 becomes:

$$S_z = \frac{1}{2} = \frac{1}{2}\Delta\Sigma + \Delta G + \langle L_z \rangle, \tag{1.23}$$

where we have written also the possible contribution from the gluons and quarks orbital angular momentum, $\langle L_z \rangle$. A direct measurement of ΔG is one of the most important measurements at COMPASS, and is part of the scientific program of other polarized semi-inclusive deep inelastic scattering experiments as HERMES, and of high energy polarized pp scattering experiments at RHIC.

1.2 Transversity

In the previous section we have introduced the two PDFs $q(x)$ and $\Delta q(x)$; at leading twist, another PDF has to be considered to fully describe the quark spin composition of the nucleon. The third distribution is the quark transverse polarization distribution, $\Delta_T q(x)$, known as transversity. It was introduced first in 1979 by Ralston and Soper [2], but only in the nineties it was the subject of an intense theoretical activity, when it was rediscovered by Artru and Mekhfi [3] and by Jaffe and Ji [4]. In the same time, on the experimental side, first proposals [9, 10] to measure transversity were put forward. In the last decade, a great interest in the transverse polarization distributions has been shown, both from the theoretical and from the experimental point of view (section 1.4).

The optical theorem relates the hadronic tensor to the imaginary part of the forward virtual Compton scattering amplitudes [43]. Thus the leading-twist distribution functions appearing in the tensor parametrization can be expressed in terms of

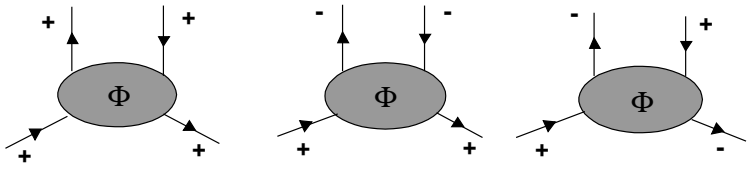

Figure 1.6: The three quark-nucleon helicity amplitudes.

the imaginary part of the quark-nucleon forward amplitudes. The amplitudes have the form $A_{\Lambda\lambda,\Lambda'\lambda'}$, where Λ, Λ' (λ, λ') are nucleon (quark) helicities. There are in general 16 amplitudes; imposing helicity conservation $(\Lambda + \lambda = \Lambda' + \lambda')$, parity and time-reversal invariance, only three amplitudes remain: $A_{++,++}, A_{+-,+-}, A_{+-,-+}$ (fig. 1.6). The two amplitudes $A_{++,++}, A_{+-,+-}$ are diagonal in the helicity basis, since the quark does not flip its helicity; $A_{++,++}$ corresponds to $q(x, S; S)$ while $A_{+-,+-}$ to the $q(x, -S; S)$ function introduced in section 1.1.2. Therefore the following relationships hold:

$$q(x) = q_+(x) + q_-(x) \sim Im(A_{++,++} + A_{+-,+-}); \quad (1.24)$$

$$\Delta q(x) = q_+(x) - q_-(x) \sim Im(A_{++,++} - A_{+-,+-}). \quad (1.25)$$

The third amplitude, $A_{+-,-+}$, is off-diagonal (helicity flip), and it can be related to a third distribution function, named transversity:

$$\Delta_T q(x) = q_\uparrow(x) - q_\downarrow(x) \sim Im(A_{+-,-+}). \quad (1.26)$$

In the helicity basis, $A_{+-,-+}$ has not a probabilistic interpretation. However, if we consider a transversity basis:

$$|\uparrow> = \frac{1}{\sqrt{2}}[|+> + i|->], \; |\downarrow> = \frac{1}{\sqrt{2}}[|+> - i|->], \quad (1.27)$$

with $\uparrow$ transverse with respect to the direction of motion, $\Delta_T q$ reads:

$$\Delta_T q(x) = q_\uparrow(x) - q_\downarrow(x) \sim Im(A_{\uparrow\uparrow,\uparrow\uparrow} - A_{\uparrow\downarrow,\uparrow\downarrow}), \quad (1.28)$$

leading to the interpretation of $\Delta_T q(x)$ as the polarized quark distribution in a nucleon polarized transversely with respect to its momentum.

At variance with the longitudinal polarized distribution, there is no gluonic contribution to transversity. A hypothetical $\Delta_T G(x)$ would imply a helicity flip gluon-nucleon amplitude, which cannot exist due to helicity conservation. In fact gluons have helicity ± 1, but the nucleon cannot undergo a helicity change of ± 2. This results in a different Q^2 evolution for transversity and helicity distributions: even if they have the same value for a certain Q^2, the function may differ at another scale.

Transversity is a chiral-odd quantity that requires the helicity of the quark to be flipped. Since all the hard processes conserve quark helicity through the quark line, to measure transversity the presence of another soft term is required. Thus transversity cannot be measured by means of the usual inclusive DIS, that it has always been the major source of information about the unpolarized and helicity PDFs. The measurement can be done involving at least two hadronic states, as in the Drell–Yan process or in the lepton nucleon polarized semi-inclusive DIS, in which $\Delta_T q(x)$ is coupled to a T-odd function as described in section 1.3.

Soffer inequality

From the definition of $q(x)$ and $\Delta q(x)$ two bounds on $\Delta q(x)$ and $\Delta_T q(x)$ can be derived :

$$|\Delta q(x)| \leq q(x)\,, \tag{1.29}$$
$$|\Delta_T q(x)| \leq q(x)\,. \tag{1.30}$$

Similar inequalities hold for the antiquark distributions. A further, more subtle, bound simultaneously involving q, Δq and $\Delta_T q$, was derived by Soffer [44]

$$q(x) + \Delta q(x) \geq 2|\Delta_T q(x)|\,. \tag{1.31}$$

Eq. 1.31 is known as the Soffer inequality. It is an important bound, which must be satisfied by the leading-twist distribution functions.

Tensor charge

The first moment of the transversity PDF is connected to the tensor charge g_T, one of the fundamental parameters characterizing the properties of the nucleon:

$$g_T = \sum_q \int dx\,[\Delta_T q(x) - \Delta_T \bar{q}(x)]. \tag{1.32}$$

The tensor charge measures the net number of transversely polarized valence quarks in a transversely polarized nucleon. Its difference from the axial charge g_A is related to the relativistic nature of the nucleon. Measurements down to small x values are required for the evaluation of the integrals.

Bakker Leader Trueman sum rule

The first moment of the transversity PDF is also connected to the spin of the nucleon. The Bakker Leader Trueman sum rule [45]

$$\frac{1}{2} = \frac{1}{2}\sum_{q}[\Delta_T q + \Delta_T \bar{q}] + \sum_{q,\bar{q},g} L_T \tag{1.33}$$

is free of the gluon contribution, and provides an independent way to access the contribution of the orbital angular momentum of q, $\bar{q}$ and g to the nucleon spin.

1.3 Semi-inclusive DIS

In semi-inclusive DIS (SIDIS), a lepton scatters off a nucleon and at least a final state hadron is detected:

$$\ell(\mathbf{k}) + \mathbf{N}(\mathbf{P}) \rightarrow \ell'(\mathbf{k'}) + \mathbf{h}(\mathbf{P_h}) + \mathbf{X}\ . \tag{1.34}$$

The corresponding hand-bag diagram is indicated in fig. 1.7. The Φ term is the same as in DIS (fig. 1.4), while the Δ indicates a quark-quark correlation function describing the way the struck quark evolves into a hadronic final state of which the hadron is detected. The cross section of the process can be factorized in the following way:

$$d\sigma^{lN\rightarrow l'hX} \sim \sum_{q} q \cdot d\sigma^{lq\rightarrow l'q'} \cdot D_q^h \tag{1.35}$$

where $d\sigma^{lq\rightarrow l'q'}$ is the hard part of the scattering, while q and D_q^h are the parton distribution functions and fragmentation functions parameterizing respectively the Φ and the Δ term in fig. 1.7.

In the unpolarized case, the fragmentation functions $D_q^h(z, Q^2)$ give the probability density for an initial quark to produce a final hadron with fractional energy z [2]. The dependence on the resolution scale Q^2 is described via a DGLAP-type equation, giving the possibility that a parton gives rise to a hadron via the radiation of an intermediate parton which fragments into the hadron. Since fragmentation functions cannot be calculated directly, they have to be derived from fits to experimental data, usually from e^+e^- annihilation [46, 47]; in a recent work [48] also data from $p\,p$ collisions and DIS experiments have been used. In order to extract the fragmentation functions from the data, some relationships based on charge and

[2]The invariant z is defined as $z = \frac{\mathbf{P}\cdot\mathbf{P_h}}{\mathbf{P}\cdot\mathbf{q}} \overset{lab}{=} \frac{E_h}{E-E'}$; in the laboratory frame, z is the fraction of available energy carried by the hadron.

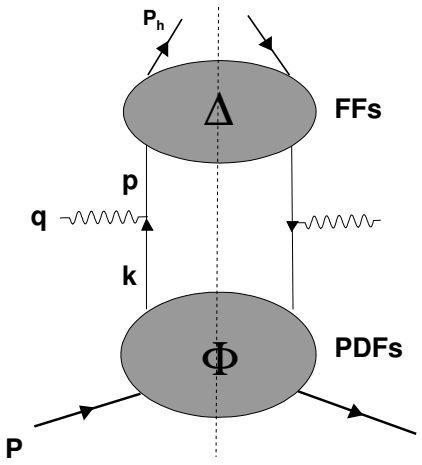

Figure 1.7: Handbag diagram for SIDIS process: the Φ box term is the same as in DIS, while the Δ box indicates the hadronization process.

isospin invariance and valence quark composition of the respective hadron are taken into account. From charge conjugation invariance we get:

$$D_q^{h^+,h^-} = D_{\bar{q}}^{h^-,h^+} \ , \ h = \pi, K \ ; \tag{1.36}$$

while from isospin symmetry for pions:

$$D_u^{\pi^+,\pi^-} = D_d^{\pi^-,\pi^+} \ . \tag{1.37}$$

When the hadron contains a valence quark of the same flavor as the fragmenting quark, the fragmentation functions are usually named *favored*, or valence-type; otherwise they are named *unfavored*, or sea-type, where the names reflect the naïve expectation. Taking into account this convention, for pions we distinguish between two types of fragmentation function :

$$\begin{aligned} D_{fav} &= D_u^{\pi^+} = D_{\bar{d}}^{\pi^+} = D_{\bar{u}}^{\pi^-} = D_d^{\pi^-} \ ; \\ D_{unf} &= D_u^{\pi^-} = D_{\bar{d}}^{\pi^-} = D_{\bar{u}}^{\pi^+} = D_d^{\pi^+} = D_s^{\pi^+} = D_{\bar{s}}^{\pi^-} = D_{\bar{s}}^{\pi^+} = D_{\bar{s}}^{\pi^-} \ . \end{aligned}$$

The extraction of fragmentation functions from data show that $D_{fav} > D_{unf}$, as expected.

In so far, transverse momentum dependent (TMD) effects have been neglected, since transverse momenta are small as compared to the longitudinal component. To

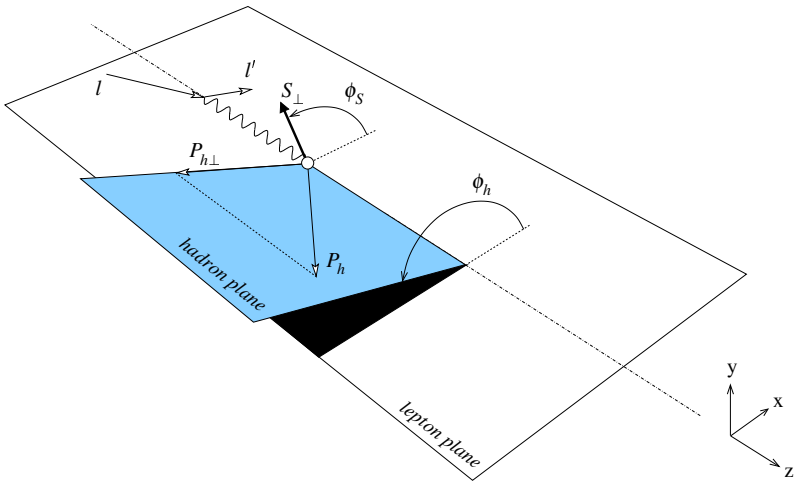

Figure 1.8: Definition of the azimuthal angles ϕ_h and ϕ_S in the "gamma-nucleon system".

completely describe SIDIS processes however both the transverse momentum of the quark inside the nucleon and the transverse momentum of the hadron with respect to the fragmenting quark have to be considered since both influence the final state hadron distribution.

1.3.1 SIDIS cross section

The SIDIS cross section can be expressed in terms of transverse momentum dependent parton distribution functions and fragmentation functions that explicitly depend on the transverse parton momentum, $\vec{k}_T$, with respect to the virtual photon and on the transverse momentum $\vec{p}_T$ of the final state hadron with respect to the fragmenting quark direction. These partonic functions, usually indicated as unintegrated functions, are a generalization of the distributions appearing in standard factorization for the collinear case, in which both $\vec{k}_T$ and $\vec{p}_T$ are ignored.

In the so called "gamma-nucleon system" (GNS, fig. 1.8) where the virtual photon direction defines the z axis, and the xz plane is the lepton scattering plane (defined by the initial and final lepton momenta), the polarized semi-inclusive DIS cross section depends on the azimuthal angle ϕ_h of the produced hadron with respect to the scattering plane, as well as on the azimuthal angle of the target nucleon spin, ϕ_S.

Assuming single photon exchange, and in case of spinless final state hadrons, the

cross section reads [49]:

$$\frac{d\sigma}{dx\,dy\,d\phi_S\,dz\,d\phi_h\,dP_T^{h\,2}} =$$

$$\frac{\alpha^2}{xyQ^2}\,\frac{y^2}{2\,(1-\varepsilon)}\left(1+\frac{\gamma^2}{2x}\right)\Bigg\{F_{UU,T}+\varepsilon\,F_{UU,L}+\sqrt{2\,\varepsilon(1+\varepsilon)}\,\cos\phi_h\,F_{UU}^{\cos\phi_h}$$

$$+\varepsilon\,\cos(2\phi_h)\,F_{UU}^{\cos 2\phi_h}+\lambda_e\,\sqrt{2\,\varepsilon(1-\varepsilon)}\,\sin\phi_h\,F_{LU}^{\sin\phi_h}$$

$$+S_\parallel\left[\sqrt{2\,\varepsilon(1+\varepsilon)}\,\sin\phi_h\,F_{UL}^{\sin\phi_h}+\varepsilon\,\sin(2\phi_h)\,F_{UL}^{\sin 2\phi_h}\right]$$

$$+S_\parallel\lambda_e\left[\sqrt{1-\varepsilon^2}\,F_{LL}+\sqrt{2\,\varepsilon(1-\varepsilon)}\,\cos\phi_h\,F_{LL}^{\cos\phi_h}\right]$$

$$+S_\perp\Bigg[\sin(\phi_h-\phi_S)\left(F_{UT,T}^{\sin(\phi_h-\phi_S)}+\varepsilon\,F_{UT,L}^{\sin(\phi_h-\phi_S)}\right)$$

$$+\varepsilon\,\sin(\phi_h+\phi_S)\,F_{UT}^{\sin(\phi_h+\phi_S)}+\varepsilon\,\sin(3\phi_h-\phi_S)\,F_{UT}^{\sin(3\phi_h-\phi_S)}$$

$$+\sqrt{2\,\varepsilon(1+\varepsilon)}\,\sin\phi_S\,F_{UT}^{\sin\phi_S}+\sqrt{2\,\varepsilon(1+\varepsilon)}\,\sin(2\phi_h-\phi_S)\,F_{UT}^{\sin(2\phi_h-\phi_S)}\Bigg]$$

$$+S_\perp\lambda_e\Bigg[\sqrt{1-\varepsilon^2}\,\cos(\phi_h-\phi_S)\,F_{LT}^{\cos(\phi_h-\phi_S)}+\sqrt{2\,\varepsilon(1-\varepsilon)}\,\cos\phi_S\,F_{LT}^{\cos\phi_S}$$

$$+\sqrt{2\,\varepsilon(1-\varepsilon)}\,\cos(2\phi_h-\phi_S)\,F_{LT}^{\cos(2\phi_h-\phi_S)}\Bigg]\Bigg\}; \tag{1.38}$$

where λ_e is the helicity of the lepton beam, $S_\parallel$ and $S_\perp$ are respectively the projection of the target polarization in the plane parallel or transverse with respect to the photon direction, and the ratio ε of longitudinal and transverse photon flux is given by:

$$\varepsilon = \frac{1-y-\frac{1}{4}\gamma^2y^2}{1-y+\frac{1}{2}y^2+\frac{1}{4}\gamma^2y^2}, \tag{1.39}$$

where $\gamma = \frac{2Mx}{Q} \sim 0$, and will be neglected in the following. The structure functions F on the r.h.s. depend on x, Q^2, z and $P_T^{h\,2}$; the first and second subscript indicate the respective polarization of beam and target (L=longitudinal, T=transverse), whereas the third subscript in $F_{UU,T}$, $F_{UU,L}$ and $F_{UT,T}^{\sin(\phi_h-\phi_S)}$, $F_{UT,L}^{\sin(\phi_h-\phi_S)}$ specifies the polarization of the virtual photon. The superscript in the structure functions indicates the different azimuthal modulation in ϕ_h and ϕ_S.

Eq. 1.38 shows that there are in total eighteen structure functions, eight of these depending on the target transverse polarization. Due to the different azimuthal modulations of each term, it is possible to build cross section asymmetries and extract each term from data.

1.3.2 Structure functions

The explicit expression for all the structure functions appearing in eq. 1.38 are given in ref. [49]. The calculations are based on the factorization of the cross section into a hard photon-quark scattering process, TMD parton distribution functions and TMD fragmentation functions.

In the cross section there are eight leading twist TMD PDF entering the parametrization of the quark-quark correlator; they are listed in table 1.2. The notation used follows ref. [49]. The letters f, g and h refer respectively to unpolarized, longitudinally and transversely polarized quark distribution. The subscript "1" means that they are leading twist quantities; subscripts "L" and "T" mean that the target nucleon is longitudinally or transversely polarized; the superscript "$\perp$" indicates the presence of transverse momentum effect.

DF	meaning
$\mathbf{f_1}(x, k_T^2)$	unpolarized distribution
$\mathbf{g_{1L}}(x, k_T^2)$	helicity distribution
$\mathbf{g_{1T}}(x, k_T^2)$	distribution of longitudinally polarized quarks in transversely polarized nucleon
$\mathbf{f_{1T}^{\perp}}(x, k_T^2)$	Sivers distribution
$\mathbf{h_{1T}}(x, k_T^2)$	quark transverse polarization along target transverse polarization
$\mathbf{h_{1L}^{\perp}}(x, k_T^2)$	quark transverse polarization along quark intrinsic transverse momentum in the longitudinal polarized target
$\mathbf{h_{1T}^{\perp}}(x, k_T^2)$	quark transverse polarization along quark intrinsic transverse momentum in the transverse polarized target
$\mathbf{h_1^{\perp}}(x, k_T^2)$	quark transverse polarization along normal to the plane defined by quark intrinsic transverse momentum and nucleon momentum in the unpolarized quark

Table 1.2: The eight leading twist PDF.

The structure functions in eq. 1.38 are related to the TMD distribution functions by convolution of the type:

$$\mathcal{C}\left[w\, f\, D\right] = x \sum_a e_a^2 \int d^2\vec{k}_T\, d^2\vec{p}_T\, \delta^{(2)}\left(\vec{k}_T - \vec{p}_T - \vec{P}_T^h/z\right) w(\vec{p}_T, \vec{k}_T)\, f_a(x, k_T^2)\, D_a(z, p_T^2); \tag{1.40}$$

here f and D are generic PDF and FF, $w(\vec{k}_T, \vec{p}_T)$ is a function of the transverse momenta, and the summation runs over quarks and antiquarks; the $\delta-$function implies transverse momentum conservation.

The unpolarized structure function in eq. 1.38 contains the unpolarized PDF f_1 (previously indicated with q) and the unpolarized fragmentation function D already introduced:

$$F_{UU,T} = \mathcal{C}\big[f_1 D\big]. \tag{1.41}$$

Out of the eight transverse structure functions of eq. 1.38, four can be expressed via leading twist PDFs:

$$F_{UT}^{\sin(\phi_h+\phi_S)} = \mathcal{C}\left[-\frac{\hat{h}\cdot\vec{p}_T}{M_h} h_1 H_1^\perp\right], \tag{1.42}$$

$$F_{UT,T}^{\sin(\phi_h-\phi_S)} = \mathcal{C}\left[-\frac{\hat{h}\cdot\vec{k}_T}{M} f_{1T}^\perp D\right], \tag{1.43}$$

$$F_{UT}^{\sin(3\phi_h-\phi_S)} = \mathcal{C}\left[\frac{2\left(\hat{h}\cdot\vec{k}_T\right)\left(\vec{k}_T\cdot\vec{p}_T\right) + \vec{k}_T^2\left(\hat{h}\cdot\vec{p}_T\right) - 4\left(\hat{h}\cdot\vec{k}_T\right)^2\left(\hat{h}\cdot\vec{p}_T\right)}{2M^2 M_h} h_{1T}^\perp H_1^\perp\right], \tag{1.44}$$

$$F_{LT}^{\cos(\phi_h-\phi_S)} = \mathcal{C}\left[\frac{\hat{h}\cdot\vec{k}_T}{M} g_{1T} D\right]; \tag{1.45}$$

where $\hat{h} = \vec{P}_T^h/|P_T^h|$.

Eq. 1.42 is related to the Collins effect (section 1.3.3); the h_1 PDF is the TMD transversity, defined as:

$$h_1(x, k_T^2) = h_{1T}(x, k_T^2) - \frac{k_T^2}{2M^2} h_{1T}^\perp(x, k_T^2); \tag{1.46}$$

this unintegrated PDF is related to the transversity distribution introduced in section 1.2 via:

$$\Delta_T q(x) = h_1(x) = \int d^2\vec{k}_T h_1(x, k_T^2)\ . \tag{1.47}$$

The fragmentation function $H_1^\perp$ appearing in eq. 1.42 is the Collins fragmentation function, describing the spin-dependent part of the fragmentation.

Eq. 1.43 describes the so called Sivers effect, that will be explained in section 1.3.4. The Sivers function $f_{1T}^\perp$ is convoluted with the unpolarized fragmentation function D.

The structure functions in eq. 1.44 and 1.45 give access to the PDFs $h_{1T}^\perp$ and the chiral even g_{1T}, convoluted with $H_1^\perp$ and D respectively.

The other four structure functions in eq. 1.38 are twist-3 contributions, and have no simple interpretation in the parton model.

The terms that have received more attention both from the experimental and from the theoretical side, are the Collins and Sivers contributions, that will be described in the following.

1.3.3 The Collins mechanism

The fragmentation function $H_1^\perp$ appearing in eq. 1.42, plays an important role in the phenomenology of transversity, and it is related to the so called Collins effect. This mechanism, which arises from final-state interaction effects and was introduced by Collins [13], is responsible for a left-right asymmetry in the fragmentation of transversely polarized quarks. The fragmentation function $H_1^\perp$ describes the spin-dependent part of the hadronization of a transversely polarized quark into a hadron; $H_1^\perp$ can be defined considering the distribution of hadrons produced from quarks with opposite polarization [43]:

$$N_{h/q\uparrow}(z,\vec{p}_T) - N_{h/q\downarrow}(z,\vec{p}_T) = \frac{|\vec{p}_T|}{M_h} sin(\phi_h - \phi_{S'}) H_1^\perp(z,p_T^2) \ . \tag{1.48}$$

The angles ϕ_h and $\phi_{S'}$ are respectively the angles of the momentum of the produced hadron and of the spin vector of the fragmenting quark with respect to the quark momentum.

In the DIS process, as dictated by QED, the directions of the final and initial quark spins in the GNS are related to each other by $\phi_{s'} = \pi - \phi_s$, thus the following relationship holds:

$$\phi_h - \phi_{S'} = \phi_h + \phi_S - \pi = \Phi_C, \tag{1.49}$$

where we have defined the Collins angle Φ_C.

Let's now consider the unpolarized term and the Collins term in the eq. 1.38. Neglecting quark transverse motion inside the target, using eq. 1.41 and 1.42, and introducing the function:

$$\Delta_T^0 D(z,p_T^2) = -\frac{|\vec{p}_T|}{M_h} H_1^\perp(z,p_T^2) \ , \tag{1.50}$$

the cross section reads[3]:

$$\begin{aligned} \frac{d\sigma}{dx\,dy\,d\phi_S\,dz\,d\phi_h\,dP_T^{h2}} &= \frac{\alpha^2}{xyQ^2} \sum_q e_q^2 \cdot \left\{ \frac{1}{2}\left[1+(1-y)^2\right] \cdot x \cdot q(x) \cdot D_q^h(z,P_T^{h2}) + \right. \\ &\left. +(1-y)\ S_\perp \sin(\Phi_C) \cdot x \cdot \Delta_T q(x) \cdot \Delta_T^0 D_q^h(z,P_T^{h2}) \right\} \ . \end{aligned} \tag{1.51}$$

[3]If we consider quark transverse motion in the nucleon, the convolution integrals in eq. 1.41 and 1.42 cannot be solved explicitly, unless we make some assumption on the parton distribution functions and fragmentation function dependence on k_T and p_T. In the usual assumption of Gaussian distributions, the effect of the convolution integral is the presence of a factor which depends on the widths of the distributions. This point will be discussed in Chapter 5.

By comparing the cross sections on oppositely polarized target nucleons one obtains from eq. 1.51 the transverse single spin asymmetry:

$$A_T^h \equiv \frac{d\sigma(\vec{S}_\perp) - d\sigma(-\vec{S}_\perp)}{d\sigma(\vec{S}_\perp) + d\sigma(-\vec{S}_\perp)} = S_\perp \cdot D_{NN} \cdot A_{Coll} \cdot \sin\Phi_C \ . \tag{1.52}$$

The "Collins asymmetry" is

$$A_{Coll} = \frac{\sum_q e_q^2 \cdot x \cdot \Delta_T q(x) \cdot \Delta_T^0 D_q^h(z, P_T^{h^2})}{\sum_q e_q^2 \cdot x \cdot q(x) \cdot D_q^h(z, P_T^{h^2})} , \tag{1.53}$$

and

$$D_{NN} = \frac{1-y}{1-y+y^2/2} \tag{1.54}$$

is the transverse spin transfer coefficient from the initial to the struck quark [50].

As evident from eq. 1.53, the Collins asymmetry gives access to the transversity distribution function; the identification of final state hadrons and the use of different targets allow to extract the different quark contribution.

1.3.4 The Sivers mechanism

A different mechanism responsible for a spin asymmetry in the cross section of SIDIS of leptons on transversely polarized nucleons was suggested by Sivers [12]. Sivers conjecture was the possible existence of a correlation between the transverse momentum $\vec{k}_T$ of an unpolarized quark in a transversely polarized nucleon and the nucleon polarization vector. Considering the number density of unpolarized quarks in opposite transversely polarized nucleons, the Sivers function can be defined as:

$$\begin{aligned} \mathcal{P}_{q/N\uparrow}(x, \vec{k}_T) - \mathcal{P}_{q/N\downarrow}(x, \vec{k}_T) &= \mathcal{P}_{q/N\uparrow}(x, \vec{k}_T) - \mathcal{P}_{q/N\uparrow}(x, -\vec{k}_T) & (1.55) \\ &= -\frac{|\vec{k}_T|}{M} S_\perp \sin(\phi_S - \phi_q)\, f_{1T}^\perp(x, k_T^2) \, . & (1.56) \end{aligned}$$

where the angle $\phi_S - \phi_q$ is the relative azimuthal angle between the target spin $\vec{S}_\perp$ and the quark transverse momentum $\vec{k}_T$, and the $f_{1T}^\perp(x, k_T^2)$ is the Sivers function. Following the notation used in [19], we define the quantity:

$$\Delta_0^T q(x, k_T^2) = -\frac{|\vec{k}_T|}{M} f_{1T}^T(x, k_T^2) \, , \tag{1.57}$$

Under the assumption that the hadron produced in the fragmentation and the fragmenting quark are collinear, i.e. that all the hadron transverse momentum originates from the intrinsic transverse momentum of the quark in the nucleon ($\vec{P}_T^h = z\vec{k}_T$),

the SIDIS cross section with the unpolarized and the Sivers term of eq. 1.38 is given by:

$$\frac{d\sigma}{dx\,dy\,d\phi_S\,dz\,d\phi_h\,dP_T^{h^2}} = \frac{\alpha^2}{xyQ^2}\sum_q e_q^2 \cdot \frac{1}{2}\left[1+(1-y)^2\right]\cdot x\cdot$$
$$\cdot\left[q(x,P_T^{h^2}/z^2) + S_\perp \sin(\Phi_S)\Delta_0^T q(x,P_T^{h^2}/z^2)\right]\cdot D_q^h(z)\,, \quad (1.58)$$

where the Sivers angle is:

$$\Phi_S = \phi_h - \phi_S\ . \quad (1.59)$$

Comparing the cross sections on oppositely polarized target nucleons, the transverse spin asymmetry of eq. 1.52 becomes

$$A_T^h \equiv \frac{d\sigma(\vec{S}_\perp) - d\sigma(-\vec{S}_\perp)}{d\sigma(\vec{S}_\perp) + d\sigma(-\vec{S}_\perp)} = S_\perp \cdot A_{Siv}\cdot \sin\Phi_S\ , \quad (1.60)$$

where the "Sivers asymmetry"

$$A_{Siv} = \frac{\sum_q e_q^2 \cdot x \cdot \Delta_0^T q(x,P_T^{h^2}/z^2)\cdot D_q^h(z)}{\sum_q e_q^2 \cdot x \cdot q(x,P_T^{h^2}/z^2)\cdot D_q^h(z)} \quad (1.61)$$

is revealed as a $\sin\Phi_S$ modulation in the number of produced hadrons.[4]

The Collins and Sivers terms in the cross section depend on the two independent angles Φ_C and Φ_S, thus measuring SIDIS on a transversely polarized target allows the Collins and the Sivers effects to be disentangled and the two asymmetries can separately be extracted from the same data.

The existence of the Sivers function requires final/initial state interaction. In the absence of interactions the Sivers function would vanish by time-reversal invariance of QCD (see e.g. Ref. [14]) and indeed it was believed for several years the Sivers function to be zero. Recently it was shown however [51, 52, 53] that these interactions are represented naturally by the gauge link that is required for a gauge invariant definition of a transverse momentum dependent parton distribution, thus the Sivers function has become a very important piece in the most fundamental issues of QCD.

A sum rule for the Sivers function was derived by Burkardt for a spin-1/2 target in QCD [54, 55]. This sum rule states that the average transverse momentum induced by the Sivers effect vanishes if one sums over all partons:

$$\langle k_T\rangle = \sum_{a=q,\bar{q},g} < k_T >_a = \int dx \int d^2k_T k_T \sum_a \Delta_0^T q(x,k_T) = 0. \quad (1.62)$$

[4] As before, considering the Gaussian dependence of parton distribution functions and fragmentation functions from k_T and p_T brings an additional factor in the asymmetry formula (see Chapter 5).

1.4 Experimental overview

Starting from the end of 90s the HERMES Collaboration at DESY, and later the COMPASS Collaboration at CERN have performed a series of measurements of azimuthal asymmetries in SIDIS processes of leptons off transversely polarized target. The first HERMES results, referring to the 2002-2003 data, have been published in ref. [56]; the data corresponding to 2002-2004 are in ref. [57], while preliminary results with all the available statistics (2002-2005 data) have been presented at the DIS07 conference [58]. The first COMPASS publication refers to the data taken in 2002 [18], while results for all the available statistics on a deuterium target (collected in years 2002-2004) are published in ref. [19].

The HERMES measurement of non zero single spin asymmetries on a proton target show for the first time that the Sivers and Collins effects are real effects, and that the transversity PDF is different from zero. The kinematical region covered by the HERMES experiment is the following: $W^2 > 10$ GeV^2, $Q^2 > 1$ (GeV/c)^2, $0.1 < y < 0.85$, $0.2 < z < 0.7$, $0.023 < x < 0.4$. The Sivers asymmetries are measured to be positive for π^+ and consistent with zero for π^-. The Collins asymmetries are positive for π^+ and negative and comparable in magnitude for π^-. Preliminary results for the asymmetries with all the available statistics [58] are shown in fig. 1.9 as a function of x, z and P_T^h.

The COMPASS Collaboration has measured for the first time Sivers and Collins asymmetries using a transversely polarized deuteron target. The kinematical range covered is $W > 5$ GeV , $Q^2 > 1$ (GeV/c)^2, $0.1 < y < 0.9$, $z > 0.2$, $0.003 < x < 0.3$, $P_T^h > 0.1$ GeV/c. The results on the entire collected statistics are shown in fig. 1.10. The asymmetries have been measured on "unidentified hadrons"; the work presented in this thesis allows the first measurement of the Collins and Sivers asymmetries on pion and kaon samples.

Independent information for the Collins fragmentation functions being non zero has been provided by the Belle measurements of hadron azimuthal asymmetries in e^+e^- annihilation [17].

The CLAS Collaboration has performed measurements of both longitudinal beam and target spin asymmetries for pion production in SIDIS off protons using an electron beam with 4.3 GeV and 5.7 GeV energy; up to now no transverse target has been used.

To conclude this short overview, one has also to quote the effort going on at RHIC and the proposal at FAIR/GSI to study transverse spin effects in $p\,p$ and $p\,\bar{p}$ collisions.

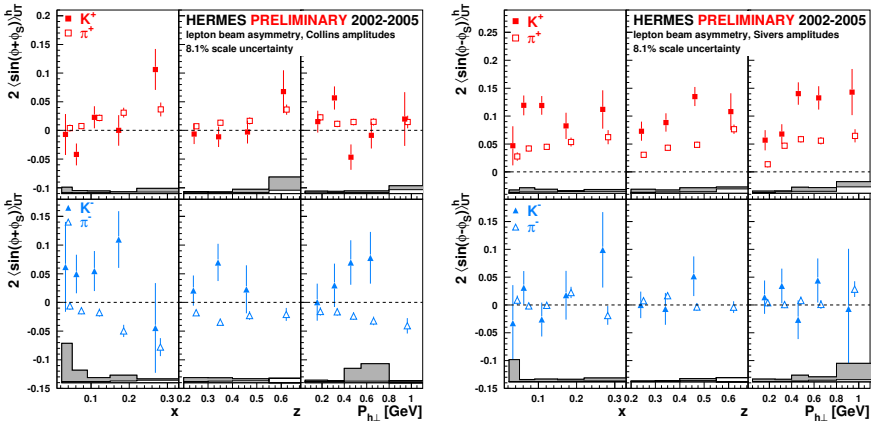

Figure 1.9: Collins amplitudes (left column) and Sivers amplitudes (right column) for charged kaons (closed symbols) and charged pions (open symbols) as function of x, z and P_T^h from HERMES experiment [58].

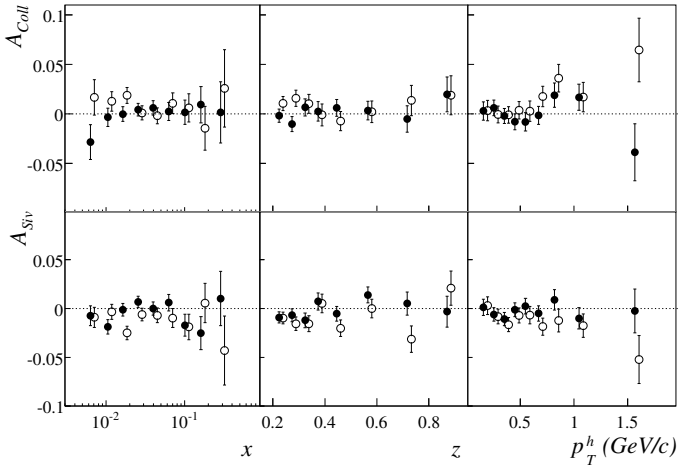

Figure 1.10: Overall results for Collins asymmetry (top) and Sivers asymmetry (bottom) against x, z and P_T^h for positive (full circles) and negative leading hadrons (open circles) from 2002, 2003, and 2004 COMPASS data [19]. Error bars are statistical only.

Chapter 2

The COMPASS spectrometer

The COMPASS experiment has been approved in 1997 to perform measurements on the nucleon spin structure with a high energy muon beam and on hadron spectroscopy using hadronic beams. From 2002 to 2007, only measurements with muon beam have been performed, apart from a pilot run with a pion beam in 2004. The data used for the measurement of the Collins and Sivers asymmetries presented here have been collected in 2003 and 2004. In the following chapter the COMPASS apparatus is described in the configuration during the 2004 run with muon beam, the configuration used in 2003 being very similar. After a brief introduction on the general principles guiding the construction and the realization of the spectrometer, a short technical description of the main components is given. A complete description can be found in [59] and in the papers referenced therein. The description of the RICH detector and of its role in COMPASS are the subject of the next chapter.

2.1 General overview

The broad physics program of the COMPASS experiment dictates specific requirements to the experimental setup. The need to collect particles in a large range in both momentum and polar angle implies a large acceptance in the apparatus, track reconstruction and identification capabilities in very different regions of the phase space. On the other hand, the very high luminosity conditions require detectors able to stand high rates and to measure tracks with high time resolution, an efficient trigger system, and finally a data acquisition system able to cope with high flux data.

To satisfy these requirements, the COMPASS apparatus is made of two different spectrometers: the Large Angle Spectrometer (LAS) and the Small Angle Spectrometer (SAS). The first is located after the target region, and it has an acceptance of ± 180 mrad. Its task is to measure and identify particles emitted at large angle from the target, before the tracks are too far away from the beam line. The second

spectrometer is located after the first one, where more energetic particles emitted at small angles from the target have moved away from the beam axis, and tracking becomes easier.

In the original project, both spectrometers have the same components: trackers, an analyzing magnet, a RICH detector, a hadronic calorimeter, an electromagnetic calorimeter and a muon filter. Up to now, part of the calorimeters and the RICH detector in the SAS are missing. The experimental setup used in 2004 is shown in picture 2.1. The picture shows also the COMPASS reference system: the z axis follows the muon beam direction, the x axis follows the horizontal direction and the y axis the vertical one. The part corresponding to positive value of x is sometimes referred in the following as "Jura side" while the part corresponding to negative value as "Saleve side", following the position of these mountains with respect to the spectrometer.

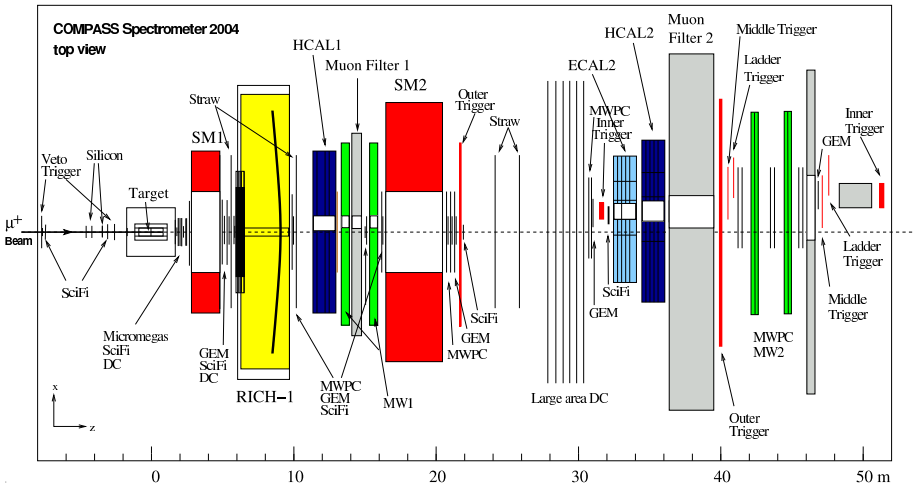

Figure 2.1: COMPASS apparatus in the configuration of the 2004 muon run.

The Large Angle Spectrometer starts at ∼2 m downstream the target. It is built around the analyzing magnet SM1. Trackers of different type placed upstream and downstream the magnet allow the measurement of the particle bending when crossing the magnetic field, and thus the reconstruction of the track momenta. After SM1, the RICH-1 detector measures the velocity of charged particles. Together with the momentum, this information allows the determination of the particle mass. The RICH-1 photon detectors are outside the acceptance and do not interfere with the particle trajectory, apart from small effects of multiple scattering in the gas radiator. Thus the particles crossing it continue their travel reaching the last part of the LAS, where the hadronic calorimeter and the muon wall are located. The hadronic calorimeter contributes to the particle identification providing a measurement of the

hadron energy. The last component is the muon filter; this device is used to identify the muons using their high penetration length: a big amount of material absorbs all the particles but the muons, that are detected with trackers downstream the absorber.

The Small Angle Spectrometer starts at ∼15 m downstream the target and it is 30 m long. It is based on the same working principles of the LAS, and is built around SM2. The main difference is the lack of the RICH detector, foreseen in the second stage of the COMPASS experiment. Moreover it is provided with an electromagnetic calorimeter, ECAL2, that can be used to detect electrons and photons.

2.2 Muon beam

The muon beam is derived from a primary proton beam of 400 GeV/c momentum extracted from the CERN SPS. The proton beam intensity is typically $1.2 \cdot 10^{13}$ protons during a spill time of 4.8 s, within a SPS cycle of 16.8 s. The protons impinge on a Beryllium target 500 mm thick yielding a secondary beam composed mostly of pions with a contamination of kaons. The pion beam momentum is selected with a resolution of 10% around the nominal value of 225 GeV/c with dipoles and quadrupoles through the beam line. Along a 600 m long "decay tunnel", a fraction of the pions decay in a muon and neutrino. Due to the parity violating nature of the pion decay, the muon beam is naturally polarized; while in the pion center of mass system all the muons are polarized, in the laboratory system the fraction of polarized muons depend on the beam phase space selected: in the COMPASS case the muons polarization is about 80%. After the decay tunnel, the hadron component of the beam is stopped by means of a hadron absorber made by nine pieces of Beryllium each 1.1 m long. The muon beam is then cleaned and selected in momentum and transported to the surface level. Before entering the experimental hall, the μ momentum (nominal value 160 GeV/c) is measured by the Beam Momentum Station (BMS), consisting of a bending magnet and six hodoscope stations located downstream and upstream the magnet. Four stations are made of horizontal strips of different pitch in order to cope with the different flux in the regions around the beam axis; two stations are made of scintillating fibers with 2 mm of diameter. The time resolution achieved by the system is around 0.3 ns; the reconstruction efficiency of each beam track is around 93% and the momentum resolution is better than 1%. After the BMS, the muons are focused on the polarized target. The incoming muon flux is of the order of $2 \cdot 10^8$ muons per SPS cycle. The beam is accompanied by a large halo, composed of muons poorly deflected or absorbed: the "near" halo, in the region within 15 cm from the beam line, accounts for ∼16% of the beam intensity, while the "far" halo accounts for about 7%.

2.3 The polarized target

The main part of the COMPASS physics program with the muon beam consists in spin asymmetry measurements, that are performed using a polarized target. Up to 2006, COMPASS took data with an isoscalar target, ^{6}LiD, characterized by a high fraction of polarized nucleons. With a good approximation ^{6}Li can be considered as formed by a spin-0 ^{4}He nucleus and a deuteron, thus the percentage of polarizable nucleons in the ^{6}LiD being $f = \frac{4}{8} = 0.5$. Taking into account the He material present in the target region for refrigeration purposes the dilution factor becomes approximately $f \sim 0.38$. The degree of polarization reached during data taking is high, larger than 40%. In 2007 COMPASS has taken data with a polarized proton target (ammonia, NH_3). The dilution factor for ammonia is lower than that of the ^{6}LiD ($f \sim 0.13$), but the polarization values are higher, around 80%.

The polarization of the target nuclei is performed via Dynamic Nucleon Polarization (DNP): this technique relies on irradiation of some paramagnetic centers in the target material (density $10^{-4} \div 10^{-3}$ per nucleus) with a microwave radiation in a strong and homogeneous magnetic field along the beam direction and at low temperature. The very low temperature needed for the polarization process ($\sim$ 200 mK), is reached with a ^{3}He-^{4}He refrigerator system. A magnetic field of 2.5 T and homogeneity of 10^{-4} is provided by a solenoid magnet. Until 2004, the COMPASS solenoid with wide aperture to match the full COMPASS spectrometer acceptance was not available, and the solenoid built for the SMC experiment, with a limited acceptance of $\pm$70 mrad, has been used instead (fig 2.2). From 2006 on, the new superconducting COMPASS solenoid magnet has been delivered and is presently in operation.

The target consists of two cells, each 60 cm long and with a diameter of 3 cm. To reduce possible systematic effects, the two cells are polarized with opposite spin direction. In longitudinal mode (nucleon spin parallel to the beam direction) the target cells polarization are reversed every 24 hours by rotating the direction of the solenoid field and changing the microwave frequencies of the two cells. During this operation, the polarization is maintained thanks to a transverse dipole field of 0.42 T. In transverse mode (nucleon spin orthogonal to the beam direction), the target material is kept in "frozen spin" mode at a temperature below 90 mK and the spin direction is maintained by the transverse dipole field. The reversal of the polarization is made exchanging the microwave frequencies of the cells after 5 to 7 days of data taking. Due to the long relaxation time of the target material (>1000 h), the polarization in the cells does not decrease significantly during the data taking period.

The structure of the target cells is clearly visible in fig. 2.3 (left), where the distribution of the reconstructed interaction vertices along the beam axis is shown. The vertices reconstructed outside the cells are due to interactions with liquid helium

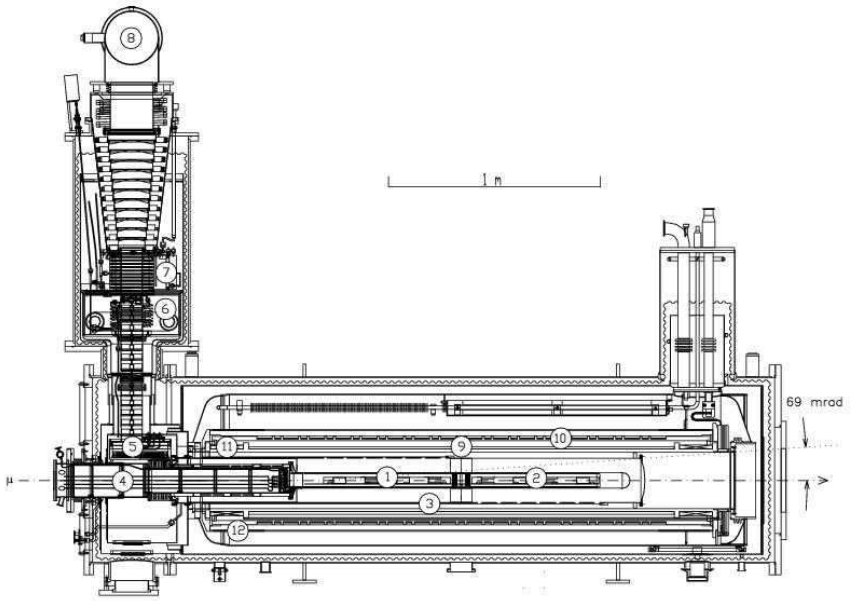

Figure 2.2: Side view of the COMPASS polarized target system: (1) upstream and (2) downstream target cell, (3) microwave cavity, (4) target holder, (5-8) ^{3}He-^{4}He refrigerator, (9) solenoid coil, (10-11) compensation coil, (12) dipole coil. The muon beam enters from the left. The two halves of the microwave cavity are separated by a thin microwave stopper.

or some other target component. The effect of the opening angle of the target solenoid is the non flat distribution of the number of reconstructed vertices along the beam axis; the number of vertices (and also of the outgoing tracks) is different for the upstream and downstream cell. As we will see in section 4.3.2, this effect is taken into account in the data analysis. The solenoid acceptance influences also the resolution on the z coordinate of the vertex: as shown in fig. 2.3 (right), it increases from about 5 mm at the downstream end of the target to 25 mm in average at the upstream end. In the direction perpendicular to the beam axis, the resolution on the vertex coordinates is 0.1 mm, due to the good resolution of the trackers detecting the beam and the scattered muon (section 2.5).

2.4 The analyzing magnets

The magnet in the first spectrometer, SM1, is a dipole magnet 110 cm long with aperture matching the spectrometer acceptance. The main component of the field goes from top to bottom; the field integral is 1 Tm and corresponds to a deflection

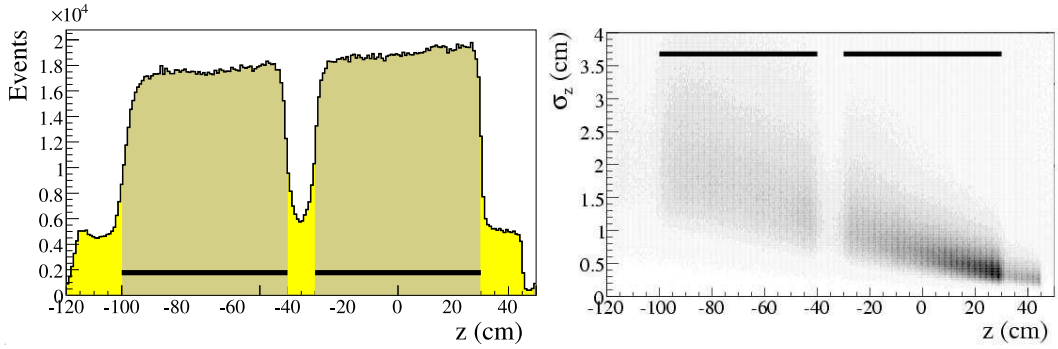

Figure 2.3: Distribution of the reconstructed vertex position z along the beam axis (left); distribution of the error σ_z vs. z (right). The solid lines show the position of the target cells.

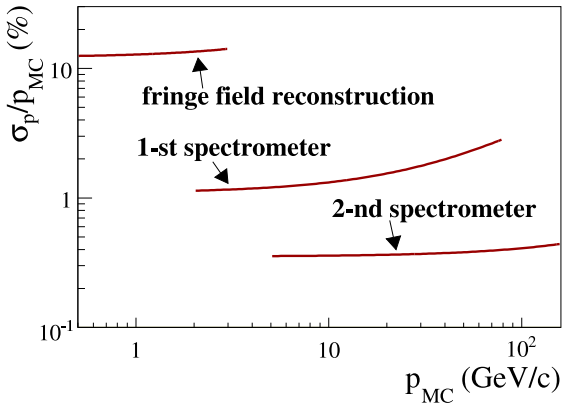

Figure 2.4: Track momentum resolution σ_p/p versus p.

of 300 mrad for particles with 1 GeV/c momentum.

The dipole magnet of the second spectrometer is 4 m long with a field integral of 4.4 Tm; as for SM1, the main field component is in the vertical direction.

Due to the different bending power of the two magnets, the momentum resolution is different for tracks reconstructed in the first or in the second spectrometer. This is shown in fig. 2.4, as a function of the particle momentum. Fringe field tracks means tracks reconstructed only before SM1, where the momentum can be measured using only the fringe field of the magnet.

2.5 The tracking system

The COMPASS tracking system consists of many tracking stations along the whole spectrometer. Each station is made of two or more detectors of the same type measuring different projections in the plane transverse to the beam direction.

Due to the large overall acceptance of the spectrometer, the region to be covered by the detectors is large and the characteristics needed change with the distance from the beam axis. Near the beam axis region, detectors should stand high particle flux and have a good time and position resolution; in the region far from the beam axis, the particle flux is less intense and the requirements for the detectors are less demanding.

The Very Small Angle Trackers (VSAT)

The beam region up to a radial distance of 2.5-3 cm is covered by eight stations of scintillating fibers and two stations of silicon detectors. These detectors measure the tracks of the incoming and scattered muon and of the hadrons produced at very small polar angles, in a very crowded environment, with a particle rate reaching 10^5 s^{-1} mm^{-2}.

The scintillating fibers have a diameter between 0.5 and 1 mm; each station is made by different planes in order to measure more than one projection. In each plane several layers, shifted one with respect to the other, are used in order to avoid low efficiency zones. The detection efficiency of scintillating fibers is above 99%, and the time resolution varies between 350 and 450 ps.

COMPASS silicons are microstrip detectors with double sided readout. The active area is 5×7 cm^2, with 50 μm pitch on both sides; the average spatial resolution is about 10 μm, time resolution is about 2.5 ns.

The Small Angle Trackers (SAT)

The region at a radial distance between 2.5 and 30-40 cm is covered by two recently developed devices employed for the first time in a high energy experiment: Micromegas (Micromesh gaseous structure) and GEM (Gas Electron Multiplier) detectors. Both devices are gaseous detectors in which the conversion and the amplification regions are separated. The working principle of the two detectors are shown in fig. 2.5 and 2.6. The performances of the detectors are very similar: the detection efficiency, time and space resolution are 97%, 9 ns and 90 μm for Micromegas and 97%, 12 ns and 70 μm for GEM respectively.

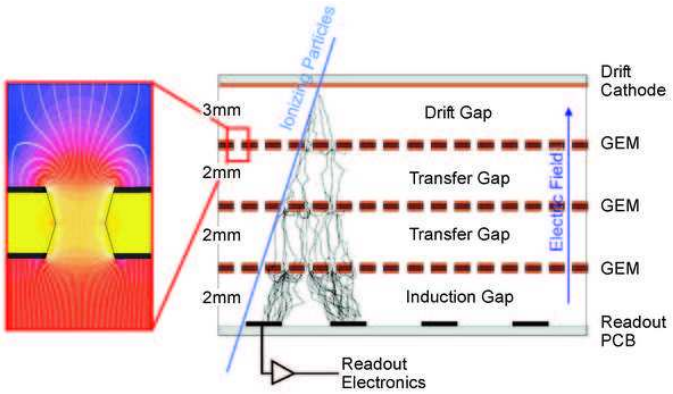

Figure 2.5: Schematic view of the GEM detectors. The gas-filled region between two parallel plate electrodes is divided by three 50 μm thin Polyimide foils with a very large number of holes ($\sim 10^4/\mathrm{cm}^2$). A Cu cladding on both sides of the foil allow the application of a potential difference of several hundreds of volts; when the primary electrons pass through the holes, multiplication avalanche occurs, and then the electrons are guided to another amplification stage or to the readout anode, formed by two sets of perpendicular strips.

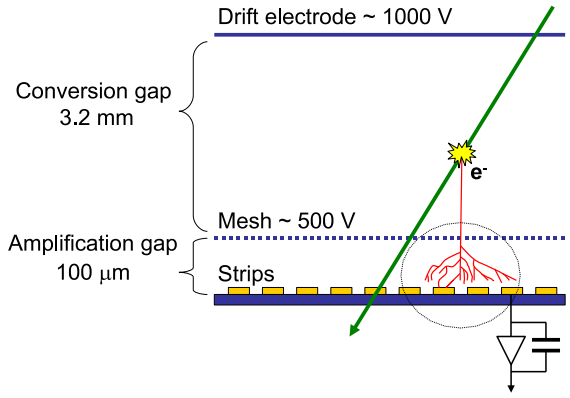

Figure 2.6: Schematic view of the Micromegas. The conversion and the amplification regions are separated by a metallic micromesh; in the conversion gap the ionization process takes place, and a moderate field of 1 KV/cm produces the drift of the primary electrons. A higher field of 50 KV/cm in the second region (100 μm gap) produces an avalanche resulting in many e^-/ions pairs. The electrons are then collected by the anode segmented in microstrips.

The Large Angle Trackers (LAT)

The reduced particle flux in the outer regions, covered by Large Angle Trackers, allows to use slower devices as drift chambers, straws and MWPC.

Three stations of Drift Chambers, each one measuring four coordinates, are placed in the first spectrometer; the active area is 180×127 cm^2, with a dead zone of 30 cm diameter near the beam region to avoid high rates. The spatial resolution of a DC is 190 μm. In the second spectrometer, there are other six drift chambers covering a very large area (500×250 cm^2, dead zone of 50-100 cm diameter); the spatial resolution is ∼500 μm.

Several stations of straw drift tubes are placed in both spectrometers, each one covering a region of 280×323 cm^2 (central dead zone of 20×10 cm^2). The tubes are made of a cylinder of plastics and a 20 μm diameter anode wire of gold plated tungsten. Each plane consists of a central zone with 6 mm diameter tubes and an outer region with 10 mm diameter. In each station three layers of tubes measure three different projections; the overall resolution for the 6 mm straw tubes plane is about 190 μm.

The tracking of particles at large angles in the SAS is mainly based on a system of eleven stations of MWPC, for a total of 34 planes; the active area is of 178×120 cm^2 (dead zone of ∼2 cm diameter), while the distance between anodic wires is 2 mm, allowing a spatial resolution of 1.6 mm.

2.6 Calorimetry

The hadron calorimeters

Both hadron calorimeters are located before the muon filters and have a double purpose in the experiment: they measure the energy of hadrons produced in the target and participate in triggering on semi-inclusive muon scattering events. The calorimeters are sampling calorimeters using stacks of iron and scintillator plates; the light collection is performed with wave-length-shifting fibers. The linearity of the energy response is of the order of a few percents for both calorimeters over different energy ranges: 0-25 GeV for HCAL1 and 10-100 GeV for HCAL2. The energy resolution can be parametrized as:

- HCAL1 σ/E =59.4%/$\sqrt{E}\otimes$ 7.6% for pions;
- HCAL2 σ/E =65%/$\sqrt{E}\otimes$ 5% for pions;

where E is expressed in GeV.

The electromagnetic calorimeter

The electromagnetic calorimeter of the second spectrometer, ECAL2, consists of 3000 lead glass modules corresponding to 16 radiation lengths in thickness. A high energy gamma ray or an electron crossing the detector, starts an electromagnetic

shower inside the lead glass. The e^+e^- pairs emit Cherenkov light that is viewed by PMTs at one side of each block. Linearity response is better than 1% until 40 GeV; the energy and spatial resolutions have been measured as:

- σ/E =5.5%/$\sqrt{E}\otimes$ 1.5%;
- σ_x =6 mm/$\sqrt{E}\otimes$ 0.5 mm;

with E in GeV.

2.7 The muon detectors

Both muon detectors (Muon Walls, MW) are made of two stations of trackers covering large surfaces ($\sim$4$\times$2 m^2) placed upstream and downstream an absorber. MW1 uses 8+8 stations of Plastic Streamer Tubes, measuring two projections; the absorber is a 60 cm long iron block. MW2 employs 6+6 planes of drift tubes measuring three projections and a 2.4 m long concrete block. The MW1 averaged tracking efficiency per plane is typically 91%, while for MW2 it is between 81 and 84%.

2.8 The trigger system

The main purpose of the trigger system is to distinguish a good event candidate in a highly crowded environment, with very small decision time and low dead time. It has also to provide a signal for the detector front-end electronics to start the recording of the data. The trigger components are four stations of two hodoscopes each, covering different regions around the beam line (for this reason the 4 stations are called "inner" (I), "middle" (M), "ladder"(L) and "outer"(O)) and a veto station made of two scintillator counters upstream the target. Moreover hadronic calorimeter information is used in some triggers. A schematic overview of the location of the trigger components in the spectrometer is shown in fig. 2.7.a.

Different techniques are used in the different kinematical regions covered shown in fig 2.7.b. For the high Q^2 region (Q^2 >0.5 (GeV/c)^2), "ladder" and "outer" hodoscope stations (H4L, H5L, H3O, H4O) are used to measure the muon scattering angle in the non-bending plane. Coincidence matrices are then used to select only the signals coming from the target region; the signal from the veto is used in anti-coincidence with the muon signal in order to reject halo muons tracks.

For lower Q^2 region, corresponding to small muon scattering angles, the target pointing technique cannot be used due to the imprecise reconstruction of the muon track using the hodoscopes only. The "inner" and "middle" hodoscope stations (H4I, H5I, H4M, H5M) measure the muon energy loss using the two spectrometer bending magnets and the trigger is given if a minimum energy loss is detected. In

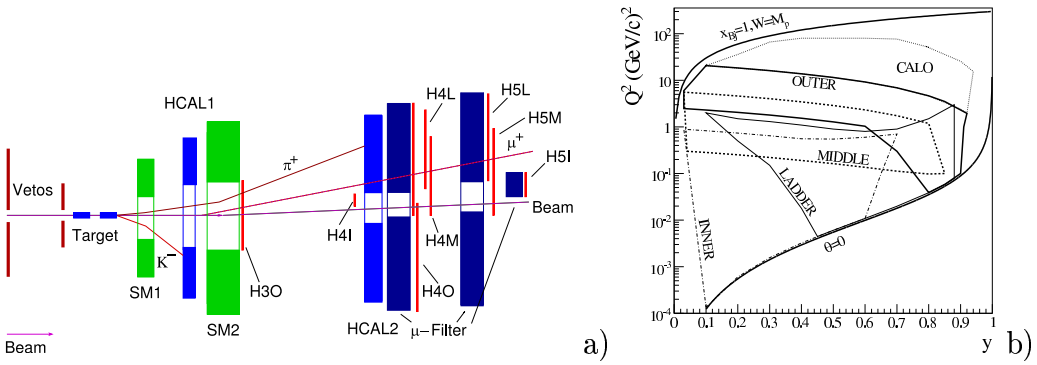

Figure 2.7: a) Schematic view of the location of the trigger components in the setup; b) The range in y and Q^2 for the four hodoscope trigger subsystems and the standalone calorimeter trigger.

addition a minimum energy deposit in the hadronic calorimeters is required, to eliminate background processes without hadron production, such as elastic scattering off electrons and nuclei or beam halo spurious signals.

The presence of an absorber in front of one of the two hodoscopes forming each station assures the rejection of electron and hadron tracks.

Together with hodoscope triggers, also a standalone calorimeter trigger is used to cover regions of high Q^2 that cannot be covered by the outer trigger. A trigger signal is generated if a minimum energy deposit in the calorimeter is left. Particular care is devoted to the cluster reconstruction, in order to reject clusters due to the pile-up of halo muon signals.

2.9 Readout electronics and data acquisition

The architecture of the data acquisition system has been dictated from the characteristics of the COMPASS environment. A large number of detector channels (∼250000), high trigger rates (10 kHz for muon beam, and up to 100 kHz for hadron beams) and big amount of data (35 kB per event, stream of 220 MB/s during spill time) suggested a pipelined and nearly dead-time free readout scheme as well recording techniques relying on buffering and parallelism.

The first stage of the data acquisition flow consists in the preamplification and discrimination of the detector signals. Data are then digitized and buffered, when possible directly in the detector front-end electronics, in custom-designed TDC and ADC modules. After the arrival of a trigger signal, the data are transferred to the readout driver modules called CATCH and GeSiCA, developed for the COMPASS experiment. Here the information arriving from different front-ends is merged for

each event, and stored in intermediate FIFOs until the transmission of the complete event to some PCs ("readout buffers") via optical fibers. CATCH and GeSiCA also distribute the trigger signals to the front-end modules and initialize them during the system startup.

In 2004, 19 PCs have been used as readout buffers. Each readout buffer contains four "spill buffer cards", used to reduce the bandwidth needed for the data flow taking advantage of the SPS duty cycle: data are written in the spill buffer cards during the spill time (4.8 s), and are then read out during the full SPS cycle (16.8 s). The grouping of the data stream corresponding to one event (event reconstruction) is made by 13 PCs named "event builders"; in these computers the "online filter" process takes place, in order to improve the purity of the trigger. The decision time for the online filter is of the order of 4 ms, and only a partial event reconstruction is possible. The decision criterion applied for the filter is based on the presence of a beam track in the event, fulfilled if a minimum number of hits in the BMS, SciFI and Si stations is present. In the event builders PCs, the data are split into files of 1 GB each (chunks) and sent to the CERN central computer center, where they are stored onto tapes of the CASTOR (CERN Advanced STORage manager) hierarchical storage system. In parallel, an Oracle database is filled with the information of each event and run. Each period of data taking is divided into sub-periods lasting one or two weeks; these are further divided in small sub-unities, called "runs", that are considered periods of stability of the apparatus conditions. Each run contains 100 or 200 spills, (corresponding to 25-50 minutes of data taking) and stores 1.5-2 million events.

2.10 The data processing

A typical data taking period lasts ∼100 days per year, corresponding to a total of ∼ 300 TB of raw data recorded. The huge amount of data collected implies a processing phase in which the data size of the files is reduced to increase the speed of following analysis. The computing power necessary to process the data with a rate comparable to the data acquisition rate is provided by the *COMPASS Computing Farm* at CERN. The reconstruction is based on CORAL (COmpass Reconstruction and AnaLysis), a framework written in C++, using object oriented techniques that allows an easy implementation of new pieces of code from different developers. The inputs for CORAL are the raw data containing the detector information digitized by the front end electronics; the information about the apparatus, such as calibration and alignment results, are stored and read from a database. Before the reconstruction phase, the data are decoded (the information on the fired detector channel is extracted) and clustered (channels fired from the same particle are grouped together). Then follows the reconstruction procedure, including track and

vertex reconstruction and particle identification. The output of CORAL, i.e. the reconstructed quantities for each event, are ROOT trees, called mini Data Summary Tapes (mDST), that are the input of the physical analysis. The data reduction factor between raw data and mDST is about 100. Also larger DST, containing detector digits, are written from CORAL; the ORACLE database manages the handling of these files.

2.11 The spectrometer upgrade

Taking profit of the long SPS shutdown in 2005, an important upgrade project of the spectrometer has been carried on, in order to improve the apparatus performances for the second part of data taking, started in 2006. The upgrade concerns the polarized target, the large area trackers in the LAS, the RICH-1 detector (see the next chapter), the electromagnetic calorimeters ECAL1, and the new tracker downstream RICH-1.

One of the most important changes in the setup is the substitution of the SMC target solenoid with the superconducting solenoid with large aperture. The new solenoid provides a field homogeneity of $\pm 4 \cdot 10^{-5}$ over the target region. The target configuration has been changed into three cells, instead of the two used until 2004: the middle cell is 60 cm long and it is polarized in opposite direction with respect to the upstream and downstream cell, each 30 cm long.

The new large acceptance allowed by the solenoid suggested the construction of two new large tracker telescopes for the LAS, placed downstream SM1: one station is made of straw tubes and the other one is a drift chamber with similar design of the DC already employed in the first part of COMPASS data taking.

The electromagnetic calorimeter ECAL1 is placed upstream HCAL1. It has large overall dimensions of 4×2.91 m^2, and is formed by blocks of three different sizes, coming from previous experiments.

A new large size tracking station (Rich wall) is placed downstream the RICH-1, in front of the ECAL1. It consists of eight layers of Mini Plastic Tubes, with the same design of those used in the MW1. The Rich wall tracker has a double role in the experiment: it measures the particles trajectories downstream RICH-1, allowing a better reconstruction of the particles crossing the detector, and it acts as a pre-shower for the ECAL1, improving its resolution.

Chapter 3

The COMPASS RICH-1

Particle identification is very important for most of the measurements performed in COMPASS, and in particular for the measurement of the Collins and Sivers asymmetries for different particles, pions and kaons. These asymmetries give access to the flavor dependent functions playing a role in the two mechanisms: the Sivers and transversity PDFs and the Collins FFs.

Hadron identification in COMPASS is mainly based on the RICH-1 detector, assuring identification capabilities in a crowded environment and good resolution values in a wide momentum range.

After a brief description of the RICH-1 detector, the reconstruction procedure and the variables characterizing the detector behavior will be discussed. This will be useful to understand the identification procedure adopted in the asymmetry analysis, described in the following chapter.

3.1 RICH-1 description

The RICH-1 [60] is a large-size Ring Imaging CHerenkov operating in COMPASS since 2001. The request to cover a wide momentum range for particle identification, from a few GeV/c up to 60 GeV/c, has suggested the use of a gaseous radiator, C_4F_{10}, in order to achieve good resolution also in the high momentum domain. The overall length of the radiator vessel ($\sim$3 m), has been chosen in order to have a large number of photons emitted from particles crossing the vessel. The transverse dimensions are also very large, to match the overall spectrometer acceptance ($\pm$250 mrad in the horizontal plane and $\pm$180 mrad in the vertical plane). The detector dimensions and the requirement of a minimal amount material in the spectrometer acceptance, dictated the final geometry (see fig. 3.1): two spherical mirror surfaces reflect the photons and focus them on 8 MWPC with CsI photocathodes located outside the spectrometer acceptance.

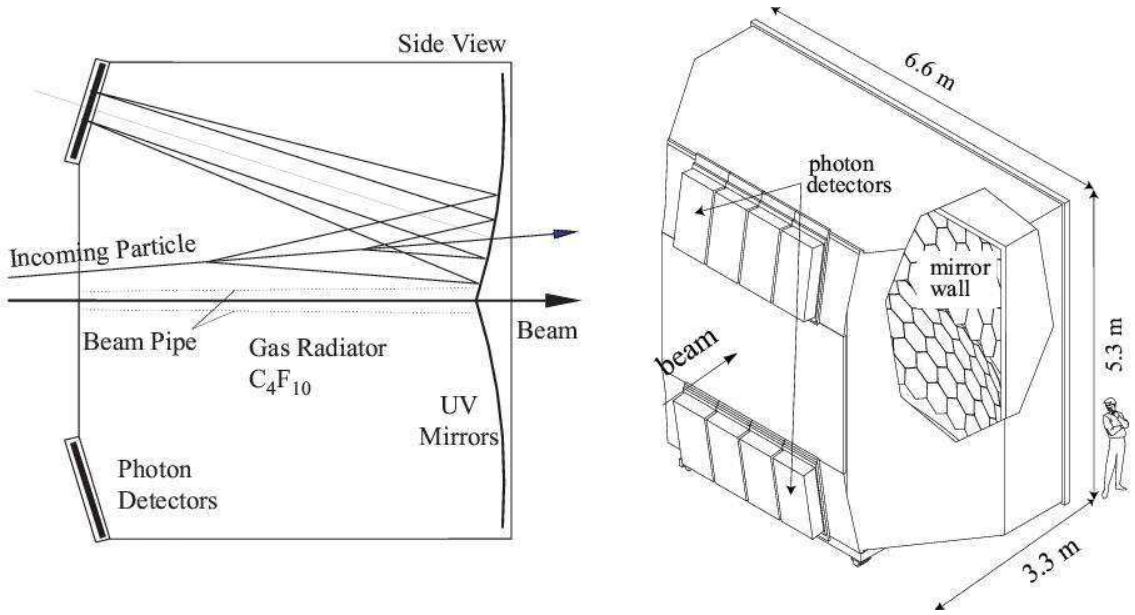

Figure 3.1: COMPASS RICH-1: principle and artistic view.

3.1.1 Gas and gas system

The RICH-1 radiator vessel has a length of ∼3 m and a volume of about 80 m^3. C_4F_{10} has been chosen as radiator due to its very low chromaticity ($dn/dE \sim 5 \cdot 10^{-5}$ at 7 eV) and a refractive index ($n - 1 = 0.0015$ for 7 eV photons) that allows hadron identification from Cherenkov threshold till momenta near to 60 GeV/c; the Cherenkov threshold for π, K and p are respectively 2.5, 9.5 and 17 GeV/c.

RICH-1 operates in the VUV wavelength domain, since the CsI quantum efficiency is different from zero only below 200 nm; therefore the radiator transparency to VUV photons is mandatory for RICH-1 operation. Since the photons are absorbed from impurities as water vapor and O_2, the level of contamination in the radiator gas is kept below 3 ppm with a dedicated gas system [61]. The system covers also different tasks: it is used to fill the radiator gas and to recover it in the storage tank, it avoids gas stratification inside the vessel and controls the radiator pressure in order to avoid mechanical stress to the thin vessel surfaces in the acceptance region and to the photodetector windows. Good transparency of the radiator, stable over months, was achieved since 2002 data taking. Figure 3.2 shows a typical transmission curve in the VUV domain, with the main contributions to the VUV light absorption: Rayleigh scattering, O_2 and H_2O.

In order to absorb the photons emitted from beam muons, that would cause a prohibitive amount of background photons, a 10 cm diameter pipe filled with Helium is positioned inside the vessel around the beam axis.

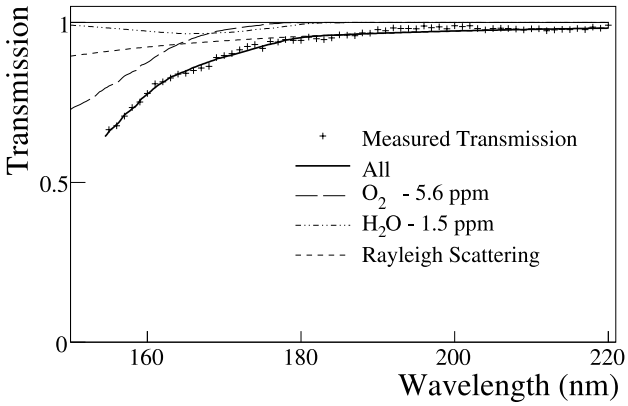

Figure 3.2: Typical UV light transmission through 1.87 m of C_4F_{10}, as measured online during data taking (crosses). The solid curve is a fit to the data. The main contributions to the UV light absorption are also shown.

3.1.2 Mirror system

The RICH-1 optical system [62] relies on two large surfaces of spherical mirrors with radius of curvature of 6.6 m. The curvature centers of the surfaces are located at ± 1.6 m distance from the beam axis, therefore the photon image is focused outside the spectrometer acceptance, where the photodetectors are located (fig. 3.1). Since the focusing surfaces are spherical, the geometrical aberration causes a small deformation of the image formed on the detector plane surfaces.

The reflecting surfaces cover an area of $\sim$21 m^2 and are made of 116 pentagonal or hexagonal mirrors (fig. 3.4); the dead zones between adjacent mirrors correspond to a 4% loss of reflecting surface. To limit the multiple scattering of particles crossing the detector, the mirrors are very thin: they are made of 7 mm of borosilicate glass covered with a layer of UV reflecting material ($\sim$ 80 nm of Al). Another layer of 30 nm MgF_2 protects the Al surface material from water vapor and O_2 contamination. The total material is about 5.5% of radiation length. The reflectance of the mirror system is above 80% in the 160-200 nm wavelength range (fig. 3.3).

Mirrors are suspended to nodal points of a net-like mechanical structure (fig. 3.4). The nodal points lay on a spherical surface and allow an angular adjustment of each mirror position with a 0.1 mrad precision.

3.1.3 Photon detectors

The photon detection system comprises 8 large-size MWPCs (576$\times$ 1152 mm^2) with CsI photocathodes [63]. The chambers are operated with CH_4 gas, transparent to VUV photons. A quartz window divides the methane from the radiator; pressure

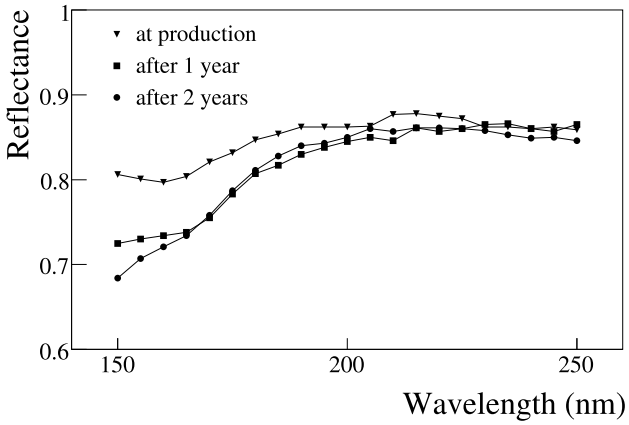

Figure 3.3: Measured reflectance for a typical mirror element. The measurements have been performed shortly after production, 1 year and 2 years later.

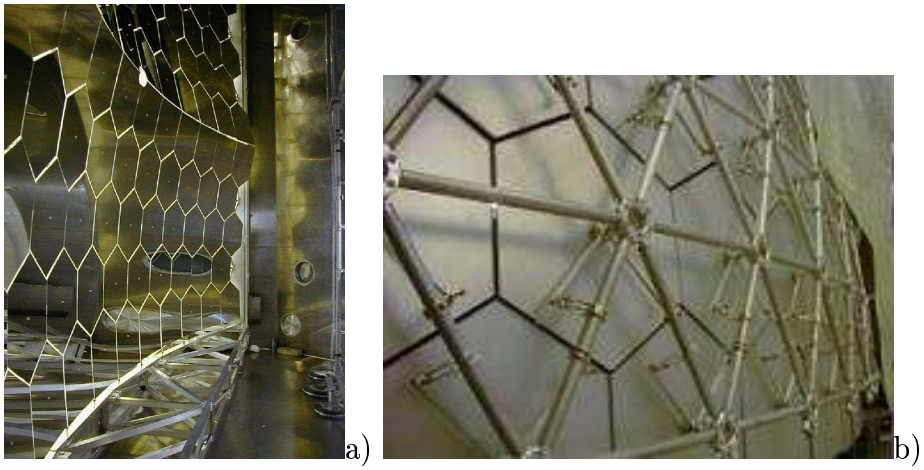

Figure 3.4: a) Picture of the reflecting surfaces of spherical mirrors; b) mechanical support structure of the mirror surfaces.

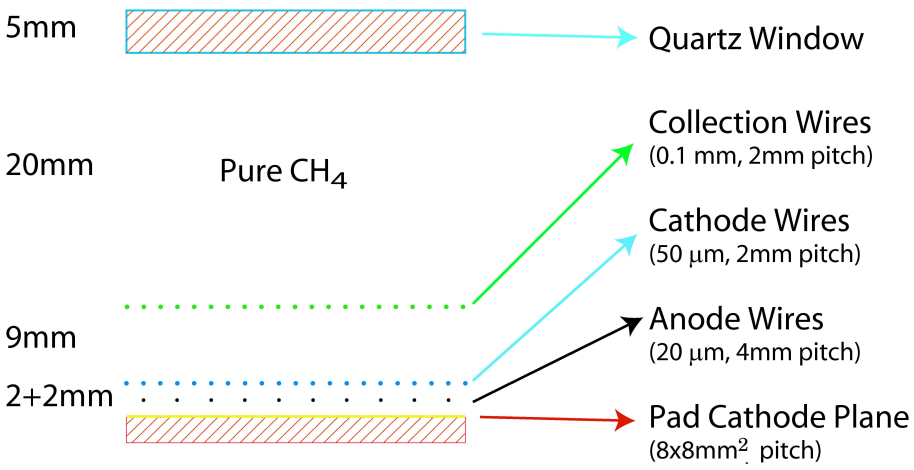

Figure 3.5: RICH-1 photon detector scheme.

gap is avoided maintaining the photodetector gas at atmospheric pressure. Each chamber has the photocathode surface segmented in 72×72 pads of 8×8 mm^2; these dimensions determine the spatial resolution of the detector. The distance between anode and cathode is 2 mm. The geometrical structure of the detectors is shown in fig. 3.5.

The CsI film on the segmented cathode is 500 nm depth, and it has a non zero quantum efficiency in the VUV domain only (fig. 3.6). The CsI material has been chosen since it is the only photon converter material stable in gaseous environment. Because of the presence of the CsI layer, photon detectors can exhibit electrical instabilities related to the high voltage and to the particle flux [64]; nevertheless great care in the mechanical construction of the MWPC and uniformity of the anode wire tension allowed to reach gain up to $5{\cdot}10^4$.

3.1.4 Readout system

The Cherenkov effect is characterized by the emission of few photons, 3 orders of magnitude below a scintillation process. This results in signals in the MWPC generated by single photo-electrons: the amplitude spectra for these signals is described by Polya functions, that can be approximated by an exponential curve for low multiplication values ($5 \cdot 10^4 \div 10^5$). It is therefore mandatory to have a readout system with reduced electronics noise and precise control of the effective threshold setting; in COMPASS RICH-1 this is obtained by using a modified version of the GASSIPLEX chip [67] and adjusting the threshold for each readout channel independently. GASSIPLEX has optimum matching with the detector signal, even if it has some intrinsic limitations: in particular an effective dead time of 3 μs, resulting from the

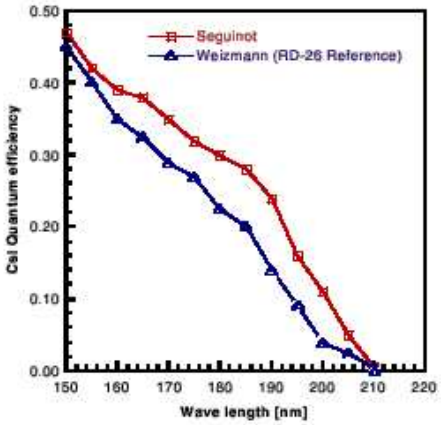

Figure 3.6: CsI quantum efficiency measured in vacuum as a function of the wavelength [65, 66].

time required for baseline restoration after the release of the track-and-hold signal.

The large number of RICH-1 electronic channels (82944) correspond to $\sim 40\%$ of the total number of COMPASS electronic channels. To reduce the data flow, empty channels are suppressed at the front end stage, and only the amplitude signals above threshold are read out and stored in local FIFO array. Data are then transmitted with optical fibers to the general acquisition system (see section 2.9) at a rate of 40 MB/s.

3.2 RICH-1 reconstruction

Fig. 3.7 shows the active pads in the photon detectors for one event; there are 6 visible rings and few active pads due to the background. A dedicated class of CORAL (section 2.10), named RICHONE [68], allows to reconstruct the interesting physical variables from the active pads in each event. The reconstruction procedure is based on two different stages:

- the **pattern recognition**, corresponding to the ring reconstruction for each track crossing the RICH-1 detector, and the determination of the Cherenkov angle; the trajectory parameters are necessary for this phase;
- the **particle identification (PID)**, in which a mass hypothesis is assigned to each particle; in this phase the particle momentum and the radiator refractive index are needed.

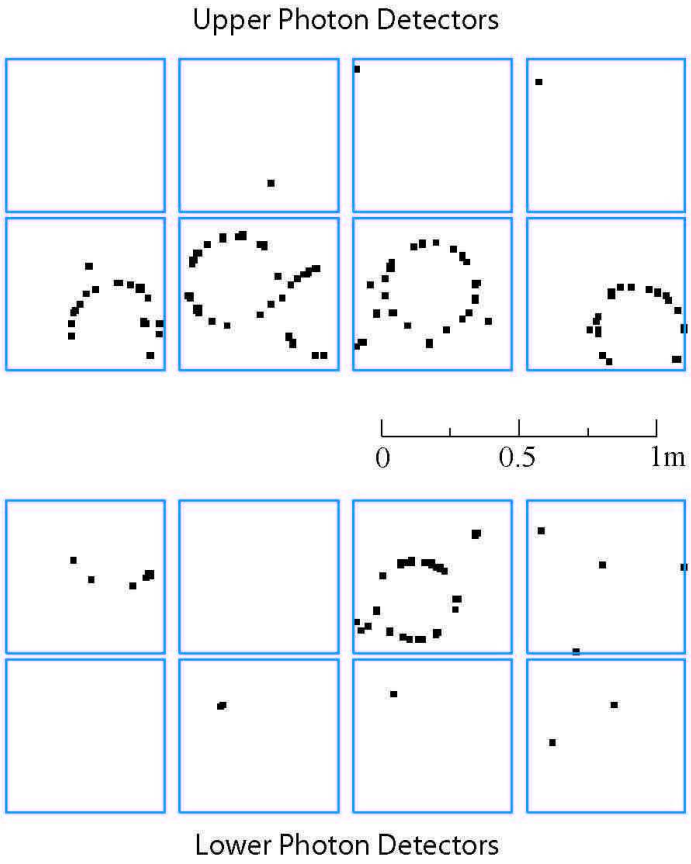

Figure 3.7: An event from the online event display of COMPASS RICH-1; the squares represent the hits with signal amplitudes larger than a threshold, individually set for each channel.

3.2.1 Pattern recognition

The ring reconstruction in RICHONE follows a method found in literature, developed by Ypsilantis e Seguinot [69]. The method is based on the knowledge of the particle trajectory inside the RICH-1 and of the coordinates of the detected photons. The values of the emission angles for each photon (θ_{Ch}, φ) are extracted from these informations. Then the ring reconstruction and the measurement of the Cherenkov angle are performed.

Clustering

In order to achieve a better determination of the photon impact point onto the photon detectors, the active adjacent pads are combined together in a cluster. The

impact point is found evaluating the mean of the position of each active pad in the cluster, weighting each pad with the corresponding pulse height information. The cluster is defined around the pad with maximum pulse height, choosing the adjacent pads with pulse height below 30% of the maximum in the x direction and below 60% in the y direction; the limit is less stringent in the y direction since the chamber wires follow this coordinate, resulting in a more broad signal.

Evaluation of θ_{Ch}

The Cherenkov photons are emitted uniformly along the particle trajectory inside the RICH-1 radiator, and are characterized by the same Cherenkov angle θ_{Ch}, (neglecting chromatic aberration) and by different azimuthal angles along the track, φ. The optical system focuses all the parallel photons, emitted in different points of the trajectory, in the same point of the detector (neglecting the spherical aberration), resulting in a ring image on the photon detector. Since the emission point of the photon along the particle trajectory is not known, the middle point of the track is taken. The Cherenkov angle is evaluated from the emission point and the photon impact point on the detectors, using the Hough transformation [69]. A good determination of the particle trajectory is mandatory in order to extract the Cherenkov angle with good precision.

Ring reconstruction

As a first approximation, for each track all the photons inside a fiducial region of aperture of 70 mrad are assumed to belong to the track; the angles θ_{Ch} and φ are then evaluated. In a correlation plot of θ_{Ch} as a function of φ, the photons belonging to the particle should distribute uniformly in the range (0-2π) in φ and around a precise value of θ_{Ch}. The ring reconstruction is based on the search of a peak in the θ_{Ch} distribution: small intervals of $\pm 3\sigma$ (where σ is the single photon resolution) on an overall range of 0-70 mrad (the maximum physical Cherenkov angle is around 55 mrad) are considered, and the interval with the maximum number of entries defines the ring. The Cherenkov angle of the particle θ_{ring} is then evaluated as the mean value of the Cherenkov angles of the photons belonging to the ring. Since the procedure finds a ring for each track, a minimal amount of 4 photons per ring is required. This helps the rejection of tracks with only background photons associated, as in the case for particles under Cherenkov threshold.

3.2.2 Particle identification

The particle identification, i.e. the assignment of a mass to a track, is based on a likelihood function, built using the Cherenkov angles of the photons, the track momentum and the refractive index. The likelihood does not depend on the last

part of the pattern recognition, the ring reconstruction, since it is evaluated using all the photons in the region of 70 mrad aperture around the particle track.

The likelihood function is made by two parts, describing respectively the probability for a photon to belong to the signal or to the background. The signal part is assumed to have a Gaussian shape, with standard deviation equal to the single photon resolution and mean value the Cherenkov angle θ^{th}_{hyp} corresponding to a mass hypothesis. The θ^{th}_{hyp} is evaluated from the mass value, the momentum and the refractive index using the formula $cos\theta_{Ch} = 1/n\beta$.

The signal probability is normalized to the mean number of photons expected from the Frank and Tamm equation ($S_0 = N_0 sin^2\theta_{Ch}$); in the expected number of photons evaluation also dead zones in the RICH-1 detector are taken into account.

A theoretic parametrization of the background contribution b is not so evident, therefore the description is taken directly from the data, taking into account some track parameters, as the track momentum and the polar angle at the RICH-1 entrance.

For a number N of detected photons, the likelihood function can be written as:

$$L_{hyp} = \frac{e^{-(S+B)}(S+B)^N}{N!} \prod_{i=1}^{N} \frac{(S_0 \frac{1}{\sqrt{2\pi}\sigma_i} e^{-\frac{(\theta_i - \theta^{th}_{hyp})^2}{2\sigma_i^2}} + b(\theta_{pol}, p))}{S+B}; \qquad (3.1)$$

where S and B are the signal and background photons integrated on the fiducial region around the particle track. The term $\frac{e^{-(S+B)}(S+B)^N}{N!}$ is the poissonian probability describing the expected number of detected photons, both signal and background contribution.

The likelihood function is evaluated for three mass hypotheses (π, K and p) and for the background hypothesis, neglecting the signal part. A first simple identification is made choosing among the 4 hypotheses the one corresponding to the highest value of the likelihood. To improve the identification purity, after having found the highest likelihood one can require the ratio of the likelihood with respect to the background hypothesis or to the second highest likelihood to be above a certain value. For this purpose the two distributions $\frac{LH}{LH_{back}}$ and $\frac{LH}{LH_{2nd}}$ are considered. The first variable is an index of the separation between a mass hypothesis and the background hypothesis; if this variable is near 1, it means that the likelihood of the identified particle and that of the background have almost the same value, implying that the distinction between particle and background hypothesis can be ambiguous. In the same way, the second variable indicates the distinction between 2 different mass hypothesis. The cuts on these distributions are tuned finding a good compromise in term of purity and efficiency of the sample. This is done maximizing the function Factor Of Merit (FOM) depending on both the statistics of the sample and on the purity; an example is $FOM = S \cdot (\frac{S}{S+B})$, where S is the number of signal

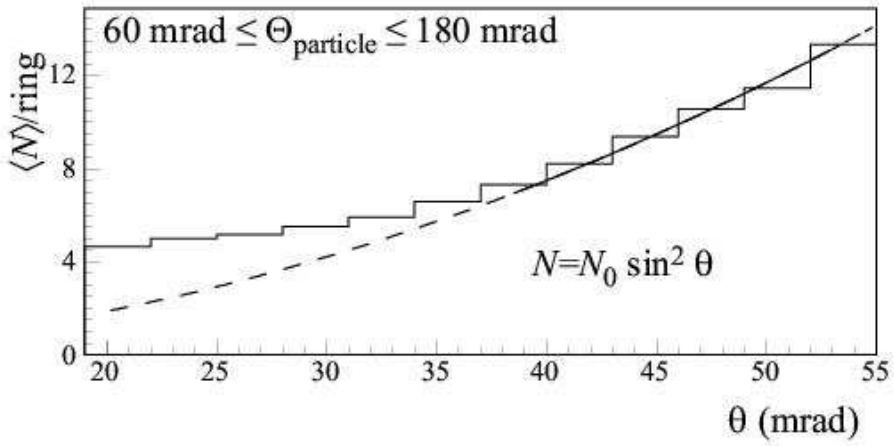

Figure 3.8: Mean number of detected photons per particle for the reconstructed ring images, as a function of the measured Cherenkov angle θ. The line is the best fit of the function $S_0 = N_0 \sin^2\theta$ in the range above 36 mrad.

particles in the sample and B the number of background particles. An example of this procedure will be described in section 4.2.3.

3.3 RICH-1 characterization

The RICH-1 performances have been monitored and studied using the data collected in COMPASS. In this section we present some aspects of the RICH-1 characterization, like the number of photons and the angular resolution. Systematic studies of RICH-1 efficiency and purity are presented in the next chapter (section 4.5).

3.3.1 Number of photons

The pattern recognition procedure allows to extract some information about RICH-1 characterization, as the number of photons per ring. In fig. 3.8 the number of photons belonging to the reconstructed rings is shown as a function of the Cherenkov angle of each ring. The distribution is fitted with the function $S_0 = N_0 sin^2\theta$, from the Frank and Tamm relationship; a good agreement between data and the theoretical curve can be observed. The fit is performed in the range above 36 mrad: the request of 4 photons per ring in the reconstruction procedure has as a consequence an excess of photons coming from background at low Cherenkov angles. From the fit, the mean number of photons emitted at saturation, namely at the maximum Cherenkov angle allowed ($\sim$55 mrad), is 14.

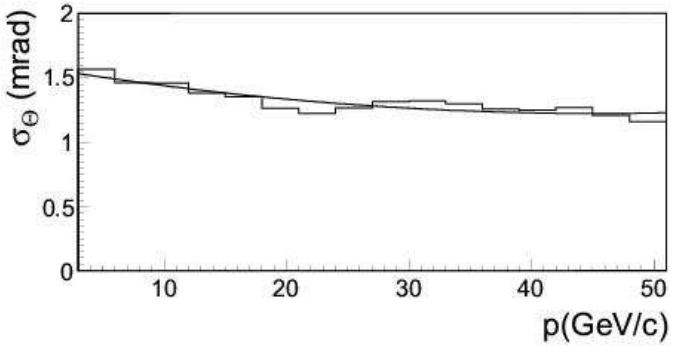

Figure 3.9: Resolution of the Cherenkov angle for a single photon for reconstructed rings, versus the particle momentum for a sample of identified pions.

To increase the purity of the identification, it is worth to introduce a cut on the minimum momentum of the particles that can be identified by the RICH-1. A natural choice would be to consider the physical Cherenkov threshold as the minimum value allowed, but we have already commented that rings with less than 4 photons per ring are rejected at the level of the pattern recognition; knowing the value N_0 of RICH-1, we can evaluate the momentum corresponding to the detection of 4 photons for each particle mass, and reject the particles with momentum below this value. In fact, the rings associated to these particles contain with high probability photons from the background and therefore the reconstructed Cherenkov angle is not correct. The Factor of Merit can be evaluated from the number of photons emitted at saturation and the maximum Cherenkov angle value:

$$N_0 = \frac{S_0}{sin^2(\theta_{Ch})} = \frac{14}{sin^2(0.055)} \sim 5000; \tag{3.2}$$

from this value, the momenta corresponding to the emission of 4 photons are evaluated as 3, 10.5 and 20 GeV/c, respectively for the pion, kaon and proton mass hypothesis. In the analysis described in this thesis, the cut on the minimum momentum was applied in the particle identification.

3.3.2 Angular resolution

Fig. 3.9 shows the single photon resolution for particles identified as pions as a function of the momentum. The resolution is extracted as the Gaussian width of the difference between the Cherenkov angle of each photon belonging to the ring and the Cherenkov angle for the pion mass hypothesis. At saturation the single photon resolution is ~1.2 mrad.

The single photon resolution is due to different factors:

- the spatial resolution of the MWPC pads;

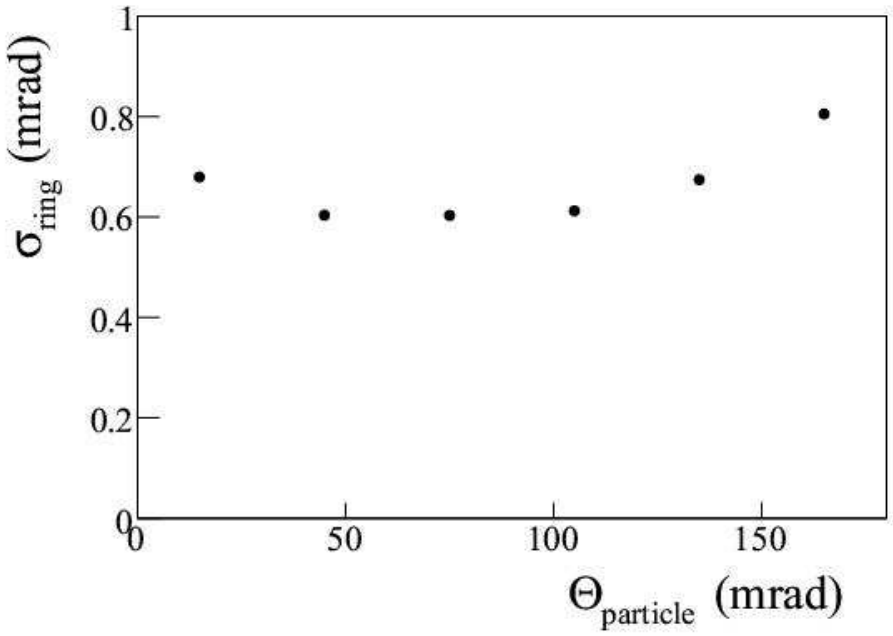

Figure 3.10: Cherenkov angle resolution for the reconstructed rings versus the particle polar angle.

- radiator chromatic aberration;
- spherical aberration of the optical system;
- misalignment in the geometry of the system;
- resolution in the reconstruction of the particles tracks;
- electronic noise on the photon detector and physical background.

The photon resolution depends also on the pattern recognition method: in RICHONE, the algorithm finds the ring that has more photons. Therefore the presence of background photons in the detector, especially in the inner zone, where the halo contribution is huge, strongly disturbs the reconstruction procedure. Moreover in this region the signal to background ratio is further decreased by the presence of the beam pipe, absorbing signal photons.

The ring resolution values are shown in fig. 3.10 as a function of the particle polar angle at the RICH-1 entrance; the mean value is around 0.6 mrad. The ring resolution does not scale perfectly with the number of photons due to the presence of background photons in the rings, diluting the signal yield.

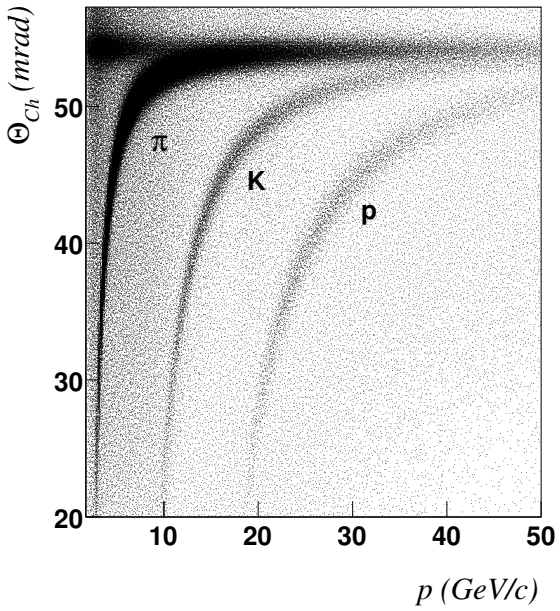

Figure 3.11: Cherenkov angles as measured with RICH-1 versus the particle momenta.

3.3.3 Mass separation

Figure 3.11 shows a plot of the Cherenkov angles as measured with RICH-1, versus the particle momentum. The bands corresponding to pions, kaons or protons are clearly visible. At high momenta, near 40 GeV/c, the different bands begin to overlap; in particular, the pion and kaon bands are close. To find the maximum momentum value allowing pion-kaon separation, the function $\sigma(p)/(\theta_K - \theta_\pi)$ has been considered: $\sigma(p)$ is the ring resolution parametrized as a function of the momentum, and $\theta_K - \theta_\pi$ is the difference between the K and π Cherenkov angles from kinematics, also depending on momentum. In fig. 3.12 the function is shown, together with the lines indicating the 3, 2, 1.5 σ separation; the corresponding momentum values are 35, 43 and 50 GeV/c respectively.

It is interesting to compare these values with those obtained using the formula from the literature:

$$p = \sqrt{\frac{\Delta m^2}{2 n_\sigma \sigma_{\theta_{ring}} \tan\theta_{Ch}}}; \tag{3.3}$$

where Δm^2 is the difference in the squared mass of the mass hypothesis. Taking the resolution value at saturation as 0.6 mrad we obtain momenta of 33, 41 and 47 GeV/c respectively for the 3, 2, 1.5 σ separation, in rather good agreement with the values extracted directly from the data.

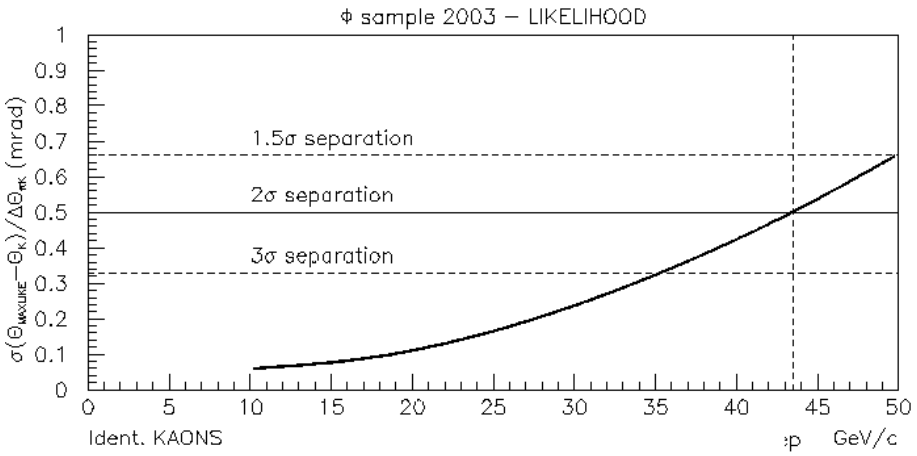

Figure 3.12: $\sigma(p)$ divided by θ_π-θ_K, the separation from kinematics, as a function of the momentum. The 2σ K/π separation line crosses the measured separation at about 43 GeV/c.

3.4 RICH-1 upgrade

The COMPASS upgrade project has been already introduced in the previous chapter; one of the major improvements implemented within this project is the upgrade of the RICH-1 detector.

RICH-1 has been in operation since 2001 and, following several improvements, it reached fully satisfactory performances in 2003. The major limitations of the detector is due to the presence of the large muon halo, bringing a high pad occupancy from background photons. The long dead-time of RICH-1 read-out, of the order of 3 μs, further decreases the signal to noise ratio. Moreover in case of minimum ionizing particles traversing the CsI-MWPCs, the probability for electrical instabilities in the photon detectors increases; this limits the maximum achievable gain and consequently the number of measured photons.

The upgrade project was studied to overcome the limitation of the RICH-1 detector, since in the second part of COMPASS data taking, the luminosity has been increased: the beam intensity is around 100 MHz (40 MHz until 2004) and the trigger rates can reach 100 kHz for the hadron program (20 kHz until 2004).

The project involves two complementary technologies. In the most central region of the detector, both the detection method and the read-out scheme are replaced. The use of Multi-Anode Photo-Multiplier Tubes (MAPMT) leads to a significant increase in the number of detected photons, thus enlarging the momentum range in which efficient PID is performed. In the external part, comprising the 75% of the active area, the existing MWPC are coupled with a new read-out based on the

APV25 chip, already used in COMPASS for GEM and silicon detectors. The dead time is reduced from 3 μs to 400 ns, bringing a large suppression of the uncorrelated background.

The RICH-1 upgrade has been successfully completed in spring of 2006. The upgraded RICH-1 performances during 2006 data taking have been monitored and indicate a fully satisfactory behavior of the detector.

Chapter 4

Measurement of the Collins and Sivers asymmetries

The first preliminary results of the COMPASS collaboration on the Collins and Sivers asymmetries have been published in 2005 [18], using the 2002 data. Final results extracted from the total statistics collected on the transversely polarized deuterium target in the years 2002-2004 have been published in January 2007 [19]. The published results are extracted from SIDIS events in which the final state hadrons are not identified. In the analysis presented in the following the hadrons have been identified as kaons and pions using the RICH-1 of the COMPASS spectrometer, and the asymmetries have been measured for the two data samples. These results have been presented for the first time at the QCD06 conference [70] and they will be published soon (paper in preparation).

The chapter is structured as follows: first we introduce the data sample on which the analysis has been performed, explaining in some details the studies concerning the RICH-1 stability in time. We then describe the criteria chosen to select SIDIS events in the data and to identify the hadrons; we give the results of the measured Collins and Sivers asymmetries on pion and kaon samples, postponing the interpretation of the results to the following chapter. We conclude the chapter with the description of the studies performed to assess the systematic error of the measurement and with the evaluation of the kaon sample purity.

4.1 Data handling

4.1.1 Data sample

For this work, the COMPASS transverse data collected in 2003 and 2004 with identification capabilities have been analyzed; during the 2002 data taking with the transversely polarized target, RICH-1 particle identification cannot be used due to

a bad C_4F_{10} transparency. The data have been taken during 13 days in 2003 and during 22 days divided in two periods in 2004.

In order to compare data with the two target spin orientations in one cell, each data taking period has been divided in 2 sub-periods (fig. 4.1); the first one (p1) with the spin of the upstream cell nucleons "up" and of the downstream cell "down" (yielding f.i. N_u^+ and N_d^-), and the second sub-period (p2) in the opposite configuration (yielding N_u^- and N_d^+). In section 4.3.2 it will be discussed how the information from the two sub-periods are combined to extract the asymmetries.

Figure 4.1: The different spin orientations in the upstream and downstream target cells in two sub-periods, p1 and p2.

Table 4.1 reports for each period the year, the name of the sub-periods, and the corresponding muon beam flux impinging on the target.

date	sub-periods	integrated muon flux
20/08 - 03/09/2003	P1G - P1H	$8 \cdot 10^{12}$
13/08 - 25/08/2004	W33 - W34	$6.3 \cdot 10^{12}$
25/08 - 05/09/2004	W35 - W36	$7.9 \cdot 10^{12}$

Table 4.1: The data used in this analysis: the first column gives the period, the second the sub-periods name, the last one the integrated muon flux.

4.1.2 Data stability

Data taking conditions stable in time are a mandatory requirement to measure small effects as cross section spin asymmetries. In particular, for the transversity measurements, it is important to assure the data stability inside each period used to extract the asymmetries. In a complex apparatus as COMPASS, there are many redundancies and several sources of possible instability in the data and it is not always possible to identify them during the data taking time. Therefore an offline analysis of the data is necessary in order to test the data stability versus time and

reject from the physical analysis runs or spills showing instability, and that could cause false asymmetries.

To monitor the apparatus performances, the stability in time of many distributions has been checked dividing the periods into runs or clusters of runs. The time stability of the reconstruction efficiencies were checked looking at the hit distributions in the about 360 detector planes and at different variables: the mean number of clusters per plane and per event, the mean number of tracks per event, the mean number of track segments in the different spectrometer regions per event, the mean number of primary vertices per event, the mean number of secondary vertices per event.

The stability was also checked monitoring the number of reconstructed K^0 mesons per primary vertex, the reconstructed K^0 mass distribution, the energy measured in the two hadronic calorimeters HCAL1 and HCAL2, the coordinate distributions of the interaction vertex, the vertex χ^2 distribution and the distributions of several kinematic observables (like x, Q^2, y, the azimuthal angles and the momenta of the scattered muon and of the hadrons). As an example, the mean $\pi\pi$ invariant mass in the K^0 region from the data collected in the first sub-period of the 2004 run is shown in fig. 4.2 as a function of time.

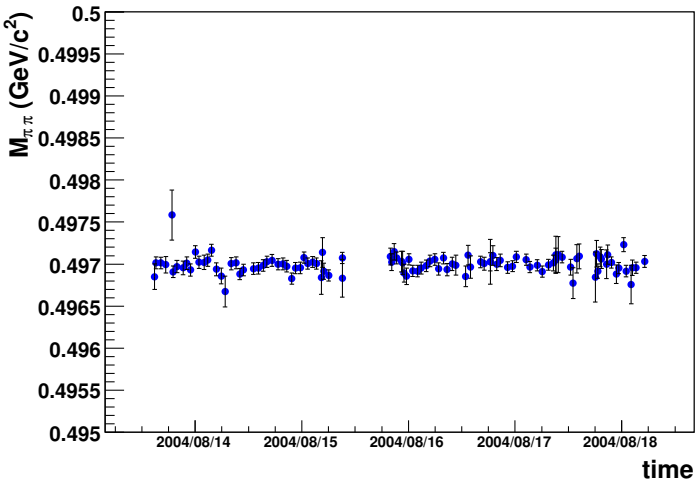

Figure 4.2: $\pi\pi$ invariant mass in the K^0 region as a function of time from August 13 to August 19, 2004.

Runs showing some instabilities were not used for the physics analysis. The runs rejected by these criteria are about 5% and 4% of the initial raw event sample of 2003 and 2004 data.

4.1.3 RICH-1 stability

The identification of hadrons as kaons or pions is made using the RICH-1 information, described in details in section 4.2.3. The stability in time of the performances of this detector has been checked with some specific tests which have been an important part of this work and are described in this section.

Monitor on likelihood shape

This monitor is based on the idea that the shape of the likelihood distributions for hadrons identified as π and as K should not change upon time[1]. To monitor the stability in time of the likelihood shape, we computed the ratio between the likelihood distribution for each run of one sub-period and the distribution on the entire sub-period considered. In the hypothesis of a shape not changing in time, this ratio should be perfectly flat; from a fit with a constant function the reduced χ^2 and the corresponding probability p_0 are taken as stability indexes. The principle of the method is given in fig. 4.3, where an example for pions from 2003 data is shown.

Together with the distributions of the likelihoods for the total sample of π and K, also some subsamples have been studied, considering four bins of the hadron polar angle at RICH-1 entrance ($0< \theta_h < 30$ mrad, $30< \theta_h < 60$ mrad, $60< \theta_h < 90$ mrad, $90< \theta_h < 120$ mrad) and four bins corresponding to the four geometrical zones in the detector: Jura up and down, Saleve up and down. For kaons the last bin in polar angle is not considered because there is not enough statistics. In fig. 4.4 the likelihood distributions in these bins have been reported.

In fig. 4.5 and 4.6, the results from the stability tests applied on the sub-period P1G are given. The left part of fig. 4.5 shows the probability p_0 values as a function of each run of the period for the likelihood distribution of identified pions (fig. 4.4), expected to be uniformly distributed between 0 and 1. The solid line in each plot is the result of a fit with a constant function, the mean value of the probabilities p_0. In the right part of fig. 4.5, the corresponding reduced χ^2 values are shown, again for the likelihood distribution of pions of fig 4.4; the solid line corresponds to a fit of the points with a constant function. Fig. 4.6 shows the probability p_0 and the χ^2 values for the hadrons identified as kaons. From the pictures, one can see that the mean probability p_0 for all the kaon and almost all the pion distributions is near 0.5, and the reduced χ^2 is near 1, as expected for good fits. The plots corresponding to the total likelihood distribution for pions and for the first two bins in polar angle exhibit low probability values and corresponding high χ^2 values; the reason for this behavior is not connected to the detector stability but to the background fluctuation, as we will comment later.

[1]Here and in the following for likelihood is intended the ratio of the likelihood of the mass hypothesis to the one of background, since this variable is used in the identification procedure (see section 3.2.2).

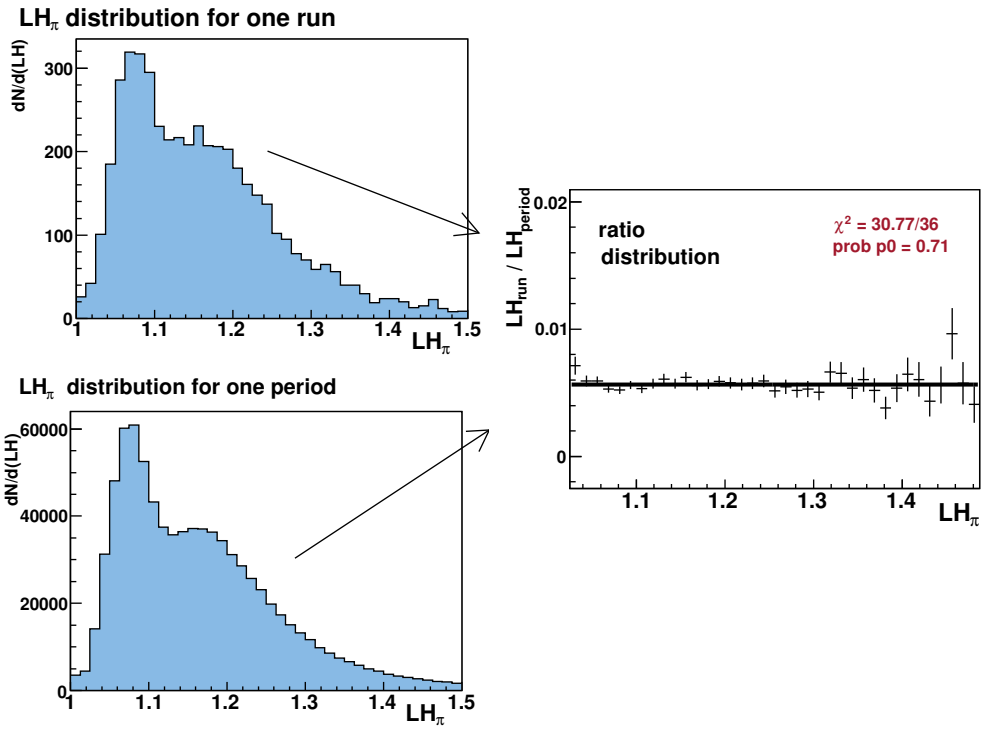

Figure 4.3: Left: the likelihood distribution of one run (top) and the likelihood distribution of the entire period (bottom). Right: the ratio of the distributions is fitted with a constant and the reduced χ^2 and the corresponding probability p_0 are taken as stability monitor.

In the χ^2 monitor (right part of fig. 4.5 and 4.6), it is possible to notice some runs showing a bad χ^2 value in more than one distribution. Some of these runs have been marked with an elliptic box in the pictures and have been labeled as "bad runs" in this monitor.

Also a structure with up and down consecutive χ^2 is present, as shown in fig. 4.7, that is a zoom of the first χ^2 plot of fig. 4.5. This is connected to the day-night effect on the multiplicities in 2003 data, as we will comment later. For the other sub-period of 2003 data, the situation is very similar to the one reported for sub-period P1G; for the two periods of 2004 data, the situation is more stable and the runs corresponding to bad χ^2 are only a few. Moreover the "structure" in the χ^2 monitor plots is absent.

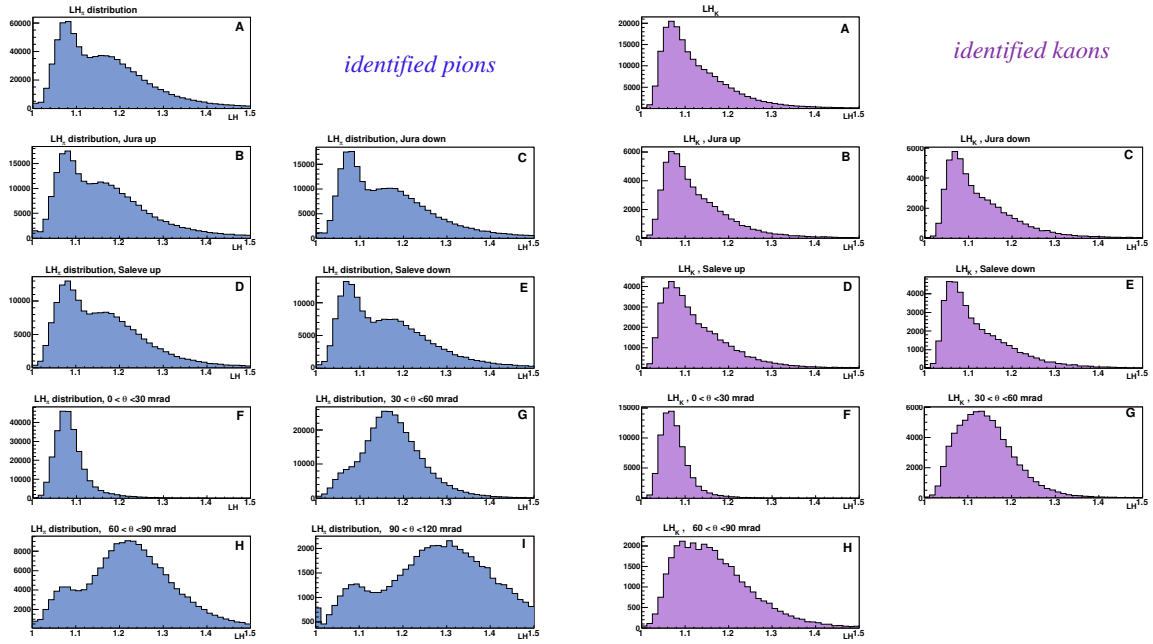

Figure 4.4: At the left, the likelihood distributions for hadrons identified as π with the likelihood method in the P1G sub-period: total sample (plot A), subsample divided according to the 4 detector regions (B: Jura up, C: Jura down, D: Saleve up and E: Saleve down), and subsample divided according to polar angle bins (F: $0< \theta_h < 30$ mrad, G: $30< \theta_h < 60$ mrad, H: $60< \theta_h < 90$ mrad, I: $90< \theta_h < 120$ mrad). At right, the corresponding likelihood distributions for the hadrons identified as kaons (the last bin in polar angle is missing because of lack of statistics.)

Sensitivity of the monitor

Before rejecting from the analysis a run marked as "bad" with the test described in the previous section, we looked for possible explanations of its instability in the run logbook of the experiment[2], where comments on all changes and instabilities of the apparatus should be written. As an example, for two of the runs marked in fig. 4.5 and 4.6 we found in the logbook the comments pointing to front-end problems, (thus not all the RICH-1 data have been recorded, bringing to a lower cathode multiplicity with respect to the standard situation), and to an increase of the RICH-1 multiplicities due to an increment of the temperature. Other reasons found in the run logbook for the RICH-1 instability were due to noisy strips (see fig 4.8) or HV problems (see also section 4.1.3).

[2]this is a web based logbook, connected to a MySQL database for the permanent storage of comments and annotations during the data taking

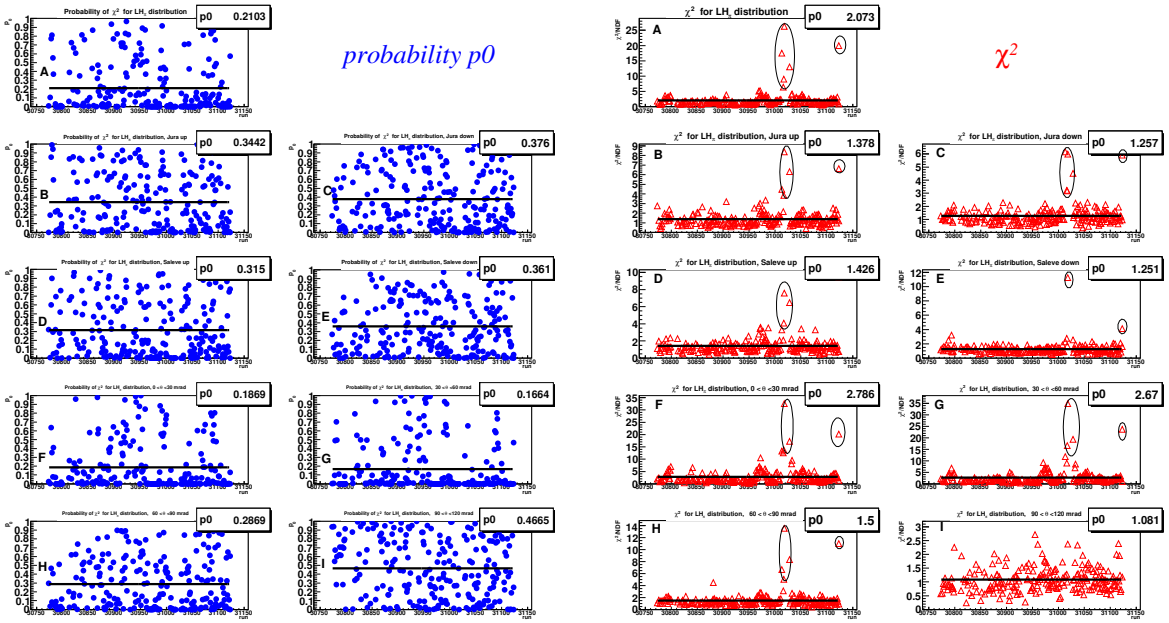

Figure 4.5: Left: probability p_0 as a function of the run number of the sub-period P1G corresponding to the likelihood distribution of identified pions, given in fig 4.4: total sample (plot A), subsample divided according to the 4 detector regions (B: Jura up, C: Jura down, D: Saleve up and E: Saleve down), and subsample divided according to polar angle bins (F: $0< \theta_h < 30$ mrad, G: $30< \theta_h < 60$ mrad, H: $60< \theta_h < 90$ mrad, I: $90< \theta_h < 120$ mrad). The solid lines are the result of a fit with a constant function, indicating a mean value for the probabilities p_0. Right: the corresponding reduced χ^2 values, for the same likelihood distributions. The solid line refers to a fit with a constant function.

Likelihood stability for pions

The likelihood distributions ratio for pions at small polar angle show a bad general behavior in the probability p_0 and χ^2 monitors. The explanation can be found considering the dependence of the likelihood distribution on the particle polar angle, clearly visible in fig. 4.9. It can be useful here to remind that for likelihood we intend the ratio of the likelihood of the mass hypothesis to the likelihood of the background hypothesis: thus the different amount of background photons from the beam halo particles in the regions closer to the beam line translates in different likelihood values. The "discontinuities" in the scatterplots are due to the fact that the likelihood calculation uses a background parametrization as a function of the hadron polar angle. The difference in the likelihood ratio shape between kaons and pions (see fig. 4.4) is due to the different Cherenkov threshold for the two masses: kaons with a momentum lower than 9 GeV/c do not enter in the sample, meaning that there are few kaons with high polar angle and high likelihood values; for this

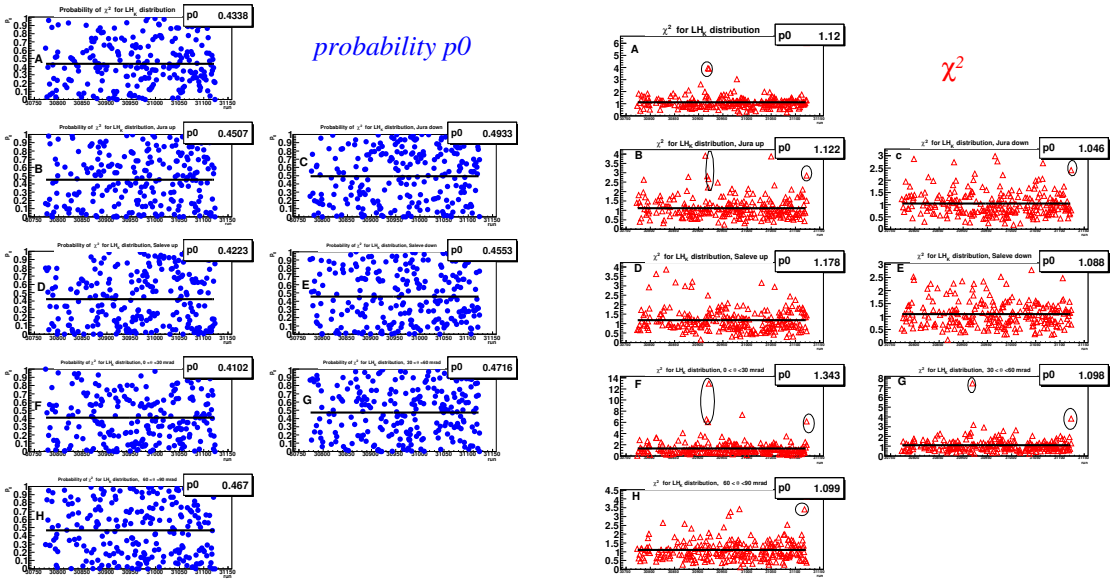

Figure 4.6: The same as in fig. 4.5, for hadrons identified as kaons.

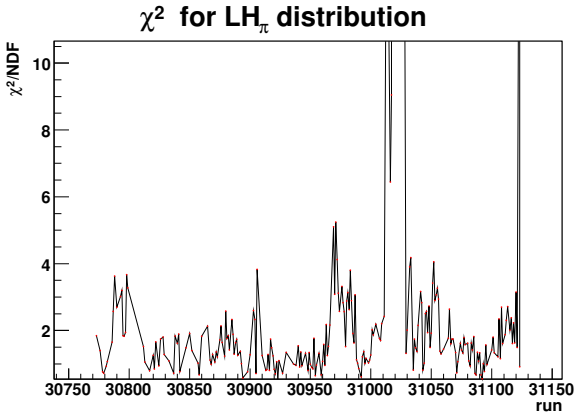

Figure 4.7: Zoom of the first χ^2 plot of fig. 4.5; a structure with up and down χ^2 is visible.

reason the likelihood distribution for kaons is more regular with respect to that for pions, and the stability monitor is more stable. It is important to note that the low probability p_0 values found in the monitor are not correlated with a bad behavior of the RICH-1, but with the different amount of background photons, that is related to the fluctuations of the beam halo intensity.

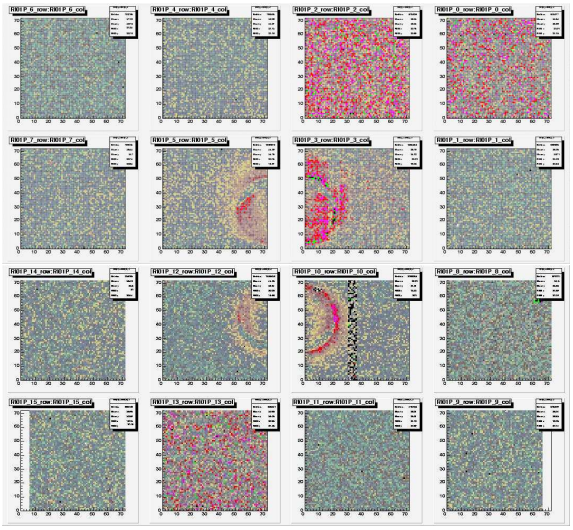

Figure 4.8: Hits distribution of the 16 photocathodes in a run with a noisy strip.

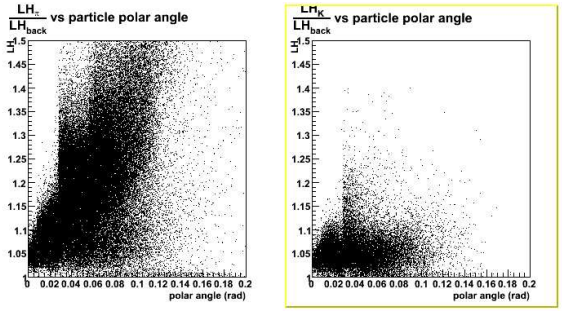

Figure 4.9: Distribution of the likelihood as a function of the particle polar angle for hadrons identified as pions (left) and as kaons (right).

RICH-1 hardware stability

As seen in the previous paragraphs, some runs labeled as bad with the χ^2 monitor are correlated with comments about the RICH-1 photocathode multiplicities in the run logbook. The cathode multiplicities are strongly related to the values of the temperature because the MWPC signal amplitude are evaluated with respect to the pedestal value. The pedestal value moves with the temperature because of the white noise presence. In the 2003 setup, only two settings (corresponding to the "day" and "night" scenario) for the thresholds were present, and the loading of the settings was done by hand. In the 2004 setup, a tool for the automatic loading of the threshold has been developed.

The connection between multiplicities and temperature values is clearly visible in the day-night effect in the transversity periods of 2003 data (fig. 4.10), for all the 16 cathodes of the RICH-1 chambers; while for the 2004 transversity periods the multiplicity distributions are very flat (fig. 4.11).

The day-night fluctuations in the multiplicity values are also visible in the χ^2 distributions for 2003 data (see fig. 4.7): this is related to the fact that the likelihood function is computed taking into account all the hits detected in the chambers, so a change in the amount of hits is strongly related to the value of the likelihood functions.

This is confirmed by the observation that almost all the runs found outside the 3σ region centered on the mean multiplicity value of at least one of the 16 cathodes, were already classified as bad in the "shape" monitor. This also explains why in the 2004 data we found only a few runs showing RICH-1 instabilities: the automatic loading of the thresholds resulted in very stable multiplicity and likelihood distributions.

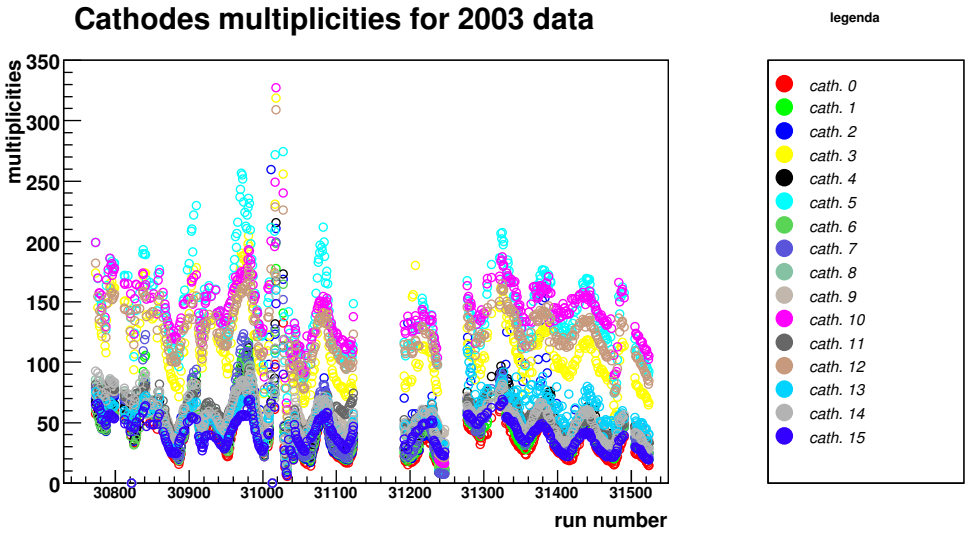

Figure 4.10: Photocathode multiplicities as a function of the run number for 2003 transversity data.

RICH-1 stability monitor spill per spill

The monitors described above have been used to identify and reject runs with stability problems in the RICH-1. A more refined stability analysis, checking the RICH-1 stability in each spill of the accepted runs has also been performed. At the end, the unstable spills of each run were rejected. The shape and the multiplicity monitors cannot be used for a stability analysis on a spill per spill basis: the histograms

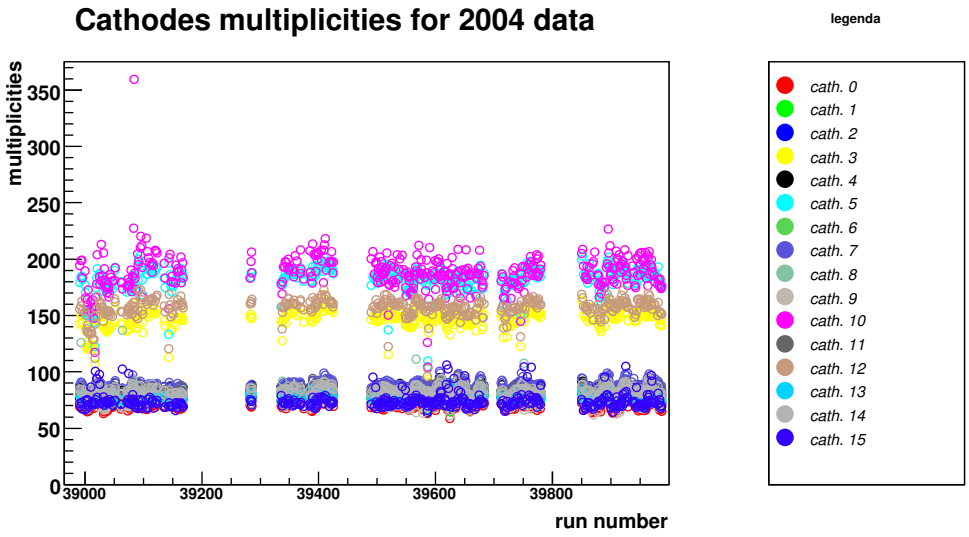

Figure 4.11: Photocathode multiplicities as a function of the run number for 2004 transversity data.

considered have only few entries for each spill and therefore are not significant. The quantity chosen to check the spill stability is the number of hadrons identified as π and K.

In the upper part of fig. 4.12, the number of hadrons identified as K and π, normalized to the number of tracks from the interaction vertex, is shown as a function of the spill number, in one sub-period of the transversity data (W33). In the middle part, the projection on the Y axis are presented with a Gaussian fit. Using the mean value μ and the standard deviation σ of the Gaussian, we built the two normal variables $\frac{N_\pi - \mu_\pi}{\sigma_\pi}$ and $\frac{N_K - \mu_K}{\sigma_K}$. The correlation between these two variables is shown in the lower part of fig. 4.12; it is due to the fact that, if we neglect the particles identified as protons (that are very few), a track can be identified either as a kaon or as a pion. If in a spill there are more tracks identified as pions, as a consequence the tracks identified as kaons are less, and vice-versa. We classified a spill as "bad" if it lied outside the ellipse giving the 3σ confidence level, as shown in the figure.

To check roughly the effectiveness of the monitor on spills basis, we show in fig. 4.13 the result of the stability analysis for one sub-period (P1H) including also the bad runs; in this figure, a big group of spills well outside the accepted region is clearly visible, corresponding to the high voltage of the MWPC being switched off after a RICH-1 gas alarm.

We decided to apply this monitor also to the run stability analysis; the plots for the sub-period P1H are shown in figure 4.14. Since in one run we have enough

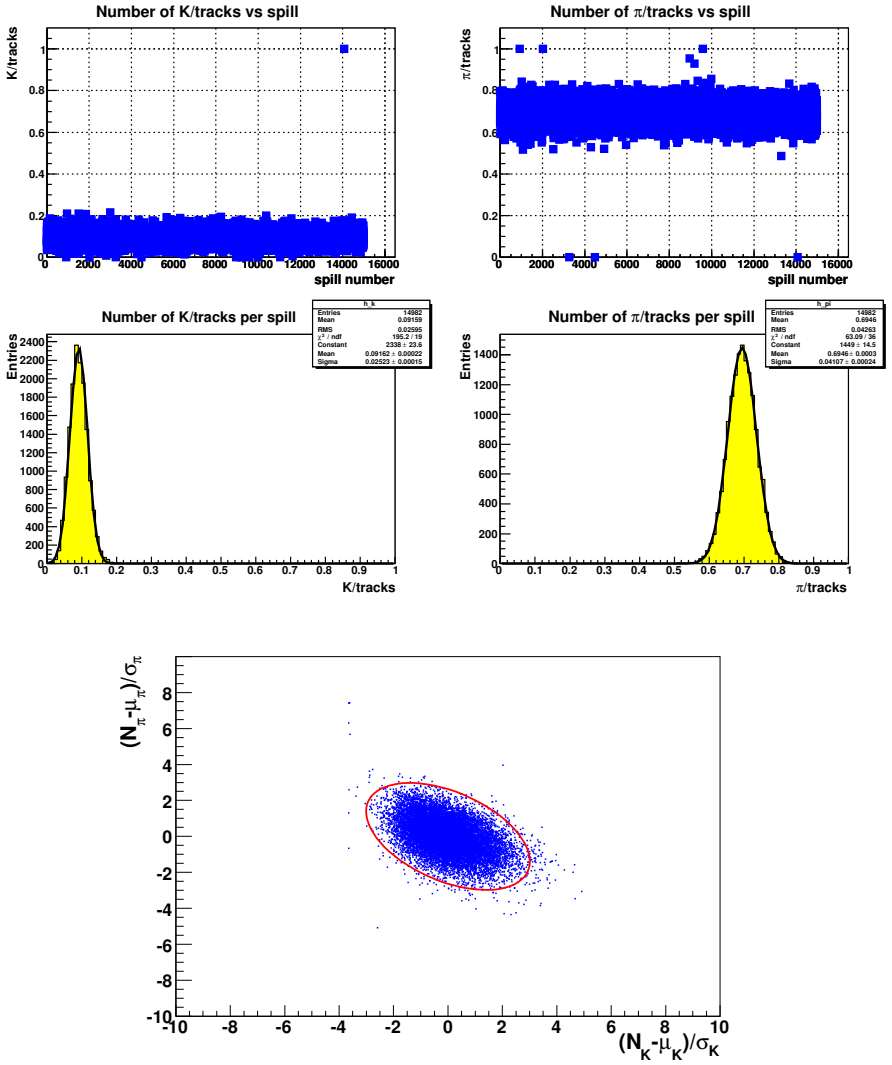

Figure 4.12: First row of plots: the number of hadrons identified as K (left) and as π (right) per track, as a function of the spill number. Second row: projection on the Y axis of the plots above with a Gaussian fit. From the values of the two Gaussians, the two variables $\frac{N_\pi - \mu_\pi}{\sigma_\pi}$ and $\frac{N_K - \mu_K}{\sigma_K}$, are built and plotted one against the other in the bottom plot. The ellipse giving the 3σ confidence level is shown. The plots refer to sub-period W33.

statistics, we divided the hadron sample in 4 subsamples: positive hadrons, negative hadrons, hadrons with polar angle at RICH-1 entrance below 30 mrad and above 30 mrad. A run was classified as bad if it was bad in at least one of the subsamples considered. Also in this case the monitor showed a good sensitivity to the RICH-1

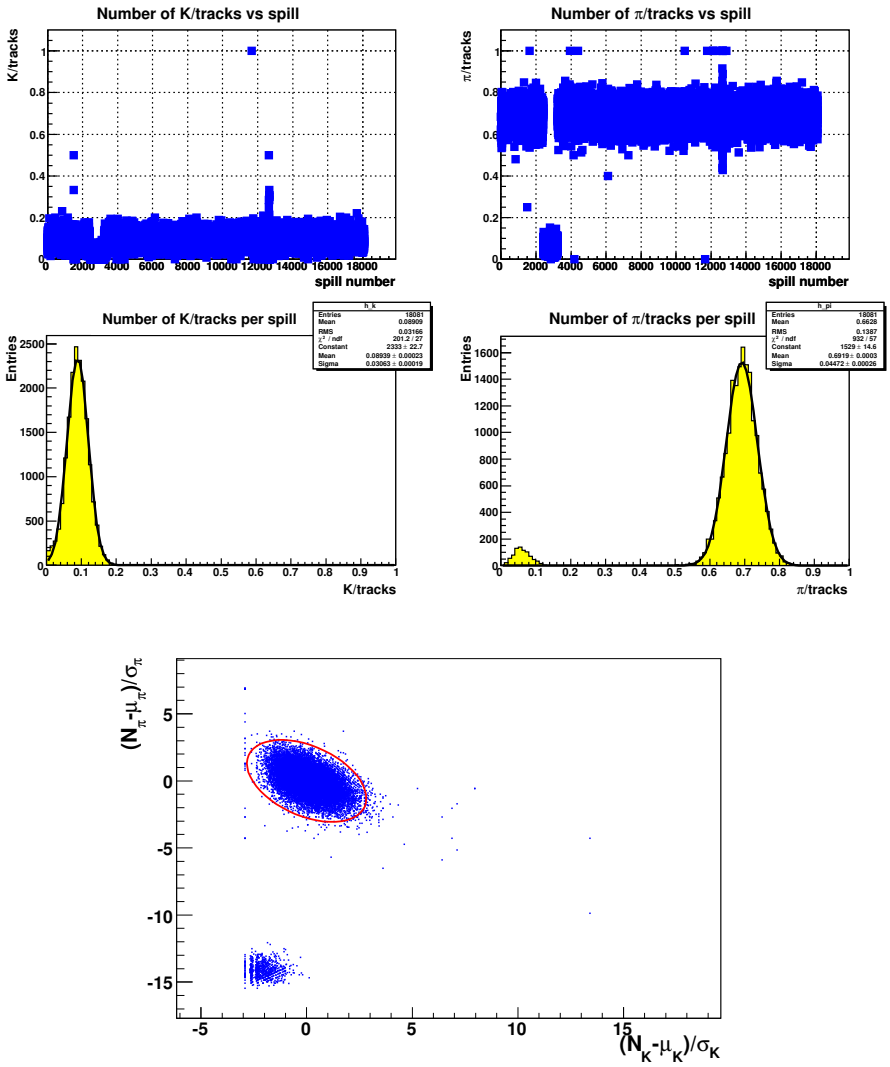

Figure 4.13: Same as in fig. 4.12, for sub-period P1H. The group of spills well outside the accepted region, correspond to the high voltage off of the RICH-1 MWPC (see text for details).

instabilities; the group of runs outside the ellipse in figure 4.14, corresponds to the turning off of the chambers HV, already described in the spill analysis.

Conclusions on RICH-1 stability

We have tested different methods to check the RICH-1 stability in time, and we have already commented that they have been found correlated with each other. As

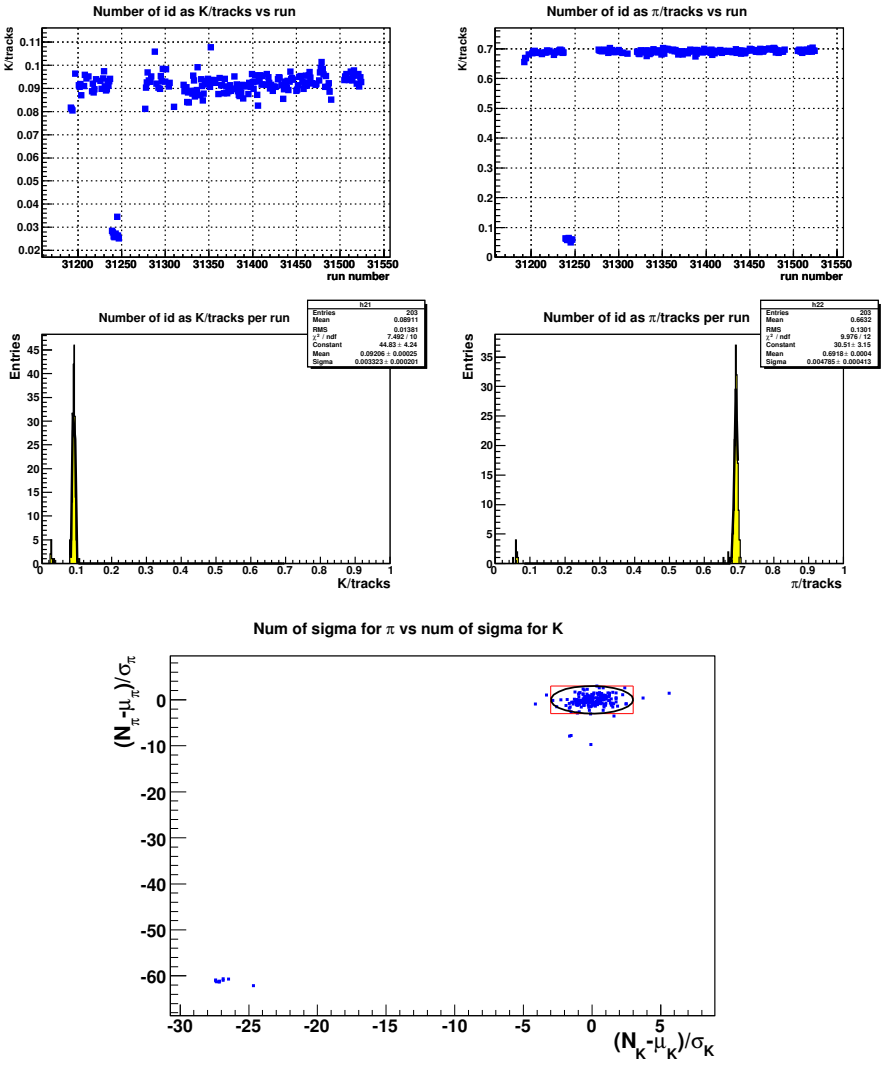

Figure 4.14: Same as in fig. 4.13, but for the stability analysis on a run per run basis (see text for details).

a final criterion, we rejected a run from the analysis if a run was classified as "bad" in more than one monitor. In the table 4.2 we report the number of runs rejected with the monitors described, for the 6 sub-periods of transversity data. In the table also the corresponding number of rejected spills is given, since a run can contain less spills than the standard value (100 or 200), if the data taking has been stopped due to some problems.

The percentage of spills classified as bad with the spill stability analysis and rejected are in table 4.3.

sub-period	bad runs	corresponding number of spills	percentage of rejected spills (%)
P1G	16	905	4.5
P1H	15	1302	7
W33	4	288	2
W34	7	335	2.6
W35	2	111	0.5
W36	2	45	0.3

Table 4.2: The number of runs (and the corresponding number of spills) rejected with the monitors described, for the 6 sub-periods of transversity data.

sub-period	Bad spills on good runs (%)
P1G	1.05
P1H	0.97
W33	0.96
W34	1.16
W35	0.98
W36	0.96

Table 4.3: The percentage of spills of good runs classified as bad and rejected from the analysis for the 6 sub-periods of transversity data.

4.2 Data analysis

4.2.1 Event selection

The first step to select DIS events in the data is the reconstruction of the interaction point of the incoming muon in the target: the "primary vertex" is defined as the intersection of two tracks associated to a particle beam muon, μ, and to the scattered muon, μ'.

A beam muon track is defined when it is reconstructed in the scintillating fibers and silicons trackers upstream of the target and its momentum is measured in the BMS. The scattered muon is defined as a positively charged track reconstructed downstream the target, going through SM1, and with momentum larger than 1 GeV/c. In the analysis, all the triggers (section 2.8) are used, even if their contribution in terms of number of events is different due to the different Q^2 kinematical regions covered. For all triggers based on the hodoscope information, the scattered muon track must be compatible with the hodoscope hits, according to the trigger matrix. In the calorimetric trigger case, a minimal number of hits is required in the

muon filters so that the amount of material traversed in the spectrometer must be larger than 66 (74) radiation lengths for tracks reconstructed in the first (second) spectrometer, respectively.

If in the same event, more primary vertices are found due to the reconstruction of more than one beam track or scattered muon track, only the "best primary vertex" is chosen for the analysis. This is defined as the one with the maximum number of outgoing tracks and, in case of equal number of tracks, the one with smaller vertex χ^2.

After the selection of the primary vertex of the event, a quality cut on the reduced χ^2 of the μ and μ' tracks is applied (χ^2 <10); moreover the momentum of the incoming beam particle is requested to be below 200 GeV/c and the number of radiation lengths traversed by the scattered muon to be larger than 30. To reject false primary vertices, the vertex coordinates are checked to be inside the target region, with a radial cut on the distance of the vertex from the target axis ($r_{vtx} < 1.3$ cm) and requiring the z_{vtx} coordinate to belong to one of the target cells (-100 cm $< z_{vtx} <$ -40 cm or -30 cm $< z_{vtx} <$ 30 cm).

To ensure the same muon beam flux in both target cells, the beam track projection at the entrance and at the exit of the target has to be inside the radial target region.

For the selection of DIS events, some standard cuts have been applied:

- $Q^2 > 1$ (GeV/c)^2, to ensure deep inelastic scattering regime;
- mass of the final hadronic state $W > 5$ GeV/c^2, to avoid the region of resonances;
- fraction energy transfer $0.1 < y < 0.9$, in order to limit the error due to radiative corrections and to warrant a good determination of y.

4.2.2 Hadron selection

To select the hadron sample for the analysis, some cuts are applied on the tracks coming from the primary vertex and not flagged as μ'.

To have a good momentum resolution, tracks reconstructed only in the fringe field of SM1 (section 2.4) are rejected; while to ensure a good resolution in the measured azimuthal angle, the transverse momentum of the particle with respect to the virtual photon direction is required to be larger than 0.1 GeV/c.

The amount of material traversed in the spectrometer from the hadron tracks has to be smaller than 10 radiation lengths; this cut reduces the muon contamination in the hadron sample, since a muon is expected to interact less and to traverse more material in the spectrometer. The calorimeter information has been used rejecting tracks with associated clusters in both hadronic calorimeters; in case of a signal in

one calorimeter, the corresponding energy is required to be larger than 5 GeV (2003 data) or 4 GeV (2004 data) in HCAL1 and larger than 5 (2003 and 2004 data) GeV in HCAL2. These limits have been chosen looking at the correlation between the calorimeter energy and the energy detected in the spectrometer, and rejecting the region corresponding to muons or electrons (leaving in the calorimeters a constant value of energy, independently from their momentum value).

A cut on the hadron relative energy has been made, requiring $z > 0.2$.

For the asymmetry evaluation, we defined also a "leading hadron" sample, since in some models [71] the asymmetries are expected to be larger for more energetic hadrons.

The leading hadron sample contains the most energetic hadron for each event (looking at the hadron with largest z) and a more stringent cut on z ($z > 0.25$) is applied. To exclude the possibility for a hadron to be wrongly identified as leading, the z contribution of all non-muonic outgoing particles of the vertex is summed and subtracted from 1. If the "missing" z is greater than the z of the identified leading hadron, clusters of higher energy are searched in the calorimeters. If such a cluster is found and no track is associated to it, then the event is discarded.

4.2.3 Particle identification

The identification procedure using the RICH-1 detector has been introduced in section 3.2.2. In the following we will describe the criteria used to define the cuts on the $\frac{LH}{LH_{back}}$ and $\frac{LH}{LH_{2nd}}$ applied for this analysis.

As a first step, hadrons are identified with a mass hypothesis if the likelihood corresponding to this mass hypothesis is the highest one. Then, some cuts on the hadron momentum are applied. The upper cut for the track momenta has been set at 50 GeV/c, corresponding to 1.5 σ separation between K and π (section 3.3.3). As regards the lower limit, we chose to cut a little above the Cherenkov threshold to avoid particles with too few Cherenkov photons emitted (section 3.3.1). The values chosen are:

- $p > p_{th_\pi} + 0.5$ GeV/c for pions;
- $p > p_{th_K} + 1.0$ GeV/c for kaons;

corresponding to a mean number of emitted photons about 4.

Cut on $\frac{LH}{LH_{back}}$ and $\frac{LH}{LH_{2nd}}$

The ratios $\frac{LH}{LH_{back}}$ and $\frac{LH}{LH_{2nd}}$ have been introduced in section 3.2.2.

The shape distribution (fig. 4.18) does not give a clear indication for a possible cut in these variables. Therefore we tuned the cuts on the data, selecting particles

coming from ϕ and ρ decay. To this end a subsample of the "all hadron" sample, with the events in which at least two opposite charged hadrons from the primary vertex were found, was used. After a cut on the sum of the relative energy of the hadron pair ($z_{h1}+z_{h2}<0.9$, see fig. 4.15), to avoid exclusive reactions, the invariant mass of these particles was computed. The invariant mass distribution is shown in fig. 4.16, for all the identified hadrons together with the distributions for the different combination of identified particles (at this stage made only choosing the mass hypothesis corresponding to the highest likelihood value): $\pi\pi$, KK and πK. In the $\pi\pi$ sample the ρ peak is visible, in the KK the ϕ peak and in the πK the K* peaks (K*(892) and K*(1430)).

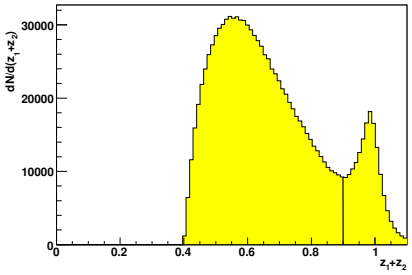

Figure 4.15: Distribution of $z_{h1}+z_{h2}$, where h1 and h2 are two opposite charged hadrons from the primary vertex; the cut on the value 0.9 to avoid exclusive reactions is shown. The distribution starts from the value 0.4 since in the selection of the hadron sample the z is cut above 0.2.

Cuts for K identification

To tune the cuts for K identification, we selected the subsample in which for both hadrons the likelihood corresponding to the K mass hypothesis is highest, and we tried different cuts in $\frac{LH_K}{LH_{back}}$, $\frac{LH_K}{LH_{2nd}}$, to maximize the "figure of merit" (FOM) for the ϕ peak. The FOM was defined considering the gain in signal and the gain in purity with respect to the initial invariant mass distribution:

$$FOM = \frac{S}{S_0} \cdot \frac{(S/B)}{(S_0/B_0)}; \tag{4.1}$$

here S_0 and B_0 refer to the signal and background values in the ϕ sample before any cut, and S and B after the cuts applied. These quantities are evaluated using a fit with a Gaussian function in the ϕ peak region plus a second order polynomial. An example of this fit is shown in fig. 4.17.

The cuts corresponding to the maximum FOM are:

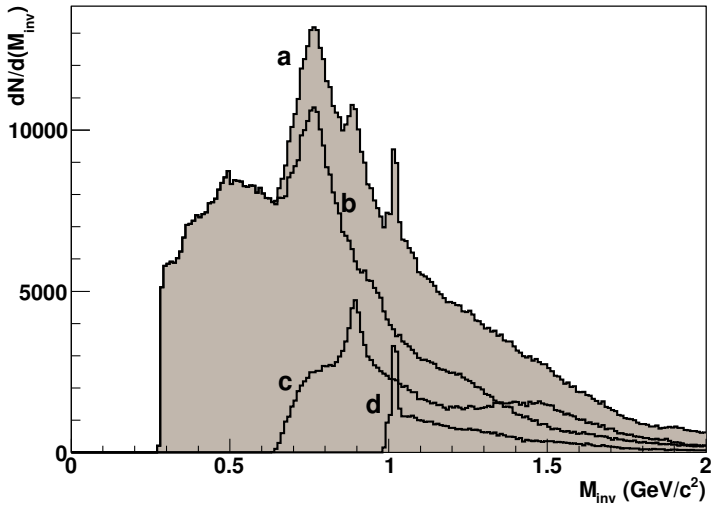

Figure 4.16: Invariant mass distributions for all the hadrons of opposite charge from the primary vertex. In (b) the invariant mass for hadrons identified as $\pi^+\pi^-$, in (c) as $K^{\pm}\pi^{\mp}$ and in (d) as K^+K^-; the sum of the three distributions is shown in (a).

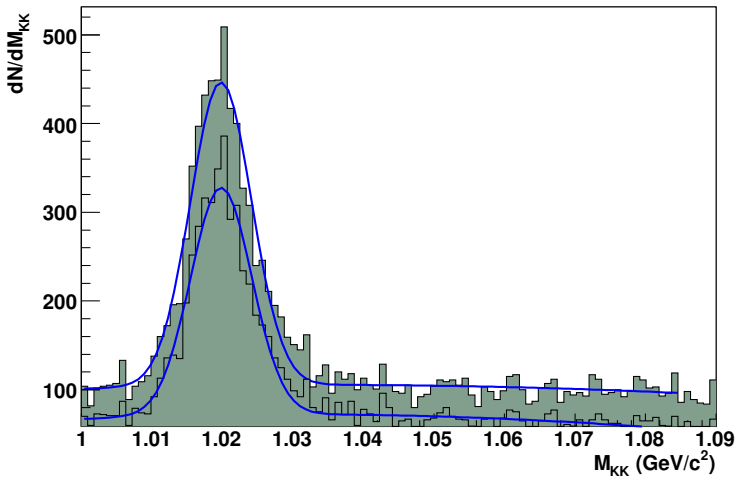

Figure 4.17: Invariant mass for opposite charged hadrons both identified as K, in the ϕ peak region, before and after the cuts applied. The curves are the results of the fit used to evaluate the figure of merit $\frac{S}{S_0} \cdot \frac{(S/B)}{(S_0/B_0)}$.

- $\frac{LH_K}{LH_{back}}$ >1.04;
- $\frac{LH_K}{LH_{2nd}} > 1.003$.

The distributions of the ratios $\frac{LH}{LH_{back}}$ and $\frac{LH}{LH_{2nd}}$ for hadrons identified as kaons before and after the cuts described are shown in fig. 4.18.

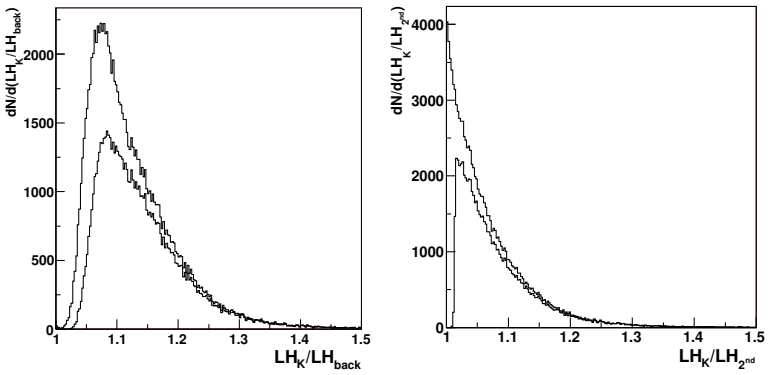

Figure 4.18: Left: $\frac{LH_K}{LH_{back}}$ distribution for hadrons identified as K, before and after the cuts described in the text are applied. Right: $\frac{LH_K}{LH_{2nd}}$ distribution for K, before and after the cuts.

Cuts for π identification

To tune the cuts for pions identification, we used the same approach used for kaons and described in the previous paragraph, using a sample of ρ. The ρ peak is visible in fig. 4.19. The cuts corresponding to the maximum value for the ρ figure of merit are:

- $\frac{LH_\pi}{LH_{back}}$ >1.03;
- $\frac{LH_\pi}{LH_{2nd}}$ >1.002.

4.2.4 Final statistics

To improve the analysis speed, a pre–cut sample with some general cuts was used. The cut criteria of this sample are:

- at least one primary vertex including a scattered muon;

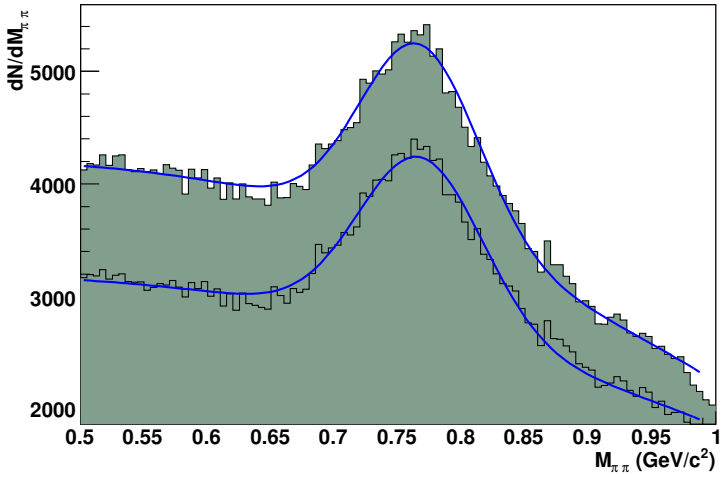

Figure 4.19: Invariant mass for opposite charged hadrons both identified as π, zoom in the ρ peak region, before and after the cuts applied. The fits shown are used to evaluate the figure of merit $\frac{S}{S_0} \cdot \frac{(S/B)}{(S_0/B_0)}$.

- at least one primary vertex resulting in a $Q^2 > 1$ (GeV/c)^2 event;
- at least one further particle from this vertex.

These basic cuts reduced the sample size by a factor of ≈ 20.

The effect of the cuts on the statistics can be seen in tables 4.4 and 4.5. Counts in table 4.4 are normalized to the pre–cut sample; the cuts applied are those used to select the DIS events. The effect of the cuts used to select the "all" hadron sample is described in table 4.5; here the counts are normalized to the number of hadrons after the cuts of table 4.4.

Finally, numbers in table 4.6 describe the effect of the RICH-1 selection on the "all" hadron sample, both for positive and negative hadrons. In the first part of this table, the label "no RICH-1 info" refers to the hadrons without RICH-1 output buffer in mDSTs (this can happen in case of particles under Cherenkov threshold), while the labels "pions", "kaons", "protons" refer to the different identification hypothesis requiring the highest likelihood value; in the second part of the table the labels "pions after cuts", "kaons after cuts" refer to the final number of K and π after application of the cuts described in previous section. Given the low percentage of protons in the data, this sample is not considered for the extraction of the asymmetries. All these numbers are for the sub-periods W35-W36, but the effect of the cuts is very similar in all the periods.

The final statistics entering the analysis for all the periods and charges as well for the "leading" and for the "all" hadron sample is given in tables 4.7 and 4.8, for

Cut	events ($\cdot 10^7$)	ratio
number of events	1.50	1
μ selection	1.49	0.99
μ' selection	1.35	0.90
$Q^2 > 1$ (GeV/c)^2	1.35	0.90
W>5 GeV/c^2	1.27	0.84
0.1<y<0.9	1.23	0.82
same beam flux in cells	0.94	0.63
vertex in target region	0.83	0.55

Table 4.4: Effect of the cuts on the event statistics for the sub-periods W35-W36.

Cut	particles ($\cdot 10^7$)	ratio
number of particles	2.02	1
$XX0 < 10$	2.01	0.99
$\chi^2 < 10$	1.96	0.97
no fringe field tracks	1.89	0.93
$P_T^h > 0.1$ GeV/c	1.64	0.81
$z > 0.2$	0.52	0.26
minimum energy in HCAL	0.49	0.24
positive hadrons, h^+	0.27	
negative hadrons, h^-	0.22	

Table 4.5: Hadron statistics for the sub-periods W35-W36; the initial number of particles in the first row is after the cuts of table 4.4.

Cut	h^+ ($\cdot 10^6$)	ratio	h^- ($\cdot 10^6$)	ratio
number of hadrons	2.71	1	2.23	1
no RICH-1 info	0.13	0.05	0.11	0.05
pions	2.08	0.77	1.80	0.80
kaons	0.41	0.15	0.28	0.12
protons	0.08	0.03	0.06	0.03
pions after cuts	2.03	0.75	1.76	0.79
kaons after cuts	0.36	0.13	0.24	0.11

Table 4.6: RICH-1 statistics for the sub-periods W35-W36; the initial number of particles in the first row is after the cuts of table 4.5.

pion and kaon samples respectively.

Period		**All π sample**		**Leading π sample**	
		π^+ $(\cdot 10^6)$	π^- $(\cdot 10^6)$	$\pi^+(\cdot 10^6)$	$\pi^-(\cdot 10^6)$
2003	P1G-P1H	1.71	1.49	1.10	0.93
2004	W33-W34	1.54	1.33	0.99	0.82
2004	W35-W36	2.03	1.76	1.30	1.09
total		5.28	4.58	3.39	2.84

Table 4.7: Final statistics for pion analysis.

Period		**All K sample**		**Leading K sample**	
		K^+ $(\cdot 10^6)$	K^- $(\cdot 10^6)$	K^+ $(\cdot 10^6)$	$K^-(\cdot 10^6)$
2003	P1G-P1H	0.31	0.21	0.24	0.14
2004	W33-W34	0.27	0.18	0.21	0.13
2004	W35-W36	0.36	0.24	0.27	0.17
total		0.94	0.63	0.72	0.44

Table 4.8: Final statistics for kaon analysis.

4.3 Asymmetry evaluation

4.3.1 Binning

The Collins and Sivers asymmetries have been evaluated as a function of one of the three variables x, P_T^h, and z after integration over the other two. No attempt has been yet done to extract the asymmetries in a 2- or 3-dimensional grid. The kinematical range of the variables has been divided in 9 or 8 bins, as shown in table 4.9. The overall distribution in x, P_T^h, z and Q^2 are shown in figure 4.20, for both the pion and kaon samples. To understand the correlation between the variables used, we report in table 4.10 the mean values of x, P_T^h, z and Q^2 for the various bins used for the asymmetry evaluation.

4.3.2 Calculation of the raw asymmetries

In section 1.3.3 and 1.3.4, we have defined the single spin asymmetries comparing the cross section on the two different spin target configuration; in particular, in eq. 1.53 and 1.60 it is shown as looking for different modulation in the asymmetry, the Collins and Sivers contributions can be accessed. The hadron yield in both effects, Collins and Sivers, depends on an azimuthal angle, $\Phi_{C,S}$ in the following way:

$$N(\Phi_{C,S}) = Fn\sigma\, a(\Phi_{C,S})(1 + A_{C,S}^{raw} sin(\Phi_{C,S})); \tag{4.2}$$

$0.003 < x < 0.008$	$0.20 \leq z < 0.25$	$0.10 < P_T^h \leq 0.20$ GeV/c
$0.008 \leq x < 0.013$	$0.25 \leq z < 0.30$	$0.20 < P_T^h \leq 0.30$ GeV/c
$0.013 \leq x < 0.020$	$0.30 \leq z < 0.35$	$0.30 < P_T^h \leq 0.40$ GeV/c
$0.020 \leq x < 0.032$	$0.35 \leq z < 0.40$	$0.40 < P_T^h \leq 0.50$ GeV/c
$0.032 \leq x < 0.050$	$0.40 \leq z < 0.50$	$0.50 < P_T^h \leq 0.60$ GeV/c
$0.050 \leq x < 0.080$	$0.50 \leq z < 0.65$	$0.60 < P_T^h \leq 0.75$ GeV/c
$0.080 \leq x < 0.130$	$0.65 \leq z < 0.80$	$0.75 < P_T^h \leq 0.90$ GeV/c
$0.130 \leq x < 0.210$	$0.80 \leq z < 1.00$	$0.90 < P_T^h \leq 1.30$ GeV/c
$0.210 \leq x < 1.000$		$1.30 < P_T^h$

Table 4.9: Bins in x, z, and P_T^h.

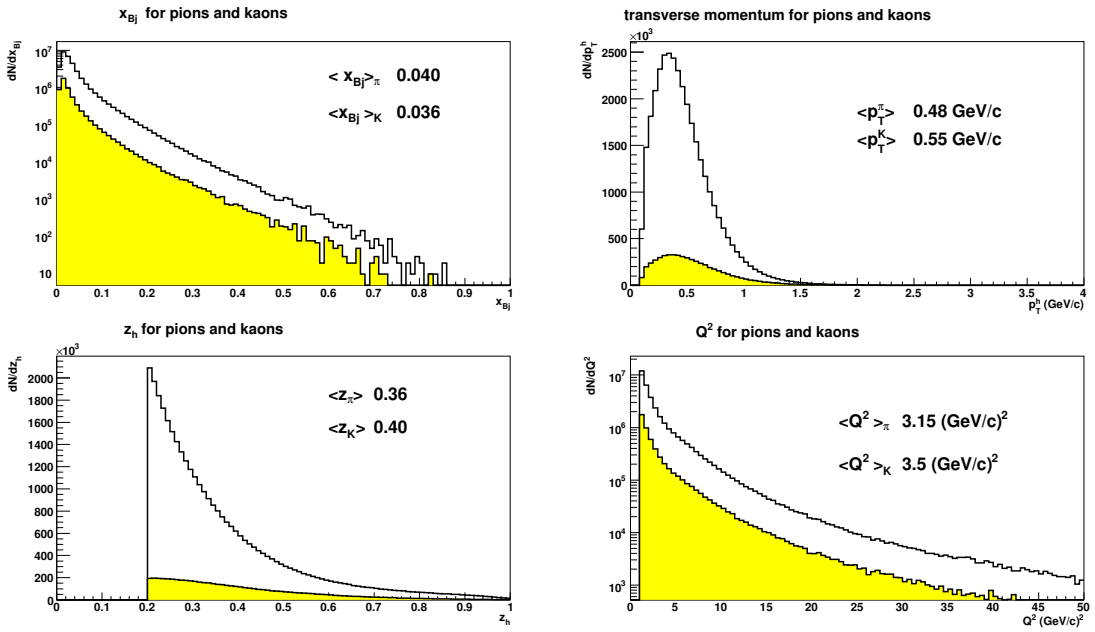

Figure 4.20: Distribution in x, P_T^h, z and Q^2 for pions (white distribution) and kaons (yellow distribution) samples. The mean values are indicated.

where F is the muon flux, n the number of target particles, σ the spin averaged cross-section, $A_{C,S}^{raw}$ the Collins and Sivers asymmetry and $a(\Phi_{C,S})$ the product of the angular acceptance and the efficiency of the spectrometer. Since the spectrometer acceptance and efficiency are largely unknown, they have to be compensated in the data analysis, taking into account that they differ between the upstream and downstream target cell. As already noted, to compensate for the acceptance effects, the measurement is always split in two sub-periods, with opposite spin orientation.

π sample, x bins				K sample, x bins			
$\langle x \rangle$	$\langle Q^2 \rangle$	$\langle z \rangle$	$\langle P_T^h \rangle$	$\langle x \rangle$	$\langle Q^2 \rangle$	$\langle z \rangle$	$\langle P_T^h \rangle$
0.0065	1.24	0.29	0.53	0.0065	1.24	0.30	0.57
0.011	1.45	0.33	0.52	0.011	1.49	0.35	0.56
0.016	1.67	0.35	0.49	0.016	1.83	0.39	0.56
0.026	1.99	0.37	0.46	0.025	2.40	0.44	0.55
0.040	2.79	0.39	0.45	0.040	3.61	0.46	0.54
0.063	4.54	0.38	0.46	0.063	5.74	0.45	0.53
0.101	7.40	0.37	0.46	0.101	9.10	0.45	0.54
0.161	11.79	0.37	0.47	0.161	14.55	0.45	0.54
0.278	23.77	0.36	0.50	0.285	28.74	0.44	0.56
π sample, P_T^h bins				K sample, P_T^h bins			
$\langle x \rangle$	$\langle Q^2 \rangle$	$\langle z \rangle$	$\langle P_T^h \rangle$	$\langle x \rangle$	$\langle Q^2 \rangle$	$\langle z \rangle$	$\langle P_T^h \rangle$
0.043	3.18	0.35	0.15	0.039	3.75	0.39	0.15
0.042	3.14	0.35	0.25	0.039	3.75	0.39	0.25
0.041	3.14	0.35	0.35	0.039	3.77	0.39	0.35
0.041	3.23	0.35	0.45	0.039	3.77	0.40	0.45
0.041	3.29	0.36	0.55	0.039	3.76	0.41	0.55
0.040	3.36	0.37	0.67	0.038	3.68	0.42	0.67
0.040	3.46	0.39	0.82	0.038	3.71	0.43	0.82
0.039	3.61	0.41	1.04	0.037	3.75	0.44	1.05
0.038	4.08	0.43	1.55	0.036	4.12	0.44	1.57
π sample, z bins				K sample, z bins			
$\langle x \rangle$	$\langle Q^2 \rangle$	$\langle z \rangle$	$\langle P_T^h \rangle$	$\langle x \rangle$	$\langle Q^2 \rangle$	$\langle z \rangle$	$\langle P_T^h \rangle$
0.037	3.43	0.22	0.43	0.028	3.97	0.22	0.52
0.039	3.37	0.27	0.45	0.032	3.99	0.27	0.52
0.041	3.33	0.32	0.48	0.035	3.92	0.32	0.53
0.042	3.28	0.37	0.49	0.038	3.87	0.37	0.55
0.044	3.19	0.44	0.52	0.042	3.74	0.45	0.56
0.046	3.03	0.56	0.54	0.046	3.44	0.57	0.58
0.046	2.74	0.72	0.54	0.051	3.25	0.71	0.62
0.045	2.40	0.88	0.47	0.052	2.93	0.87	0.62

Table 4.10: The x, P_T^h, z and Q^2 mean bin values. The first table is for the selected x bins, the second for the P_T^h bins and the third for the z bins. The four columns to the left are for the pion sample, the four columns at the right for the kaon sample.

If the angles are always calculated assuming spin up, we get two different rate distributions depending on the real spin direction, as this assumption introduces a

phase of π in the angle definitions:

$$N^{\uparrow}(\Phi_{C,S}) = Fn\sigma a^{\uparrow}(\Phi_{C,S})(1 + A^{raw}_{C,S} sin(\Phi_{C,S})); \tag{4.3}$$
$$N^{\downarrow}(\Phi_{C,S}) = Fn\sigma a^{\downarrow}(\Phi_{C,S})(1 - A^{raw}_{C,S} sin(\Phi_{C,S})). \tag{4.4}$$

To extract the asymmetries, we used the so called "double ratio method". In this method, the information of both target cells (u, d) and sub-periods $(p1, p2)$ with opposite target spin orientation (fig. 4.1), are used simultaneously, defining the ratio:

$$F(\Phi) = \frac{N^{\uparrow,p2}_u(\Phi) N^{\uparrow,p1}_d(\Phi)}{N^{\downarrow,p1}_u(\Phi) N^{\downarrow,p2}_d(\Phi)}; \tag{4.5}$$

here Φ stands for $\Phi_{C,S}$.
Writing explicitly the event yield dependence on Φ, we obtain:

$$\begin{aligned} F(\Phi) &= \frac{F_{p2} n_u \sigma a^{\uparrow p2}_u(\Phi)(1 + A^{raw}_{C,S} sin(\Phi)) F_{p1} n_d \sigma a^{\uparrow p1}_d(\Phi)(1 + A^{raw}_{C,S} sin(\Phi))}{F_{p1} n_u \sigma a^{\downarrow p1}_u(\Phi)(1 - A^{raw}_{C,S} sin(\Phi)) F_{p2} n_d \sigma a^{\downarrow p2}_d(\Phi)(1 - A^{raw}_{C,S} sin(\Phi))} \\ &= C \frac{a^{\uparrow p2}_u(\Phi) a^{\uparrow p1}_d(\Phi)}{a^{\downarrow p1}_u(\Phi) a^{\downarrow p2}_d(\Phi)} \frac{(1 + A^{raw}_{C,S} sin(\Phi))(1 + A^{raw}_{C,S} sin(\Phi))}{(1 - A^{raw}_{C,S} sin(\Phi))(1 - A^{raw}_{C,S} sin(\Phi))} \\ &\approx C \frac{a^{\uparrow p2}_u(\Phi) a^{\uparrow p1}_d(\Phi)}{a^{\downarrow p1}_u(\Phi) a^{\downarrow p2}_d(\Phi)} \cdot (1 + 4 A^{raw}_{C,S} sin(\Phi)) \end{aligned} \tag{4.6}$$

at the first order in $A^{raw}_{C,S}$.
The ratio is calculated in 16 equal bins over the range of $\Phi_{C,S}$ and plotted against $\Phi_{C,S}$. The statistical error on the ratio is estimated from eq. 4.5 as:

$$\sigma^2_{F(\Phi)} = [F(\Phi)]^2 \cdot \left[\frac{1}{N^{\uparrow,p2}_u} + \frac{1}{N^{\uparrow,p1}_d} + \frac{1}{N^{\downarrow,p2}_u} + \frac{1}{N^{\downarrow,p1}_d} \right]. \tag{4.7}$$

The ratio values as a function of $\Phi_{C,S}$ are fitted with a sin amplitude with two free parameters, $par(0) \cdot (1 + par(1) sin(\Phi))$; from $par(1)$ we extract the asymmetry as $A^{raw}_{C,S} = par(1)/4$.

No systematic effect is expected assuming the following "reasonable" condition to hold:

$$\frac{a^{\uparrow p2}_u(\Phi) a^{\uparrow p1}_d(\Phi)}{a^{\downarrow p1}_u(\Phi) a^{\downarrow p2}_d(\Phi)} = const, \tag{4.8}$$

or

$$\frac{a^{\uparrow p2}_u(\Phi)}{a^{\downarrow p2}_d(\Phi)} = const \frac{a^{\downarrow p1}_u(\Phi)}{a^{\uparrow p1}_d(\Phi)}. \tag{4.9}$$

This assumption means, that the ratio of the acceptances of the up– and downstream cell stays constant during the two sub-periods. Note that a test on the costant acceptances can be done considering the variable:

$$R(\Phi) = \frac{N_u^{\uparrow p2}(\Phi) N_d^{\downarrow p2}(\Phi)}{N_u^{\downarrow p1}(\Phi) N_d^{\uparrow p1}(\Phi)}; \tag{4.10}$$

since in this ratio the term containing the asymmetry vanishes:

$$R(\Phi) \sim C \frac{a_u^{\uparrow p2}(\Phi) a_d^{\downarrow p2}(\Phi)}{a_u^{\downarrow p1}(\Phi) a_d^{\uparrow p1}(\Phi)}; \tag{4.11}$$

in section 4.4.4 we will check our assumption of constant spectrometer acceptance.

4.3.3 Collins asymmetry

The Collins asymmetry is extracted from the raw asymmetry through the expression:

$$A_{Coll} = \frac{A_C^{raw}}{D_{NN} \cdot f \cdot P}; \tag{4.12}$$

where D_{NN} is the depolarization factor, f the target dilution factor and P the target polarization (see also section 1.3.3). The depolarization factor $D_{NN} = \frac{2(1-y)}{1+(1-y)^2}$ is calculated from the kinematics of each event; it is evaluated in each bin for all the events entering in the asymmetry extraction, and the mean value for each bin is taken. The dilution factor is taken constant as $f = 0.38$. The values of target polarization, are in table 4.11.

sub-period	Runs	Polarization (%)	
		upstream	downstream
P1G	30772-31038	-49.70	52.78
P1H	31192-31247	49.39	-42.60
P1H	31277-31524	51.31	-44.63
W33	38991-39168	50.70	-43.52
W34	39283-39290	-44.80	45.97
W34	39325-39430	-38.60	40.35
W34	39480-39545	-46.14	47.41
W35	39548-39780	-46.44	47.44
W36	39850-39987	49.89	-42.76

Table 4.11: Target polarization values for the 2003/2004 transversity periods.

4.3.4 Sivers asymmetry

The Sivers asymmetry is extracted from the raw asymmetry through the expression

$$A_{Siv} = \frac{A_S^{raw}}{f \cdot P} \; ; \tag{4.13}$$

in the Sivers effect the D_{NN} is equal to 1, since the photon couples to an unpolarized quark in a transversally polarized nucleon, and the kinematic factor $(1 - y + y^2/2)$ is identical to the one in unpolarized scattering.

4.3.5 Results

The results for the Collins and Sivers asymmetries from the 2003–2004 data can be found in fig. 4.21 for the "all pions" and "all kaons" sample and in fig. 4.22 for the "leading pion" and "leading kaon" one, separately for positive and negative hadrons. The errors bars are the statistical errors only, since the systematic effects were found to be negligible (section 4.4). The overall asymmetries are the result of a weighted mean of the asymmetry values from each transversity data taking period. As apparent from the figures, all the measured asymmetries are small and compatible with zero within the error bars. Since all the measured asymmetries are close to zero, the measurements for charged pions and kaons are not corrected for the purity of the samples (see section 4.5). We refer to the next chapter for an interpretation of the results, here we only anticipate that some phenomenological work giving a consistent description of these results together with the results from other experiments (HERMES and BELLE) are going on from different groups.

The results have been shown for the first time at QCD06 conference [70]; a paper containing the results and the description of the analysis is in preparation and will be submitted to Phys.Lett.B journal.

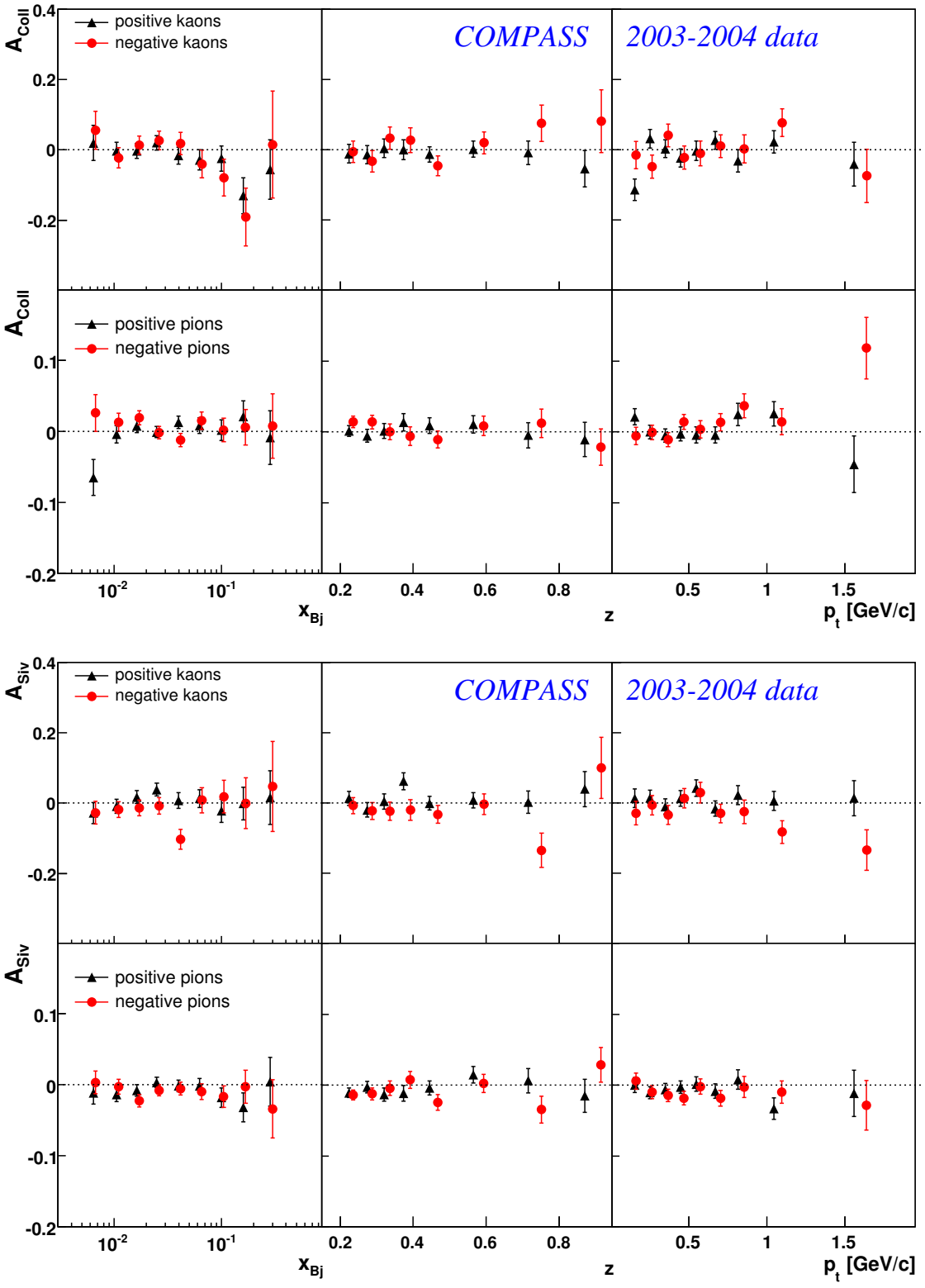

Figure 4.21: COMPASS 2003-2004 data, deuteron target: Collins (top) and Sivers (bottom) asymmetries for all hadrons identified as pions and kaons, as a function of x, z and P_T^h variables. The triangles refer to positive hadrons, the circles to negative.

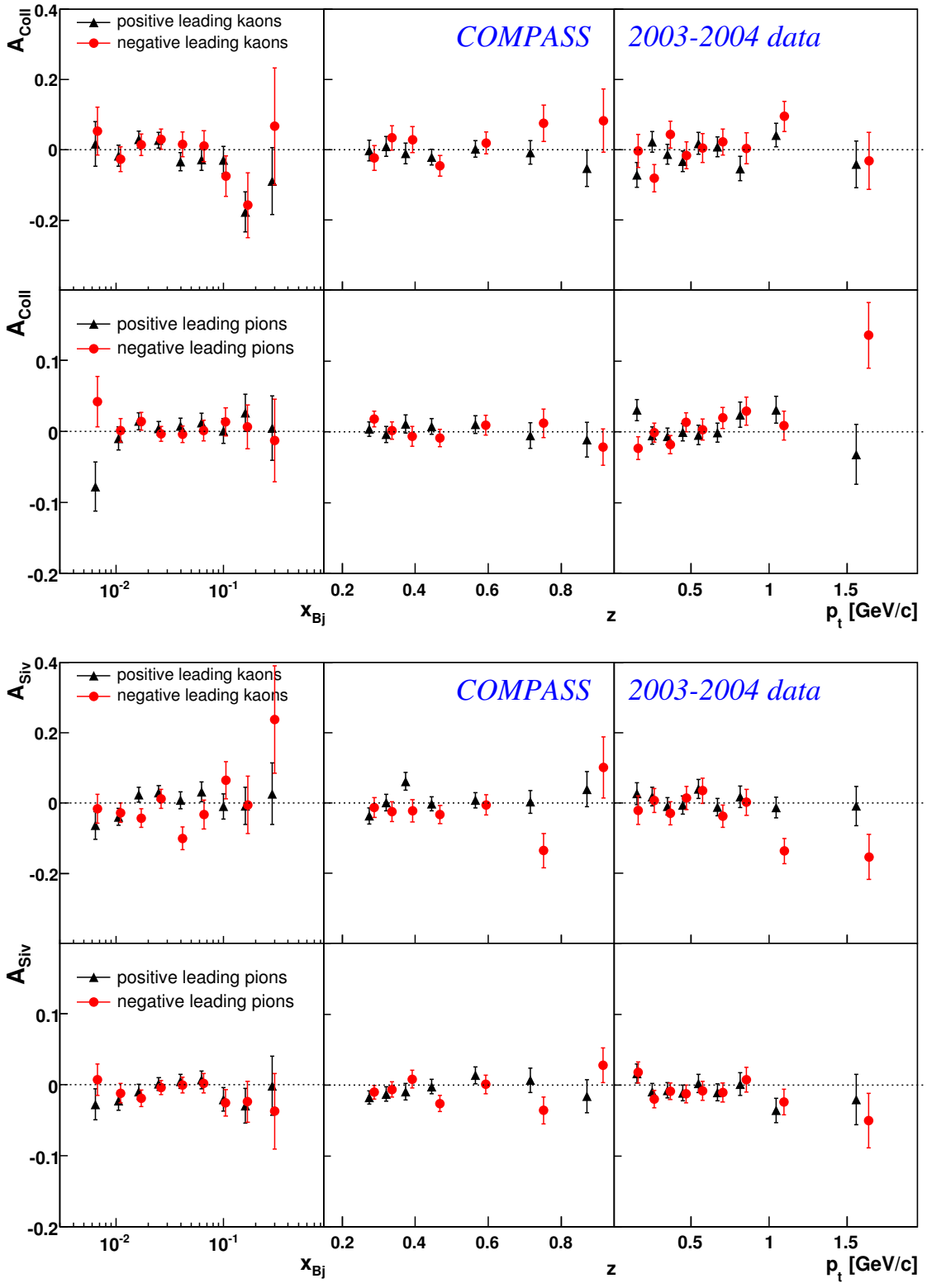

Figure 4.22: COMPASS 2003-2004 data, deuteron target: Collins (top) and Sivers (bottom) asymmetries for leading hadrons identified as pions or as kaons. The triangles refer to positive hadrons, the circles to negative.

4.4 Systematic studies

In order to evaluate possible false asymmetries and to investigate the stability of the physics results, many tests were done on the "unidentified" sample, whose results were already published in [19].

As regards the false asymmetries studies, asymmetries expected to be zero have been built splitting the two target cells in two parts and combining the data from the same cell or scrambling the data collected in a "random" way. The mean values of all the resulting false asymmetries were found to be compatible with zero, as it should.

For the influence of possible acceptance effects on the physics results, the asymmetries were evaluated for different subsamples of the data, and checking that the results were compatible with each other. The subsamples have been created dividing the data according to the position of the primary vertex inside the target, to the region of the spectrometer in which the scattered muon was measured (see also below), to the trigger of each event, to the time in which the data were recorded.

The result of all these tests and studies was that the systematic error is well below the statistical one. For the analysis on the identified hadrons, π and K, only the most significant of the mentioned tests have been done, since the data were already shown to be stable and the possible effect of the RICH-1 instabilities ruled out thanks to the RICH-1 stability studies (section 4.1.3).

4.4.1 Correlation between the asymmetries

To check the possible correlation between the Sivers and Collins asymmetries that could arise from a non uniform acceptance in (ϕ_h, ϕ_S), the asymmetries for charged hadrons have been estimated also fitting simultaneously the Collins and Sivers terms [19]. For each kinematic bin, the estimator:

$$A(\phi_h, \phi_S) = \frac{N_u^{\uparrow,p2}(\phi_h, \phi_S) N_d^{\uparrow,p1}(\phi_h, \phi_S)}{N_u^{\downarrow,p1}(\phi_h, \phi_S) N_d^{\downarrow,p2}(\phi_h, \phi_S)}; \tag{4.14}$$

has been fitted with the following function:

$$H(\phi_h, \phi_S) = a_1 + a_2 sin(\phi_h + \phi_S - \pi) + a_3 sin(3\phi_h - \phi_S) + a_4 sin(\phi_h - \phi_S) + a_5 cos(\phi_h - \phi_S); \tag{4.15}$$

here the first term should be one, the second and the fourth terms are respectively the Collins and the Sivers contributions and the other two the remaining leading twist contributions. The fit has been performed in each kinematic bin, that has been split into 8×8 bins in (ϕ_h, ϕ_S). The Collins and Sivers asymmetries and their errors estimated with this fit are essentially the same of the values obtained with the one dimensional analysis, taking into account the statistical error, as expected from the

orthogonality of the different terms. The correlation coefficients of the Collins and Sivers asymmetries as given by the fit turn out to be small, in the range from -0.25 to 0.25 [72], due to the non uniform population of the (ϕ_h, ϕ_S) bins. The fit has been performed also with the complete cross section expression with 9 terms, considering also the non leading twist components, and the same results for the Collins and Sivers asymmetries have been obtained.

The conclusions from these tests is that, considering the smallness of the measured asymmetries for charged hadrons, the effect of the correlation between the Sivers and Collins terms is negligible. Since the acceptance in (ϕ_h, ϕ_S) is the same for $\pi^{\pm}$, $K^{\pm}$, also for the present data the correlation has negligible effects.

4.4.2 Hadrons from vector meson decays

The amount of hadrons coming from vector mesons decay in the pion and kaon samples could give problems in the interpretation of the measured asymmetries, even if presently there is not a clear indication from the theory that these hadrons are really a contamination of the signal and that they should be threated in a different way. To estimate the possible effect on the asymmetries presented here, the exclusive ρ and ϕ mesons have been selected in the data. The Collins and Sivers asymmetries have been estimated for the charged hadrons coming from the ρ and ϕ decay, finding results compatible with zero.

4.4.3 Periods compatibility

As already said in section 4.3.5, the final evaluation of the asymmetries is based on the weighted mean of the asymmetries from every single data taking period. As an example, in picture 4.23, we show the results on the Collins asymmetries for the 3 data taking periods (left) and the asymmetries after the mean evaluation. From this picture, it can be noted that the results from the different periods are in agreement within 1σ, indicating that the periods are compatible and can be joined together for the analysis.

To check the periods compatibility quantitatively, we consider the distribution:

$$f_i = \frac{A_i - \langle A \rangle}{\sqrt{\sigma_i^2 - \sigma_{\langle A \rangle}^2}} \quad i = 1, 3$$

where A_i are the asymmetries of each x, P_T^h, z bin and $\langle A \rangle$ is the corresponding weighted mean, our final result. We used in the denominator the difference of the variances to take into account the correlation between A_i and $\langle A \rangle$. The f_i variables have been built for different subsamples (all/leading, π/K, positive/negative,

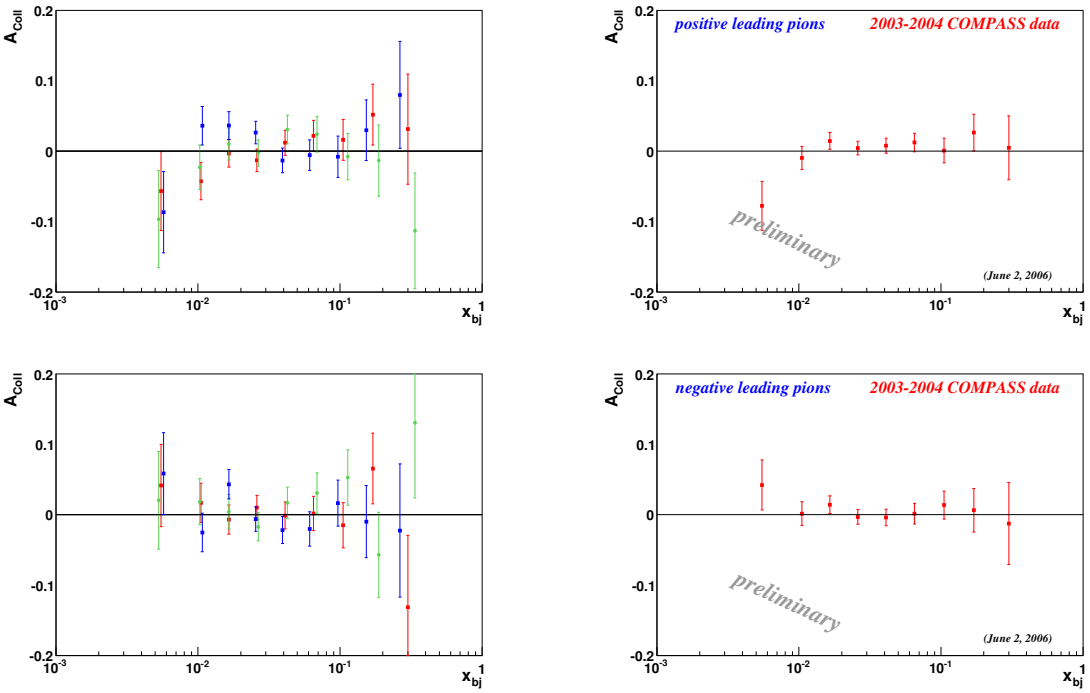

Figure 4.23: Collins asymmetries for 2003 – 2004 vs. x for positive leading pions (top) negative leading pions (bottom). On the left the contributions of the single periods are shown and on the right the weighted mean. The color code for the pictures with the contributions of the single period is: red points for P1G-P1H, green points for W33-W34, blue points for W35-W36.

Collins/Sivers...); as expected, they all follow a Standard Normal distribution; in fig. 4.24 the distributions for the leading π and leading K subsamples can be seen as an example.

The Standard Normal RMS values and their error, σ_{RMS}, for the subsamples considered, are shown in table 4.12 for "all hadrons sample" and for "leading hadrons sample"; from the table, it can be seen that only the K^- subsample has a RMS larger than 1 by about 2 σ_{RMS}. For this reason, we investigated further this particular subsample, considering separately the x, P_T^h, z bins: see results in table 4.13. The z bins show no problem, while the x and P_T^h bins are compatible with 1 within 2σ; the reason can be found out looking in the figures 4.25 and 4.26, where the contributions of the single sub-period are shown: for the K^- asymmetries vs x and P_T^h, in very few points the asymmetries of the three periods are far more than 1σ, but no systematic effect appears in the plots. This effect can be due to the lower statistics in this specific sample.

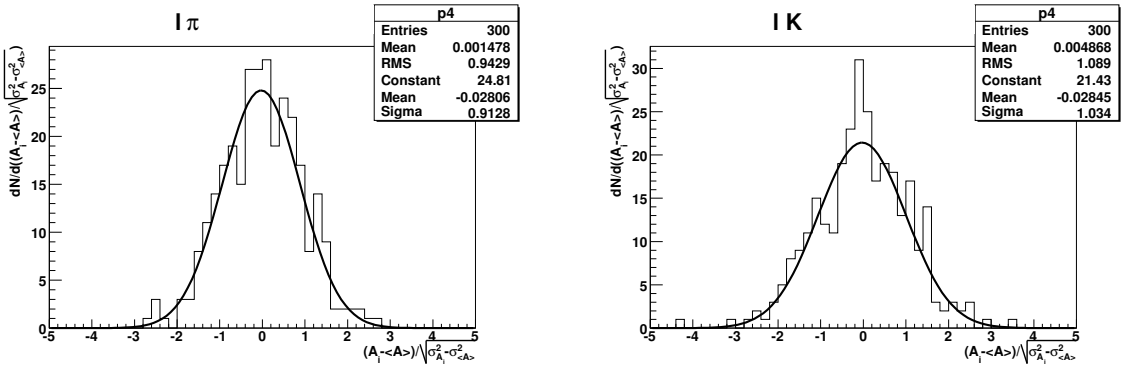

Figure 4.24: f_i distributions for leading π (left) and leading K (right) subsample for the different asymmetries; the number of the entries in the histogram, 300, is the number of all the asymmetries we measure: 300=2 ×2×(9+9+7)×3 ((Collins-Sivers)×(positive-negative) × (number of bins in x, z and P_T^h)×(3 data taking periods).

	RMS	σ_{RMS}		RMS	σ_{RMS}
all π	1.012	0.041	leading π	0.943	0.036
all K	1.097	0.048	leading K	1.089	0.048
Collins all π	1.020	0.059	Collins leading π	0.928	0.050
Collins all K	1.148	0.074	Collins leading K	1.068	0.066
Sivers all π	1.004	0.057	Sivers leading π	0.957	0.053
Sivers all K	1.045	0.062	Sivers leading K	1.109	0.071
all π^+	1.018	0.059	leading π^+	0.976	0.055
all π^-	1.005	0.057	leading π^-	0.909	0.048
all K^+	0.989	0.056	leading K^+	0.977	0.055
all K^-	1.196	0.081	leading K^-	1.190	0.082

Table 4.12: Compatibility of the results from the three different periods of data taking: RMS values of the variable $(A_i - \langle A\rangle)/\sqrt{\sigma_i^2 - \sigma^2_{\langle A\rangle}}$ and their error for different all and leading hadron subsamples of events. The spread of the data is compatible with the statistical fluctuations.

4.4.4 Test of the acceptance ratios

From the number of events we build the ratio $R(\Phi)$:

$$R(\Phi) \;=\; \frac{N_u^{\uparrow}(\Phi)N_d^{\downarrow}(\Phi)}{N_u^{\downarrow}(\Phi)N_d^{\uparrow}(\Phi)}, \quad \Phi = \Phi_C, \Phi_S \tag{4.16}$$

that should be, as already described in section 4.3.2, constant in Φ if the spectrometer is stable during the running period. The constancy of R over the range of Φ

	bins	RMS	σ_{RMS}
leading K^-	x,P_T^h,z	1.190	0.082
leading K^-	x	1.24	0.15
leading K^-	P_T^h	1.29	0.16
leading K^-	z	0.96	0.14
leading K^-	x,Collins	1.25	0.21
leading K^-	x,Sivers	1.34	0.25
leading K^-	P_T^h,Collins	1.15	0.18
leading K^-	P_T^h,Sivers	1.32	0.24

Table 4.13: Compatibility of the results from the three different periods of data taking: RMS values of the variable $(A_i - \langle A \rangle)/\sqrt{\sigma_i^2 - \sigma_{\langle A \rangle}^2}$ and their error σ_{RMS} for different leading K^- subsamples of events.

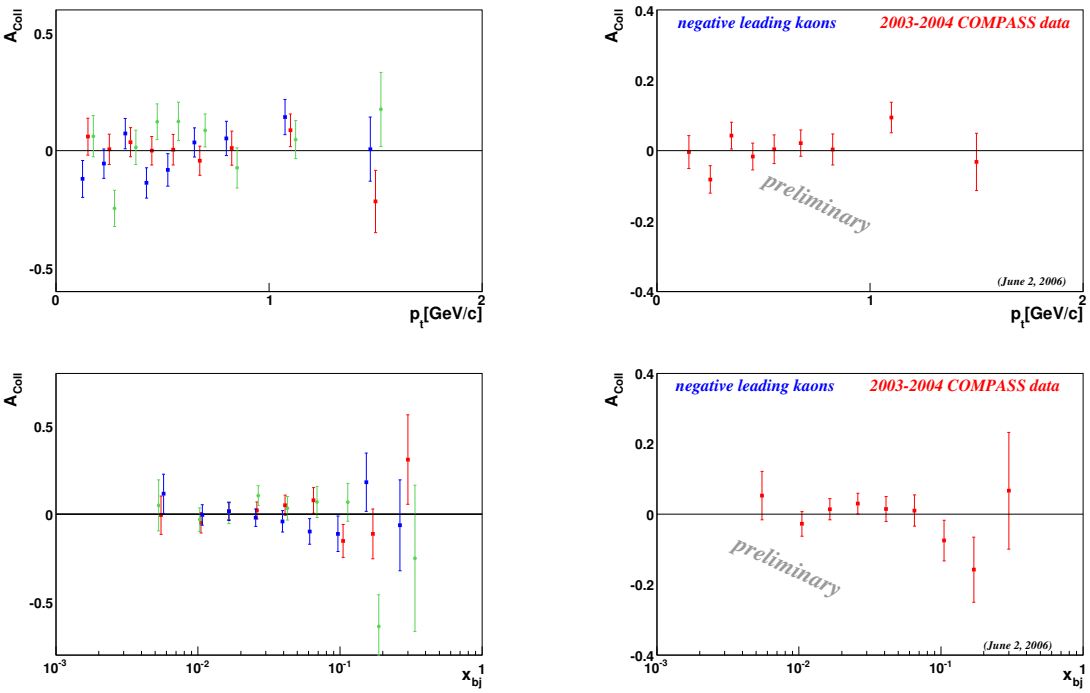

Figure 4.25: Asymmetries for negative leading kaons sample: Collins vs. P_T^h (top), Collins vs x (2nd row). On the left hand side the contributions of the single periods are shown and on the right hand side the weighted mean. The color code for the pictures with the contributions of the single periods is: red points for P1G-P1H, green points for W33-W34, blue points for W35-W36.

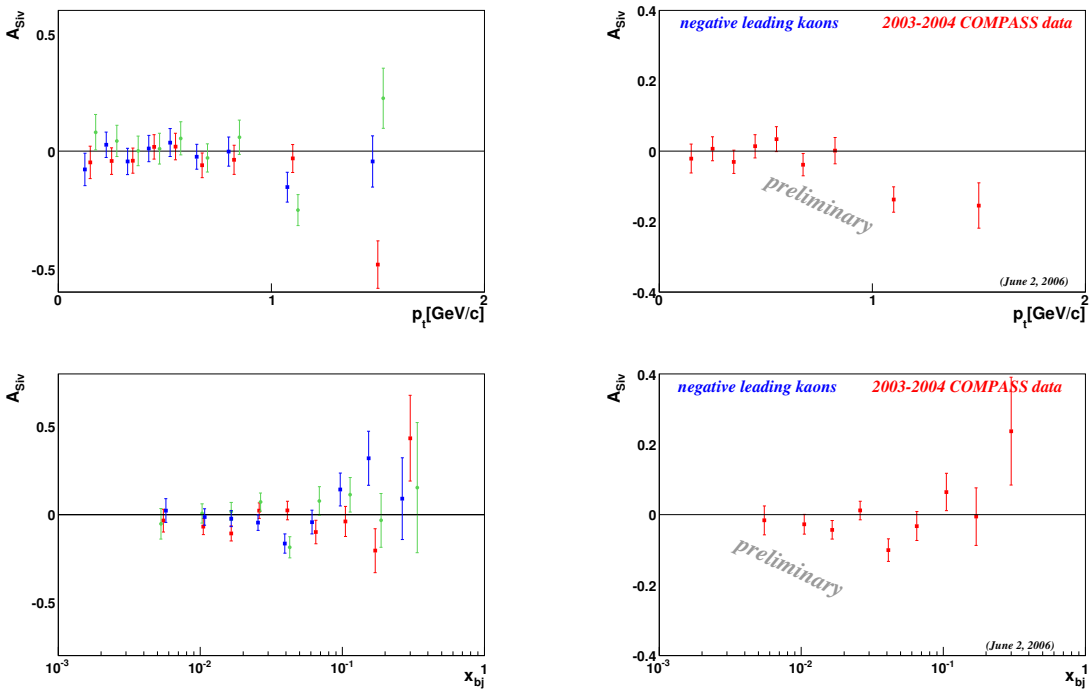

Figure 4.26: As in fig. 4.25, for Sivers asymmetries.

implies a constant ratio of acceptances.

The ratio R has been calculated for each bin of x, z, P_T^h for the 16 bins of the Collins and Sivers angles for leading and all hadrons, for positive and negative K and π. For each variable bins, the distribution of R vs Φ was fitted with a constant. All R distributions resulted to be flat; an example from sub-periods W35-W36 in the 9 x bins can be found in fig. 4.27 and 4.28 for all pions sample and for all kaons sample.

To test the goodness of the fits, we compared the distribution of the χ^2 of the fits with the theoretical distribution corresponding to 15 degrees of freedom (constant fit on 16 Φ bins); in fig. 4.29 it can be noted that the distributions (for both the all hadron sample and the leading hadron one) are in good agreement with the theoretical curve.

In figure 4.30, the χ^2 distribution of the two parameter fit on $F(\Phi)$ used to extract the asymmetries is compared to the expected χ^2 distribution for 14 degrees of freedom. Also in this case a good agreement can be observed.

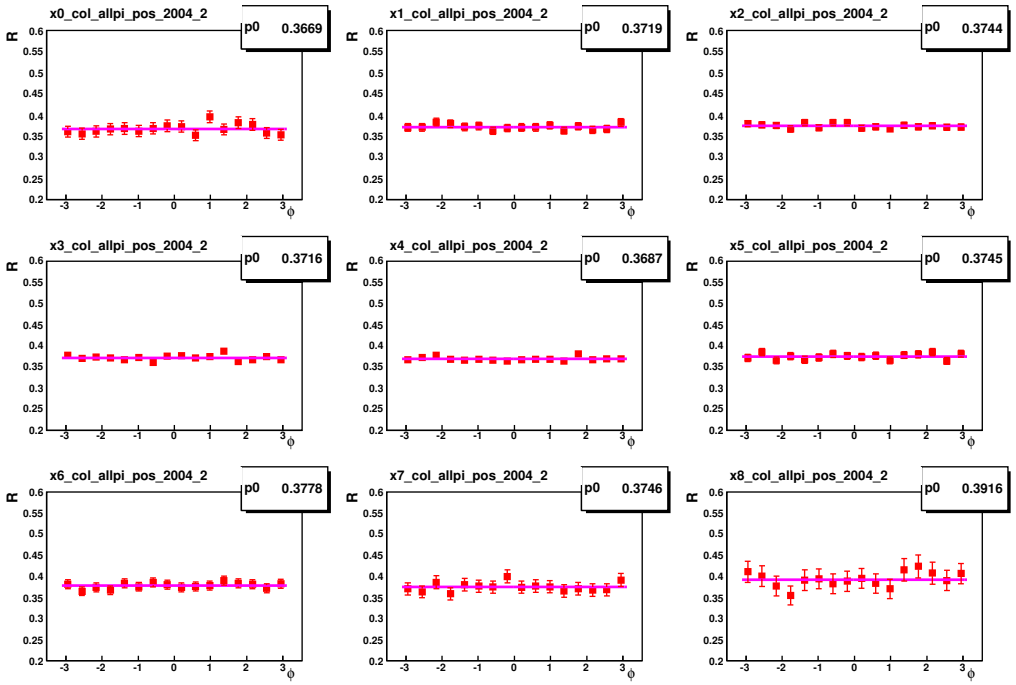

Figure 4.27: Distribution of R(Φ) vs $\Phi_{Collins}$ for the all pion sample in the 9 x bins, for the period W35-W36. The lines are fits with a constant function.

4.4.5 Splitting the detector in geometrical regions

To check a possible effect of the RICH-1 acceptance and efficiency on the measured asymmetries, we considered 4 subsamples of the total statistics selecting the azimuthal angle $\Phi_{\mu'}$ of the scattered muon:

- $0 < \Phi_{\mu'} < \pi/2$;
- $\pi/2 < \Phi_{\mu'} < \pi$;
- $\pi < \Phi_{\mu'} < 3\pi/2$;
- $3\pi/2 < \Phi_{\mu'} < 2\pi$;

since this angle is correlated to the hadron angle, the splitting is sensitive to the different regions of the RICH-1 in which the hadron is identified.

For each region, the asymmetry is calculated using the same method as for the full data set. Also in this case, the spread of the data results to be compatible with statistics, as confirmed by the pull distribution, that follow a Standard Normal with a RMS around 1.

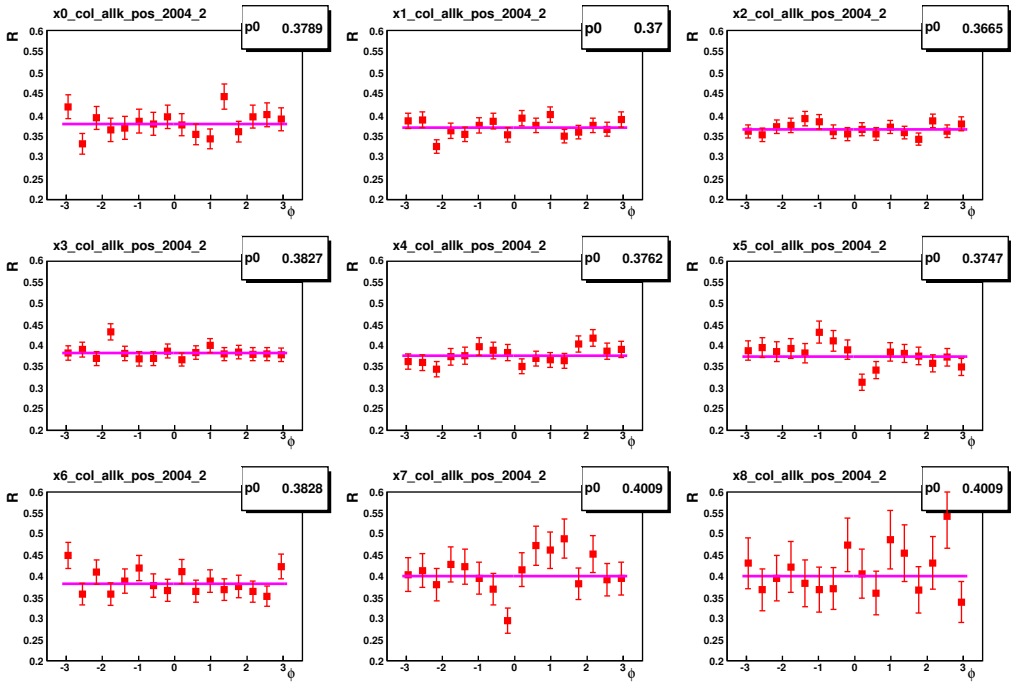

Figure 4.28: Same as in fig. 4.27, for the all kaon sample.

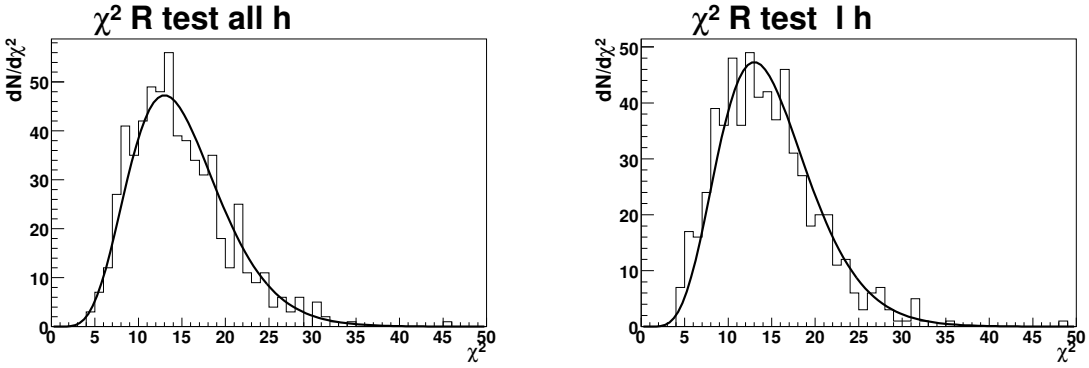

Figure 4.29: χ^2 distribution of fit with a constant on the $R(\Phi)$ compared to the χ^2 distribution for $ndf = 15$; at left for all hadron sample, at right for leading hadrons. The normalization is to the number of entries in the histogram.

4.5 RICH-1 purity

An important piece of information for the analysis comes from the knowledge of the purity of the identified sample; this is important especially for the kaon sample, for which we can expect a relevant contamination from pions, since they are produced

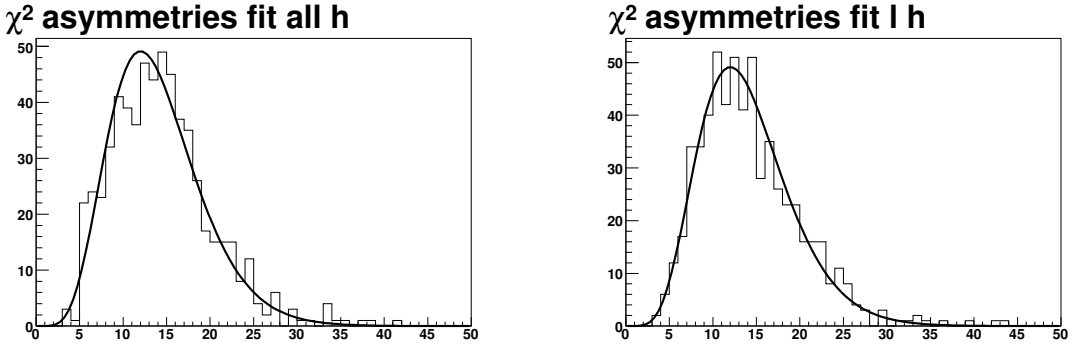

Figure 4.30: χ^2 distribution of the two parameter fit on $F(\Phi)$ compared to the χ^2 distribution for $ndf = 14$; at left for all hadron sample, at right for leading hadrons. The normalization is to the number of entries in the histogram.

in a much larger amount.

4.5.1 True and identified hadrons

After the identification procedure, the hadron sample is divided in subsamples of K, π or p; we define the vector, $\overrightarrow{I}$, of the number of the identified hadrons:

$$\overrightarrow{I} = (N_\pi^I, N_K^I, N_p^I); \tag{4.17}$$

$\overrightarrow{I}$ is connected with the true number of hadrons present in the data, $\overrightarrow{T}$:

$$\overrightarrow{T} = (N_\pi^T, N_K^T, N_p^T), \tag{4.18}$$

by the relationship

$$\overrightarrow{I} = M \cdot \overrightarrow{T}, \tag{4.19}$$

where M is a matrix containing the RICH identification probabilities:

$$\begin{pmatrix} N_\pi^I \\ N_K^I \\ N_p^I \end{pmatrix} = \begin{pmatrix} P(\pi \to \pi) & P(K \to \pi) & P(p \to \pi) \\ P(\pi \to K) & P(K \to K) & P(p \to K) \\ P(\pi \to p) & P(K \to p) & P(p \to p) \end{pmatrix} \cdot \begin{pmatrix} N_\pi^T \\ N_K^T \\ N_p^T \end{pmatrix}.$$

The matrix diagonal elements are the RICH-1 identification efficiencies, for example $P(K \to K)$ is the probability for a kaon to be identified as a kaon; the off-diagonal terms are the misidentification probabilities: for example, the term $P(\pi \to K)$ is the probability for a pion to be identified as a kaon.

If for simplicity we neglect the proton contribution, the expression above becomes:

$$\begin{pmatrix} N_\pi^I \\ \\ N_K^I \end{pmatrix} = \begin{pmatrix} P(\pi \to \pi) & P(K \to \pi) \\ \\ P(\pi \to K) & P(K \to K) \end{pmatrix} \cdot \begin{pmatrix} N_\pi^T \\ \\ N_K^T \end{pmatrix}.$$

Writing explicitly the expression of the number of identified K, N_K^I, we obtain the following relationship:

$$N_K^I = P(\pi \to K) \cdot N_\pi^T + P(K \to K) \cdot N_K^T, \tag{4.20}$$

that shows how the number of hadrons identified as K by the RICH-1 is due to two different contributions: the first term, $P(\pi \to K) \cdot N_\pi^T$, is the number of π that have been identified wrongly as K, while the second term, $P(K \to K) \cdot N_K^T$, is the number of true K that have been identified correctly. This last term is what we need to assess the purity value for the K sample:

$$Purity(K) = \frac{N_K^{T|I}}{N_K^I} = \frac{P(K \to K) \cdot N_K^T}{N_K^I}. \tag{4.21}$$

The first relationship in eq. 4.21 is the purity definition: $N_K^{T|I}$ is the number of true K in the sample of N_K^I, identified K; the second relationship is written explicitly using the RICH-1 kaon efficiency. N_K^I is known from the data after the identification procedure. Knowing the matrix coefficients, we can extract also the term N_K^T from data, inverting the relationship in eq. 4.19:

$$\overrightarrow{T} = M^{-1} \cdot \overrightarrow{I}. \tag{4.22}$$

Writing explicitly N_K^T, eq. 4.21 becomes:

$$Purity(K) = \frac{P(K \to K) \cdot N_K^T}{N_K^I} = \frac{1 - \frac{P(\pi \to K)}{P(\pi \to \pi)} \cdot \frac{N_\pi^I}{N_K^I}}{1 - \frac{P(\pi \to K)}{P(\pi \to \pi)} \cdot \frac{P(K \to \pi)}{P(K \to K)}}; \tag{4.23}$$

and we need to evaluate all the M matrix elements to get the purity.

The purity of the pion sample can be extracted in the same way as for the K sample:

$$Purity(\pi) = \frac{N_\pi^{T|I}}{N_\pi^I} = \frac{P(\pi \to \pi) \cdot N_\pi^T}{N_\pi^I} = \frac{1 - \frac{P(K \to \pi)}{P(K \to K)} \cdot \frac{N_K^I}{N_\pi^I}}{1 - \frac{P(\pi \to K)}{P(\pi \to \pi)} \cdot \frac{P(K \to \pi)}{P(K \to K)}}. \tag{4.24}$$

4.5.2 RICH-1 identification probabilities

The M matrix elements are the RICH-1 identification probabilities. They have been extracted from data selecting a ϕ and a K^0 sample.

To evaluate $P(K \to \pi)$ and $P(K \to K)$, we need a source of K in order to see how well the RICH-1 identifies them. To this end, we consider the particles coming from the decay of the ϕ meson and to have a clean sample we select exclusive ϕ in the data searching events with the following signature:

- best primary vertex in the target with μ and $\mu^{'}$;
- 2 and only 2 outgoing hadrons defined as in section 4.2.2 of opposite charge from the primary vertex; select events $\mu + N \to \mu' + h^+ + h^-$;
- inelasticity: $I = \frac{((missing\,mass)^2 - M^2)}{2M} < 2.5$ GeV/c^2, where M is the nucleon mass, and the missing mass is evaluated for the reaction $\mu + N \to \mu' + h^+ + h^-$;

all the hadrons coming in $M_\phi \pm 1\sigma$ are considered K and are used to compute $P(K \to \pi)$ and $P(K \to K)$. We evaluate the parameters independently for positive and negative particles, since the RICH-1 behavior is slightly different for opposite charges; in the evaluation of the probabilities for the positive hadrons, the negative one is requested to be identified as a K, to reduce the background under the ϕ peak; vice-versa for the negative particle. In this way the background under the ϕ peak is about 5% (instead of the 12% found before applying this cut).

For the evaluation of the remaining parameters of the matrix, $P(\pi \to \pi)$ and $P(\pi \to K)$, a pion sample is obtained considering the hadrons coming from the decay of the K^0 meson. The selection is based on the following requests:

- best primary vertex in the target with μ and $\mu^{'}$;
- secondary vertex V_0 with 2 outgoing hadrons of opposite charge;
- $Z_{V0} > 50$ cm, to avoid the target region.

Also in this case we require the particle of opposite charge to be identified by RICH-1 while evaluating the probabilities for the other one. The background under the K^0 peak is about 2%.

The overall results for the RICH-1 identification probabilities for positive and negative hadrons are:

$$M^+ = \begin{pmatrix} P(\pi^+ \to \pi^+) & P(K^+ \to \pi^+) \\ P(\pi^+ \to K^+) & P(K^+ \to K^+) \end{pmatrix} = \begin{pmatrix} 0.94 & 0.28 \\ 0.018 & 0.55 \end{pmatrix},$$

$$M^- = \begin{pmatrix} P(\pi^- \to \pi^-) & P(K^- \to \pi^-) \\ P(\pi^- \to K^-) & P(K^- \to K^-) \end{pmatrix} = \begin{pmatrix} 0.93 & 0.29 \\ 0.027 & 0.59 \end{pmatrix}.$$

Applying these values to the equation 4.23 and 4.24, and using the ratio of identified pions to kaons in data ($N^I_{\pi^+}/N^I_{K^+} \sim 5.8$ and $N^I_{\pi^-}/N^I_{K^-} \sim 7.5$) we obtain:

$$purity(K^+) = 0.90\ ; \qquad purity(K^-) = 0.78\ ;$$
$$purity(\pi^+) = 0.92\ ; \qquad purity(\pi^-) = 0.95\ .$$

These results give only a rather rough indication of the purity values, because they are integrated over the hadron phase space. This effect is not negligible because the RICH-1 performances depend very much upon the hadron phase space.

One way to take into account the phase space is to evaluate the purity for each hadron of the sample, using different matrix coefficients depending on particle polar angle and momentum, and considering then the purity mean value :

$$Purity(K) = \frac{1}{N^I_K} \sum_{i=0}^{N^I_K} Purity(\theta_i, p_i). \tag{4.25}$$

It has to be noted that here to evaluate $Purity(\theta_i, p_i)$, one needs to know also the ratio $\frac{N^I_\pi}{N^I_K}$ as a function of θ_i and p_i; in section 4.5.4 it will be shown how this dependence is taken into account.

4.5.3 Matrix parametrization

To parametrize the matrix as a function of the hadron phase space, we evaluate the coefficients in different bins of momentum and particle polar angle at RICH-1 entrance window. The bins are:

$$\begin{aligned}
3\,GeV/c \leq\ & p\ < 6\,GeV/c; \\
6\,GeV/c \leq\ & p\ < 10\,GeV/c; \\
10\,GeV/c \leq\ & p\ < 15\,GeV/c; \\
15\,GeV/c \leq\ & p\ < 20\,GeV/c; \\
20\,GeV/c \leq\ & p\ < 25\,GeV/c; \\
25\,GeV/c \leq\ & p\ < 30\,GeV/c; \\
30\,GeV/c \leq\ & p\ < 40\,GeV/c; \\
40\,GeV/c \leq\ & p\ < 50\,GeV/c;
\end{aligned}
\qquad
\begin{aligned}
0\,rad <\ & \theta\ < 0.030\,rad; \\
0.030\,rad \leq\ & \theta\ < 0.060\,rad; \\
0.060\,rad \leq\ & \theta\ < 0.090\,rad; \\
0.090\,rad \leq\ & \theta\ .
\end{aligned}$$

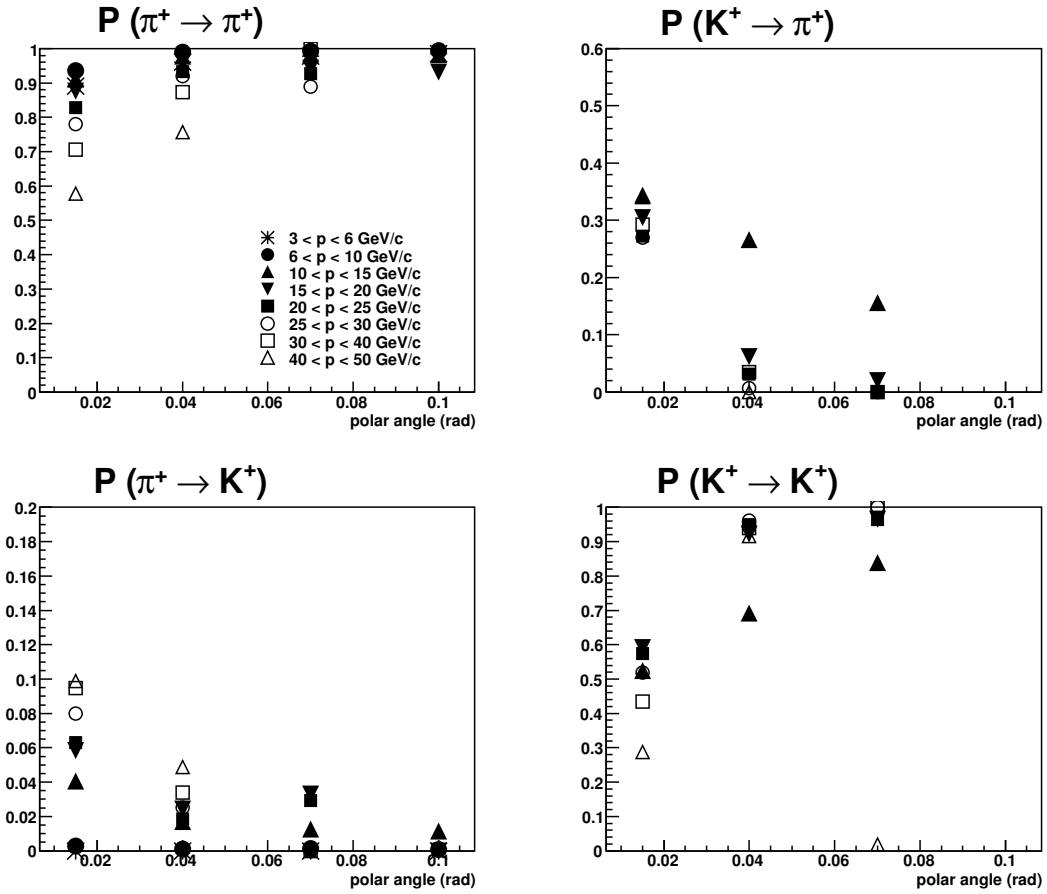

Figure 4.31: The picture shows the parametrization of the matrix containing the RICH-1 identification probabilities for positive hadrons as a function of particle polar angle and momentum. The four pads corresponds to the four probabilities considered: the dependence of the probabilities from the particle polar angle is in the abscissa, while the momentum dependence is given by the different sets of points.

In the evaluation of $P(K \to K)$ and $P(K \to \pi)$ the first two bins in momentum are missing because they are below the kaon Cherenkov threshold, while the last polar angle bin is missing because of lack of statistics.

The matrix elements are given in fig. 4.31 for positive particles and in fig. 4.32 for negative ones. In each figure, the four plots correspond to the four probabilities considered: the particle polar angle is in the abscissa axis, while the momentum dependence is given by the different sets of points.

Since we want to use the matrix coefficients for each possible value of θ and p, an interpolation between the points and an extrapolation to uncovered ranges of θ

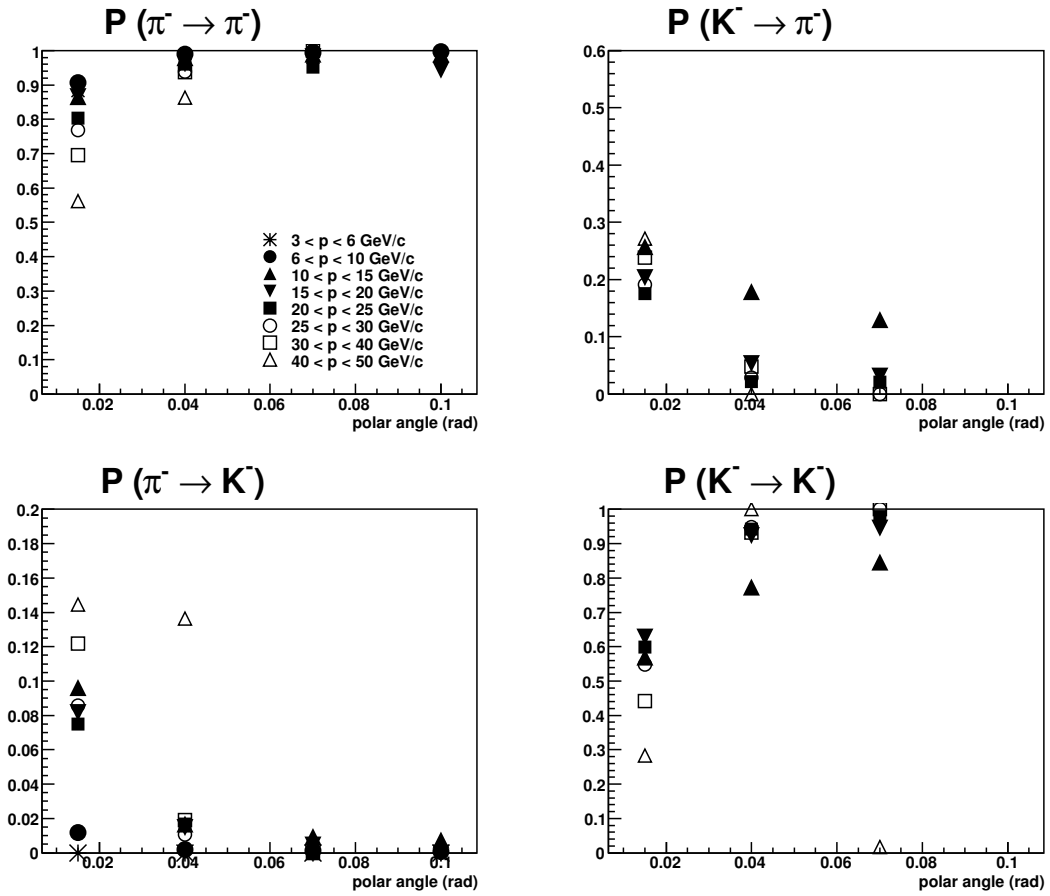

Figure 4.32: The same as in fig. 4.31, for negative hadrons.

and p are needed. We used:

- a linear interpolation and extrapolation in the small polar angle and momentum region;
- a constant value in the large polar angle and momentum region.

The results over all the interesting regions are shown in fig 4.33 and 4.34; the superimposed points are the measured points, already shown in fig. 4.31 and 4.32. The overall trend can be understood on the basis of RICH-1 behavior.

4.5.4 Purity results

The K sample purity has been evaluated in each bin of x, P_T^h and z in which the transverse spin asymmetries are measured. For each bin, the dependence of $\frac{N_\pi^I}{N_K^I}$ from

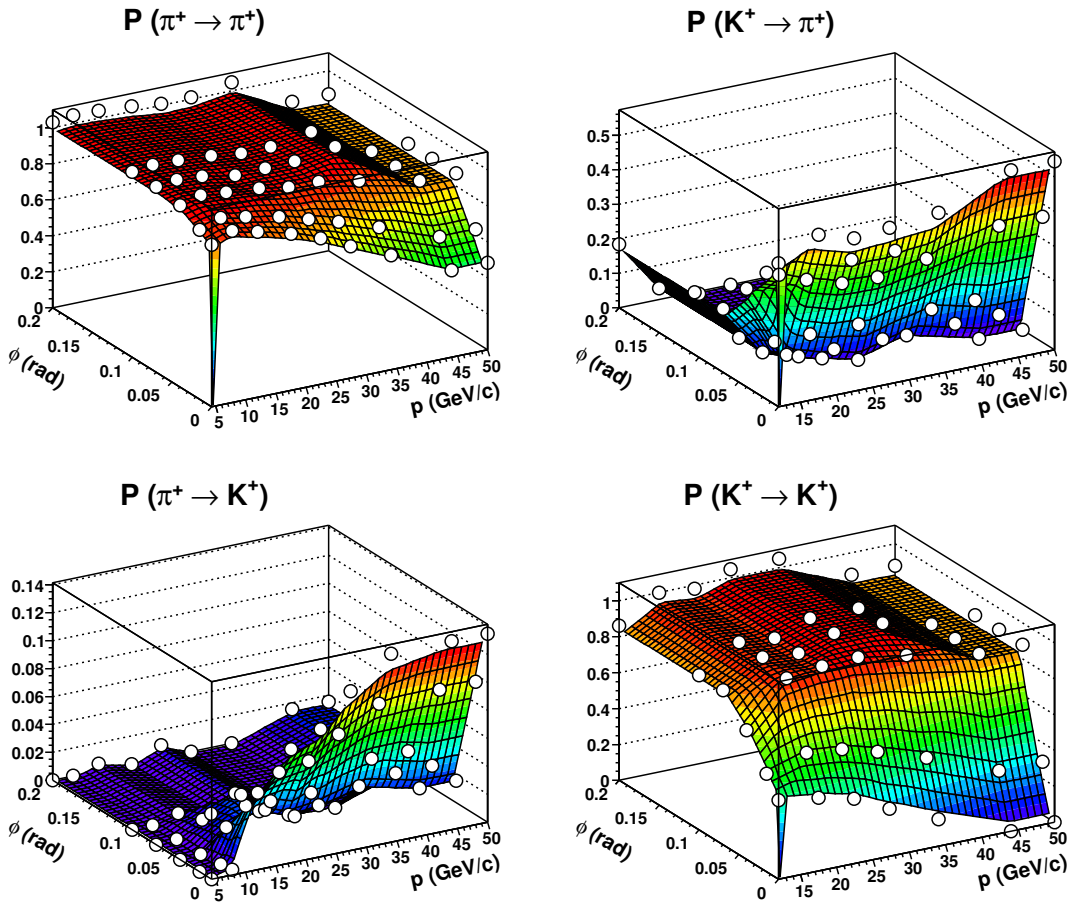

Figure 4.33: The surfaces in the four plots represent the RICH-1 identification probabilities for positive hadrons after the interpolation and the extrapolation procedure described in the text; the superimposed points are the measured points of fig. 4.31 (the points have been put a little above the real value to allow a better view of the surface). In the axis, the momentum goes up to 50 GeV/c and the polar angle up to 0.2 rad.

particle polar angle and momentum has been taken from data.

The results for the K sample purity are shown in fig. 4.35, respectively for x, P_T^h and z bins. The two different sets of data points in each plot correspond to positive K (red circles) and negative K (blue squares). As a general comment, one can note that the purity values are high, around 80%. The 2 first x bins show lower values, around 50-60%, because they correspond to small particle polar angles, the region near the beam pipe, where RICH-1 efficiency decreases due to the presence of background photons from the beam halo.

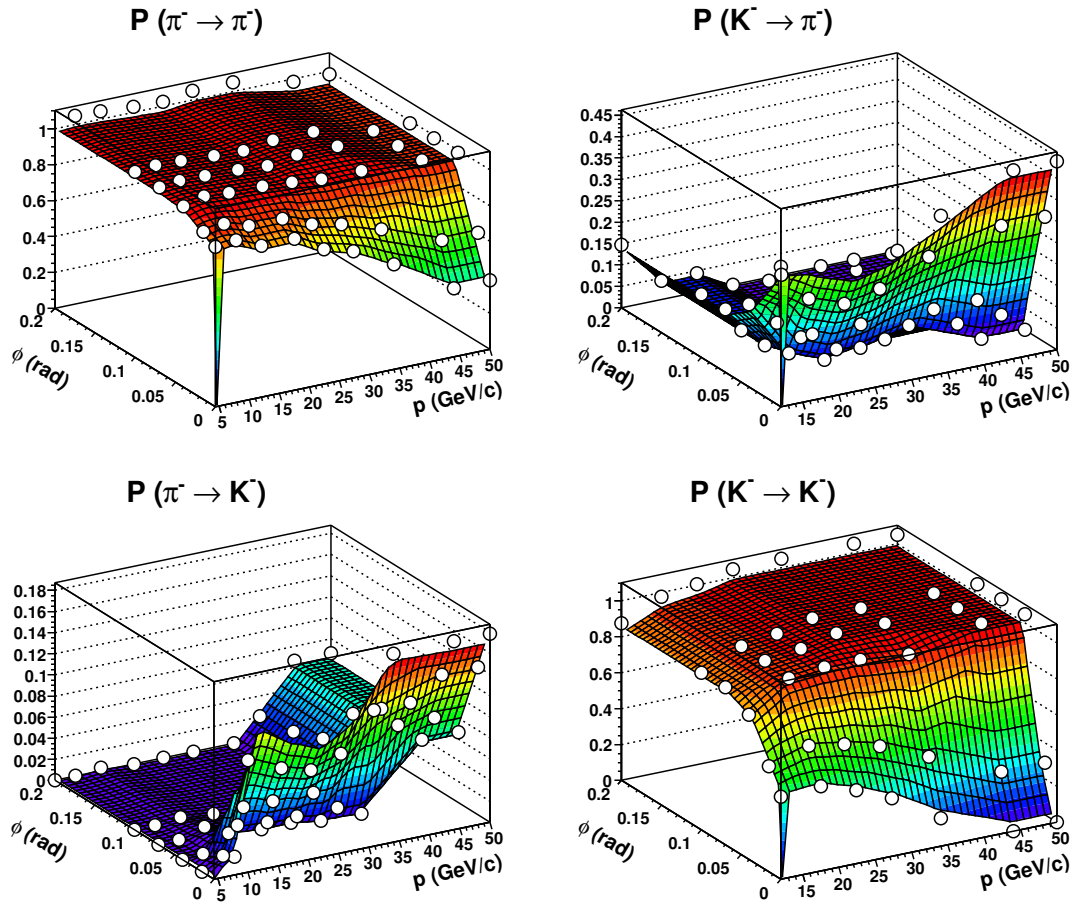

Figure 4.34: The same as in fig. 4.33, for negative hadrons

The errors shown are an upper limit estimated in the following way:

$$\sigma_{purity} = Max(|purity_{min} - purity|, |purity_{max} - purity|), \tag{4.26}$$

where $purity$ is the measured purity value, $purity_{min}$ and $purity_{max}$ the lower and the upper limit for it. $purity_{min}$ has been estimated from the errors on the matrix probability coefficients, minimizing the numerator of eq. 4.23 (replacing the $P(\pi, K)$ term with $P(\pi, K) + \sigma_{P(\pi,K)}$, $P(\pi, \pi)$ with $P(\pi, \pi) - \sigma_{P(\pi,\pi)}$) , and maximizing the denominator (replacing the $P(K, \pi)$ term with $P(K, \pi) - \sigma_{P(K,\pi)}$, $P(K, K)$ with $P(K, K) + \sigma_{P(K,K)}$). The term $purity_{max}$ has been estimated in the same way, taking the opposite sign of the σ.

In fig. 4.35 a different purity behavior for positive and negative kaons can be noted. The difference is due to the fact that from our measurement:

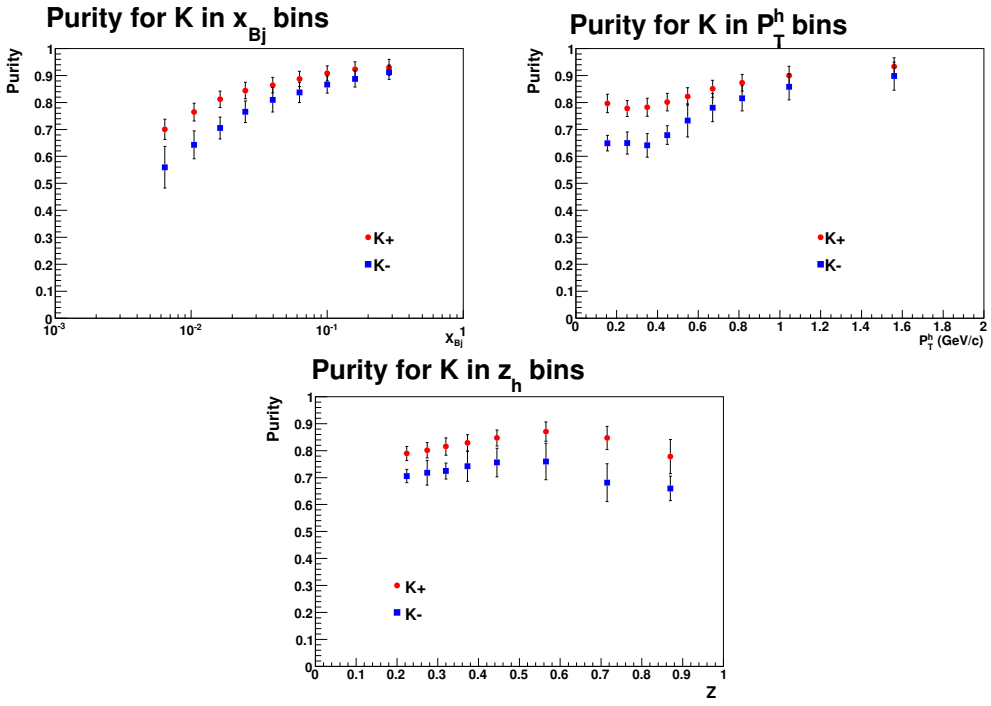

Figure 4.35: Purity of K sample in the x, P_T^h and z bins used in transversity analysis. The red points correspond to positive K, the blue squares to negative.

- $\frac{N^I_{\pi^-}}{N^I_{K^-}} > \frac{N^I_{\pi^+}}{N^I_{K^+}}$;
- $\frac{P(\pi^- \to K^-)}{P(\pi^- \to \pi^-)} > \frac{P(\pi^+ \to K^+)}{P(\pi^+ \to \pi^+)}$;

both the contributions decrease the purity of the negative particle sample, as can be seen from equation 4.23. The effect of the two contributions has been tested in the following way:

- applying the purity formula on the negative sample using the identification probabilities for positive hadrons: in this case one still obtains lower purity for negative K, due to the N_π/N_K contribution;
- applying the purity formula on the negative sample using the N^I_π/N^I_K values for positive hadrons; in this case one still obtains lower purity for negative K, due to the $\frac{P(\pi \to K)}{P(\pi \to \pi)}$ contribution;
- applying the purity formula on the negative sample using both the identification probabilities and N^I_π/N^I_K values for positive hadrons; in this case one obtains purity for negative hadrons of the same order of those for positive.

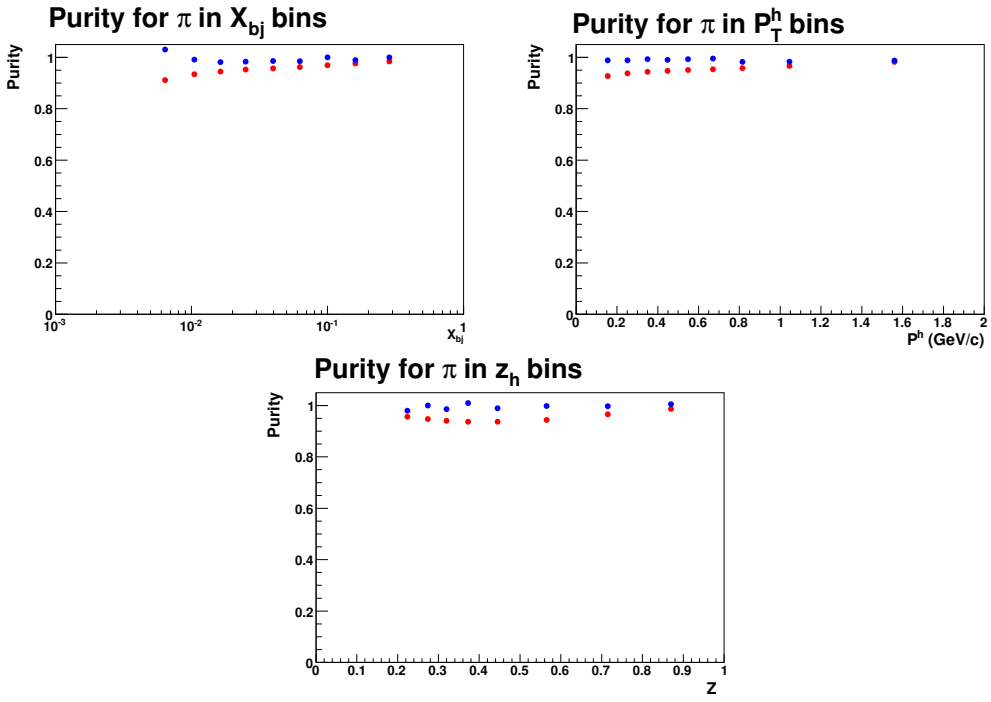

Figure 4.36: Purity of pion sample in the x, P_T^h and z bins used in transversity analysis. The red points correspond to positive pions, the blue squares to negative.

This simply means that the distributions of θ and p have almost the same shape for positive and negative hadrons .

In fig. 4.36 the results for the pion purities are shown. The values are higher than those for kaons, and always between 90% and 100%, as expected.

Using the purity values, the measured asymmetries can be corrected for the contamination. In our case, all the asymmetries are very small, thus the correction has not been applied because the measured values would not change.

Chapter 5

Extraction of the transversity and Sivers distribution functions

The results on the Collins and Sivers asymmetries presented in the previous chapter can be used to extract information about the different distribution functions appearing in the asymmetry formulas. To this end, the COMPASS results obtained on a deuterium target have to be combined with the Collins and Sivers asymmetries on a proton target, recently measured by the HERMES experiment at HERA, both for a pions and a kaons sample[1]. Information about the Collins fragmentation functions can be accessed also from specific azimuthal asymmetries arising in e^+e^- annihilations, and data on this channel are available from the Belle collaboration.

Combining together the measurements of these experiments, it is possible to perform a flavor separation analysis, with the aim of extracting the distribution functions for the different quark flavors. The Sivers functions are extracted from the Sivers asymmetries measured by the COMPASS and the HERMES experiments; both the Collins fragmentation functions and the transversity distribution functions are extracted from the Collins asymmetries measured by COMPASS and HERMES and from the Belle asymmetries.

In this chapter the results on the flavor separation analysis we have performed are presented. In the first part, the fit procedure is described: we give some details about the method, the error analysis, the PDFs and FFs used as an input for the fit. We then start the analysis of the Sivers asymmetries introducing the formulas with the explicit dependence on the different quark flavors. As a starting point, we extract the Sivers functions for the u and d-quark following a work in literature, using a simple parametrization. We then generalize the approach introducing more complex parametrization for the Sivers PDFs, and we extract them from the HERMES and COMPASS data.

[1]COMPASS data on a proton target have been collected in 2007, therefore results for this run will be available in the next years.

For the analysis of Collins effect, the Belle data have been analyzed with the aim of extracting the favored and unfavored Collins fragmentation functions. Different asymmetries measured by Belle have been used for this part. It is shown that from this data, it is possible to extract the ratio of the Collins FFs, but not their size. The Belle data are then analyzed together with SIDIS data from HERMES and COMPASS, and both the Collins fragmentation functions and the transversity PDFs for the u and d-quark are extracted.

5.1 Fit procedure

The problem of extracting unknown functions combining data from different experiments has been studied by different groups, that have provided parameterizations for the unpolarized and helicity PDFs and FFs. The problem to extract the transversity and the Sivers PDFs from the data is similar, but the data available for this purpose are very few, therefore some simplifications are needed in the analysis. For example at this stage the parametrization used for the functions have been chosen with few free parameters, and the systematic errors of the experiments have been neglected.

5.1.1 χ^2 minimization

To fit at the same time data from different experiments, we built a χ^2 variable in the following way:

$$\chi^2 = \sum_i \frac{(A_i^{exp} - A_i^{th}(\alpha_1, ..., \alpha_N))^2}{\sigma_i^2} \ . \tag{5.1}$$

The sum over the index i is on all the asymmetries considered in the analysis. The A_i^{exp} are the measured asymmetries and σ_i their corresponding errors; A_i^{th} are the theoretical expression for the asymmetries, depending on the unknown functions we want to obtain (transversity distribution functions, Collins fragmentation functions or Sivers functions). The unknown PDFs and FFs are parametrized and therefore depend on some parameters $\alpha_1, ..., \alpha_N$. The minimization of the χ^2 gives the set of parameters, together with their errors, that fit the experimental data.

The minimization of the χ^2 has been made with the dedicated package MINUIT [73] by Frank James, imported in the ROOT [74] framework.

MINUIT gives the possibility to use different minimization algorithms. We chose to start the minimization procedure with MIGRAD, that is the best known minimization algorithm, used as a default by programs as ROOT and PAW[75]. This method uses the function derivatives, therefore it depends strongly from the knowledge of these, and fails when they are very inaccurate. The routine MIGRAD gives also the error matrix, evaluating it as the inverse of the matrix of the second derivative χ^2 with respect to the parameters. In the case MIGRAD fails to converge, we switched to

the SIMPLEX algorithm, that is much slower than MIGRAD but does not use the first derivatives; this means that it is much more robust in case of large fluctuations in the function value. However, the information about parameter errors is not reliable, and correlation coefficients are not given at all. After the minimum has been found by means of MIGRAD and SIMPLEX, a search for additional distinct local minima is started calling the algorithms IMPROVE and SEEK (this is a MC search for minima); in case a real new minimum is found, MIGRAD is called again. In some specific cases of problematic fits, we apply an iterative procedure of fixing and releasing some of the parameters, in order to help the convergence of the problem.

The convergence of the problem is defined when the estimated vertical distance to the minimum is less than a tolerance parameter that we fixed as 0.0001. As a default, MINUIT tries to achieve a fast convergence using the fewest possible number of function calls, with the risk that the precision defined by the user is not obtained. We avoid this behavior setting a flag in the program that allows MINUIT to waste calls in order to be sure that the values found are precise.

The errors on the parameters are given using the HESSE routine, that calculates the full matrix of second derivatives of the function with respect to the parameters, and inverts it. This method takes into account the correlation between the parameters, but not the non-linearities of the problem, since it approximates the χ^2 shape at the minimum with a parabolic shape.

5.1.2 Error analysis

Once the error matrix and its inverse, the Hessian matrix, are known, one can estimate not only the uncertainties on the parameters $\{\alpha_1, ..., \alpha_N\}$, but also the uncertainty ΔX for any physical quantity X depending on them, provided the dependence can be approximated by a linear expansion around the χ^2 minimum. In order to avoid such assumption, we used the mathematical method of the *Lagrange undetermined multiplier* [76, 77, 78], that estimates ΔX in a way that takes into account the variation of χ^2 over the entire parameter space $\{\alpha_1, ..., \alpha_N\}$.

Let X_0 be the value of X for the parameters minimizing the χ^2, which is the best estimate of X. For a fixed value of λ, called the Lagrange multiplier, one performs a new minimization with respect to the fit parameters $\{\alpha_1, ..., \alpha_N\}$, of the quantity

$$F = \chi^2 + \lambda(X - X_0)\,, \tag{5.2}$$

to obtain a pair of values $(\chi^2(\lambda), X(\lambda))$. At this new minimum, $\chi^2(\lambda)$ is the lowest possible χ^2 for the corresponding value $X(\lambda)$ of the physical variable X. Thus one achieves a *constrained fit* in which χ^2 is minimized for a particular value of X (fig. 5.1.a).

By repeating the minimization for many values of λ, one maps out the parametrically defined curve $(\chi^2(\lambda), X(\lambda))$ (fig. 5.1.b). Since λ is just the parameter for this

curve, its value is of no particular physical significance. The error on X is taken as the variation of X necessary for the χ^2 to raise to $\chi^2_{min} + 1$, corresponding to 1σ standard deviation. In the case of linear dependence of X from the parameters the associated probability content is 68%.

The essential feature of the Lagrange Multiplier method is that the full parameter space $\{\alpha_1, ..., \alpha_N\}$ is explored in the minimization procedure, not just the immediate neighborhood of the original χ^2 minimum as in the Hessian method, and no approximation based on a small deviation from the original minimum is needed. The only drawback to the Lagrange Multiplier method is that it can be slow computationally, since it requires a separate series of minimizations for each point in which the observable X is of interest.

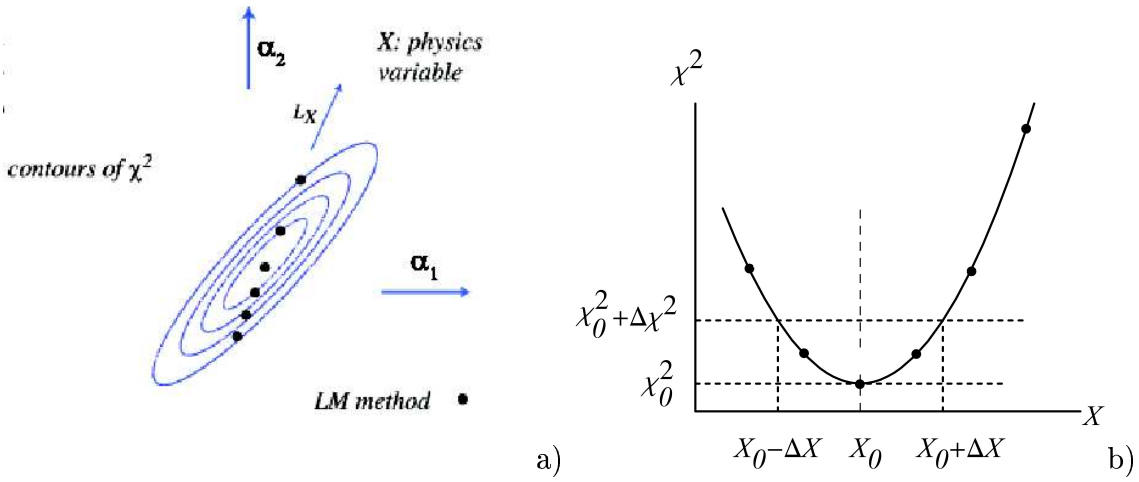

Figure 5.1: **a)** The Lagrange Multiplier Method provides sample points along the curve L_x in the parameter space; **b)** for a given tolerance $\Delta\chi^2$, the uncertainty on X is evaluated as ΔX; the solid points correspond to the sample points on the curve L_x on the left side of the plot. Figures taken from [76].

5.1.3 Constraint on the extracted functions

As seen in Chapter 1, the transversity distribution function has to obey the Soffer bound, while the Sivers and Collins functions have to obey their positivity bounds. Let's consider as an example the positivity bound for Sivers PDF:

$$|\Delta^0_T q(x)| < q(x) \ . \tag{5.3}$$

To impose the constraint in the fit we applied the so called "penalty method": after the χ^2 is minimized, the condition 5.3 is checked for each x (on a grid of 100 points).

If the condition is fulfilled for each x, we do not perform further minimizations. If the condition is not fulfilled for at least one x, we add to the χ^2 a term measuring the positivity violation in the following way:

$$\chi^2 \to \chi^2 + \sum_i \frac{(|\Delta_T^0 q(x_i)| - q(x_i))^2}{err^2}; \tag{5.4}$$

where the sum is on all the x for which the bound was not fulfilled. The term "err" corresponds to the uncertainty on $q(x)$. For convenience, one takes a constant value (we chose 0.01), which means that a small violation of positivity condition is only mildly penalized. A further minimization is then performed. Note that this method is somehow arbitrary in the choice of the x grid on which the condition is checked and in the fixed value of err chosen.

5.1.4 Unpolarized PDFs and FFs

Since the asymmetry formulas for the Collins and Sivers asymmetries depend on the unpolarized PDFs and FFs, we need to use some existing parameterizations for them as an input to the fit. Moreover, together with the helicity PDFs, they are also used to impose constraints on the distribution functions.

Different parameterizations for the PDFs exist in literature from the work of different groups. In all the fits presented in the following, we have used the GRV98 LO parameterizations for the unpolarized quark distributions [79], and the GRSV2000 LO parameterizations for the polarized quark distributions [80]. They are shown in figure 5.2 for $Q^2 = 2.4$ (GeV/c)^2. The PDF parameterizations refer to a proton target. Using the relationship between the PDF in the proton and in a neutron, we can write the PDF for a deuteron target:

$$\begin{aligned}
u^d(x) &= u^p(x) + u^n(x) = u^p(x) + d^p(x); \\
d^d(x) &= d^p(x) + d^n(x) = d^p(x) + u^p(x); \\
s^d(x) &= s^p(x) + s^n(x) = 2 \cdot s^p(x); \\
\bar{u}^d(x) &= \bar{u}^p(x) + \bar{u}^n(x) = \bar{u}^p(x) + \bar{d}^p(x); \\
\bar{d}^d(x) &= \bar{d}^p(x) + \bar{d}^n(x) = \bar{d}^p(x) + \bar{u}^p(x); \\
\bar{s}^d(x) &= \bar{s}^p(x) + \bar{s}^n(x) = 2 \cdot \bar{s}^p(x);
\end{aligned} \tag{5.5}$$

that can be summarize as:

$$\begin{aligned}
u^d(x) &= d^d(x) = u^p(x) + d^p(x); \\
s^d(x) &= \bar{s}^d(x) = 2 \cdot s^p(x) = 2 \cdot \bar{s}^p(x); \\
\bar{u}^d(x) &= \bar{d}^d(x) = \bar{u}^p(x) + \bar{d}^p(x).
\end{aligned} \tag{5.6}$$

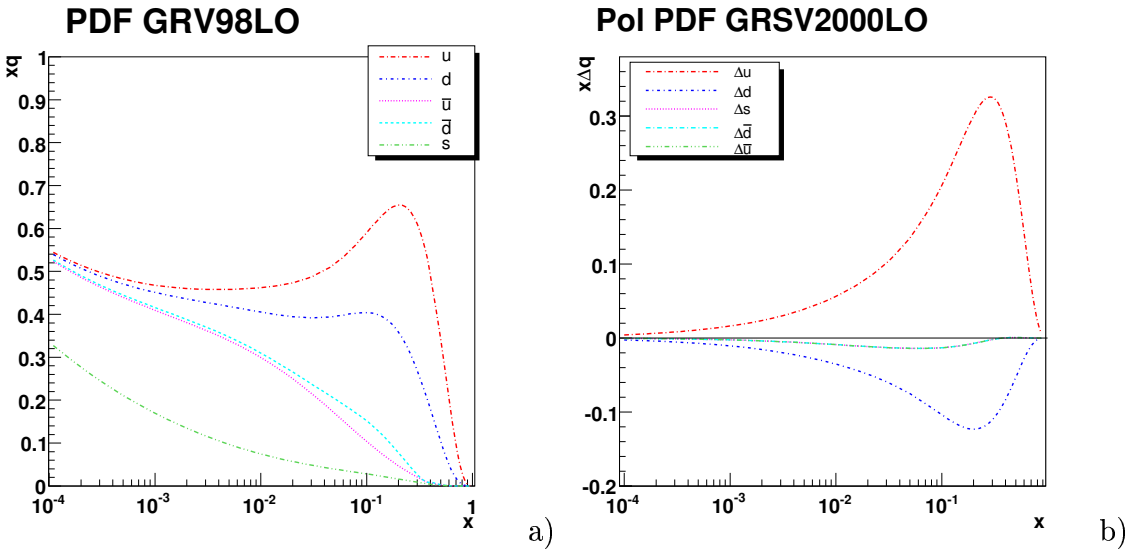

Figure 5.2: **a)** Unpolarized PDFs from the GRV98 LO parametrization at $Q^2 = 2.4$ (GeV/c)^2; **b)** Helicity PDFs, standard scenario, from the GRSV2000 LO parametrization at $Q^2 = 2.4$ (GeV/c)^2.

The parametrization for the fragmentation functions are taken from Kretzer's work [46], where, in addition to eq. 1.36 and 1.37, the following hierarchies are assumed:

$$D_d^{\pi^+} = D_{s,\bar{s}}^{\pi^+} < D_u^{\pi^+} = D_{\bar{d}}^{\pi^+} \; ; \tag{5.7}$$

$$D_{\bar{u}}^{K^+} = D_{d,\bar{d}}^{K^+} < D_u^{K^+} < D_{\bar{s}}^{K^+} \; . \tag{5.8}$$

Eq. 5.7 and 5.8 should derive from the valence structure of pions and kaons. Writing explicitly all the fragmentation functions:

$$\begin{aligned}
D_1 &= D_u^{\pi^+} = D_{\bar{d}}^{\pi^+} = D_{\bar{u}}^{\pi^-} = D_d^{\pi^-} \; ; \\
D_2 &= D_u^{\pi^-} = D_{\bar{d}}^{\pi^-} = D_{\bar{u}}^{\pi^+} = D_d^{\pi^+} = D_s^{\pi^+} = D_s^{\pi^-} = D_{\bar{s}}^{\pi^+} = D_{\bar{s}}^{\pi^-} \; ; \\
D_3 &= D_s^{K^-} = D_{\bar{s}}^{K^+} \; ; \\
D_4 &= D_u^{K^+} = D_{\bar{u}}^{K^-} \; ; \\
D_5 &= D_u^{K^-} = D_{\bar{d}}^{K^-} = D_d^{K^-} = D_{\bar{s}}^{K^-} = D_{\bar{u}}^{K^+} = D_{\bar{d}}^{K^+} = D_d^{K^+} = D_s^{K^+} \; ;
\end{aligned}$$

note that in this notation D_1 and D_2 are respectively the favored and unfavored fragmentation functions introduced in section 1.3. They are shown in picture 5.3 for $Q^2 = 2.4$ (GeV/c)^2. The integrals of the fragmentation functions entering in the asymmetry formulas as function of x have been evaluated numerically in the

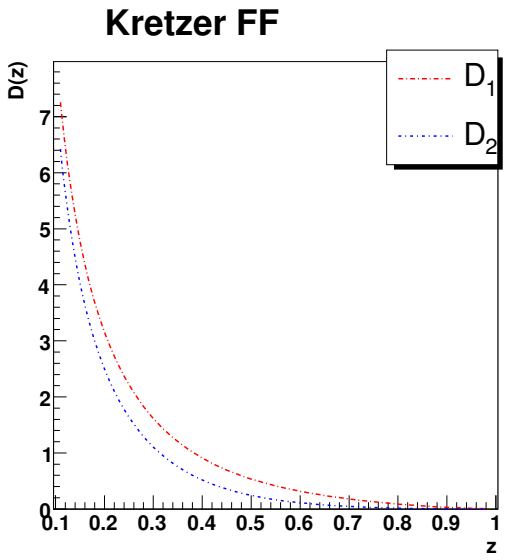

Figure 5.3: Fragmentation functions D_1 and D_2 from Kretzer parametrization at $Q^2 = 2.4$ (GeV/c)^2.

z range of the experiments: $0.2 < z < 0.7$ for HERMES, $z > 0.2$ for COMPASS. No acceptance effect has been taken into account; indeed for COMPASS data, we have checked with a full chain of MC simulation that the apparatus acceptance as function of z is flat. The different values of Q^2 in the different x bins has been taken into account in the PDF and FF evaluation for COMPASS; for HERMES, a Q^2 mean value of 2.4 (GeV/c)^2 has been considered, since the Q^2 variation in the x range in less pronounced.

5.2 SIDIS cross section with Collins and Sivers terms

We start the analysis of Collins and Sivers effect in SIDIS following the approach of ref. [81]. In this paper it is assumed that the transverse momentum of the hadron in the GNS $\vec{P}_T^h$ is entirely given by the transverse-momentum dependence in the Sivers and Collins functions. The hypothesis is that the contributions to it from other factors will result in a smearing effect, which may be considered sub-dominant. This hypothesis was already introduced in sections 1.3.3 and 1.3.4, and lead us to the formulas 1.51 and 1.58. Considering together the Collins and Sivers terms in the cross section expression, and integrating over the modulus of the hadron transverse

momentum, the general expression is [81]:

$$\frac{d\sigma}{dx\,dy\,dz\,d\phi_h} = \frac{d\sigma_{UU}}{dx\,dy\,dz} - sin(\phi_h - \phi_S)\frac{d\sigma_{UT}^{Sivers}}{dx\,dy\,dz} - sin(\phi_h + \phi_S)\,\frac{d\sigma_{UT}^{Collins}}{dx\,dy\,dz}; \quad (5.9)$$

with:

$$\frac{d\sigma_{UU}}{dx\,dy\,dz} = \frac{4\pi\alpha_{\rm em}^2 s}{Q^4}\,(1-y+y^2/2)\,x\,q(x)\,D_q^h(z), \quad (5.10)$$

$$\frac{d\sigma_{UT}^{Sivers}}{dx\,dy\,dz} = |\vec{S}_\perp|\frac{4\pi\alpha_{\rm em}^2 s}{Q^4}\,(1-y+y^2/2)\,x\,\Delta_0^T q(x)\,D_q^h(z), \quad (5.11)$$

$$\frac{d\sigma_{UT}^{Collins}}{dx\,dy\,dz} = |\vec{S}_\perp|\frac{4\pi\alpha_{\rm em}^2 s}{Q^4}\,(1-y)\,x\,\Delta_T q(x)\,\Delta_T^0 D_q^h(z). \quad (5.12)$$

where we have introduced the integrated Sivers and Collins functions:

$$\Delta_0^T q(x) = \int d^2\vec{k}_T \Delta_0^T q(x,k_T^2), \quad (5.13)$$

$$\Delta_T^0 D_q^h(z) = \int d^2\vec{p}_T \Delta_T^0 D_q^h(z,p_T^2); \quad (5.14)$$

these two terms are respectively connected to the so called (1/2)-transverse momentum of the Sivers function and of the Collins fragmentation function defined for instance in [82, 83] in the following way:

$$\Delta_0^T q(x) = 2f_{1T}^{\perp q\,(1/2)}(x) = 2\int d^2\vec{k}_T \frac{|\vec{k}_T|}{2M} f_{1T}^{\perp q}(x,k_T^2), \quad (5.15)$$

$$\Delta_T^0 D_q^h(z) = -2H_1^{\perp\,q(1/2)}(z) = -2\int d^2\vec{p}_T \frac{|\vec{p}_T|}{2zM_h} H_1^{\perp\,q}(z,p_T^2). \quad (5.16)$$

5.3 Sivers analysis

Within the approach described in the previous paragraph, the formula for the Sivers asymmetry as function of x can be evaluated as:

$$A_{Sivers}(x) = -\frac{\int dzdy \frac{d\sigma_{UT}^{Sivers}}{dxdydz}}{\int dzdy \frac{d\sigma_{UU}}{dxdydz}}; \quad (5.17)$$

the integral over y in eq. 5.17 cancels out because it is the same in the numerator and denominator; the integral over z can be factorized due to the approximations applied

in the previous paragraph. Introducing the integral of the unpolarized fragmentation functions, $D_q^h = \int_{z_{min}}^{z_{max}} D_q^h(z)\,dz$, the Sivers asymmetry can be written as:

$$A_{Sivers}(x) = -\frac{\sum_q e_q^2 \cdot \Delta_0^T q(x) \cdot D_q^h}{\sum_q e_q^2 \cdot q(x) \cdot D_q^h}; \tag{5.18}$$

and can be directly compared with the HERMES and COMPASS measured asymmetries.

From this formula, one can write the explicit expression for pions on a proton target:

$$A_{Sivers}^{p,\pi^+} = -\frac{4\Delta_0^T u D_1 + \Delta_0^T d D_2 + 4\Delta_0^T \bar{u} D_2 + \Delta_0^T \bar{d} D_1 + (\Delta_0^T s + \Delta_0^T \bar{s}) D_2}{4uD_1 + dD_2 + 4\bar{u}D_2 + \bar{d}D_1 + (s+\bar{s})D_2} \tag{5.19}$$

$$A_{Sivers}^{p,\pi^-} = -\frac{4\Delta_0^T u D_2 + \Delta_0^T d D_1 + 4\Delta_0^T \bar{u} D_1 + \Delta_0^T \bar{d} D_2 + (\Delta_0^T s + \Delta_0^T \bar{s}) D_2}{4uD_2 + dD_1 + 4\bar{u}D_1 + \bar{d}D_2 + (s+\bar{s})D_2} \tag{5.20}$$

and for a deuterium target:

$$A_{Sivers}^{d,\pi^+} = -\frac{(\Delta_0^T u + \Delta_0^T d)(4D_1 + D_2) + (\Delta_0^T \bar{u} + \Delta_0^T \bar{d})(4D_2 + D_1) + 2(\Delta_0^T s + \Delta_0^T \bar{s}) D_2}{(u+d)(4D_1 + D_2) + (\bar{u} + \bar{d})(4D_2 + D_1) + 2(s+\bar{s})D_2} \tag{5.21}$$

$$A_{Sivers}^{d,\pi^-} = -\frac{(\Delta_0^T u + \Delta_0^T d)(4D_2 + D_1) + (\Delta_0^T \bar{u} + \Delta_0^T \bar{d})(4D_1 + D_2) + 2(\Delta_0^T s + \Delta_0^T \bar{s}) D_2}{(u+d)(4D_2 + D_1) + (\bar{u} + \bar{d})(4D_1 + D_2) + 2(s+\bar{s})D_2} \tag{5.22}$$

in all the above formulas we didn't write the x dependence of the PDF and Sivers functions for simplicity.

5.3.1 Fit of pion asymmetries

In the following, the HERMES and COMPASS Sivers pion asymmetries as function of x are fitted in order to extract the Sivers functions for the u and d-quark. The outline is as follows:

- in the first part, the Sivers functions are parametrized as in [81], and different set of data are fitted:
  - the 2002-2004 HERMES data; the extracted Sivers functions are then used to make predictions for the COMPASS asymmetries;
  - the 2002-2004 HERMES data and present COMPASS data; the compatibility of the results obtained in this and in the previous fit is checked;

  - the 2002-2005 HERMES data;
  - the 2002-2005 HERMES data and present COMPASS data;

- a more general parametrization for the Sivers PDFs is then introduced, and the 2002-2005 HERMES data and present COMPASS data are fitted, imposing the positivity constraint for the Sivers functions in the fit; in this part:
  - the extracted Sivers functions are compared with the unpolarized PDFs and with the results obtained fitting the data without the positivity constraint;
  - the predictions for HERMES and COMPASS asymmetries as function of z are evaluated and compared with the data;
  - the effect of the introduction of the FFs transverse momentum Gaussian dependence is estimated;
  - the Sivers functions are compared with predictions from some models.

We start the analysis of Sivers asymmetries considering the approach of Vogelsang and Yuan' paper [81]. The fit was made on 2002-2004 HERMES π^+ and π^- data [57], while the 2002 COMPASS data [18] were used as a comparison for the predictions. In the asymmetry expression, the s-quark and the antiquark contributions are neglected, and only the Sivers functions for u and d-quark are assumed to be different from zero; also in the denominator, only the u and d-quark contributions are considered. Therefore eq. 5.19 and 5.20 read:

$$A_{Sivers}^{p,\pi^+} = -\frac{4\Delta_0^T u D_1 + \Delta_0^T d D_2}{4uD_1 + dD_2}, \tag{5.23}$$

$$A_{Sivers}^{p,\pi^-} = -\frac{4\Delta_0^T u D_2 + \Delta_0^T d D_1}{4uD_2 + dD_1}. \tag{5.24}$$

The parametrization used for the Sivers functions is the following:

$$\begin{aligned} \Delta_0^T u(x) &= S_u x(1-x)u(x) \\ \Delta_0^T d(x) &= S_d x(1-x)u(x) \end{aligned} \tag{5.25}$$

where $u(x)$ is the unpolarized u-quark PDF (containing both the valence and sea contribution), and S_u and S_d are two free parameters. Note that in this parametrization, the two functions are constrained to have the same behavior with respect to x, and the only free parameter is the size of the functions.

Vogelsang and Yuan fitted both the Sivers asymmetries as functions of x and z; the result quoted in the paper is the following:

$$\begin{aligned} S_u &= -0.81 \pm 0.07 \ ; \\ S_d &= 1.86 \pm 0.28 \ . \end{aligned} \tag{5.26}$$

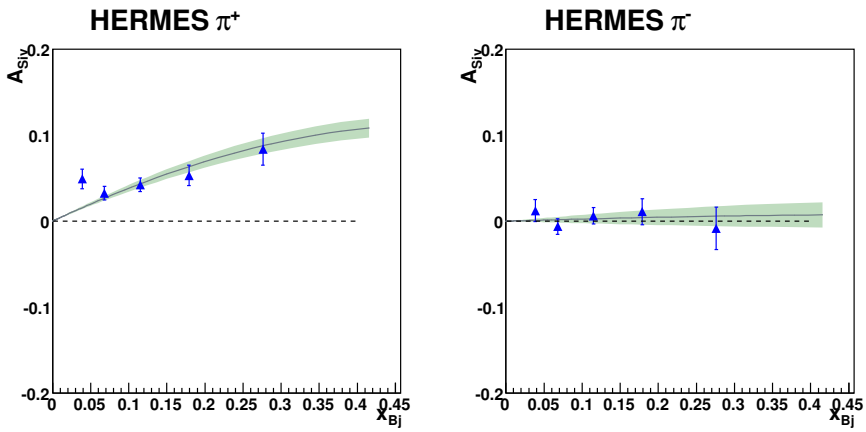

Figure 5.4: Result of the fit of 2002-2004 HERMES data with parametrization of eq. 5.25. The bands correspond to 1-σ error.

The result obtained with our fit is essentially the same:

$$\begin{aligned} S_u &= -0.76 \pm 0.09 \ ; \\ S_d &= 1.83 \pm 0.35 \ ; \\ \chi^2/NDF &= 12.0/8 \sim 1.5 \ ; \end{aligned} \tag{5.27}$$

the small differences in the parameters and their errors are due to the fact that we fit only the asymmetries as a function of x. The result of the fit compared with the measured HERMES asymmetries are shown in fig. 5.4, while the corresponding Sivers functions are shown in fig. 5.5. In all these figures, the PDFs multiplied by x are shown.

With the same assumptions used for the proton target, on deuteron eq. 5.21 and 5.22 become:

$$A_{Sivers}^{d,\pi^+} = -\frac{(\Delta_0^T u + \Delta_0^T d)(4D_1 + D_2)}{(u+d)(4D_1 + D_2)} = -\frac{\Delta_0^T u + \Delta_0^T d}{u+d} \ ; \tag{5.28}$$

$$A_{Sivers}^{d,\pi^-} = -\frac{(\Delta_0^T u + \Delta_0^T d)(4D_2 + D_1)}{(u+d)(4D_2 + D_1)} = -\frac{\Delta_0^T u + \Delta_0^T d}{u+d} \ . \tag{5.29}$$

The predictions for COMPASS are not in agreement with the present data, as shown in fig. 5.6, while they were reasonably in agreement with the old 2002 data, with larger error bars. Introducing the COMPASS data in the fit, the parameters are the following:

$$\begin{aligned} S_u &= -0.54 \pm 0.06 \ ; \\ S_d &= 0.84 \pm 0.12 \ ; \\ \chi^2/NDF &= 32.9/26 \sim 1.26 \ ; \end{aligned} \tag{5.30}$$

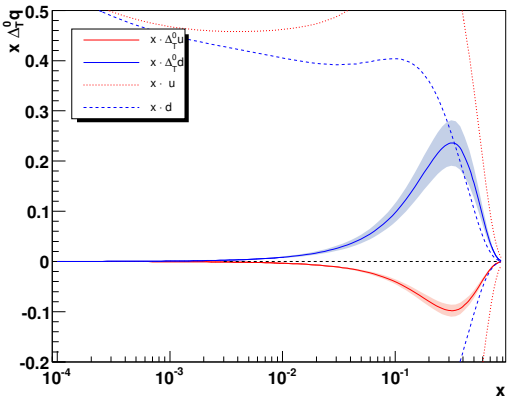

Figure 5.5: The resulting Sivers functions for u and d-quark from the fit of HERMES data. The dotted lines are the positivity bounds given by the unpolarized PDFs. The bands correspond to 1-σ error.

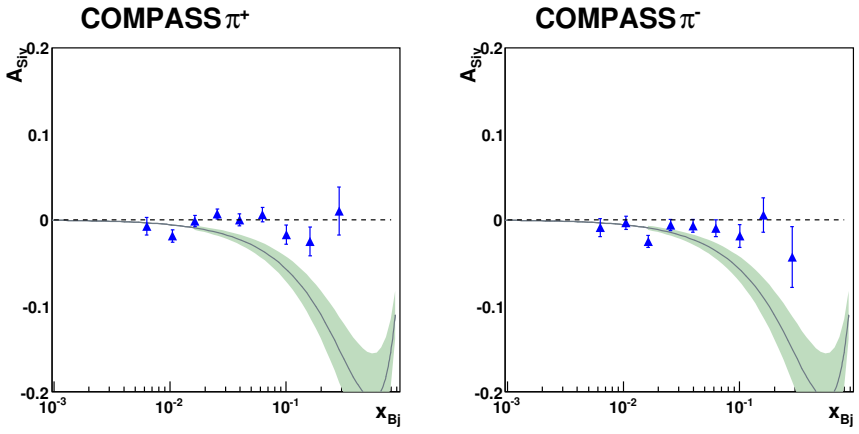

Figure 5.6: Prediction for COMPASS data using the result from the fit of 2002-2004 HERMES data. The bands correspond to 1-σ error.

In fig. 5.7, the fit results are shown: the curve for the HERMES π^+ asymmetries is almost unchanged, while the π^- data description is slightly worse with respect to the previous fit. On the contrary the COMPASS data are well described. It is important to notice that the error on the parameters is very much reduced with respect to the previous result, and the Sivers PDFs for u and d-quark have now similar size (we recall that in this approach the two functions are constrained to have the same shape), as can be seen in fig. 5.7.c. In the figure it can be noted also that the bound for the Sivers PDFs is now naturally fulfilled.

The parameters obtained with the two fits are quite different. To check the compatibility of the results using or not the COMPASS data, we considered the ellipses corresponding to 1, 2 and 3σ (fig. 5.8): the larger set of ellipses corresponds to the fit of the HERMES data only, the smaller one to the fit of both the HERMES and COMPASS data. For each set, the confidence level associated to the three ellipses is respectively 39%, 86% and 99%. It is clear that the two solutions are marginally compatible; evaluating the χ^2 of the fit of the HERMES data in the point corresponding to the result from the fit of the HERMES and COMPASS data, the compatibility is less than 1%.

In spring of 2007, new preliminary results from the 2002-2005 data have been produced by the HERMES collaboration [58]. The size of the Sivers asymmetries is the same as for the previous data, while the error bars are very much reduced. Using the new data in the fit, the results are very similar to those obtained previously, both for the fit of HERMES data only (to be compared to eq. 5.27):

$$\begin{aligned} S_u &= -0.75 \pm 0.06 \ ; \\ S_d &= 1.81 \pm 0.24 \ ; \\ \chi^2/NDF &= 23/8 \sim 2.8 \ ; \end{aligned} \tag{5.31}$$

and for the fit of HERMES and COMPASS data (to be compared to eq. 5.30):

$$\begin{aligned} S_u &= -0.55 \pm 0.04 \ ; \\ S_d &= 0.94 \pm 0.11 \ ; \\ \chi^2/NDF &= 53/26 \sim 2.04 \ . \end{aligned} \tag{5.32}$$

In both cases, the parameter errors are slightly smaller, while the χ^2 is higher. The results of the two fits are respectively in fig. 5.9 and 5.10. The corresponding Sivers u and d-functions extracted from the two fits are shown in fig. 5.11. The picture is similar to the previous one; in particular, without the COMPASS data, the d-quark Sivers function is much larger than that for the u-quark, and the positivity bound is violated.

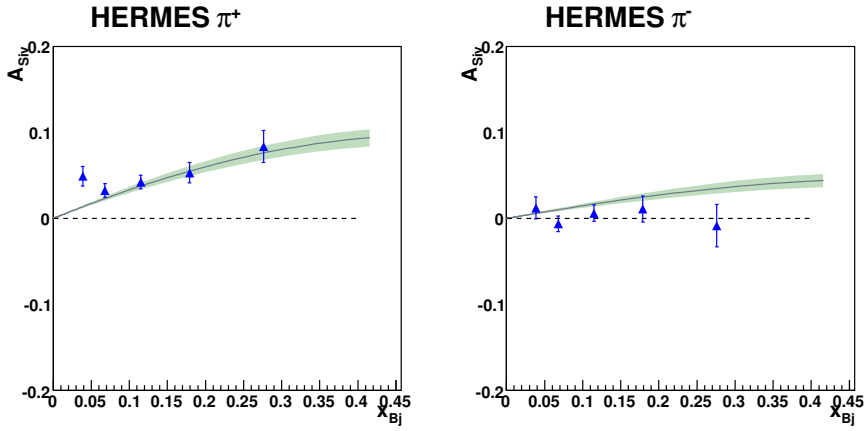

a)

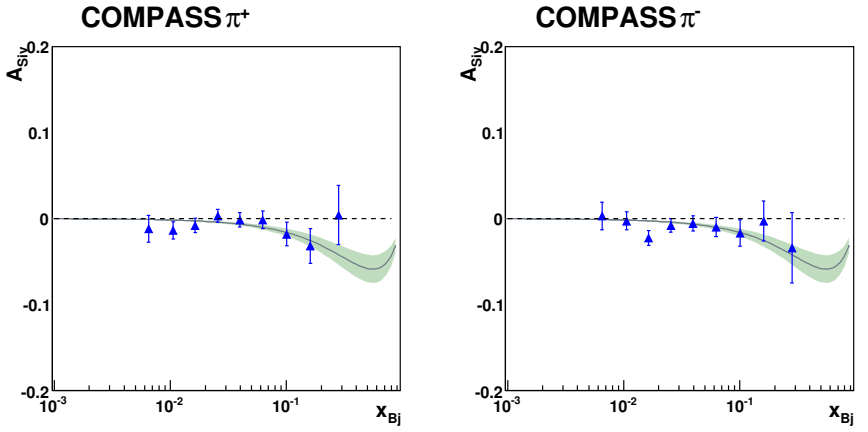

b)

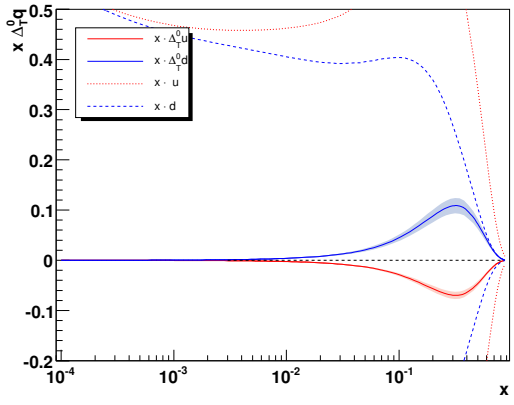

c)

Figure 5.7: Result of the fit of 2002-2004 HERMES (a) and COMPASS data (b) with parametrization of eq. 5.25; the resulting Sivers functions for u and d-quark are shown in (c). The bands correspond to 1-σ error.

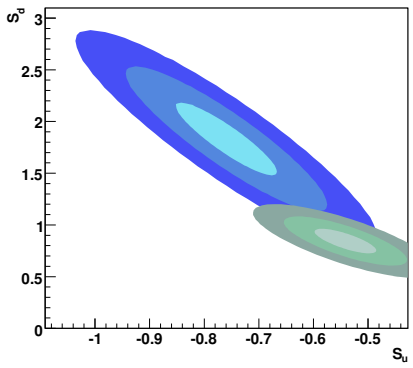

Figure 5.8: Error ellipses corresponding to 1, 2 and 3σ for the fit on only HERMES data (larger ellipses), and on the HERMES and COMPASS data (smaller ellipses).

To have a better description of the data, we introduce a more general parametrization for the Sivers functions, not depending on the unpolarized u-quark PDF:

$$\begin{aligned} \Delta_0^T u(x) &= S_u x^{\alpha_u}(1-x)^{\beta_u} \ ; \\ \Delta_0^T d(x) &= S_d x^{\alpha_d}(1-x)^{\beta_d} \ ; \end{aligned} \tag{5.33}$$

in this way both the size and the shape of the two functions can be different. Moreover, we consider all the unpolarized PDFs in the denominator of the asymmetry expressions, and not only the u and d-quark contributions. Also, the positivity constraints for the Sivers functions are included in the fit with the method described in section 5.1.3. The values obtained are the following:

$$\begin{aligned} S_u &= -0.29 \pm 0.09 \qquad & S_d &= 0.59 \pm 0.31 \\ \alpha_u &= -0.27 \pm 0.10 \qquad & \alpha_d &= -0.19 \pm 0.17 \\ \beta_u &= 2.65 \pm 0.81 \qquad & \beta_d &= 2.93 \pm 1.03 \\ \chi^2/NDF &= 37/22 \sim 1.68 \ . \end{aligned} \tag{5.34}$$

The comparison with the data is shown in fig. 5.12.a and 5.12.b. The description of the HERMES π^+ is similar to that already obtained with the previous simpler parametrization, while the description of the HERMES π^- is slightly better but still not satisfactory. The description of the COMPASS data is slightly better, in particular at the highest x.

The extracted Sivers PDFs are in fig. 5.12.c; the size of the two functions is similar to that already obtained, while the shape as function of x is different, in particular the maximum value is reached at lower x. Moreover, the errors bars of the functions at high x are larger, since the shape cannot be well constrained due to

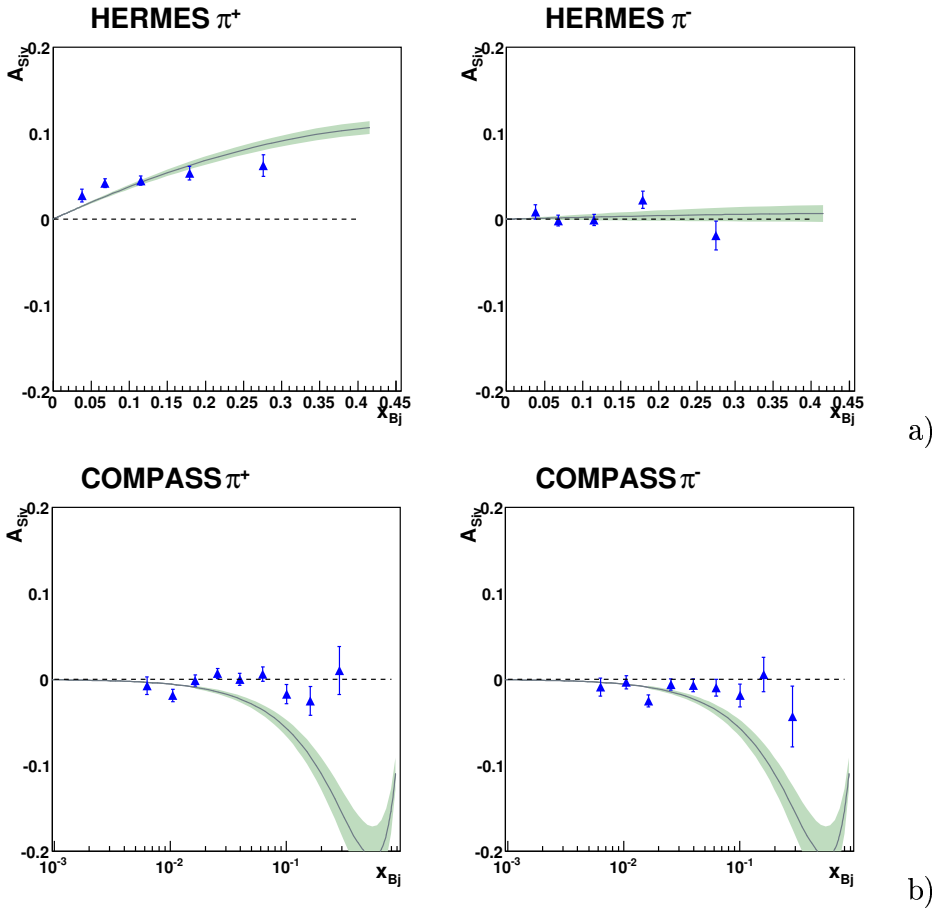

Figure 5.9: Result of the fit of 2002-2005 HERMES (a) and predictions for COMPASS data (b) with parametrization of eq. 5.25.

the lack of data points in that region. Even using this more general parametrization, the Sivers functions for u and d-quark obtained from the fit show a valence-like behavior (they are both suppressed at low x). This is clear in fig. 5.13, where the comparison between the unpolarized total and valence PDF and Sivers functions for u and d-quark is shown. Performing the same fit without the constraint for the Sivers PDFs, one obtains essentially the same results, apart for a small violation of the bound for the d-quark at high x, as visible in fig. 5.14.

The predictions for the asymmetries as function of z have been evaluated and are compared with the data in fig. 5.15. The predictions are evaluated from eq. 5.17, without the integration over z, and integrating over x. Thus, the extracted Sivers functions and the PDFs have been integrated over x, respectively in the numerator and in the denominator of the asymmetry formulas. The integration range has been evaluated for the two different experiments taking into account the kinematical cuts

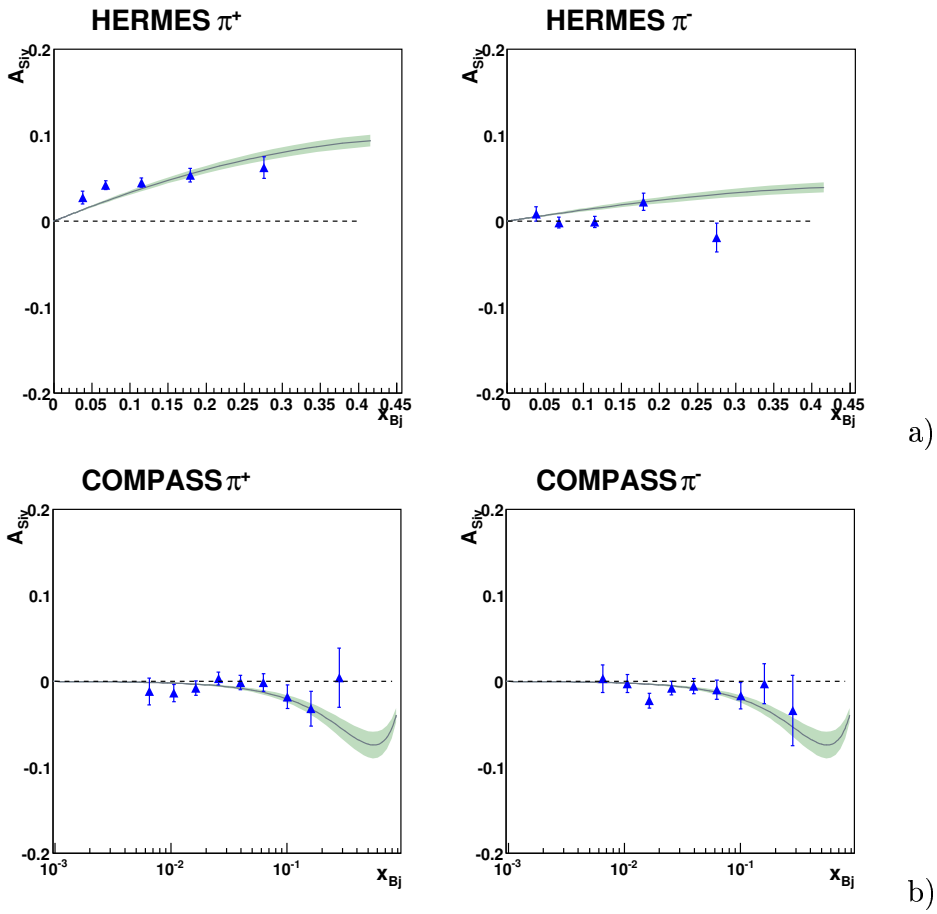

Figure 5.10: Result of the fit of 2002-2005 HERMES (a) and of COMPASS data (b) with parametrization of eq. 5.25.

applied in the analysis. Also, it has been checked that in the integration a flat acceptance in x can be considered. This has been done evaluating with LEPTO the acceptance in x of the two experiments due to the kinematical cuts and the apparatus geometrical acceptance. The predictions using the acceptance from MC or a flat acceptance are essentially the same. As can be seen, the data are well described. Still, the dependence on z of the asymmetries (in particular the HERMES π^- asymmetries) is not obvious and can be due to the fact that the transverse momentum dependence of the fragmentation functions is neglected here.

In [82, 84] the dependence of the PDF and the FF on the intrinsic transverse momenta is assumed to be Gaussian, in order to be able to integrate the cross section expression on the hadron transverse momentum. The Gaussian form of the

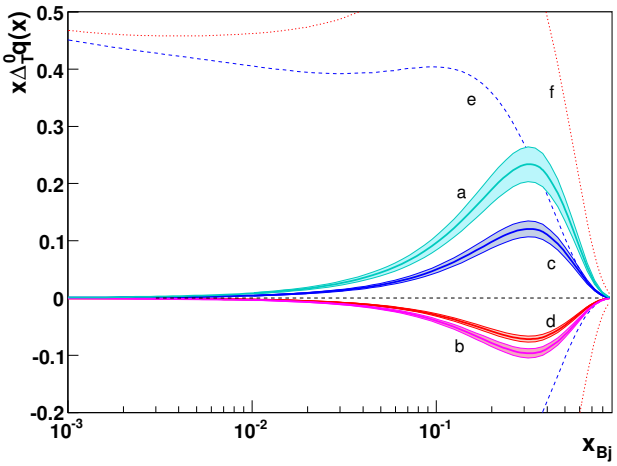

Figure 5.11: Sivers functions for u and d-quark extracted from the fit with parametrization 5.25, using 2002-2005 HERMES data only (curves a, b), and HERMES and the present COMPASS data (curves c, d). Curves e, f are the positivity bounds given by the unpolarized PDFs.

distribution functions is as follows:

$$q(x, k_T^2) = q(x)\,\frac{1}{\pi\langle k_T^2\rangle}\,e^{-k_T^2/\langle k_T^2\rangle}, \tag{5.35}$$

and

$$D_q^h(z, p_T^2) = D_q^h(z)\,\frac{1}{\pi\langle p_T^2\rangle}\,e^{-p_T^2/\langle p_T^2\rangle}; \tag{5.36}$$

so that

$$\int d^2\vec{k}_T\; q(x, k_T) = q(x), \tag{5.37}$$

and

$$\int d^2\vec{p}_T\; D_q^h(z, p_T) = D_q^h(z)\;. \tag{5.38}$$

The widths of the two Gaussian, $\langle k_T^2\rangle$ and $\langle p_T^2\rangle$, are unknown and assumed to be the same for each quark flavor or hadron produced. In [84] the two parameters have been fixed through a global fit of EMC and E655 data of the unpolarized SIDIS azimuthal asymmetries. In [82] the dependence of the hadron transverse momentum from z in HERMES data is fitted with a function of the form:

$$\langle P_T^h(z)\rangle = \frac{\sqrt{\pi}}{2}\sqrt{z^2\langle k_T^2\rangle + \langle p_T^2\rangle}\;, \tag{5.39}$$

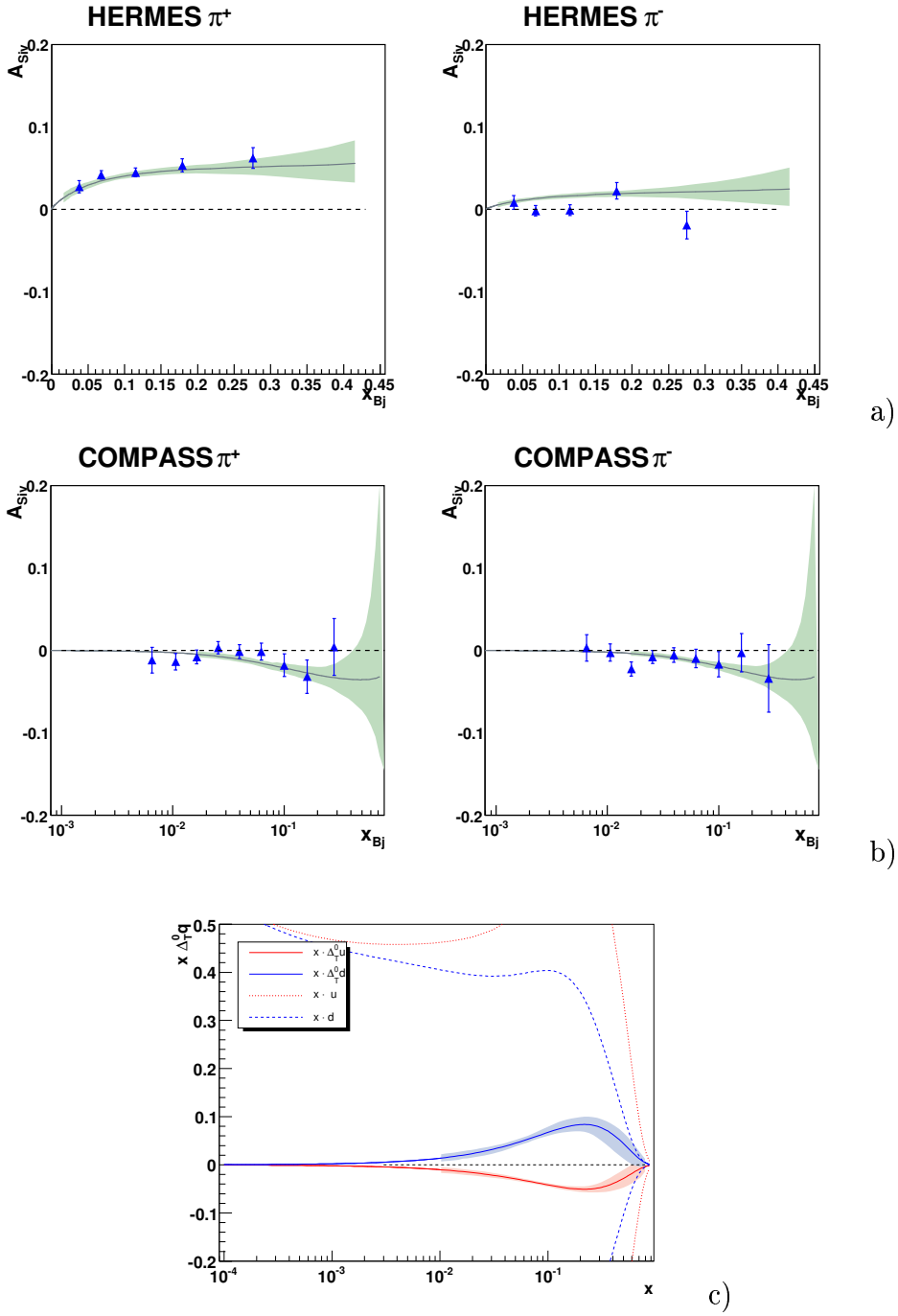

Figure 5.12: Result of the fit of the 2002-2005 HERMES (a) and the present COMPASS data (b) with parametrization of eq. 5.33; the resulting Sivers functions for u and d-quark are shown in (c). The bands correspond to 1-σ error.

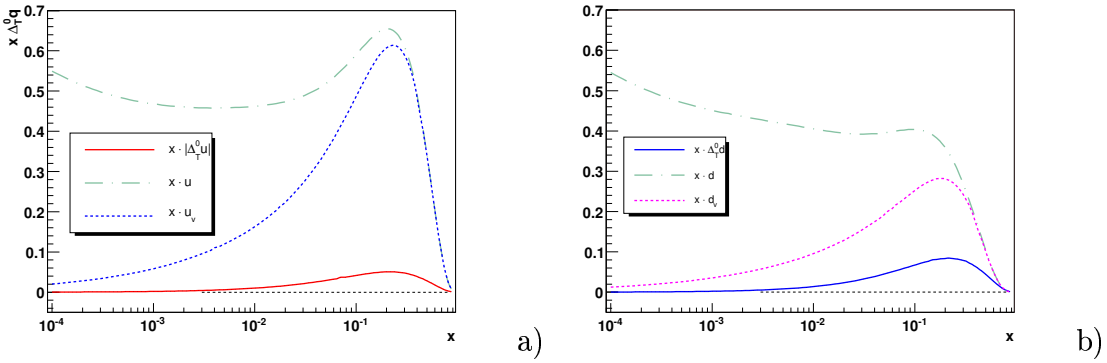

Figure 5.13: Comparison between the absolute values of the Sivers functions for u -quark (a) and d-quark (b) from the fit and the unpolarized total and valence PDFs for u and d-quark from [79].

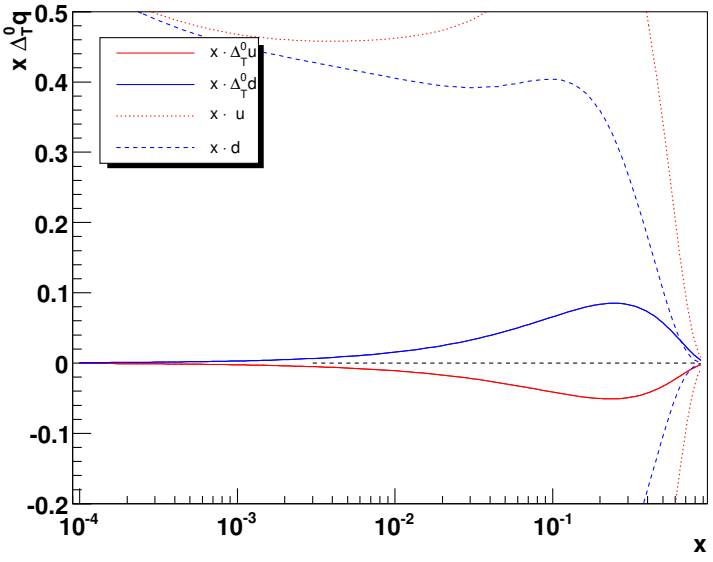

Figure 5.14: Sivers functions for u and d-quark, obtained with the parametrization of eq. 5.33, without imposing the positivity constraint in the fit. The d-quark slightly violates the corresponding bound at high x; the result after imposing the constraint in the fit are in fig. 5.12.c.

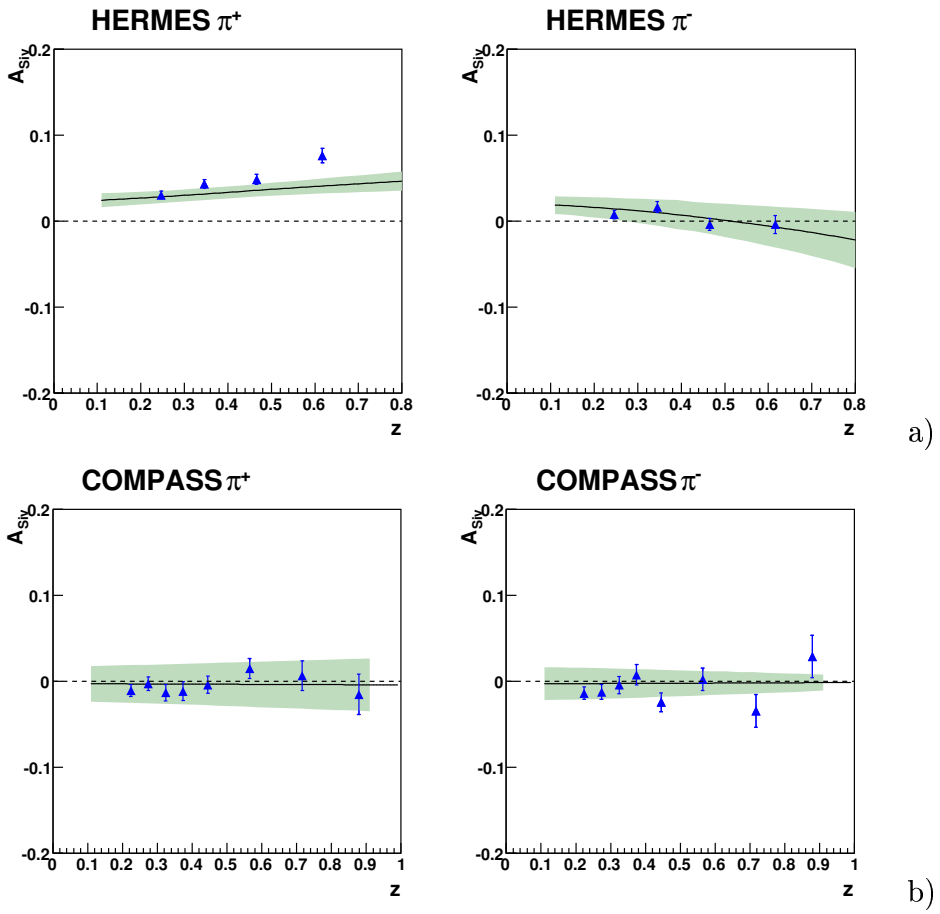

Figure 5.15: Asymmetries as function of z predicted using the extracted Sivers functions of fig. 5.12.c for HERMES (a) and COMPASS (b), compared with the measured points.

where $\langle k_T^2 \rangle$ and $\langle p_T^2 \rangle$ are the free parameters of the fit. The values found with the two different approaches are similar:

$$[84]: \ \langle k_T^2 \rangle = 0.25\,(\mathrm{GeV/c})^2, \ \langle p_T^2 \rangle = 0.20\,(\mathrm{GeV/c})^2 \ ; \tag{5.40}$$

$$[82]: \ \langle k_T^2 \rangle = 0.33\,(\mathrm{GeV/c})^2, \ \langle p_T^2 \rangle = 0.16\,(\mathrm{GeV/c})^2 \ . \tag{5.41}$$

Also the dependence of the Sivers functions from k_T is assumed to be Gaussian, with the width $\langle k_{siv}^2 \rangle$ unknown (in [84] it is a free parameter of the fit, and in [82] it is limited using the positivity bound). The integration of the cross section over $\vec{P}_T^h$ brings a "Gaussian term" $a_G = \frac{\sqrt{\pi}}{2} \frac{M}{\sqrt{\langle k_{siv}^2 \rangle + \langle p_T^2 \rangle / z^2}}$ in the Sivers asymmetry formula, containing the z variable. The results for the Sivers functions obtained in this work are in qualitative agreement with the Sivers PDFs found in [82, 84], but there are some differences that can be due to the different models used for the parton transverse momenta, and indicate a possible source of systematic uncertainties.

The QCD prediction with a large number of colors N_C [85] for the Sivers functions gives:

$$\Delta_0^T u(x, k_T^2) = -\Delta_0^T d(x, k_T^2), \tag{5.42}$$

valid with accuracy $\sim 1/N_c$, in qualitative agreement with the results given in 5.34. Under certain assumptions [86], another prediction for the Sivers functions is the large x-behavior as $(1-x)^5$. The Sivers functions obtained from our fit have a β coefficient smaller than 5, but again in qualitative agreement; in any case, it should be stressed that the Sivers functions behavior at high x is badly constrained from the present data.

Fig. 5.16 shows the integrals of the Sivers functions as obtained from the fit: each point corresponds to the integral between the corresponding x value in abscissa and the maximum value of x allowed, fixed at 0.9. The errors shown correspond to the bands in fig. 5.12.c; no systematic effect (such as the parametrization used, the PDF and FF sets used...) is taken into account: therefore the integral values and their errors have to be considered only a rough estimation. The integrals for the two Sivers functions are respectively:

$$\begin{aligned} \int_{0.01}^{0.9} dx\, \Delta_0^T u(x) &= -0.15 \pm 0.04\ ; \\ \int_{0.01}^{0.9} dx\, \Delta_0^T d(x) &= 0.23^{+0.06}_{-0.07}\ ; \end{aligned}$$

the two integrals have opposite sign and are similar in size, compatibly with the Burkardt sum rule (section 1.3.4) assuming that the sea quark and gluon Sivers functions are negligible with respect to the u and d-quark Sivers PDFs. This is also in agreement with Brodsky's argument [87], that the gluon orbital angular momentum in a nucleon should be zero. In this paper, the connection between the Sivers mechanism for the single spin asymmetries and the orbital angular momentum of the quarks and the gluons in the nucleon is revisited; the COMPASS zero asymmetries measured on deuterium are used as evidence of the gluon mechanism to be small with respect to the quark mechanism.

The work done here to extract the Sivers functions from available data can be improved. In particular the use in the fit of the asymmetries as function of z and P_T^h taking into account the correlations between the asymmetries in the different bins, and a more general parameterization of the asymmetries will give a better understanding of the overall picture. Also, no systematic errors have been considered. A possible source of systematics is the influence of the PDF and FF parameterizations on the results of the fits. In particular, recently a set of FF has been extracted with a new analysis [48], in which also data from pp collisions and DIS experiments have been used. The pion FFs extracted with this analysis and with Kretzer's are similar, and correspond in a 10-20% difference in the integrals over z. It will be interesting

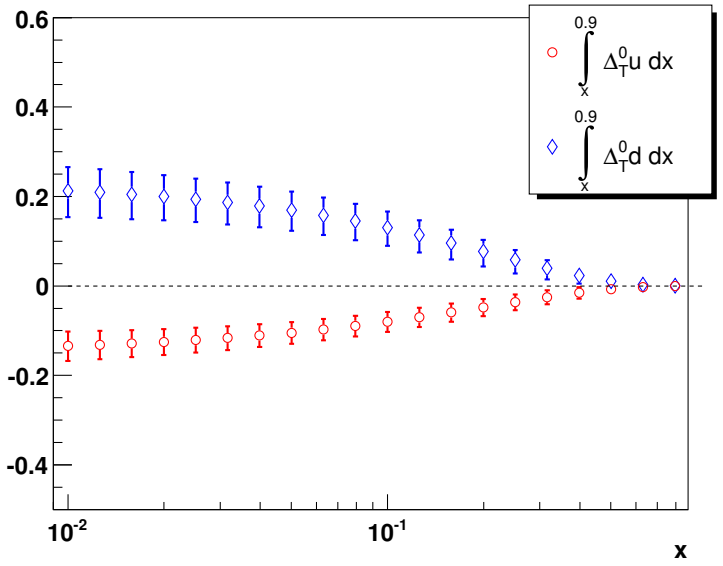

Figure 5.16: Integrals of the Sivers function for the u and d- quark shown in figure 5.12.c. Each point corresponds to the integral between the corresponding x value in abscissa and the maximum value of x allowed, fixed at 0.9.

to test the different parametrizations in a fit including also the kaon asymmetries, since the integrals of the FF for kaons in the two parameterizations differ up to a factor 4. The FF from [48] are shown in fig. 5.17.a for π^+ and in 5.17.b for K^+. In the middle panels of the figures, the comparison with the FF from Kretzer [46] is shown; in the lower panels, the comparison with another available set of FF [88].

5.4 Collins analysis

The Collins case is more complicated with respect to the Sivers one, since in the asymmetry formula, two sets of unknown functions appear: the transversity distribution functions and the Collins fragmentation functions. On the other hand, further information on the Collins fragmentation function can be achieved from specific azimuthal asymmetries arising in e^+e^- annihilations measured by the Belle collaboration [17].

There are different approaches in the literature to extract the two sets of unknown functions. In the Vogelsang and Yuan approach [81], only the HERMES SIDIS data are used to extract the Collins fragmentation functions, while the transversity distributions are assumed to saturate the Soffer bound. In the work of Efremov, Goeke and Schweitzer [83], the integrated Collins fragmentation function are extracted with

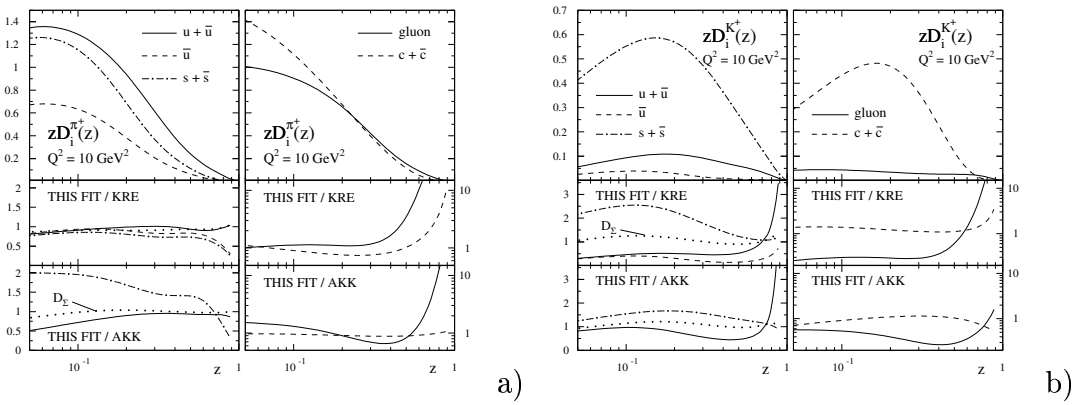

Figure 5.17: Upper panels: individual fragmentation functions $zD_i^h(z, Q^2)$ at $Q^2 = 10\,\mathrm{GeV}^2$ taken from [48] for π^+ (a) and for K^+ (b). Middle panels: ratios of fragmentation functions from [48] to the ones of Kretzer [46]. Lower panels: ratios of fragmentation functions from [48] to the ones of AKK [88]; note that $D_{\bar{u}}^{\pi^+}$ is not available in the AKK analysis.

two independent fits: one on HERMES data (using for the transversity distributions the prediction from the quark soliton model) and another from Belle data, and the two different analyzing powers are compared. Finally Anselmino *et al.* [90], made a simultaneous fit of HERMES, COMPASS and Belle, extracting both the Collins fragmentation functions and the transversity functions.

Here, we first extract the Collins fragmentation functions from the Belle data, then we perform a global fit of all the existing pion data from Belle, HERMES and the COMPASS results presented in this thesis.

5.4.1 Collins effect in e^+e^- annihilation

The Collins effect can be studied in e^+e^- annihilation with the production in the final state of two hadrons emitted in opposite directions. If we consider the process $e^+e^- \to h_1 h_2 X$, the hadron h_2 will be produced with a specific azimuthal distribution with respect to the axis defined by h_1 in the e^+e^- center of mass frame (fig. 5.18).

If we assume the Gaussian model for the transverse momentum dependence of the Collins fragmentation functions, the azimuthal dependence can be written

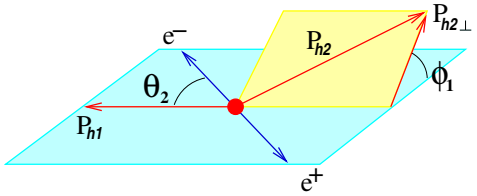

Figure 5.18: Kinematics of the process $e^+e^- \to h_1h_2X$ and the definitions of azimuthal angles in the e^+e^- rest frame.

as [17, 83]:

$$\frac{d^4\sigma(e^+e^-\to h_1h_2X)}{d\cos\theta_2 dz_1 dz_2 d\phi_1} = \frac{3\alpha^2}{Q^2}\Big[(1+\cos^2\theta_2)D_q^h(z_1)D_{\bar{q}}^h(z_2) + \cos(2\phi_1)\,\sin^2\theta_2\, C_{Gauss}\Delta_T^0 D_q^h(z_1)\Delta_T^0 D_{\bar{q}}^h(z_2)\Big]. \tag{5.43}$$

The sum over all quark and antiquark flavors weighted with the squared electric charge is implicit here and in the following formula. In the formula, Q^2 is the center of mass energy square of the lepton pair (Q^2 =10.52 (GeV/c)^2 at Belle), $z_i = 2E_{h_i}/Q$ and $C_{\rm Gauss}$ is given by:

$$C_{\rm Gauss}(z_1,z_2) = \frac{4}{\pi}\,\frac{z_1 z_2}{z_1^2+z_2^2}\,. \tag{5.44}$$

This term differs by a factor 4 with respect to the one in ref. [83], due to the different notation used: the term $D_q^h(z)$ is twice the term $H^{\perp(1/2)}(z)$ used in [83]. From eq. 5.43, the following observable can be defined:

$$A_1 = 1+\cos(2\phi_1)\,\frac{\langle\sin^2\theta_2\rangle}{\langle 1+\cos^2\theta_2\rangle}\,\frac{C_{\rm Gauss}\Delta_T^0 D_q^h(z_1)\Delta_T^0 D_{\bar{q}}^h(z_2)}{D_q^h(z_1)D_{\bar{q}}^h(z_2)}\,, \tag{5.45}$$

where the average over θ_2 of the term $f_\theta = \langle\sin^2\theta_2\rangle/(\langle 1+\cos^2\theta_2\rangle)$ can be calculated from the acceptance of the Belle detector [17]. If we consider the production of pairs of pions with the same charge ("like-sign" pion pairs), the A_1 term reads:

$$\begin{aligned}
A_1^L &= 1+\cos(2\phi_1)\,f_\theta\, C_{Gauss}P^L \\
&= 1+\cos(2\phi_1)\,f_\theta\, C_{Gauss}\{4\Delta_T^0 D_u^{\pi^+}(z_1)\Delta_T^0 D_{\bar{u}}^{\pi^+}(z_2) + \\
&\quad +4\Delta_T^0 D_u^{\pi^-}(z_1)\Delta_T^0 D_{\bar{u}}^{\pi^-}(z_2) + \Delta_T^0 D_d^{\pi^+}(z_1)\Delta_T^0 D_{\bar{d}}^{\pi^+}(z_2) + \\
&\quad +\Delta_T^0 D_d^{\pi^-}(z_1)\Delta_T^0 D_{\bar{d}}^{\pi^-}(z_2) + \Delta_T^0 D_s^{\pi^+}(z_1)\Delta_T^0 D_{\bar{s}}^{\pi^+}(z_2) + \\
&\quad +\Delta_T^0 D_s^{\pi^-}(z_1)\Delta_T^0 D_{\bar{s}}^{\pi^-}(z_2)\}/\{\Delta_T^0 D_q^h \to D_q^h\} \\
&= 1+\cos(2\phi_1)\,f_\theta\, C_{Gauss}\{5\Delta_T^0 D_{fav}(z_1)\Delta_T^0 D_{unf}(z_2) + \\
&\quad +5\Delta_T^0 D_{unf}(z_1)\Delta_T^0 D_{fav}(z_2) + 2\Delta_T^0 D_{unf}(z_1)\Delta_T^0 D_{unf}(z_2)\} \\
&\quad /\{\Delta_T^0 D_q \to D_q^h\},
\end{aligned} \tag{5.46}$$

where the notation $\Delta_T^0 D_q^h \to D_q^h$ means that the denominator has the same form of the numerator, but with the unpolarized fragmentation functions instead of the polarized. The index "fav" refers to the hadronization of a u-quark in a π^+ or a d-quark in a π^-.

Considering the production of "unlike-sign" pion pairs, the A_1 term becomes:

$$\begin{aligned} A_1^U &= 1+\cos(2\phi_1)\, f_\theta\, C_{Gauss} P^U \\ &= 1+\cos(2\phi_1)\, f_\theta\, C_{Gauss}\{4\Delta_T^0 D_u^{\pi^+}(z_1)\Delta_T^0 D_{\bar{u}}^{\pi^-}(z_2) + \\ &\quad +4\Delta_T^0 D_u^{\pi^-}(z_1)\Delta_T^0 D_{\bar{u}}^{\pi^+}(z_2) + \Delta_T^0 D_d^{\pi^+}(z_1)\Delta_T^0 D_{\bar{d}}^{\pi^-}(z_2) + \\ &\quad +\Delta_T^0 D_d^{\pi^-}(z_1)\Delta_T^0 D_{\bar{d}}^{\pi^+}(z_2) + \Delta_T^0 D_s^{\pi^+}(z_1)\Delta_T^0 D_{\bar{s}}^{\pi^-}(z_2) + \\ &\quad +\Delta_T^0 D_s^{\pi^-}(z_1)\Delta_T^0 D_{\bar{s}}^{\pi^+}(z_2)\}/\{\Delta_T^0 D_q^h \to D_q^h\} \\ &= 1+\cos(2\phi_1)\, f_\theta\, C_{Gauss}\{5\Delta_T^0 D_{fav}(z_1)\Delta_T^0 D_{unf}(z_2) + \\ &\quad +7\Delta_T^0 D_{unf}(z_1)\Delta_T^0 D_{unf}(z_2)\}/\{\Delta_T^0 D_q \to D_q^h\}. \end{aligned} \tag{5.47}$$

One can note that in both the A_1^L and A_1^U the product of favored and unfavored functions appear.

To eliminate false asymmetries coming from the detector acceptance, the Belle collaboration considers the ratio between the unlike-sign and the like-sign pion pair production, A_1^U and A_1^L:

$$\begin{aligned} A_{UL} &\equiv \frac{A_1^U}{A_1^L} = \frac{1+\cos(2\phi_1)\, f_\theta\, C_{Gauss} P^U}{1+\cos(2\phi_1)\, f_\theta\, C_{Gauss} P^L} \\ &\sim 1+\cos(2\phi_1)\, f_\theta\, C_{Gauss}(P^U - P^L)\ , \end{aligned} \tag{5.48}$$

where $P^U - P^L$ is given by

$$\begin{aligned} P^U - P^L = \Bigg[&\frac{5\Delta_T^0 D_{fav}(z_1)\Delta_T^0 D_{fav}(z_2) + 7\Delta_T^0 D_{unf}(z_1)\Delta_T^0 D_{unf}(z_2)}{5D_{fav}(z_1)D_{fav}(z_2) + 7D_{unf}(z_1)D_{unf}(z_2)} + \\ -&\frac{5\Delta_T^0 D_{fav}(z_1)\Delta_T^0 D_{unf}(z_2) + 5\Delta_T^0 D_{unf}(z_1)\Delta_T^0 D_{fav}(z_2) + 2\Delta_T^0 D_{unf}(z_1)\Delta_T^0 D_{unf}(z_2)}{5D_{fav}(z_1)D_{unf}(z_2) + 5D_{unf}(z_1)D_{fav}(z_2) + 2D_{unf}(z_1)D_{unf}(z_2)} \Bigg]\ . \end{aligned} \tag{5.49}$$

The systematic error of this method was estimated to be small [17].

5.4.2 Fit of e^+e^- data

In this part the Belle data are fitted with the aim of extracting the favored and unfavored Collins FFs. The outline is as follows:

- the Belle data [17] are fitted using the same parametrization for the Collins FFs used in [83];

- the same fit is performed on the new preliminary Belle data [91], and the consistency of the results obtained from the fits on the two Belle data sets is checked;
- the new Belle data are fitted using a more general parametrization for the Collins FFs;
- in the end, another type of azimuthal asymmetry measured by Belle is considered.

We first fit the Belle data [17] using the same parametrization used in ref. [83] for the favored and unfavored Collins fragmentation functions:

$$\Delta_T^0 D_a(z) = C_a \, z \, D_a(z), \quad a = fav, unf. \tag{5.50}$$

The parameters we obtain are the following:

$$\begin{aligned} C_{fav} = 0.32 \pm 0.21 \qquad & C_{unf} = -1.05 \pm 0.61; \\ \chi^2/NDF \;\sim\; & 4/8 \sim 0.5. \end{aligned} \tag{5.51}$$

The corresponding Collins FFs are shown in fig. 5.19. At variance with the usual fragmentation functions, the Collins FFs have opposite sign and the unfavored one is larger than the favored even if with larger error bar. Since eq. 5.49 is symmetric with respect to the exchange of the signs of the 2 coefficients C_{fav} and C_{unf}, the choice of sign in 5.51 is arbitrary.

The result quoted in [83] is the following:

$$C_{fav} = 0.15 \ , \quad C_{unf} = -0.45 \ ; \tag{5.52}$$

there is a good agreement with our result, taking into account that here the Collins fragmentation function is defined to be two times bigger than that used in [83]. It is not possible to compare the parameter errors, since they are not quoted in the paper. The result of the fit is shown in fig. 5.20.

In 2007, new preliminary Belle results [91] obtained on a larger amount of data have been made available: the "old" published data correspond to 29 fb^{-1}, while the "new" preliminary data correspond to 547 fb^{-1}, therefore they bring a substantial improvement on the statistical accuracy of the measurement. This can be seen comparing figure 5.20, containing the old data points, and fig 5.22.a, showing the new data.

The same fit of the new Belle data gives a very different result: the two coefficients for the favored and unfavored Collins fragmentation functions have equal sign (also in this case we cannot determine which sign it is), and the favored function is more than 2 times larger then the unfavored one:

$$\begin{aligned} C_{fav} \;&=\; 1.17 \pm 0.19 \ , \quad C_{unf} = 0.71 \pm 0.27 \\ \chi^2 \;&=\; 16.5/8 \ \sim 2. \end{aligned} \tag{5.53}$$

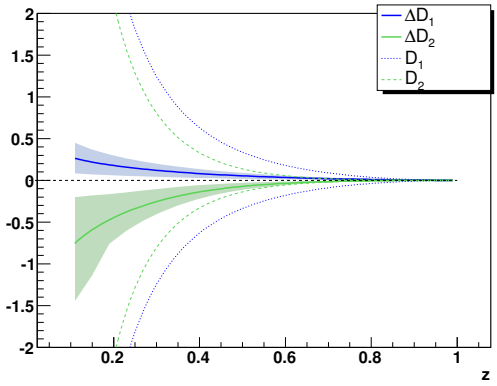

Figure 5.19: Extracted Collins fragmentation functions from fit on Belle data using parametrization of eq. 5.50. The bands correspond to 1σ error.

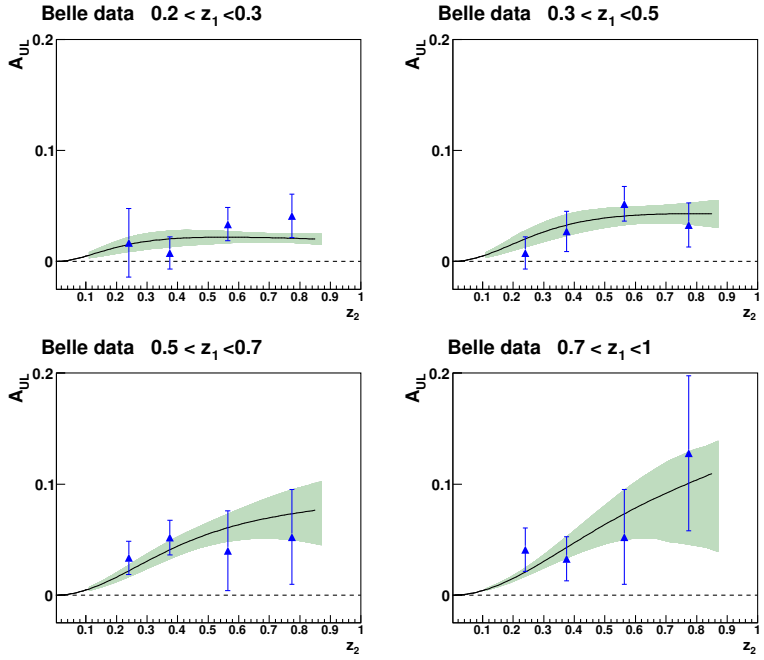

Figure 5.20: Fit of Belle data with parametrization of eq. 5.50. The bands correspond to 1σ error.

The extracted Collins FFs are in fig. 5.21, while the fit results in fig. 5.22, left part; to help in the comparison with the previous fit, on the right hand side the new data with the corresponding fit are shown together with the old data points and their fit.

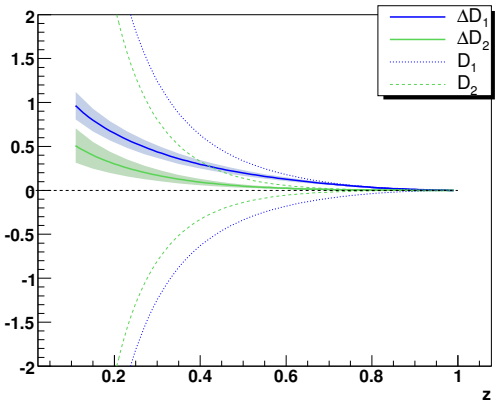

Figure 5.21: Extracted Collins fragmentation functions from fit on new Belle data using parametrization of eq. 5.50. The bands correspond to 1σ error.

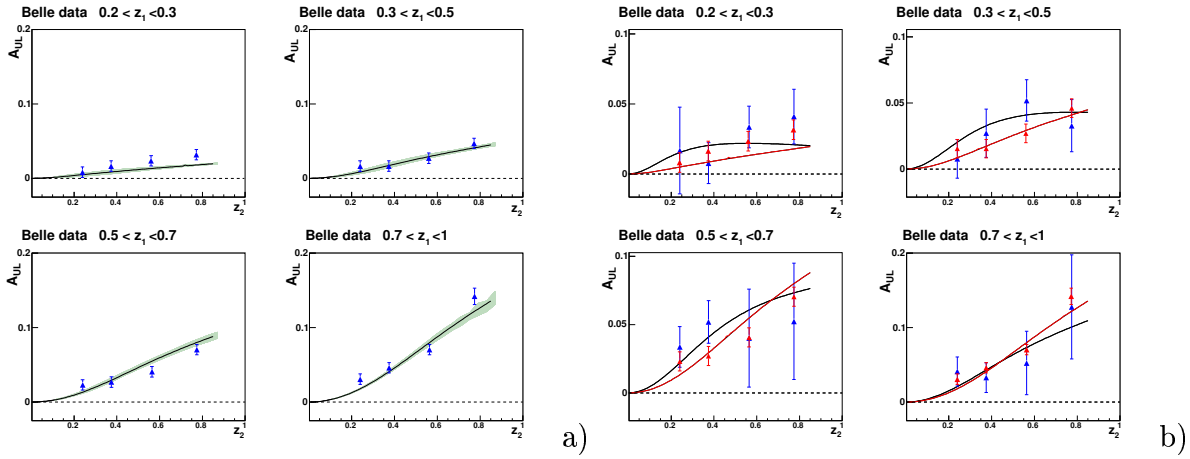

Figure 5.22: **a)** fit of new Belle data with parametrization of eq. 5.50; **b)** Comparison between the fit of new and old data: the red points and red line correspond to the new set, while the blue points and black line to the old set, already presented in fig. 5.20.

To check the consistency of the two fit results, we considered their confidence regions. In fig. 5.23, left part, the 1σ confidence regions in the plane (C_{unf}, C_{fav}) are shown: the regions do not touch but it can be seen that the region corresponding to the new data (the thicker one) seem to be a prolongation of the region corresponding to the old data. In the right part of fig. 5.23, the regions corresponding to 2σ error:

in this case the confidence region for the new data is contained completely in that of the old data. Therefore we conclude that, despite of the very different results we get in the two fits, the two set of Belle data are in very good agreement. An important point is that, even if the new data from Belle are very precise, the allowed range for the Collins fragmentation functions is large; also the relative signs of the two Collins fragmentation functions is not defined. On the contrary the relationship between them is very well defined. In this sense, results in eq. 5.53 must be considered as only one of the possible solutions. For example, in fig. 5.24.a, curves corresponding to 10

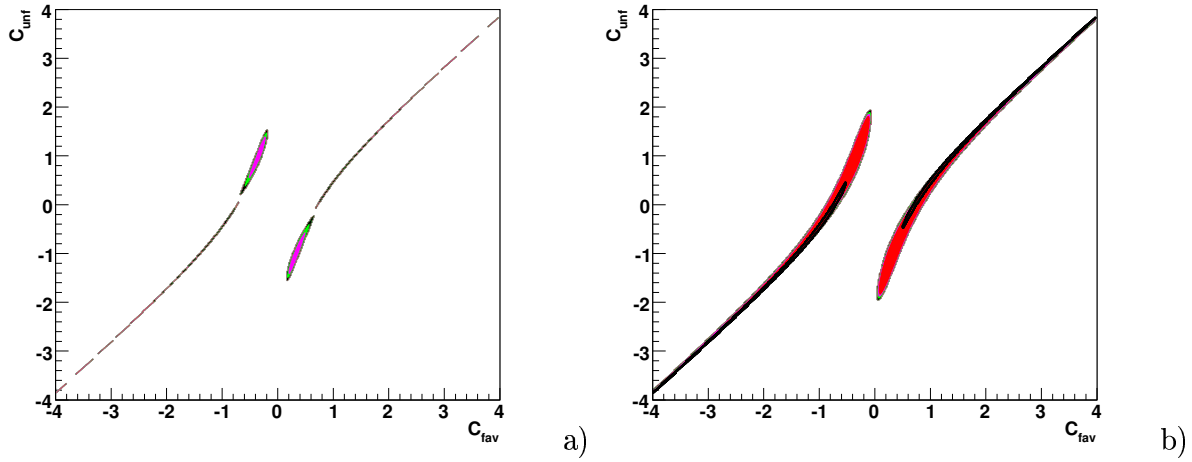

Figure 5.23: **a)** The 1σ error confidence regions for the fit of old and new Belle data; **b)** The 2σ error confidence regions for the fit of old and new Belle data; the region for the new data is contained in the one of the old data.

different pairs of values (C_{unf}, C_{fav}) lying along the confidence region (fig. 5.24.b) are shown: all the curves are very close, and the variation of the corresponding χ^2 is very low. Also, the minimum position depends somehow on the initial value of the parameters.

We have also considered a more general expression for the Collins fragmentation functions:

$$\Delta_T^0 D_a(z) = C_a\, z^\gamma\, (1-z)^\delta D_a(z) \quad a = fav, unf; \tag{5.54}$$

with γ and δ coefficients equal for the 2 functions (a fit with γ and δ different for favored and unfavored FFs would bring 6 free parameters for 10 independent points). With this parametrization, the fit is not stable, and the confidence region in the parameter space (C_{unf}, C_{fav}) has a similar shape already seen in fig. 5.23. Different results are found depending on the initial condition of the parameters; still, the fit seems to indicate Collins fragmentation functions with equal sign and

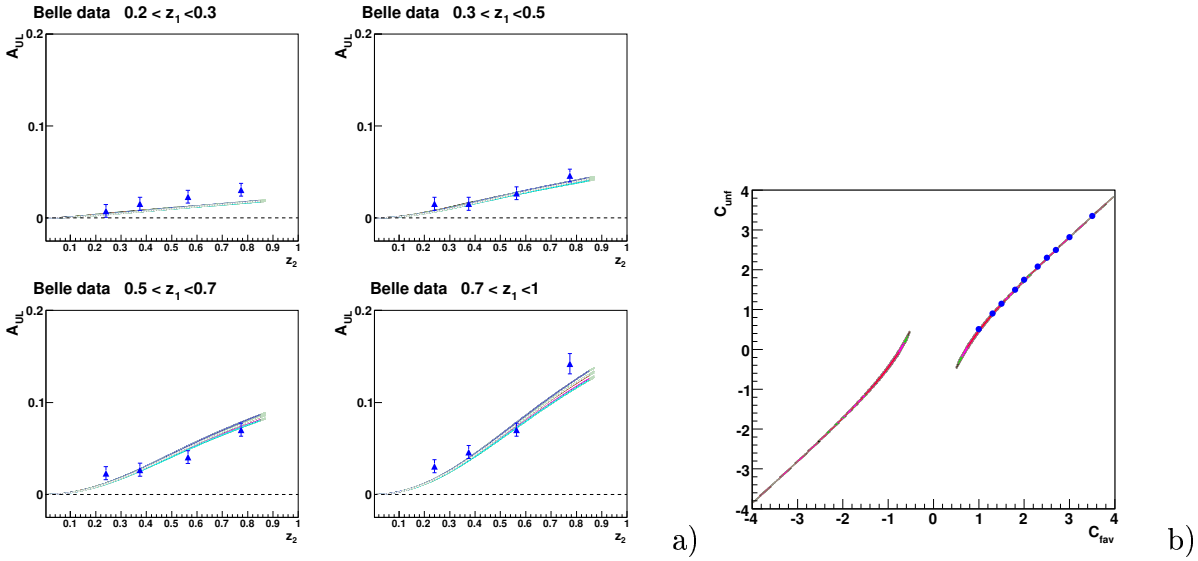

Figure 5.24: **a)** Ten different curves obtained varying the parameters C_{unf}, C_{fav} along the confidence regions in the (C_{unf}, C_{fav}) plane as shown in **b)**.

negative values of γ and δ, with δ around 1 and γ lower than 1. The Belle data are better described with this parametrization (fig. 5.25): in particular in the first bin of z_1, the fitting curve is higher for $z \to 1$ and follows the behavior of the points. The curve shown in the figure refers to this result on the parameters:

$$\begin{aligned} C_{fav} &= 0.16 \pm 0.03\,, \quad C_{unf} = 0.10 \pm 0.03 \\ \gamma &= -0.54 \pm 0.20\,, \quad \delta = -1.14 \pm 0.13 \\ \chi^2 &= 1.6/6 \sim 0.3. \end{aligned} \tag{5.55}$$

Another observable from Belle

Following the suggestion in ref [83], the Belle collaboration also measured a different asymmetry. The A_{UL} asymmetry described is built measuring the unlike- and like-sign asymmetries A_1^U and A_1^L; a third asymmetry A_1^C can be accessed observing a neutral and a charged pion. In terms of the favored and unfavored Collins functions,

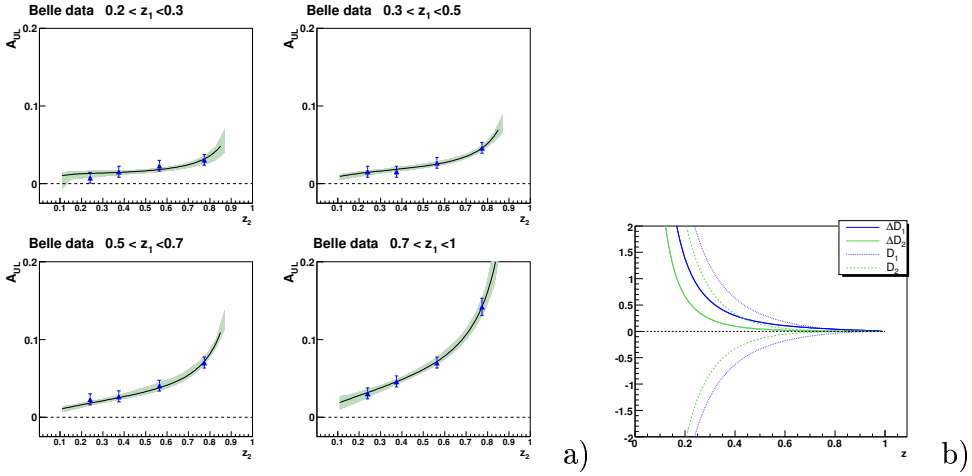

Figure 5.25: Fit of new Belle data (a) with the parametrization of eq. 5.54 and resulting Collins FFs (b).

the A^C reads:

$$\begin{aligned}
A_1^C &= 1+\cos(2\phi_1)\, f_\theta\, C_{Gauss} P^C \\
&= 1+\cos(2\phi_1)\, f_\theta\, C_{Gauss}\{4\Delta_T^0 D_u^{\pi^+}(z_1)\Delta_T^0 D_{\bar{u}}^{\pi^0}(z_2) + \\
&\quad +4\Delta_T^0 D_u^{\pi^-}(z_1)\Delta_T^0 D_{\bar{u}}^{\pi^0}(z_2) + \Delta_T^0 D_d^{\pi^+}(z_1)\Delta_T^0 D_{\bar{d}}^{\pi^0}(z_2) + \\
&\quad +\Delta_T^0 D_d^{\pi^-}(z_1)\Delta_T^0 D_{\bar{d}}^{\pi^0}(z_2) + \Delta_T^0 D_s^{\pi^+}(z_1)\Delta_T^0 D_{\bar{s}}^{\pi^0}(z_2) + \\
&\quad +\Delta_T^0 D_s^{\pi^-}(z_1)\Delta_T^0 D_{\bar{s}}^{\pi^0}(z_2)\}/\{\Delta_T^0 D_q^h \to D_q^h\} \\
&= 1+\cos(2\phi_1)\, f_\theta\, C_{Gauss} \\
&\quad \{5(\Delta_T^0 D_{fav}(z_1)+\Delta_T^0 D_{unf}(z_1))(\Delta_T^0 D_{fav}(z_2)+\Delta_T^0 D_{unf}(z_2)) + \\
&\quad +4\Delta_T^0 D_{unf}(z_1)\Delta_T^0 D_{unf}(z_2)\}/\{\Delta_T^0 D_q \to D_q^h\}\ . \qquad (5.56)
\end{aligned}$$

The observable measured by Belle is built considering the double ratio between the A^C and A^U asymmetries:

$$\begin{aligned}
A_{UC} &\equiv \frac{A^C}{A^U} \\
&= \frac{1+\cos(2\phi_0) f_\theta\, C_{Gauss} P^C}{1+\cos(2\phi_0) f_\theta\, C_{Gauss} P^U} \\
&\sim 1+\cos(2\phi_0) f_\theta\, C_{Gauss}(P^C - P^U)\ , \qquad (5.57)
\end{aligned}$$

where $P^C - P^U$ is given by:

$$P^C - P^U = \left[\frac{5(\Delta_T^0 D_{fav}(z_1) + \Delta_T^0 D_{unf}(z_1))(\Delta_T^0 D_{fav}(z_2) + \Delta_T^0 D_{unf}(z_2)) + 4\Delta_T^0 D_{unf}(z_1)\Delta_T^0 D_{unf}(z_2)}{5(D_{fav}(z_1) + D_{unf}(z_1))(D_{fav}(z_2) + D_{unf}(z_2)) + 4D_{unf}(z_1)D_{unf}(z_2)} - \frac{5\Delta_T^0 D_{fav}(z_1)\Delta_T^0 D_{fav}(z_2) + 7\Delta_T^0 D_{unf}(z_1)\Delta_T^0 D_{unf}(z_2)}{5D_{fav}(z_1)D_{fav}(z_2) + 7D_{unf}(z_1)D_{unf}(z_2)}\right] . \quad (5.58)$$

Together with the new preliminary data on A_{UL}, Belle collaboration gave also results for the A_{UC} asymmetry. We performed a fit of these data to see if the correlation between the two Collins functions is less strong in this type of measurement with respect to the unlike- and like-sign asymmetry. The results obtained confirm our previous observations: also with this observable, it is not possible to fix independently the two Collins fragmentation functions. For example, fitting the data with the parametrization of eq. 5.50, the confidence region in the (C_{unf}, C_{fav}) plane (fig. 5.27) is very similar to the previous already obtained, apart from the fact that in this case only fragmentation functions with the same sign are favored. The fitting curve in this case gives a very good agreement with the Belle asymmetries (fig. 5.26) already using a simple parameterization for the Collins fragmentation functions with only a free parameter (eq. 5.50).

From these observations, we can conclude that this new asymmetry allows to extract the relationship between the favored and unfavored Collins FFs again, but not their absolute value. We refrain from using both asymmetries at the same time since the asymmetries are correlated (in both cases the unlike-pions combination enter in the double ratio method).

5.4.3 Fit of Collins asymmetries

In this section, the azimuthal asymmetries measured by the Belle Collaboration are analyzed together with the charged pion Collins asymmetries measured by HERMES and COMPASS. The outline is as follows:

- the formulas for the Collins asymmetries on a proton and a deuterium target are introduced;
- the 2002-2004 HERMES data are fitted as in [81], assuming the transversity distribution to saturate the Soffer bound, while the Collins FFs are parametrized and extracted from the fit; from the results, the prediction for COMPASS asymmetries as function of x, for HERMES and COMPASS as function of z and for Belle are computed and compared with the data;
- the Gaussian dependence hypothesis upon k_T for the transversity distribution is introduced in the formulas;

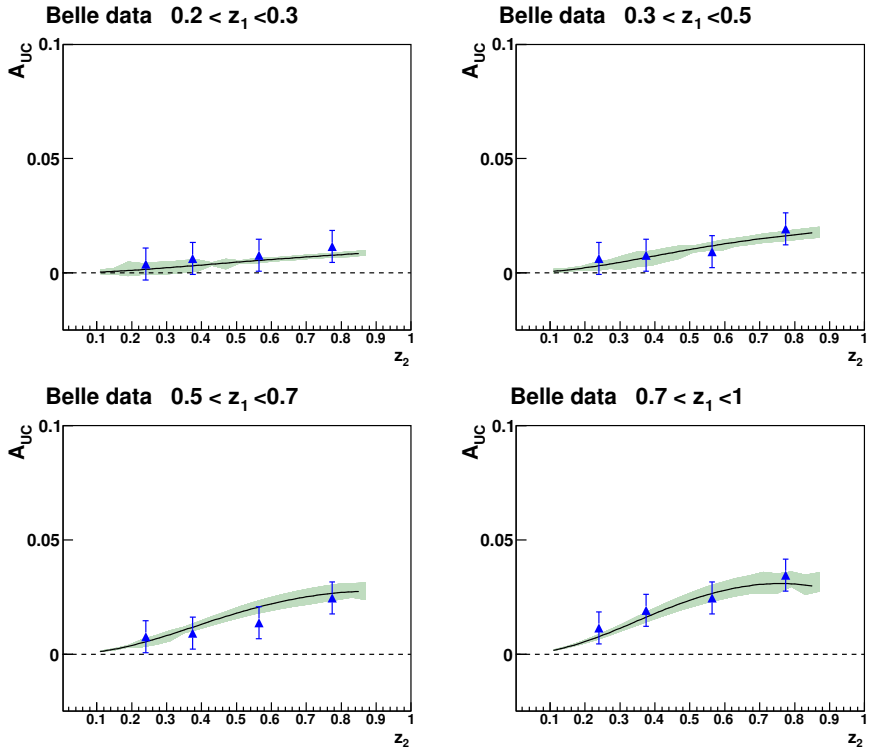

Figure 5.26: Fit with parametrization of eq. 5.50 on Belle A_{UC} asymmetries.

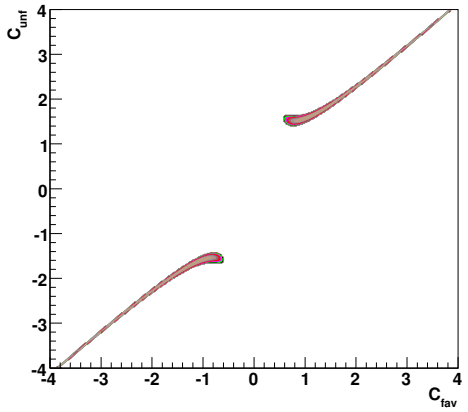

Figure 5.27: The confidence regions for the fit of new Belle A_{UC} asymmetries. The shape of the region is similar to that of fig. 5.23, corresponding to the A_{UL} asymmetries.

- the 2002-2005 HERMES pion data, the present COMPASS data and the new Belle data are fitted, using general parametrization both for the Collins FFs and for the transversity distributions; the fit is performed with and without imposing the Soffer bound;
  - the extracted transversity functions are compared with the helicity and unpolarized PDFs;
  - the prediction for COMPASS and HERMES asymmetries as function of z are evaluated and compared with the data;
  - the extracted transversity functions are compared with predictions from some models;
- in the last part, some considerations about the sign of the functions extracted and the effect of the COMPASS data in the fit are reported.

As for the Sivers case, we start the analysis of the Collins effect following the approach of [81], described in section 5.2. From eq. 5.10 and 5.12, the Collins asymmetry as function of x in SIDIS can be written as:

$$A_{Collins}(x) = -\frac{\Delta_T^0 D_q^h \int dy \frac{1-y}{x^2y^2} x\Delta_T q(x)}{D_q^h \int dy \frac{1-y+y^2/2}{x^2y^2} xq(x)}; \tag{5.59}$$

where the term D_q^h in the denominator of eq. 5.59 is the fragmentation function integrated over z, while the $\Delta_T^0 D_q^h$ term is the integral of the Collins fragmentation function over $\vec{P}_T^h$ and z, already defined in eq. 5.16. At variance with Sivers case, the integrals over y in the denominator and numerator do not cancel out. In the analysis of COMPASS data, the asymmetries have been extracted factorizing out the term $D_{NN} = (1-y+y^2/2)/(1-y)$ (see section 4.3.3), so we can neglect the contribution of the y integrals to the asymmetries. In HERMES analysis, the approach is different: in ref. [56, 57], two types of asymmetries are presented: the "virtual-photon" and the "lepton-beam" asymmetries. The lepton-beam and virtual-photon asymmetries differ by a factor:

$$\frac{1-y}{\frac{1+R}{1+\gamma^2}(1-y)+y^2/2} \tag{5.60}$$

where R is the ratio of cross sections for longitudinally and transversally polarized virtual photons on an unpolarized target, and $\gamma = \frac{2Mx}{Q}$ (already introduced in section 1.1). The difference with the asymmetries shown by COMPASS is the presence of the R and the γ^2 terms. Both terms can be neglected at first order; moreover the R term is not measured and its relevance in the formula is not clear. In the new preliminary HERMES data, only the lepton-beam asymmetries are presented.

In the following, we fit the lepton-beam asymmetries considering in the corresponding asymmetry formula the D_{NN} factor for the HERMES kinematics, with $R = 0$ and $\gamma = 0$. The D_{NN} is evaluated from MC using LEPTO. In the simulation the kinematical cuts in HERMES analysis and the apparatus acceptance are taken into account; fig. 5.28.a shows the mean value of y as a function of x, as obtained from the simulation and from real data [89]; the agreement is very good. Fig. 5.28.b shows the mean value of D_{NN} as a function of x; the curve shown is used in the asymmetry formula for HERMES. As a further cross check of the simulation reliability, we have performed the same exercise for the COMPASS kinematics. The values of D_{NN} from data and from MC are in fig. 5.29.

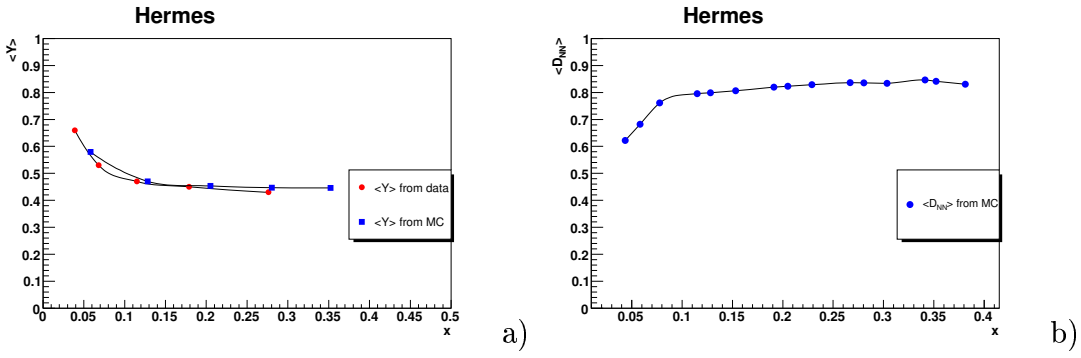

Figure 5.28: **a)** Comparison of $\langle y \rangle$ from data and from MC as a function of x, for HERMES; **b)** $\langle D_{NN} \rangle$ from MC as a function of x , for HERMES.

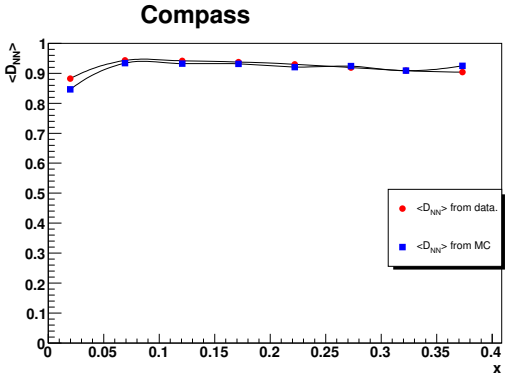

Figure 5.29: Comparison of $\langle D_{NN} \rangle$ from data and from MC as a function of x, for COMPASS.

Considering the sum over the different flavors, and neglecting the y integral for clarity, the asymmetry expression becomes:

$$A_{Collins}(x) = -\frac{\sum_q e_q^2 \cdot \Delta_T^0 D_q^h \cdot \Delta_T q(x)}{\sum_q e_q^2 \cdot D_q^h \cdot q(x)}; \tag{5.61}$$

and as for the Sivers case, we can write it explicitly for the production of pions on a proton target:

$$A_{Collins}^{p,\pi^+} = -\frac{4\Delta_T u \Delta_T^0 D_{fav} + \Delta_T d \Delta_T^0 D_{unf} + 4\Delta_T \bar{u} \Delta_T^0 D_{unf} + \Delta_T \bar{d} \Delta_T^0 D_{fav} + (\Delta_T s + \Delta_T \bar{s}) \Delta_T^0 D_{unf}}{4uD_{fav} + dD_{unf} + 4\bar{u}D_{unf} + \bar{d}D_{fav} + (s+\bar{s})D_{unf}} \tag{5.62}$$

$$A_{Collins}^{p,\pi^-} = -\frac{4\Delta_T u \Delta_T^0 D_{unf} + \Delta_T d \Delta_T^0 D_{fav} + 4\Delta_T \bar{u} \Delta_T^0 D_{fav} + \Delta_T \bar{d} \Delta_T^0 D_{unf} + (\Delta_T s + \Delta_0^T \bar{s}) \Delta_T^0 D_{unf}}{4uD_{unf} + dD_{fav} + 4\bar{u}D_{fav} + \bar{d}D_{unf} + (s+\bar{s})D_{unf}} \tag{5.63}$$

and, considering eq. 5.6, on a deuterium target:

$$A_{Collins}^{d,\pi^+} = \frac{(\Delta_T u + \Delta_T d)(4\Delta_T^0 D_{fav} + \Delta_T^0 D_{unf}) + (\Delta_T \bar{u} + \Delta_T \bar{d})(4\Delta_T^0 D_{unf} + \Delta_T^0 D_{fav})}{(u+d)(4D_{fav} + D_{unf}) + (\bar{u}+\bar{d})(4D_{unf} + D_{fav}) + 2(s+\bar{s})D_{unf}} + \\ + \frac{2(\Delta_T s + \Delta_T \bar{s})\Delta_T^0 D_{unf}}{(u+d)(4D_{fav} + D_{unf}) + (\bar{u}+\bar{d})(4D_{unf} + D_{fav}) + 2(s+\bar{s})D_{unf}} \tag{5.64}$$

$$A_{Collins}^{d,\pi^-} = \frac{(\Delta_T u + \Delta_T d)(4\Delta_T^0 D_{unf} + \Delta_T^0 D_{fav}) + (\Delta_T \bar{u} + \Delta_T \bar{d})(4\Delta_T^0 D_{fav} + \Delta_T^0 D_{unf})}{(u+d)(4D_{unf} + D_{fav}) + (\bar{u}+\bar{d})(4D_{fav} + D_{unf}) + 2(s+\bar{s})D_{unf}} + \\ + \frac{2(\Delta_T s + \Delta_T \bar{s})\Delta_T^0 D_{unf}}{(u+d)(4D_{unf} + D_{fav}) + (\bar{u}+\bar{d})(4D_{fav} + D_{unf}) + 2(s+\bar{s})D_{unf}} \tag{5.65}$$

In eq. 5.64 and 5.65 the asymmetries are positive since in COMPASS the asymmetries are extracted as a $sin(\phi_h + \phi_s - \pi)$ modulation.

The author of [81] fitted the HERMES asymmetries [57] assuming the transversity distribution functions to saturate the Soffer bound (section 1.2 and fig. 5.30). For the Collins fragmentation functions, two simple sets of parameterizations have been used:

$$SET\ I: \begin{aligned} \Delta_T^0 D_{fav}(z) &= C_f z(1-z) D_{fav}(z) \\ \Delta_T^0 D_{unf}(z) &= C_u z(1-z) D_{fav}(z) \end{aligned} \tag{5.66}$$

$$SET\ II: \begin{aligned} \Delta_T^0 D_{fav}(z) &= C_f z(1-z) D_{fav}(z) \\ \Delta_T^0 D_{unf}(z) &= C_u z(1-z) D_{unf}(z) \end{aligned} \tag{5.67}$$

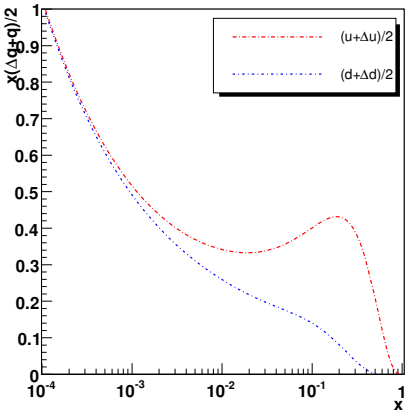

Figure 5.30: The limit for the transversity PDFs imposed by the Soffer bound for transversity distribution at Q^2 =2.41 (GeV/c)^2.

In the first set, the z dependence for both the Collins fragmentation functions is the same, only the magnitude is a free parameter; in the second set, the z dependence is different for the u and d-quark, dictated from the unpolarized fragmentation functions. Only the u and d-quarks have been considered in the numerator, while in the denominator also the $\bar{u}$ and $\bar{d}$ contributions are considered[2]. With these assumptions, eq. 5.62 and 5.63 read:

$$A^{p,\pi^+}_{Collins} = -\frac{4\Delta_T u \Delta^0_T D_{fav} + \Delta_T d \Delta^0_T D_{unf}}{4uD_{fav} + dD_{unf} + 4\bar{u}D_{unf} + \bar{d}D_{fav}} ; \quad (5.68)$$

$$A^{p,\pi^-}_{Collins} = -\frac{4\Delta_T u \Delta^0_T D_{unf} + \Delta_T d \Delta^0_T D_{fav}}{4uD_{unf} + dD_{fav} + 4\bar{u}D_{fav} + \bar{d}D_{unf}} . \quad (5.69)$$

The results quoted in the paper are the following:

$$SET\ I: \begin{aligned} C_f &= -0.29 \pm 0.04 \\ C_u &= 0.33 \pm 0.04 \end{aligned} \quad (5.70)$$

$$SET\ II: \begin{aligned} C_f &= -0.29 \pm 0.02 \\ C_u &= 0.56 \pm 0.07 \end{aligned} \quad (5.71)$$

to be compared with our results:

$$SET\ II: \begin{aligned} C_f &= -0.27 \pm 0.05 \\ C_u &= 0.31 \pm 0.05 \end{aligned} \quad (5.72)$$

[2]At variance with Sivers case, where $\bar{u}$ and $\bar{d}$ were neglected also in the denominator.

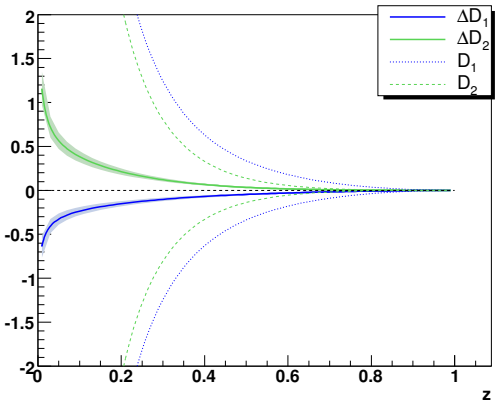

Figure 5.31: Extracted Collins fragmentation functions from the fit on HERMES data, using parametrization in eq. 5.67.

$$\begin{aligned} SET\,II: C_f &= -0.27 \pm 0.05 \\ C_u &= 0.50 \pm 0.08\ . \end{aligned} \tag{5.73}$$

The values are in good agreement for both sets, and the errors are larger according to the fact that we fit only the asymmetries depending on x, while in the paper also the data on z have been fitted. The extracted Collins fragmentation functions using the $SET\,II$ are in fig. 5.31. The fit describes well the HERMES data (fig. 5.32.a), and the predictions for COMPASS as a function of x are shown in fig. 5.32.b and are in agreement with the data. The predictions as a function of z for HERMES and COMPASS are also in good agreement with the data (fig. 5.33.a and 5.33.b), while the description of Belle data (fig. 5.33.c) is not satisfactory. In particular, the factor $(1-z)$ in the parametrization is needed in the description of SIDIS data since the asymmetries do not increase much with z, while the Belle asymmetries show an opposite behavior; this factor makes the predictions for all the Belle asymmetries close to zero.

If we assume that the transverse momentum of the hadron is not due only to the $\vec{p}_t$ dependence of the Collins FFs, and one takes into account also the initial $\vec{k}_t$ of the quark, the asymmetry formula 5.61 becomes [90, 83]:

$$A_{Collins}(x) = -\frac{\sum_q e_q^2 \cdot \Delta_T^0 D_q^h \cdot B_g \cdot \Delta_T q(x)}{\sum_q e_q^2 \cdot D_q^h \cdot q(x)}. \tag{5.74}$$

The term B_g is:

$$B_g(z) = \frac{1}{\sqrt{1 + z^2 \cdot \langle k_{\Delta q}^2 \rangle / \langle p_{\Delta D}^2 \rangle}}, \tag{5.75}$$

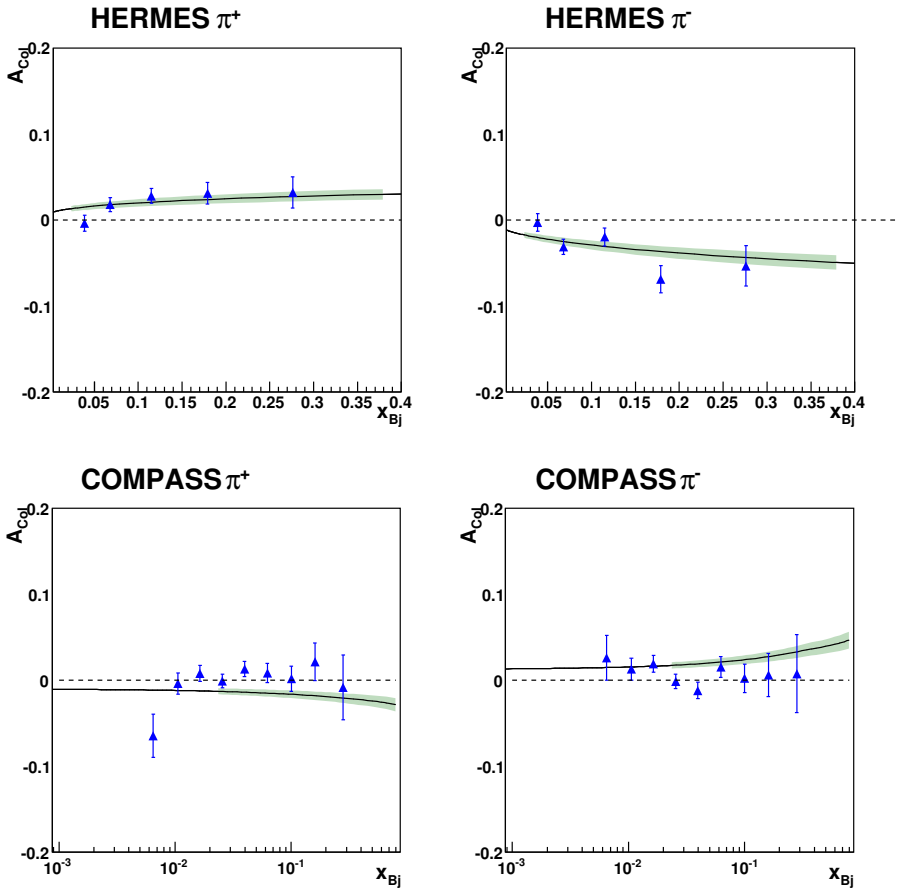

Figure 5.32: **a)** Result of the fit for HERMES data, using parametrization in eq. 5.67; **b)** prediction for COMPASS.

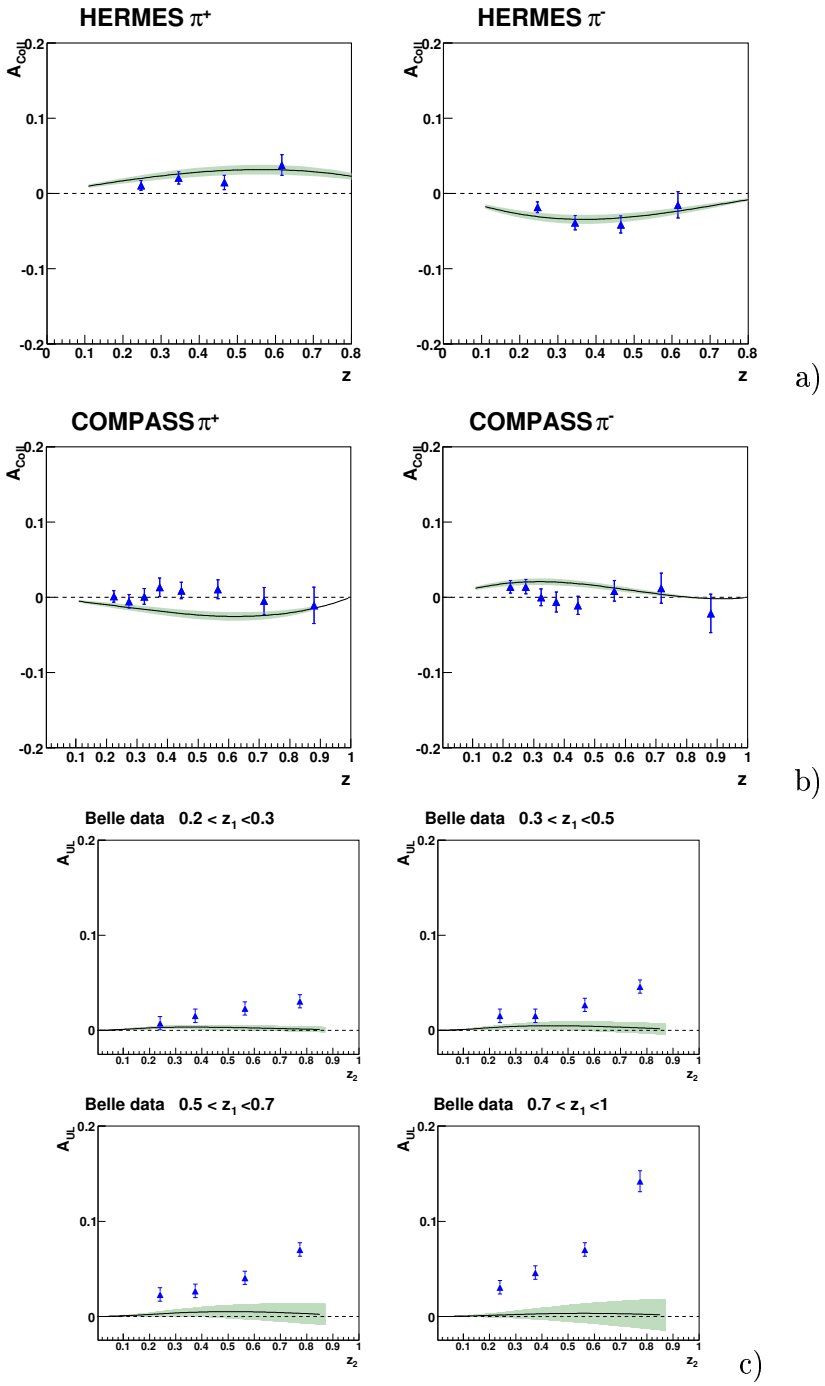

Figure 5.33: Prediction as a function of z using the extracted Collins fragmentation functions of fig. 5.31 for HERMES data (a), for COMPASS (b) and for Belle (c).

and since it decreases mildly with z, it describes the behavior of the SIDIS data without the need of including a term as $(1-z)$ in the parametrization for the Collins fragmentation functions. The terms $\langle k^2_{\Delta q}\rangle$ and $\langle p^2_{\Delta D}\rangle$ are respectively the widths of the Gaussian describing the transverse momentum dependence of the transversity and Collins fragmentation function, and are unknown. One approach is to fit them from data [90][3], or extract from data only the values $\langle B_g \cdot \Delta^0_T D\rangle$ where the mean is on the z range of the experiments [83]. Our approach is to assume that $\langle k^2_{\Delta q}\rangle \sim \langle p^2_{\Delta D}\rangle$, and consequently to put their ratio to 1 in the asymmetry formula.

For the Collins fragmentation functions we choose the parametrization:

$$\Delta^0_T D_a(z) \;=\; C_a z^\gamma (1-z)^\delta D_a(z), \;\; a = fav, unf \tag{5.76}$$

with the same γ and δ coefficients for the favored and unfavored Collins fragmentation functions. For the transversity distribution function, we choose the same parametrization used in the Sivers case:

$$\Delta_T q(x) \;=\; S_q x^\alpha (1-x)^\beta, \;\; q = u, d; \tag{5.77}$$

but in this case the α and β coefficients are the same for u and d. The reason why we consider α, β, γ and δ to be independent on flavor is to avoid too many free parameters in the fit. As in ref. [90], we perform a global fit of the data from COMPASS , HERMES and Belle. We use the COMPASS pion asymmetries presented in this thesis, the new HERMES and new Belle data. We consider only the transversity functions for u and d-quark, and the complete denominator in the asymmetry expression. We first perform a fit free from constraints, to see if the positivity limit for the Collins fragmentation functions and the Soffer bound for the transversity distribution function are naturally fulfilled. The parameters from the fit are the following:

$$\begin{aligned}
C_{fav} &= -0.08 \pm 0.02 & S_u &= 3.9 \pm 4.3 \\
C_{unf} &= 0.16 \pm 0.06 & S_d &= -4.3 \pm 4.8 \\
\gamma &= 0.01 \pm 0.20 & \alpha &= 0.49 \pm 0.39 \\
\delta &= -0.99 \pm 0.12 & \beta &= 2.7 \pm 2.1 \\
\chi^2/NDF &= 26.5/30 \sim 0.89;
\end{aligned} \tag{5.78}$$

and the corresponding curves are in fig. 5.34 and 5.35. The description of the data is good for all the experiments, but the d-quark transversity function strongly violates the corresponding Soffer bound; the u-quark transversity PDF and the Collins fragmentation functions violate mildly the corresponding limits only at high x and z, respectively. Including the constraint on all the functions in the fit, the

[3]More precisely, the transversity PDFs width is assumed to be the same of the unpolarized PDFs, while the width of the Collins FF is taken as $\langle p^2_{\Delta D_q}\rangle = (M^2 * \langle p^2\rangle)/(\langle p^2\rangle + M^2)$, with M free parameter of the fit.

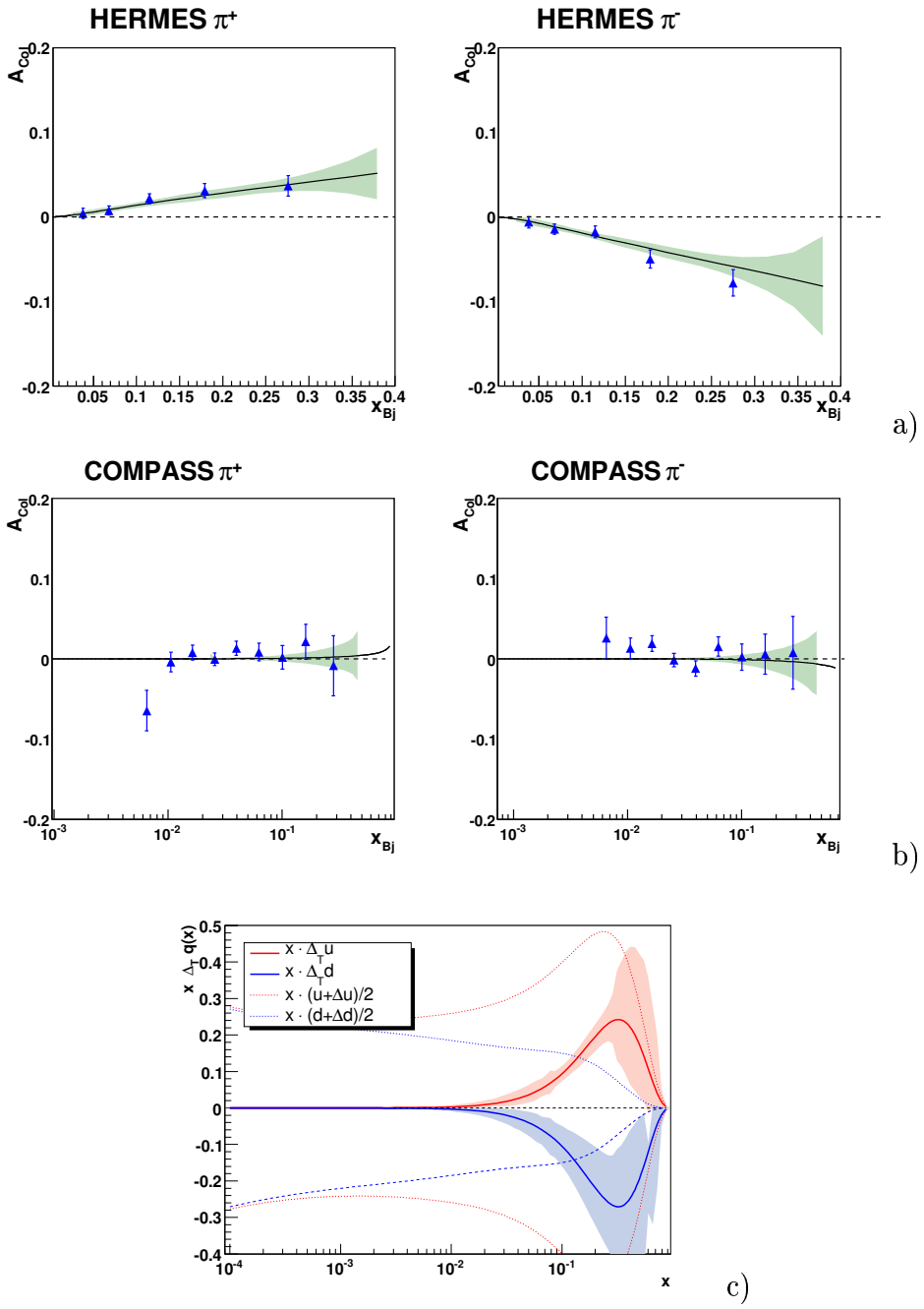

Figure 5.34: Result of the fit of HERMES (a) and COMPASS data (b) with parametrization of eq. 5.76 and 5.77; the resulting transversity functions for u and d-quark are shown in c: the dotted lines are the Soffer bound given by the unpolarized and polarized PDFs. The bands correspond to 1-σ error.

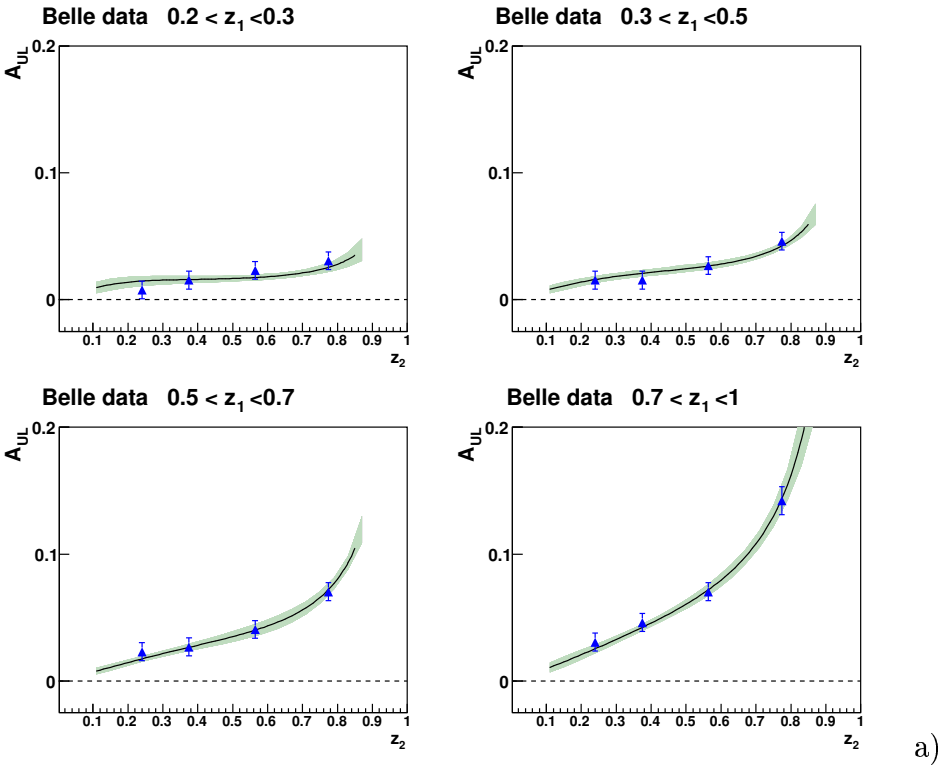

a)

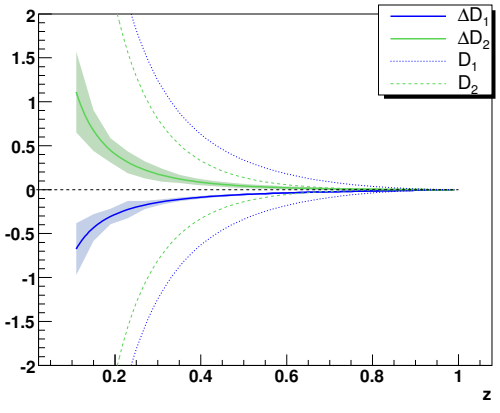

b)

Figure 5.35: Result of the fit of Belle (a) with parametrization of eq. 5.76 and 5.77; the resulting favored and unfavored Collins fragmentation functions are shown in c. The bands correspond to 1-σ error.

parameters are:

$$\begin{aligned} C_{fav} &= -0.087 \pm 0.018 & S_u &= 41 \pm 10 \\ C_{unf} &= 0.17 \pm 0.05 & S_d &= -11 \pm 1 \\ \gamma &= 0.04 \pm 0.18 & \alpha &= 1.28 \pm 0.12 \\ \delta &= -0.96 \pm 0.12 & \beta &= 6.55 \pm 0.18 \\ \chi^2/NDF &= 29.5/30 \sim 0.98. \end{aligned} \tag{5.79}$$

The description of the data is still rather good, as visible from fig. 5.36 and 5.37 and from the χ^2 of the fit. The parameters for the Collins fragmentation functions are very similar to those obtained with the unconstrained fit, since they almost fulfill the positivity constraint. On the contrary, the parameters for the u and d-quark have changed very much, as expected, since the violation of the Soffer bound for the d-quark was strong, and a change in the parameters for the d-quark is reflected in those for the u-quark since they have the same parametrization in the fit.

The extracted transversity distributions are different from zero and opposite in sign. Also the Collins FFs are opposite in sign, at variance with what was suggested by the new Belle data. The results are the first indication of the order of magnitude of the transversity PDFs and Collins FFs, but more data are needed in order to better constrain the different functions and to understand more deeply the data. In particular, the global fit performed can be improved including in the analysis also the asymmetries as function of z and P_T^h, taking into account the correlation between the different asymmetries, and the K data, that can also provide information on the sea quark transversity PDFs. Moreover, also COMPASS data on proton are needed in order to constrain better the transversity distributions. More data can be useful also in order to simplify the error analysis. In fact, at variance with the simpler Sivers case, the Lagrange method to extract the error bands has given some problems. The fit is highly non linear, and small variation of the parameters give huge fluctuation in the χ^2 value, even in the region around the minimum; as a result, it is difficult to follow the behavior of the χ^2 versus the function of which we are evaluating the error band. Thus the error bands shown in the fig. 5.34- 5.37 have to be considered as an indication of the size of the error.

In fig. 5.38 the transversity PDFs are compared to the unpolarized valence PDFs and polarized PDFs. It can be noted that the transversity PDFs are similar to the helicity PDFs, but smaller in size. This is an indication that the relativistic effects in the nucleon are important, since in absence of relativistic effects the transversity and helicity distributions would coincide. The transversity distributions evaluated from some models and extracted from the global fit of Anselmino *et al.* are shown in fig. 5.39.a.

In fig. 5.40, the integrals of the transversity distribution functions are shown. As already commented for the Sivers case (fig. 5.16) the integral values and their errors

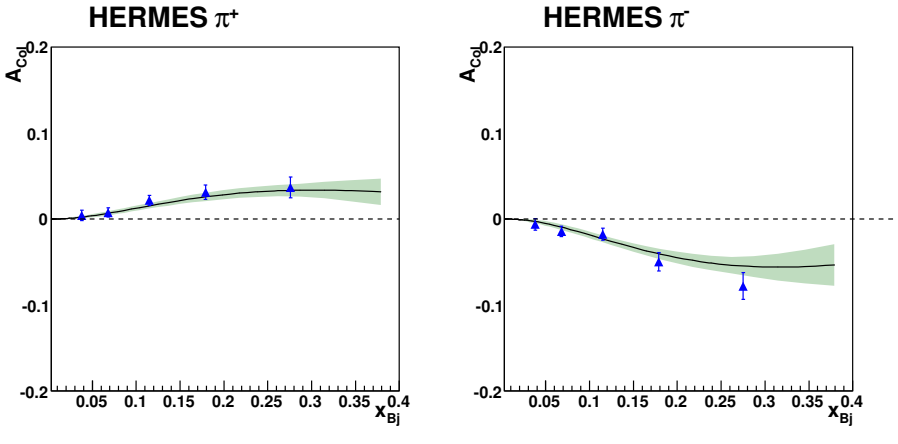

a)

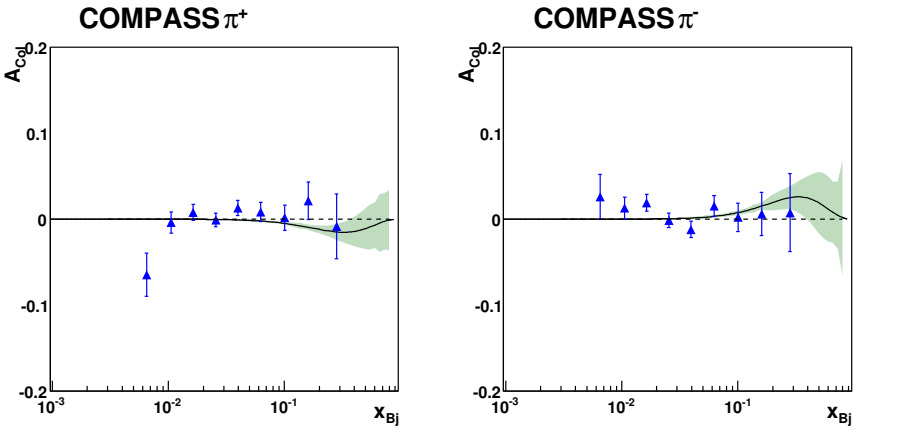

b)

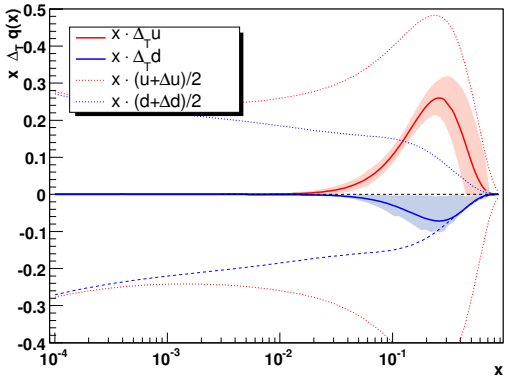

c)

Figure 5.36: Same as in fig. 5.34, but including the constraints on the transversity and Collins functions in the fit.

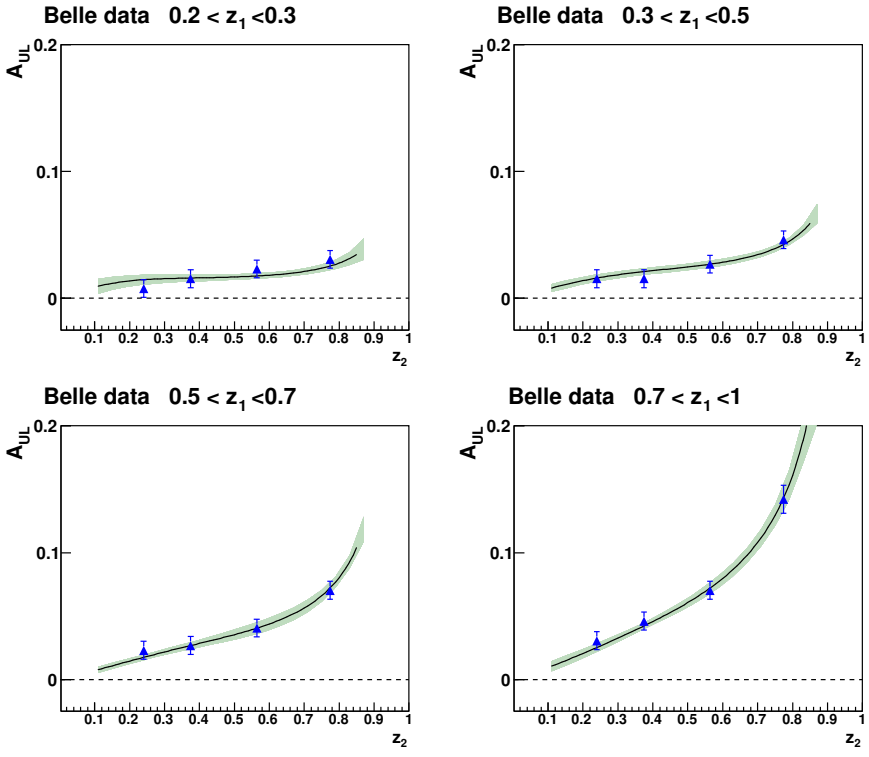

a)

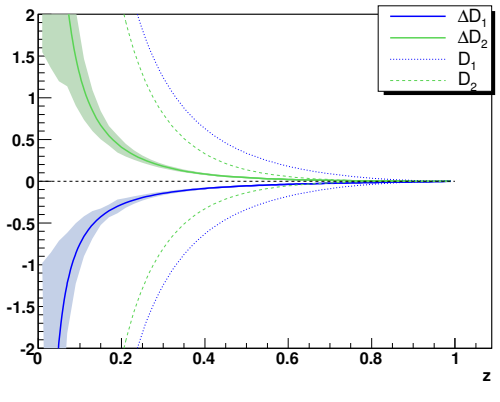

b)

Figure 5.37: Same as in fig. 5.35, but including the constraints on the transversity and Collins functions in the fit.

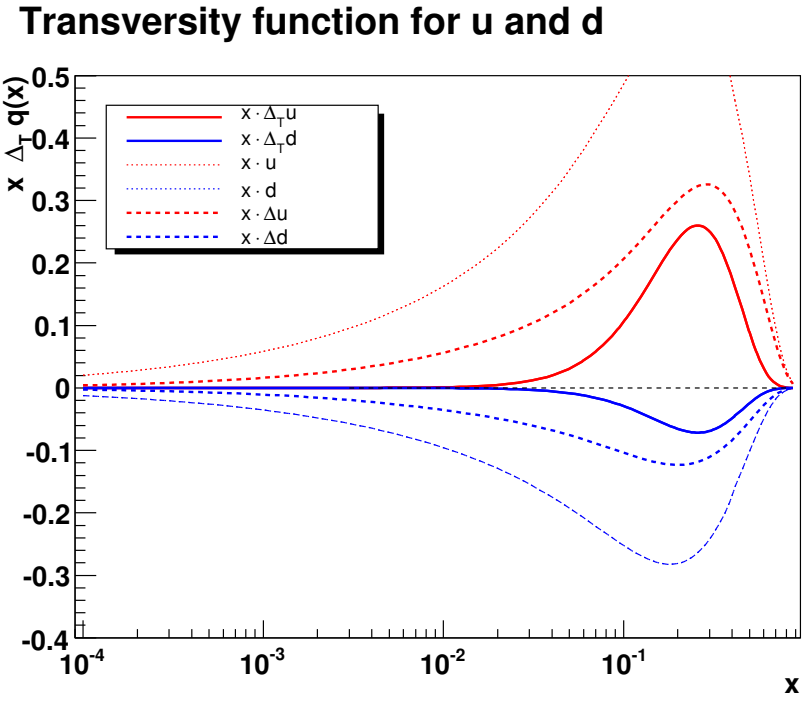

Figure 5.38: Comparison between the transversity PDFs for u and d-quark and the unpolarized valence and polarized PDFs (the unpolarized d-quark PDF is drawn with opposite sign for the comparison).

have to be considered only a rough estimation, since systematic effects are not taken into account. The integrals for the two transversity distributions are respectively:

$$\delta_u = \int_{0.01}^{0.9} dx\, \Delta_T u(x) \;=\; 0.39^{+0.14}_{-0.13}\ ;$$
$$\delta_d = \int_{0.01}^{0.9} dx\, \Delta_T d(x) \;=\; -0.11^{+0.11}_{-0.06}\ .$$

We can compare these integrals with values of the tensor charge (see section 1.2) from models assuming that the transversity PDFs for $\bar{u}$ and $\bar{d}$-quark are negligible with respect to those for the u and d-quark. In table 5.1, some values for the tensor charge evaluated with different models are reported: our results are marginally compatible with the predictions, that are all in agreement and higher in absolute value with respect to our result. Clearly, a precise determination of the first moment of the transversity PDFs would need more data at low as well as at high x.

The predictions as function of z for HERMES and COMPASS data are shown in fig. 5.41.a and 5.41.b respectively, and show a reasonably good agreement with the data.

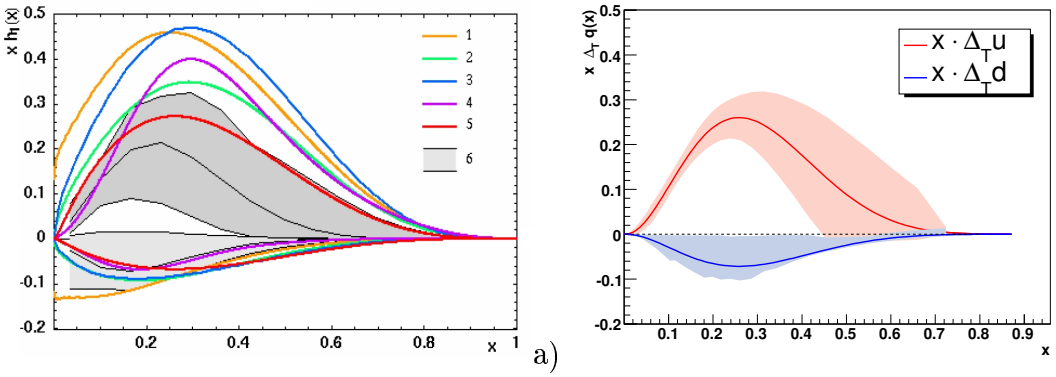

Figure 5.39: a) The transversity PDFs for u and d-quark from some models (curve 1: [92]; 2: [93]; 3: [94]; 4: [95]; 5: [96]) and extracted from the global fit of Anselmino *et al.* (6: [90]). Figure taken from [97]. b) the transversity PDFs for u and d-quark extracted in this work.

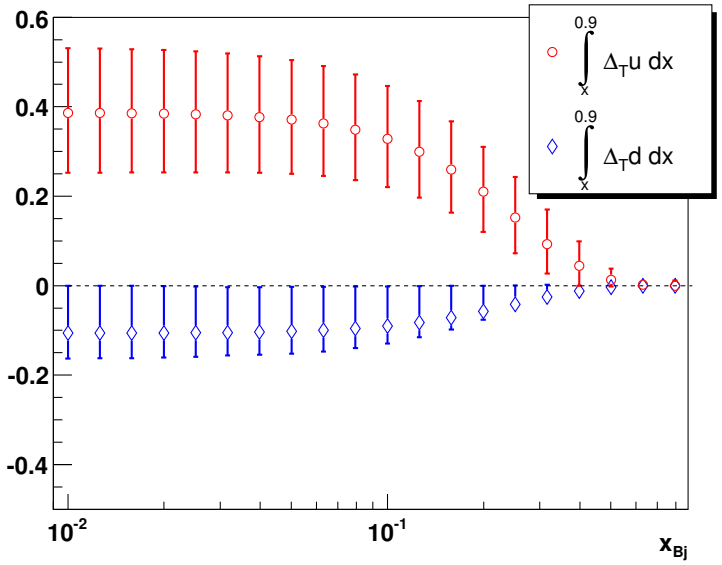

Figure 5.40: Integrals of the transversity PDF for the u and d-quark shown in figure 5.36.c. Each point correspond to the integral between the corresponding x value in abscissa and the maximum value of x allowed, fixed at 0.9.

	δ_u	δ_d
non relativistic quark model	0.97	-0.24
MIT bag model	0.99	-0.25
color-dielectric model	0.99	-0.25
chiral quark soliton model 1	0.97	-0.37
chiral quark soliton model 2	0.77	-0.29
chiral quark model	0.72	-0.13
light cone model	0.85	-0.21
spectator model	0.83	-0.17
lattice	0.80	-0.22

Table 5.1: Values for the tensor charge for u and d-quark evaluated at Q^2=10 (GeV/c)^2 in different models. The table is taken from [43].

Consideration about the fragmentation function and transversity signs

We have seen in the previous paragraph that the two Collins fragmentation functions have opposite signs, as well as the two transversity functions. Even if the relative sign is fixed from the fit, there is an ambiguity in the absolute signs of the functions: in fact, both the following possibilities :

$$\begin{aligned} I)\ \ & \Delta_T^0 D_{fav}(z) < 0 \qquad \Delta_T u(x) > 0 \\ & \Delta_T^0 D_{unf}(z) > 0 \qquad \Delta_T d(x) < 0 \end{aligned}$$

$$\begin{aligned} II)\ \ & \Delta_T^0 D_{fav}(z) > 0 \qquad \Delta_T u(x) < 0 \\ & \Delta_T^0 D_{unf}(z) < 0 \qquad \Delta_T d(x) > 0 \end{aligned}$$

result in the same sign of the asymmetries, as visible considering the numerators for the asymmetries on a proton and a deuterium target:

$$\begin{aligned} A_{Collins}^{p,\pi^+} &\sim -(4\Delta_T u \Delta_T^0 D_{fav} + \Delta_T d \Delta_T^0 D_{unf}) \\ A_{Collins}^{p,\pi^-} &\sim -(4\Delta_T u \Delta_T^0 D_{unf} + \Delta_T d \Delta_T^0 D_{fav}) \\ A_{Collins}^{d,\pi^+} &\sim (\Delta_T u + \Delta_T d)(4\Delta_T^0 D_{fav} + \Delta_T^0 D_{unf}) \\ A_{Collins}^{d,\pi^-} &\sim (\Delta_T u + \Delta_T d)(4\Delta_T^0 D_{unf} + \Delta_T^0 D_{fav}) \ . \end{aligned}$$

As regards the Belle data, we have already commented how the relative sign of the Collins fragmentation functions cannot be determined from these data.

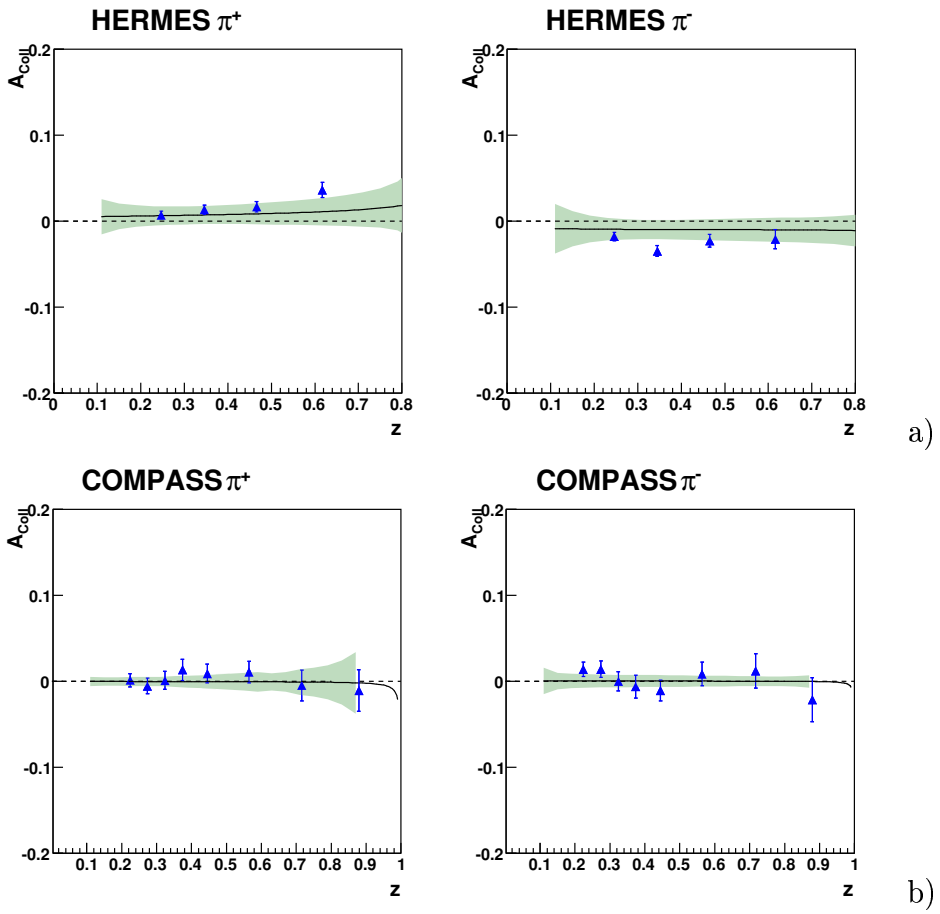

Figure 5.41: Prediction as function of z for HERMES (a) and COMPASS data (b), using the extracted transversity PDFs and Collins FFs of fig. 5.36 and 5.37.

Effect of COMPASS data in the fit

We have seen that from the new Belle data it is possible to determine a relationship between the favored and unfavored Collins FFs, but not their relative sign. In particular, assuming their relative size to be more or less the same, we have the two possibilities: $\Delta_T^0 D_{fav} \sim \pm \Delta_T^0 D_{unf}$. The solution with both the FFs with equal sign is not in agreement with HERMES results, since it implies the asymmetries on π^+ and π^- to be the same:

$$\begin{aligned} A_{Collins}^{p,\pi^+} &\sim -\Delta_T^0 D_{fav}(4\Delta_T u + \Delta_T d) \\ A_{Collins}^{p,\pi^-} &\sim -\Delta_T^0 D_{fav}(4\Delta_T u + \Delta_T d) \end{aligned}$$

while the HERMES asymmetries are positive for π^+ and negative for π^-. On the contrary, the solution with the Collins FFs with opposite signs brings the following

asymmetries for HERMES :

$$A_{Collins}^{p,\pi^+} \sim -\Delta_T^0 D_{fav}(4\Delta_T u - \Delta_T d)$$
$$A_{Collins}^{p,\pi^-} \sim -\Delta_T^0 D_{fav}(-4\Delta_T u + \Delta_T d)$$

in agreement with the data.

The $\Delta_T d$ contribution in the above formulas is smaller than the $\Delta_T u$, due to the factor 4 in front of $\Delta_T u$; so the sign of $\Delta_T u$ must be opposite to that of $\Delta_T^0 D_{fav}$ (as we have from the result of the global fit), but we cannot determine which sign it is, an ambiguity that, as already commented, cannot be solved even including the COMPASS data in the fit.

To understand in an intuitive way the effect of the COMPASS data in the fit, we performed the fit of HERMES and Belle asymmetries only. The fit is unstable, and gives different solutions depending on the initial value of the parameters. This can be understood since on a proton target the $\Delta_T d$ cannot be constrained, due to the dominant contribution of the u-quark. The result of COMPASS on a deuterium target implies the further constraint $\Delta_T d \sim -\Delta_T u$, meaning that the sign for the d-quark transversity PDF is opposite to that of the u-quark, and that the size of the two PDFs has to be more or less the same. With this additional condition, the fit has only one solution and the functions can be extracted.

5.5 Predictions for COMPASS proton data

In 2007 COMPASS has taken data using a NH_3 target. The statistics collected should allow to measure the Sivers and Collins asymmetries with the same error bars of the asymmetries measured on a deuterium target, taking into account the different dilution factor and the different reachable polarization value of the two materials (f ~0.38 and 0.17 , P ~0.50 and 0.80, respectively for LiD_6 and NH_3). Assuming that both the Sivers and the Collins effects have the same magnitude at different Q^2, we are able to predict the size of the asymmetries for COMPASS. The predictions as a function of x are shown in fig. 5.42.a for Sivers asymmetries and in fig. 5.42.b for Collins asymmetries. The curves are compared with the asymmetries curves for HERMES resulting from the fit (for the Collins case, the curves for HERMES have been changed in sign and have not been multiplied by the D_{NN} factor to help in the comparison). Both the Sivers and the transversity PDFs are the same for COMPASS and HERMES, since no evolution with Q^2 has been taken into account in the fit. The unpolarized PDFs and the FFs in the denominator have been evaluated at the two different mean Q^2 values (Q^2 =3.5 $(GeV/c)^2$ for COMPASS and Q^2 =2.4 $(GeV/c)^2$ for HERMES), as well as the FFs and the Collins FFs in the numerator. The different integration range in z for the FFs has been taken into account. The prediction for COMPASS are very similar to the result obtained from

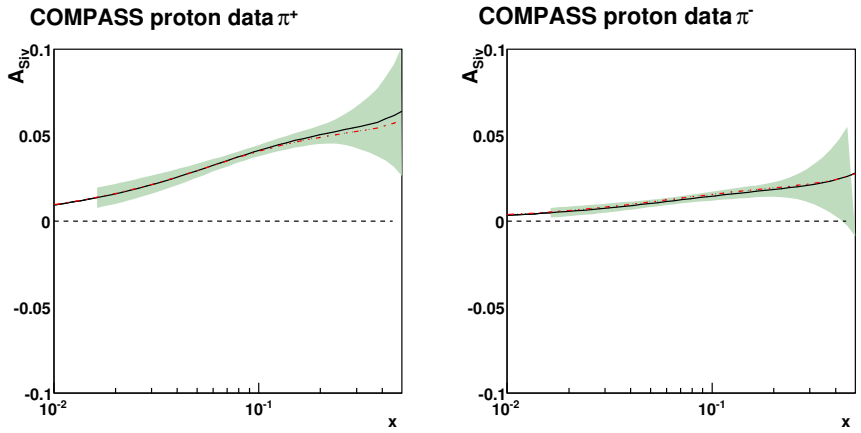

a)

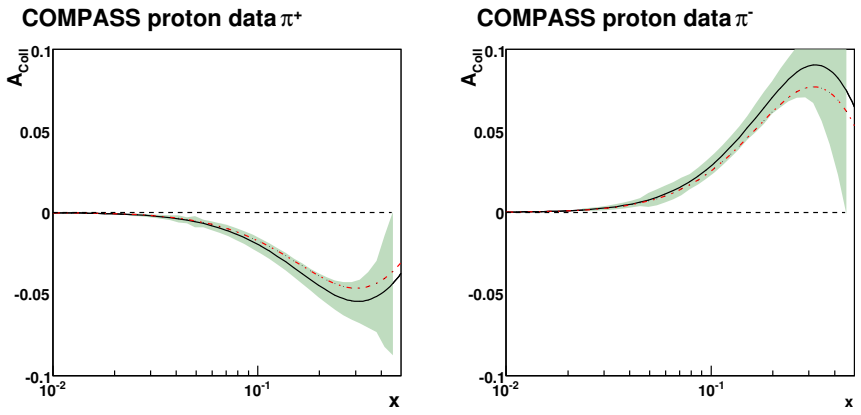

b)

Figure 5.42: Prediction as function of x for COMPASS measuring on a proton target the Sivers asymmetries (a) and the Collins asymmetries (b). The dashed lines are the curves for HERMES data obtained from the fit (fig. 5.12 and 5.36).

HERMES on a proton target. The comparison between the measured asymmetries and the predictions will be interesting in order to understand the Q^2 dependence of the transverse spin effects, confirming or not that the approach followed in this work of interpretation of the results is correct.

Conclusions and outlook

In the years 2002-2004 the COMPASS experiment took data with a μ^+ beam of 160 GeV/c and a transversely polarized ^{6}LiD target to measure transverse spin effects in SIDIS, a topic which received much attention in the last years, both from the theoretical and from the experimental side. The study of these effects is considered of great importance in the field of spin physics, a really new territory.

Results for the Collins and Sivers asymmetries for not identified hadrons have already been published. In this thesis the same asymmetries have been evaluated for charged pions and kaons, identified using the RICH-1 detector of the experiment. This work has required a deep understanding of the experimental technique, of the COMPASS spectrometer and the full analysis chain. A good knowledge of the RICH-1 response during data taking has been necessary in order to tune the cuts used to identify the hadrons and to keep under control the systematic of the measurement. This last aspect is of big importance since the effect one wants to measure is very small. For this reasons, an extensive study of the RICH-1 performances has been performed, ranging from the stability in time of the detector, to the evaluation of the purity of the K sample. All the systematic effects which could bias the results have been evaluated, with the conclusion that the systematic errors are smaller than the statistical ones.

As in the case for the not identified charged hadrons, the measured asymmetries for both the pion and the kaon samples are small, and compatible with zero within the statistical errors, at variance with the non zero Sivers and Collins asymmetries measured by HERMES on a proton target at lower energy. These results can be explained with the hypothesis that in a deuterium target there is a cancellation between the neutron and the proton asymmetries.

The last part of the thesis has been dedicated to a first global analysis of all the existing data related to the Collins and Sivers asymmetries for charged pions, namely the results presented in this thesis, and the HERMES and the Belle measurements. The Belle measurements have highlighted a non zero correlation between the azimuthal angles of the hadrons produced in e^+e^- annihilation, and give convincing and independent evidence of the Collins FFs being non zero.

The method used to fit all the data in order to extract the transversity and Sivers parton distribution functions is based on a χ^2 method, built comparing the measured

asymmetries with the corresponding theoretical expression. The parameterizations of the PDFs and FF have been chosen to be simple, mainly because of the few experimental points available. No systematic errors have been taken into account in the fitting procedure at this stage.

From the flavor separation analysis for the Sivers effect, we can draw the following conclusions:

- the impact of the COMPASS data is clearly visible considering the analysis using only HERMES data, in which the d-quark Sivers function results to be bigger than that of the u-quark; the comparison between the analysis of HERMES and both HERMES and COMPASS shows also that the data sets from the two experiments are marginally compatible, an effect that can be due to the over simplified analysis;

- in spite of the simplicity of the model which has been used in the interpretation of the data, which assumes that the hadron transverse momentum is due to the $\vec{k}_T$ of the quark, the description of the data is satisfactory and the predictions of the asymmetries as a function of z are in good agreement with the data;

- the Sivers functions for the u and the d-quark turn out to have opposite signs and similar size; this result is in agreement with the large-N_C QCD limit;

- the integrals of the Sivers functions are in agreement with the Burkardt sum rule. This is also in agreement with Brodsky argument, that the gluon orbital angular momentum in the nucleon should be zero;

- the positivity bound for the u-quark Sivers function is naturally fulfilled; while for the d-quark it is slightly violated at large x, where in any case there are no data points.

As regards the Collins FF, a quite interesting quantity by itself, it has been shown that the new, very precise Belle data allow to extract the ratio between the favored and unfavored Collins fragmentation functions. The Belle data do not allow to determine the sign of the Collins FFs but this ambiguity can be solved analyzing these data together with the SIDIS data. Indeed Belle data are necessary in the global analysis since the SIDIS data alone do not allow the extraction of both the transversity distribution functions and the Collins FF.

Due to the higher complexity of the Collins global analysis with respect to the Sivers one, parameterizations with less free parameters for the unknown distribution have been used. The conclusions from this analysis are the following:

- the favored and the unfavored Collins fragmentation functions have opposite signs and similar size; the positivity constraint is naturally fulfilled by both FFs;

- the COMPASS measurements of zero asymmetries on a deuterium target allow to extract the transversity PDF for d-quark, that is not constrained by HERMES and Belle data;

- the transversity functions for u and d-quark have opposite signs; the Soffer bound for the u-quark is naturally fulfilled, while the d-quark considerably violates the Soffer bound; the description of the data is slightly worse if we impose the constraint for the d-quark in the fit, but is still satisfactory;

- despite the considerably range of COMPASS data, the determination of the first moment of the transversity PDF is not yet possible: low x measurements for proton (COMPASS) are still needed as well as high x data for both proton and neutron; hopefully JLab will provide that in near future.

The work done has shown that it is already possible to extract important information on the transversity and Sivers distribution from the available data. Even if the knowledge about these functions is increasing considerably, still the road for a complete understanding of the Collins and Sivers effects is long. A more refined and complete analysis with respect to the one presented in this thesis, and respect to the analyses existing in the literature, is needed in order to gather more precise information. The use in the fit of different parametrization for parton distribution functions and fragmentation function can give a hint for a source of systematic effects of the analysis, as well as the inclusion of the systematic errors from the experiments. One of the points where the analysis can be improved is the inclusion in the fit of all the measured SIDIS asymmetries, as a function of x,z, and P_T^h, after having taken into account the correlation between the different measurements. The inclusion in the global analysis of the K data both from COMPASS and HERMES might possibly allow a first extraction of the functions for the strange quarks, presently not known.

In the future more information on transversity can be obtained by including in the global analysis the two-π asymmetries already measured at HERMES on protons and at COMPASS on deuterium. The "interference" fragmentation function is being measured by the Belle Collaboration, therefore the two-π asymmetries measured in SIDIS will allow independent extraction of transversity. Information on the energy dependence of the measured effects will be provided by COMPASS data on a proton target, taken in 2007, and still to be analyzed. In the same line, also the SIDIS measurements with a transversely polarized target foreseen at JLab (with beam energy of 6 and 12 GeV) will bring complementary information. Moreover these measurements will provide a global view on the transverse spin effects in SIDIS, providing information also on the other TMD parton distribution functions and fragmentation functions. All these data conclude the exploring part of the SIDIS measurements, that has the big advantage, with respect to the Drell-Yann processes, to allow a flavor separation analysis. Obviously, to reach a knowledge of transversity

distribution function at the same level of the helicity distribution function, more data with a better precision will be needed in a second phase.

Bibliography

[1] J. Ashman *et al.* [European Muon Collaboration], Nucl. Phys. B **328**, 1 (1989).

[2] J. P. Ralston and D. E. Soper, Nucl. Phys. B **152**, 109 (1979).

[3] X. Artru and M. Mekhfi, Z. Phys. C **45**, 669 (1990).

[4] R. L. Jaffe and X. D. Ji, Phys. Rev. Lett. **67**, 552 (1991).

[5] G. Bunce *et al.*, Phys. Rev. Lett. **36**, 1113 (1976).

[6] J. Antille *et al.*, Phys. Lett. B **94**, 523 (1980).

[7] B. A. Khachaturov *et al.*, *In *Protvino 1986, Proceedings, High energy spin physics, vol. 2*, 83-85.*

[8] D. L. Adams *et al.* [FNAL-E704 Collaboration], Phys. Lett. B **264**, 462 (1991); A. Bravar *et al.* [FNAL E704 Collaboration], Phys. Rev. Lett. **77**, 2626 (1996).

[9] G. Bunce *et al.*, Part. World **3**, 1 (1993).

[10] The HELP Collaboration, B. Vuaridel *et al.*, CERN reports LEPC 93-14, LEPC/P7 (1993).

[11] J. Adams *et al.* [STAR Collaboration], Phys. Rev. Lett. **92**, 171801 (2004) [arXiv:hep-ex/0310058].

[12] D. W. Sivers, Phys. Rev. D **41**, 83 (1990).

[13] J. C. Collins, Nucl. Phys. B **396**, 161 (1993) [arXiv:hep-ph/9208213].

[14] P. J. Mulders and R. D. Tangerman, Nucl. Phys. B **461**, 197 (1996) [Erratum-ibid. B **484**, 538 (1997)] [arXiv:hep-ph/9510301].

[15] D. Boer, Phys. Rev. D **60**, 014012 (1999) [arXiv:hep-ph/9902255].

[16] U. D'Alesio and F. Murgia, Phys. Rev. D **70**, 074009 (2004) [arXiv:hep-ph/0408092].

[17] K. Abe *et al.* [Belle Collaboration], Phys. Rev. Lett. **96**, 232002 (2006) [arXiv:hep-ex/0507063].

[18] V. Y. Alexakhin *et al.* [COMPASS Collaboration], Phys. Rev. Lett. **94**, 202002 (2005) [arXiv:hep-ex/0503002].

[19] E. S. Ageev *et al.* [COMPASS Collaboration], Nucl. Phys. B **765**, 31 (2007) [arXiv:hep-ex/0610068].

[20] M. Anselmino, A. Efremov, E. Leader, Phys. Rep. 261, 1 (1995).

[21] E. Leader and E. Predazzi, "An Introduction to Gauge Theories and the New Physics", Cambridge University Press (1985).

[22] S. Chekanov *et al.* [ZEUS Collaboration], Eur. Phys. J. C **21**, 443 (2001) [arXiv:hep-ex/0105090]; S. Chekanov *et al.* [ZEUS Collaboration], Phys. Rev. D **70**, 052001 (2004) [arXiv:hep-ex/0401003].

[23] C. Adloff *et al.* [H1 Collaboration], Eur. Phys. J. C **21**, 33 (2001) [arXiv:hep-ex/0012053]; C. Adloff *et al.* [H1 Collaboration], Eur. Phys. J. C **30**, 1 (2003) [arXiv:hep-ex/0304003].

[24] L. W. Whitlow, E. M. Riordan, S. Dasu, S. Rock and A. Bodek, Phys. Lett. B **282**, 475 (1992).

[25] A. C. Benvenuti *et al.* [BCDMS Collaboration], Phys. Lett. B **223**, 485 (1989).

[26] M. R. Adams *et al.* [E665 Collaboration], Phys. Rev. D **54**, 3006 (1996).

[27] M. Arneodo *et al.* [New Muon Collaboration], Nucl. Phys. B **483**, 3 (1997) [arXiv:hep-ph/9610231].

[28] W. M. Yao *et al.* [Particle Data Group], J. Phys. G **33**, 1 (2006).

[29] P. L. Anthony *et al.* [E142 Collaboration], Phys. Rev. D **54**, 6620 (1996) [arXiv:hep-ex/9610007].

[30] K. Abe *et al.* [E143 collaboration], Phys. Rev. D **58**, 112003 (1998) [arXiv:hep-ph/9802357].

[31] K. Abe *et al.* [E154 Collaboration], Phys. Rev. Lett. **79**, 26 (1997) [arXiv:hep-ex/9705012].

[32] P. L. Anthony *et al.* [E155 Collaboration], Phys. Lett. B **463**, 339 (1999) [arXiv:hep-ex/9904002]; P. L. Anthony *et al.* [E155 Collaboration], Phys. Lett. B **493**, 19 (2000) [arXiv:hep-ph/0007248].

[33] X. Zheng *et al.* [Jefferson Lab Hall A Collaboration], Phys. Rev. C **70**, 065207 (2004) [arXiv:nucl-ex/0405006].

[34] A. Airapetian *et al.* [HERMES Collaboration], Phys. Lett. B **442**, 484 (1998) [arXiv:hep-ex/9807015]; K. Ackerstaff *et al.* [HERMES Collaboration], Phys. Lett. B **404**, 383 (1997) [arXiv:hep-ex/9703005].

[35] B. Adeva *et al.* [Spin Muon Collaboration], Phys. Rev. D **58**, 112002 (1998); B. Adeva *et al.* [Spin Muon Collaboration], Phys. Rev. D **60**, 072004 (1999) [Erratum-ibid. D **62**, 079902 (2000)].

[36] E. S. Ageev *et al.* [COMPASS Collaboration], Phys. Lett. B **612**, 154 (2005) [arXiv:hep-ex/0501073].

[37] P. L. Anthony *et al.* [E155 Collaboration], Phys. Lett. B **458**, 529 (1999) [arXiv:hep-ex/9901006].

[38] P. L. Anthony *et al.* [E155 Collaboration], Phys. Lett. B **553**, 18 (2003) [arXiv:hep-ex/0204028].

[39] J. Ashman *et al.* [European Muon Collaboration], Phys. Lett. B **206**, 364 (1988).

[40] B. Adeva *et al.* [Spin Muon Collaboration], Phys. Rev. D**58**, 112001 (1998).

[41] G. Altarelli and G. Parisi, Nucl. Phys. B **126**, 298 (1977); V. N. Gribov and L. N. Lipatov, Sov. J. Nucl. Phys. **15**, 438 (1972) [Yad. Fiz. **15**, 781 (1972)]; Y. L. Dokshitzer, Sov. Phys. JETP **46**, 641 (1977) [Zh. Eksp. Teor. Fiz. **73**, 1216 (1977)].

[42] G. Altarelli and G. G. Ross, Phys. Lett. B **212**, 391 (1988).

[43] V.Barone, P. G. Ratcliffe, "Transverse spin physics", World Scientific (2003).

[44] J. Soffer, Phys. Rev. Lett. **74**, 1292 (1995) [arXiv:hep-ph/9409254].

[45] B. L. G. Bakker, E. Leader and T. L. Trueman, Phys. Rev. D **70**, 114001 (2004) [arXiv:hep-ph/0406139].

[46] S. Kretzer, Phys. Rev. D **62**, 054001 (2000) [arXiv:hep-ph/0003177].

[47] B. A. Kniehl, G. Kramer and B. Potter, Phys. Rev. Lett. **85**, 5288 (2000) [arXiv:hep-ph/0003297].

[48] D. de Florian, R. Sassot and M. Stratmann, Phys. Rev. D **75**, 114010 (2007) [arXiv:hep-ph/0703242]; Phys. Rev. D **76**, 074033 (2007) [arXiv:0707.1506 [hep-ph]].

[49] A. Bacchetta, M. Diehl, K. Goeke, A. Metz, P. J. Mulders and M. Schlegel, JHEP **0702**, 093 (2007) [arXiv:hep-ph/0611265].

[50] V. Barone, A. Drago and P. G. Ratcliffe, Phys. Rept. **359**, 1 (2002) [arXiv:hep-ph/0104283].

[51] S. J. Brodsky, D. S. Hwang and I. Schmidt, Phys. Lett. B **553**, 223 (2003) [arXiv:hep-ph/0211212].

[52] J. C. Collins, Phys. Lett. B **536**, 43 (2002) [arXiv:hep-ph/0204004].

[53] A. V. Belitsky, X. Ji and F. Yuan, Nucl. Phys. B **656**, 165 (2003) [arXiv:hep-ph/0208038].

[54] M. Burkardt, Phys. Rev. D **69**, 091501 (2004) [arXiv:hep-ph/0402014].

[55] M. Burkardt, Phys. Rev. D **69**, 057501 (2004) [arXiv:hep-ph/0311013].

[56] A. Airapetian *et al.* [HERMES Collaboration], Phys. Rev. Lett. **94**, 012002 (2005) [arXiv:hep-ex/0408013].

[57] L. Pappalardo [HERMES Collaboration], *Prepared for 14th International Workshop on Deep Inelastic Scattering (DIS 2006), Tsukuba, Japan, 20-24 Apr 2006*; proceedings World Scientific (2007), 667.

[58] M. Diefenthaler [HERMES Collaboration], proceedings of DIS 2007, page 579; arXiv:0706.2242 [hep-ex].

[59] P. Abbon *et al.* [COMPASS Collaboration], Nucl. Instrum. Meth. A **577**, 455 (2007) [arXiv:hep-ex/0703049].

[60] E. Albrecht *et al.*, Nucl. Instr. and Meth. A 553, 215 (2005), and references therein.

[61] E. Albrecht *et al.*, Nucl. Instr. and Meth. A 502, 266 (2003).

[62] E. Albrecht *et al.*, Nucl. Instr. and Meth. A 502, 236 (2003).

[63] E. Albrecht *et al.*, Nucl. Instr. and Meth. A 502, 112(2003).

[64] E. Albrecht *et al.*, Nucl. Instr. and Meth. A 518, 586 (2004).

[65] J. Seguinot, G. Charpak, Y. Giomataris, V. Peskov, J. Tischhauser and T. Ypsilantis, Nucl. Instrum. Meth. A **297**, 133 (1990).

[66] G. Malamud, P. Mine, D. Vartsky, B. Equer, A. Breskin and R. Chechik, Nucl. Instrum. Meth. A **343**, 121 (1994).

[67] J. C. Santiard *et al.*, GASSIPLEX: a low noise analog signal processor for read-out of gaseous detectors, presented at the 6th Pisa Meeting on Advanced Detectors, La Biodola, Isola d'Elba, Italy (1994).

[68] G. Baum *et al.*, Nucl. Instr. and Meth. A 502, 315 (2003).

[69] T. Ypsilantis, J. Seguinot, Nucl. Instr. and Meth. A 343, 30 (1994).

[70] F. Sozzi on behalf of the [COMPASS Collaboration], "Transversity signals at COMPASS ", *presented for 13th International Conference In Quantum Chromodynamics (QCD06)*; Nucl. Phys. B **174C**, 47 (2007).

[71] X. Artru, "The transverse spin", Proceedings of 10th Rhodanien Seminar, [arXiv:hep-ph/0207309].

[72] B. Parsamyan [COMPASS Collaboration], arXiv:0709.3440 [hep-ex].

[73] F. James and M. Roos, Comput. Phys. Commun. **10**, 343 (1975).

[74] R. Brun and F. Rademakers, Nucl. Instrum. Meth. A **389**, 81 (1997).

[75] R. Brun, O. Couet, C. E. Vandoni and P. Zanarini, Comput. Phys. Commun. **57**, 432 (1989).

[76] D. Stump *et al.*, Phys. Rev. D **65**, 014012 (2002) [arXiv:hep-ph/0101051].

[77] J. Pumplin, D. R. Stump and W. K. Tung, Phys. Rev. D **65**, 014011 (2002) [arXiv:hep-ph/0008191].

[78] R. Brock, D. Casey, J. Huston, J. Kalk, J. Pumplin, D. Stump and W. K. Tung, arXiv:hep-ph/0006148.

[79] M. Gluck, E. Reya and A. Vogt, Eur. Phys. J. C **5**, 461 (1998) [arXiv:hep-ph/9806404].

[80] M. Gluck, E. Reya, M. Stratmann and W. Vogelsang, Phys. Rev. D **63**, 094005 (2001) [arXiv:hep-ph/0011215].

[81] W. Vogelsang and F. Yuan, Phys. Rev. D **72**, 054028 (2005) [arXiv:hep-ph/0507266].

[82] J. C. Collins, A. V. Efremov, K. Goeke, S. Menzel, A. Metz and P. Schweitzer, Phys. Rev. D **73**, 014021 (2006) [arXiv:hep-ph/0509076]. J. C. Collins *et al.*, arXiv:hep-ph/0510342.

[83] A. V. Efremov, K. Goeke and P. Schweitzer, Phys. Rev. D **73**, 094025 (2006) [arXiv:hep-ph/0603054].

[84] M. Anselmino, M. Boglione, U. D'Alesio, A. Kotzinian, F. Murgia and A. Prokudin, Phys. Rev. D **71**, 074006 (2005) [arXiv:hep-ph/0501196]. M. Anselmino, M. Boglione, U. D'Alesio, A. Kotzinian, F. Murgia and A. Prokudin, Phys. Rev. D **72**, 094007 (2005) [Erratum-ibid. D **72**, 099903 (2005)] [arXiv:hep-ph/0507181].

[85] P. V. Pobylitsa, arXiv:hep-ph/0301236.

[86] A. V. Efremov, K. Goeke, S. Menzel, A. Metz and P. Schweitzer, Phys. Lett. B **612**, 233 (2005) [arXiv:hep-ph/0412353].

[87] S. J. Brodsky and S. Gardner, Phys. Lett. B **643**, 22 (2006) [arXiv:hep-ph/0608219].

[88] S. Albino, B.A. Kniehl, and G. Kramer, Nucl. Phys. B725, 181 (2005); B734,50 (2006).

[89] U. Elschenbroich, Ph.D. thesis, "Transverse Spin Structure of the Proton Studied in Semi-inclusive DIS ", Universiteit Gent, Feb 2006.

[90] M. Anselmino, M. Boglione, U. D'Alesio, A. Kotzinian, F. Murgia, A. Prokudin and C. Turk, Phys. Rev. D **75**, 054032 (2007) [arXiv:hep-ph/0701006].

[91] A. Ogawa, M. Grosse Perdekamp, R. C. Seidl and K. Hasuko [Belle Collaboration], AIP Conf. Proc. **915**, 575 (2007).

[92] J. Soffer, M. Stratmann and W. Vogelsang, Phys. Rev. D **65**, 114024 (2002) [arXiv:hep-ph/0204058].

[93] V. A. Korotkov, W. D. Nowak and K. A. Oganesian, Eur. Phys. J. C **18**, 639 (2001) [arXiv:hep-ph/0002268].

[94] P. V. Pobylitsa and M. V. Polyakov, Phys. Lett. **B 389** (1996) 350 [arXiv:hep-ph/9608434].
P. Schweitzer, D. Urbano, M. V. Polyakov, C. Weiss, P. V. Pobylitsa and K. Goeke, Phys. Rev. D **64**, 034013 (2001) [arXiv:hep-ph/0101300]. AIP Conf. Proc. **549**, 659 (2002).

[95] M. Wakamatsu, Phys. Lett. B **509**, 59 (2001) [arXiv:hep-ph/0012331].

[96] B. Pasquini, M. Pincetti and S. Boffi, Phys. Rev. D **72**, 094029 (2005) [arXiv:hep-ph/0510376].

[97] A. Bacchetta, "Transversity: present and future"; talk given at ECT* Workshop Transverse momentum, spin, and position distributions of partons in hadrons, Trento, Italy, 11 - 15 June, 2007.

Acknowledgments

I would like to thank prof. Paolo Schiavon, my PhD tutor and supervisor of my thesis, who has always followed my activity in these years and who has taught me a lot, both from the scientific and from the human point of view. I would like to thank prof. Anna Martin, supervisor of this thesis, who has introduced me to the transverse spin physics: thanks for all the discussions and explanations and for her enthusiasm on the subject.

Thanks to all colleagues of the Trieste COMPASS group guided and coordinated by prof. Franco Bradamante, thanks for the friendly atmosphere and for all their support. Thanks to Silvia Dalla Torre and Fulvio Tessarotto for coordinating my work during the first year of PhD, thanks for all the time spent for many explanations. Thanks to Elena Rocco and Marco Apollonio for the amusing laboratory sessions. Thanks to Andrea Bressan, for his help when I was starting the analysis work and for his support. Thanks to Renato Birsa and Benigno Gobbo for being always ready to solve any computing problem. Thanks to all the people with whom I share the office: Vinicio Duic, Giulia Pesaro, Giulio Sbrizzai and Stefano Levorato.

Thanks to all COMPASS people with whom I have worked along these years, in particular thanks to Roland Windmolders for the discussions about the error analysis in global fits. I would like to thank for their help with the interpretation of the results Mauro Anselmino, Feng Yuan, and thanks in particular to Alexei Prokudin for many useful discussions. I also would like to thank the HERMES Collaboration, in particular Delia Hash, for providing me the numerical results of their measured asymmetries, and prof. Klaus Rith for having accepted to be the referee of this thesis, and for his comments on it.